Soils and Rocks
Volume 42, N. 3
2019

ISSN 1980-9743

Soils and Rocks

Soils and Rocks

An International Journal of Geotechnical and Geoenvironmental Engineering

Volume 42, N. 3
September-December 2019

SOILS and ROCKS

An International Journal of Geotechnical and Geoenvironmental Engineering

Editor Paulo Scarano Hemsi - Aeronautics Institute of Technology, Brazil

Co-editor José Couto Marques - University of Porto, Portugal

Soils and Rocks publishes papers in English in the broad fields of Geotechnical Engineering, Engineering Geology and Geoenvironmental Engineering. The Journal is published in April, August and December. Subscription price is US$ 90.00 per year. The journal, with the name "Solos e Rochas", was first published in 1978 by the Graduate School of Engineering, Federal University of Rio de Janeiro (COPPE-UFRJ). In 1980 it became the official magazine of the Brazilian Association for Soil Mechanics and Geotechnical Engineering (ABMS), acquiring the national character that had been the intention of its founders. In 1986 it also became the official Journal of the Brazilian Association for Engineering Geology and the Environment (ABGE) and in 1999 became the Latin American Geotechnical Journal, following the support of Latin-American representatives gathered for the Pan-American Conference of Guadalajara (1996). In 2007 the journal acquired the status of an international journal under the name of Soils and Rocks, published by the Brazilian Association for Soil Mechanics and Geotechnical Engineering (ABMS), Brazilian Association for Engineering Geology and the Environment (ABGE) and Portuguese Geotechnical Society (SPG). In 2010, ABGE decided to publish its own journal and left the partnership.

Soils and Rocks

1978,	1 (1, 2)
1979,	1 (3), 2 (1,2)
1980-1983,	3-6 (1, 2, 3)
1984,	7 (single number)
1985-1987,	8-10 (1, 2, 3)
1988-1990,	11-13 (single number)
1991-1992,	14-15 (1, 2)
1993,	16 (1, 2, 3, 4)
1994-2010,	17-33 (1, 2, 3)
2011,	34 (1, 2, 3, 4)
2012-2018,	35-41 (1, 2, 3)
2019,	**42 (1, 2, 3),**

ISSN 1980-9743 CDU 624.131.1

“Ad hoc” Reviewers (2019)

Adilson do Lago Leite
UFOP
Adrian Torrico Siacara
USP
Adriana Ahrendt Talamini
UFPR
Aldo Durand Farfán
UENF
Alex Sy
KLOHN
Ana Elisa Silva de Abreu
UNICAMP
Ana Paula Fernandes Silva
UNL
Ana Vieira
LNEC
André Luis Brasil Cavalcante
UnB
André Pacheco de Assis
UnB
António Alberto Correia
UC
António Roque
LNEC
Antonio Thomé
UPF
Armando Manuel Nunes Antão
UNL
Bernadete Ragoni Danziger
UERJ
Bruna de Carvalho Faria Lima Lopes
Strathclyde
Bruno Teixeira Lima
UFF
Camila Woldam Clemente
UFPR
Carina Maria Lins Costa
UFRN
Caroline Tomazoni Santos
UFPR
Cássio Eduardo L. de Paiva
UNICAMP
Celeste Jorge
LNEC
Celso Romanel
PUC Rio
Cláudio Fernado Mahler
UFRJ
Cláudio Michael Wolle
USP
Cristhian Mendoza
UN Colombia
Denise Gerscovich
UERJ
Diego de Freitas Fagundes
FURG
Dimas Betioli Ribeiro
ITA
Eda Quadros
ISRM
Eder Carlos Guedes dos Santos
UFGO
Edgar Rodriguez Rincon
UM Nueva Granada
Edmundo Rogério Esquível
USP
Eduardo Fortunato
LNEC
Elisabeth Ritter
UERJ
Eloi Campos
UnB
Ennio Marques Palmeira
UnB
Erisvaldo Juvêncio
FIOCRUZ
Fernando Schnaid
UFRGS
Filipe Telmo Jeremias
LNEC
Francesco Tinti
U Bologna
Francisco Rezende Lopes
UFRJ
Gilson de F.N. Gitirana Jr.
UFGO
Giovana Bizão Georgetti
UFU
Gisleine Coelho de Campos
IPT
Gregório Luís Silva Araújo
UnB
Gustavo Rocha Vianna
Novasolo
Helena Polivanov
UFRJ
Heraldo Luiz Giacheti
UNESP
Heraldo Nunes Pitanga
UFV
Indiara Giugni
Consultant
Isabel Lopes
TPF
Isabela Monici Raimondi
USP
Jair de Jesus Arrieta Baldovino
UTFPR
Jean Lucas de Passos Belo
ITA
Jean Rodrigo Garcia
UFU
Jefferson Lins da Silva
USP
João Alexandre Paschoalin Filho
U Nove de Julho
João Bilé Serra
LNEC
João Francisco Alves Silveira
SBB
João Marcos Vaillant
CEFET
Joaquim Carlos Barbosa Queiróz
UFPA
Joaquim Teodoro Romão Oliveira
UNICAP
John Small
U Sydney
José Grazina
UC
José Maria de Barros
IPT
José Orlando Avesani Neto
USP
José Tadeu Balbo
USP
Juliana Gardenalli Freitas
UNIFESP
Juliana Lukiantchuki
UEM
Kátia Vanessa Bicalho
UFES
Kurt André Amann
FEI
Leonardo Becker
UFRJ
Luís Ribeiro e Sousa
UP
Luísa Braga
LNEC
Manoel Isidro Miranda Neto
UFF
Márcio Fernandes Leão
UFV
Marco Antônio Alcantara
UNESP
Marcus Guadagnin Moravia
ITA
Marcus Pacheco
UERJ
Mariana Consiglio Kasemodel
USP
Mário Vicente Riccio Filho
UFJF
Marlísio Oliveira Cecílio Junior
Bureau
Mauricio Sales
UFGO
Michal Sejnoha
Czech Tech U
Miguel Pando
U North Carolina
Miriam Gonçalves Miguel
UNICAMP
Miroslav Broucek
Czech Tech U
Moisés Failache
U São Carlos
Nima Rostami Alkhorshid
UFI
Nuno M. da Costa Guerra
UNL
Nuno Raposo
I P Viseu
Olavo Francisco dos Santos Jr.
UFRN
Otávio Coaracy Brasil Gandolfo
IPT
Paola Arab
USP
Paola Monaco
U L’ Aquila
Patrício Pires
UFES
Paulo César Lodi
UNESP
Paulo Coelho
UC
Paulo Gustavo Cavalcante Lins
UFBA
Paulo José Rocha Albuquerque
UNICAMP
Pedro Domingos Marques Prietto
UPF
Pedro Guedes de Melo
CONSULGEO
Pérsio Leister de Almeida Barros
UNICAMP
Pierre Breul
U Clermont Auvergne
Rafaela Cardoso
IST
Renato Angelim
UFGO
Renato Pinto Cunha
UnB
Rodolfo Moreda Mendes
CEMADEN
Rogério Mota
LNEC
Rogerio Pinto Ribeiro
USP
Ronaldo Alves Medeiros Jr.
UFPR
Ronaldo Lima Gomes
UESC
Sérgio Filipe Veloso Marques
UFRGS
Tácio de Campos
PUC Rio
Tallyta da Silva Curado
IFGO
Tatiana Tavares Rodriguez
UFJF
Thiago Luiz Coelho Morandini
CEFET
Thiago Porto
UFOP
Waldemar Coelho Hachich
USP
Werner Bilfinger
Vecttor

ISSN 1980-9743

SOILS and ROCKS

An International Journal of Geotechnical and Geoenvironmental Engineering

Publication of

ABMS - Brazilian Association for Soil Mechanics and Geotechnical Engineering

SPG - Portuguese Geotechnical Society

Volume 42, N. 3, September-December 2019

Table of Contents

Articles

Static and Seismic Pile Foundation Design by Load Tests and Calculation Models

(3rd Dr. Victor de Mello Goa Lecture, presented on September 20th, 2019, in Farmagudi, Goa, India)

P.S. Sêco e Pinto

Abstract. In this paper geotechnical design is addressed and particularly Static and Seismic Pile Foundation Design by Load Tests and Calculation Models. Within this framework Eurocode 7 - *Geotechnical Design* and Eurocode 8 - *Design of Structures for Earthquake Resistance* are introduced. The ultimate limit states and the serviceability limit states are discussed. Potential liquefiable soils and remedial measures are addressed. Two case histories related with pile design, namely the New Tagus bridge foundation design and the pile design and liquefaction potential evaluation of Leziria bridge foundations based in Eurocodes 7 and 8, are presented. Some conclusions are drawn.

Keywords: bridges, case histories, eurocodes, liquefaction, pile foundations.

Foreword

Prof. Victor de Mello acted as President of the International Society for Soil Mechanics and Foundations Engineering during the tenure 1981-1985 and will be remembered for his actions and passion to implement geotechnical activities worldwide.

Professor Victor de Mello is a man of prodigious energy and fine intellect. A genial thinker, Victor de Mello was one the bright talents that have enlightened the Geotechnical Engineering road.

I had the opportunity to meet Prof. Victor de Mello in Mozambique in 1972, when he was acting as Consulting Expert for Massingir dam and I was initiating my first steps in geotechnical engineering. My debt of gratitude for him is so huge and I would like to recall this Master who taugh me to think, to investigate, to be in Geotechnique and whose friendship was for me a great lesson.

Professor Victor de Mello was often invited to be Keynote Speaker at international conferences of geotechnical engineering and other events and we always listened to his lectures with great interest and pleasure, as they were challenging and opened new avenues of research.

I would like to highlight from Prof. Victor de Mello outstanding curriculum: i) his solid scientific background and research contributions to the advancement of knowledge of embankment dams and special foundations; ii) his significant contribution as author/co-author of papers for Journals, widely accepted throughout the world; (iii) his excellent lecturing and teaching ability to communicate, to support and to encourage students; (iv) his skill to establish synergies with Industry.

His legacy will last for many generations and will always be a source of great inspiration for all geotechnical engineers.

Victor de Mello has oriented his existence to a great and noble ideal and has always taught us that the correct method to learn science is to pursue the discovery of the scientific truth.

His legacies, where the Scientist, the Professor and the Engineer are integrated into one soul, were the beauty and the truth friendly given. I believe that everybody will fully agree with me in classifying his activity with five E's - Exciting, Elegant, Efficient, Excellent and Extraordinary. But it is not sufficient to remember the Master, it is important to follow his example, to give continuity with energy and perseverance to his heritage. This will be the best contribution of the current and next generations to honor Victor de Mello memory.

1. Introduction

The Commission of the European Communities (CEC) initiated in 1975 the establisment of a set of harmonized technical rules for the structural and geotechnical design of buildings and civil engineering works based on article 95 of the EC Treaty. In a first stage, they would serve as alternative to the national rules applied in the various Member States and in a final stage they will replace them.

From 1975 to 1989, the Commission, with the help of a Steering Committee with Representatives of the Member Ststes, developed the Eurocodes programme.

The Commission, the Member states of the EU and EFTA decided in 1989, based on an agreement between the Commission and CEN, to transfer the preparation and the publication of the Eurocodes to CEN.

Pedro S. Sêco e Pinto, Dr., Consulting Geotechnical Engineer, National Laboratory of Civil Engineering (LNEC), University of Coimbra, Coimbra, ISSMGE President (2005-2009), Portugal. e-mail: pinto.pss@gmail.com.
Invited Lecture, no discussions.
DOI: 10.28927/SR.423211

The Structural Eurocode programme comprises the following standards:

EN 1990 Eurocode - Basis of structural design
EN 1991 Eurocode 1 - Actions on structures
EN 1992 Eurocode 2 - Design of concrete structures
EN 1993 Eurocode 3 - Design of steel structures
EN 1994 Eurocode 4 - Design of composite steel and concrete structures
EN 1995 Eurocode 5 - Design of timber structures
EN 1996 Eurocode 6 - Design of masonry structures
EN 1997 Eurocode 7 - Geotechnical design
EN 1998 Eurocode 8 - Design of structures for earthquake resistance
EN 1999 Eurocode 9 - Design of aluminium structures.

The work performed by the Commission of the European Communities (CEC) in preparing the "Structural Eurocodes" in order to establish a set of harmonised technical rules is impressive.

The current tendency is to prepare unified codes for different regions but keeping the freedom for each country to choose the safety level defined in each National Document of Application. The global safety factor was replaced by partial safety factors applied to actions and to the strength of materials.

In this lecture, a summary of the main topics covered by Eurocodes 7 and 8 for Static and Seismic Pile Foundation Design by Load Tests and Calculation Models is addressed for a better understanding of the New Tagus and Leziria bridges foundation design.

In dealing with these topics, we should never forget the memorable lines of Lao-Tze, Maxin 64 (550 B.C.):

> *"The journey of a thousand miles begins with one step".*

2. Eurocode 7 - Geotechnical Design

2.1. Introduction

The Eurocode 7 (EC7) "Geotechnical Design" gives a general basis for the geotechnical aspects of the design of buildings and civil engineering works. A link is established between the design requirements addressed in Part 1 and the results of laboratory tests and field investigations run according to standards, codes and other accepted documents covered by Part 2.

EN 1997 is concerned with the requirements for strength, stability, serviceability and durability of structures. Other requirements, *e.g.* concerning thermal or sound insulation, are not considered.

2.2. Eurocode 7 - Geotechnical design - Part 1

The following subjects are covered in EN 1997-1 - Geotechnical Design:

Section 1: General
Section 2: Basis of geotechnical design
Section 3: Geotechnical data
Section 4: Supervision of construction, monotoring and maintenance
Section 5: Fill, dewatering, ground improvement and reinforcement
Section 6: Spread foundations
Section 7: Pile foundations
Section 8: Anchorages
Section 9: Retaining structures
Section 10: Hydraulic failure
Section 11: Overall stability
Section 12: Embankments.

2.2.1. Design requirements

The following factors shall be considered when determining the geotechnical design requirements:

- site conditions with respect to overall stability and ground movements;
- nature and size of the structure and its elements, including any special requirements such as the design life;
- conditions with regard to its surroundings (neighbouring structures, traffic, utilities, vegetation, hazardous chemicals, etc.);
- ground conditions;
- groundwater conditions;
- regional seismicity;
- influence of the environment (hydrology, surface water, subsidence, seasonal changes of temperature and moisture

For each geotechnical design situation it shall be verified that no relevant limit state is exceeded.

Limit states can occur either in the ground or in the structure or by combined failure in the structure and the ground.

Limit states should be verified by one or a combination of the following methods: design by calculation, design by prescriptive measures, design by load tests and experimental models and an observational method.

To establish geotechnical design requirements, three Geotechnical Categories, 1, 2 and 3 are introduced:

- Geotechnical Category 1 includes small and relatively simple structures.
- Geotechnical Category 2 includes conventional types of structure and foundation with no exceptional risk or difficult soil or loading conditions.
- Geotechnical Category 3 includes: (i) very large or unusual structures; (ii) structures involving abnormal risks, or unusual or exceptionally difficult ground or loading conditions; and (iii) structures in highly seismic areas.

2.2.2. Geotechnical design by calculation

Design by calculation involves:

- actions, which may be either imposed loads or imposed displacements, for example from ground movements;
- properties of soils, rocks and other materials;

- geometrical data;
- limiting values of deformations, crack widths, vibrations, etc.
- calculation models.

The calculation model may consist of: (i) an analytical model; (ii) a semi-empirical model; or (iii) a numerical model.

Where relevant, it shall be verified that the following limit states are not exceeded:

- loss of equilibrium of the structure or the ground, considered as a rigid body, in which the strengths of structural materials and the ground are insignificant in providing resistance (EQU);
- internal failure or excessive deformation of the structure or structural elements, including footings, piles, basement walls, etc., in which the strength of structural materials is significant in providing resistance (STR);
- failure or excessive deformation of the ground, in which the strength of soil or rock is significant in providing resistance (GEO);
- loss of equilibrium of the structure or the ground due to uplift by water pressure (buoyancy) or other vertical actions (UPL);
- hydraulic heave, internal erosion and piping in the ground caused by hydraulic gradients (HYD).

The selection of characteristic values for geotechnical parameters shall be based on derived values resulting from laboratory and field tests, complemented by well-established experience.

The characteristic value of a geotechnical parameter shall be selected as a cautious estimate of the value affecting the occurrence of the limit state.

For limit state types STR and GEO in persistent and transient situations, three Design Approaches are outlined. They differ in the way they distribute partial factors between actions, the effects of actions, material properties and resistances. In part, this is due to differing approaches to the way in which allowance is made for uncertainties in modeling the effects of actions and resistances.

In Design Approach 1, partial factors are applied to actions, rather than to the effects of actions and ground parameters.

In Design Approach 2, partial factors are applied to actions or to the effects of actions and to ground resistances.

In Design Approach 3, partial factors are applied to actions or the effects of actions from the structure and to ground strength parameters.

It shall be verified that a limit state of rupture or excessive deformation will not occur.

It shall be verified serviceability limit states in the ground or in a structural section, element or connection.

2.2.3. Design by prescriptive measures

In design situations where calculation models are not available or not necessary, the exceedance of limit states may be avoided by the use of prescriptive measures. These involve conventional and generally conservative rules in the design, and attention to specification and control of materials, workmanship, protection and maintenance procedures.

2.2.4. Design by load tests and experimental models

When the results of load tests or tests on large or small scale models are used to justify a design, the following features shall be considered and allowed for:

- differences in the ground conditions between the test and the actual construction;
- time effects, especially if the duration of the test is much less than the duration of loading of the actual construction;
- scale effects, especially if small models are used. The effect of stress levels shall be considered, together with the effects of particle size.

Tests may be carried out on a sample of the actual construction or on full scale or smaller scale models.

2.2.5. Observational method

When prediction of geotechnical behaviour is difficult, it can be appropriate to apply the approach known as “the observational method”, in which the design is reviewed during construction.

The following requirements shall be met before construction is started:

- the limits of behaviour which are acceptable shall be established;
- the range of possible behaviour shall be assessed and it shall be shown that there is an acceptable probability that the actual behaviour will be within the acceptable limits;
- a plan of monitoring shall be devised, which will reveal whether the actual behaviour lies within the acceptable limits. The monitoring shall make this clear at a sufficiently early stage and with sufficiently short intervals to allow contingency actions to be undertaken successfully;
- the response time of the instruments and the procedures for analyzing the results shall be sufficiently rapid in relation to the possible evolution of the system;
- a plan of contingency actions shall be devised, which may be adopted if the monitoring reveals behaviour outside acceptable limits.

2.3. Eurocode 7 - Part 2

EN 1997-2 is intended to be used in conjunction with EN 1997-1 and provides rules supplementary to EN 1997-1 related to the:

- planning and reporting of ground investigations;
- general requirements for a number of commonly used laboratory and field tests;
- interpretation and evaluation of test results;
- derivation of values of geotechnical parameters and coefficients.

The field investigation programme shall contain:

- a plan with the locations of the investigation points including the types of investigations;
- the depth of the investigations;
- the type of samples (category, etc.) to be taken including specifications on the number and depth at which they are to be taken;
- specifications on the groundwater measurement;
- the types of equipment to be used;
- the standards that are to be applied.

The laboratory test programme depends in part on whether comparable experience exists.

The extent and quality of comparable experience for the specific soil or rock should be established.

The results of field observations on neighbouring structures, when available, should also be used.

The tests shall be run on specimens representative of the relevant strata. Classification tests shall be used to check whether the samples and test specimens are representative.

This can be checked in an iterative way. In a first step, classification tests and strength index tests are performed on as many samples as possible to determine the variability of the index properties of a stratum. In a second step, the representativeness of strength and compressibility tests can be checked by comparing the results of the classification and strength index tests of the tested sample with entire results of the classification and strength index tests of the stratum.

Figure 1 shows the flow chart that demonstrates the link between design and field and laboratory tests. The design part is covered by EN 1997-1; the parameter values part is covered by EN 1997-2.

3. Eurocode 8 - Design of Structures for Earthquake Resistance

3.1. Introduction

Eurocode 8 (EC8), "Design of Structures for Earthquake Resistance", deals with the design and construction of buildings and civil engineering works in seismic regions and it is divided in six Parts.

Part 1 is divided in 10 sections:

Section 1 - contains general rules, seismic actions and rules for buildings;

Section 2 - contains the basic performance requirements and compliance criteria applicable to buildings and civil engineering works in seismic regions;

Section 3 - gives the rules for the representation of seismic actions and their combination with other actions;

Section 4 - contains general design rules relevant specifically to buildings;

Section 5 - presents specific rules for concrete buildings;

Section 6 - gives specific rules for steel buildings;

Section 7 - contains specific rules for composite steel-concrete buildings;

Section 8 - presents specific rules for timber buildings;

Section 9 - gives specific rules for masonry buildings;

Section 10 - contains fundamental requirements and other relevant aspects for the design and safety related to base isolation.

Further Parts include the following:

Part 2 contains provisions relevant to bridges.

Part 3 presents provisions for the seismic strengthening and repair of existing buildings.

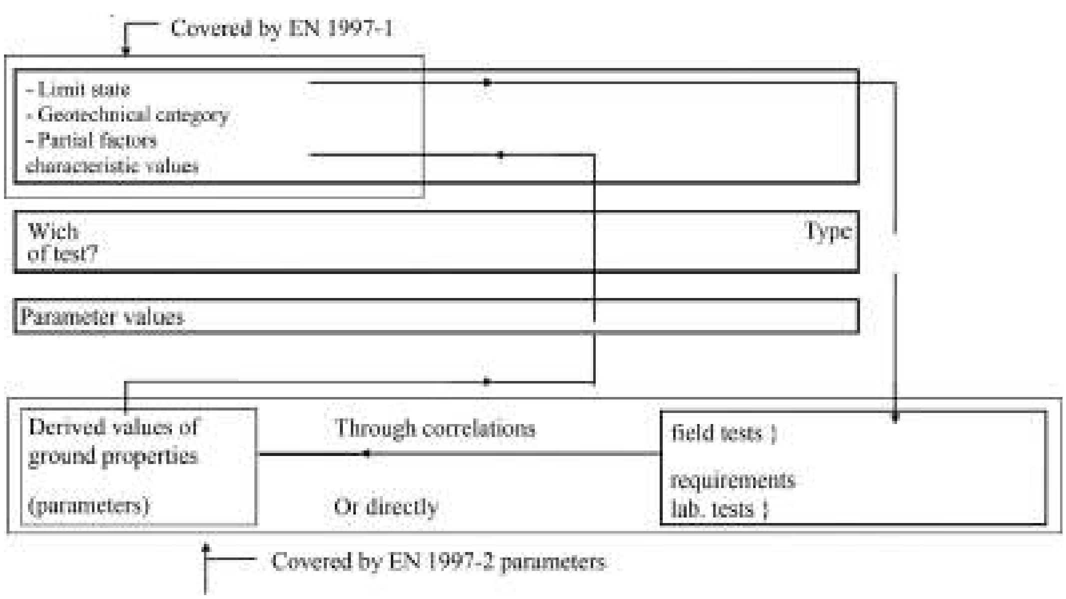

Figure 1 - Flow chart that demonstrates the link between design and field and laboratory tests.

Part 4 gives specific provisions relevant to tanks, silos and pipelines.

Part 5 contains specific provisions relevant to foundations, retaining structures and geotechnical aspects and complements the rules of Eurocode 7, which do not cover the special requirements of seismic design.

Part 6 presents specific provisions relevant to towers, masts and chimneys.

3.2. Seismic action

The definition of Actions (with the exception of seismic actions) and their combinations is treated in Eurocode 1 "Actions on Structures".

In general, the national territories are divided by the National Authorities into seismic zones, depending on the local hazard.

The earthquake motion in EC 8 is represented by the elastic response spectrum definedα_g by 3 components.

In EC 8, in general, the hazard is described in terms of a single parameter, *i.e.* the value α_g of the effective ground acceleration in rock or firm soil called "design ground acceleration" (Fig. 2) expressed in terms of: a) the reference seismic action associated with a probability of exceedance (P_{NCR}) of 10 % in 50 years; or b) a reference return period (T_{NCR}) = 475, where: S_e (T) elastic response spectra, T: vibration period of a linear single-degree-of-freedom system, α_g: design ground acceleration, T_B, T_C: limits of the constant spectral acceleration branch, T_D: value defining the beginning of the constant displacement response range of the spectra, S: soil factor with reference value 1.0 for subsoil class A, η: damping correction factor with reference value 1.0 for 5 % viscous damping.

It is recommended the use of two types of spectra: Type 1 if the earthquake has a surface wave magnitude, M_s, greater than 5.5, and Type 2 in other cases.

The seismic motion may also be represented by ground acceleration time-histories and related quantities (velocity and displacement).

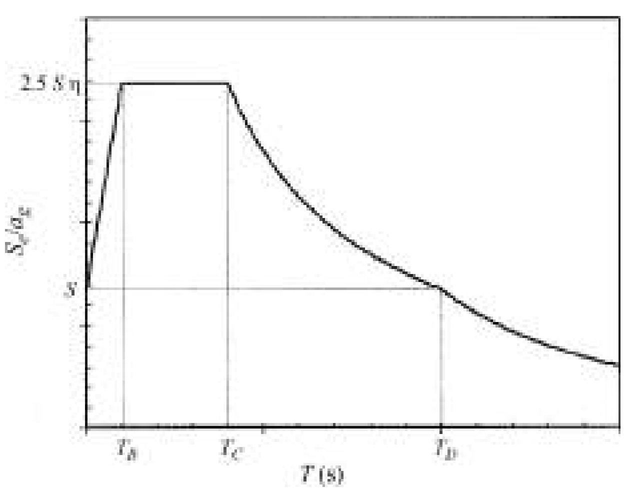

Figure 2 - Elastic response spectra (after EC8).

Artificial accelerograms shall match the elastic response spectrum. The number of the accelerograms to be used shall give a stable statistical measure (mean and variance) and a minimum of 3 accelerograms should be used and also some others requirements should be satisfied.

For structures with special characteristics, spatial models of the seismic action shall be used based on the principles of the elastic response spectra.

3.3. Ground conditions and soil investigations

For the ground conditions five ground types A, B, C, D and E are considered:

Ground type A - rock or other geological formation, including at most 5 m of weaker material at the surface, characterized by a shear wave velocity V_s of at least 800 m/s;

Ground type B - deposits of very dense sand, gravel or very stiff clay, at least several tens of m in thickness, characterized by a gradual increase of mechanical properties with depth shear wave velocity between 360-800 m/s, N_{SPT} > 50 blows and c_u > 250 kPa.

Ground type C - deep deposits of dense or medium dense sand, gravel or stiff clay with thickness from several tens to many hundreds of meters, characterized by a shear wave velocity from 160 m/s to 360 m/s, N_{SPT} from 15 to 50 blows and c_u from 70 to 250 kPa.

Ground type D - deposits of loose to medium cohesionless soil (with or without some soft cohesive layers), or of predominantly soft to firm cohesive soil, characterized by a shear wave velocity less than 180 m/s, N_{SPT} less than 15 and c_u less than 70 kPa.

Ground type E - a soil profile consisting of a surface alluvium layer with *Vs*,30 values of type C or D and thickness varying between about 5 m and 20 m, underlain by stiffer material with *Vs*,30 > 800 m/s.

Ground type S_1 - deposits consisting - or containing a layer at least 10 m thick - of soft clays/silts with high plasticity index (PI > 40) and high water content, characterized by a shear wave velocity less than 100 m/s and c_u between 10-20 kPa.

Ground type S_2 - deposits of liquefiable soils, of sensitive clays, or any other soil profile not included in types A-E or S_1.

For the five Ground type the recommended values for the parameters S, T_B, T_C, T_D, for Type 1 and Type 2 are given in Tables 1 and 2.

The recommended Type 1 and Type 2 elastic response spectra for ground types A to E are shown in Figs. 3 and 4.

The recommended values of the parameters for the five ground types A, B, C, D and E for the vertical spectra are shown in Table 3. These values are not applied for ground types S_1 and S_2.

Table 1 - Values of the parameters describing the Type 1 elastic response spectra.

Ground type	S	T_B (s)	T_C (s)	T_D (s)
A	1.0	0.15	0.4	2.0
B	1.2	0.15	0.5	2.0
C	1.15	0.20	0.6	2.0
D	1.35	0.20	0.8	2.0
E	1.4	0.15	0.5	2.0

Table 2 - Values of the parameters describing the Type 2 elastic response spectra.

Ground type	S	T_B (s)	T_C (s)	T_D (s)
A	1.0	0.05	0.25	1.2
B	1.35	0.05	0.25	1.2
C	1.5	0.10	0.25	1.2
D	1.8	0.10	0.30	1.2
E	1.6	0.05	0.25	1.2

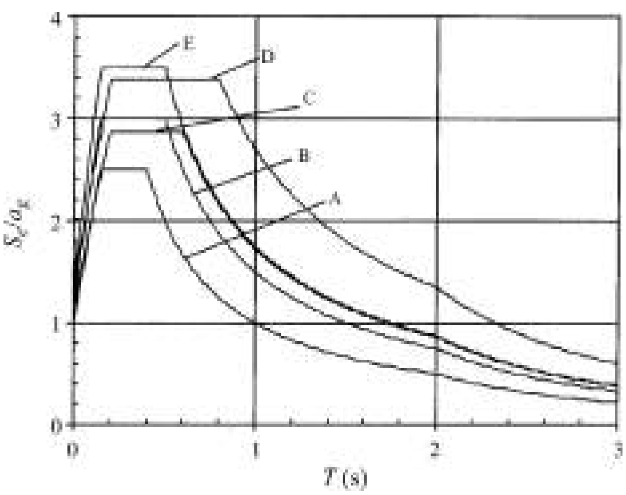

Figure 3 - Recommended Type 1 elastic response spectra (after EC8).

4. Foundation Design

4.1. Introduction

The foundation system is presented, with particularly emphasis to soil-structure interaction. The serviceability limit states are introduced.

For pile design, the following limit states shall be considered (Eurocode 7, 1997a): (i) loss of overall stability; (ii) bearing resistance failure of the pile foundation; (iii) uplift or insufficient tensile resistance of the pile foundation; (iv) failure in the ground due to transverse loading of the pile foundation; (v) structural failure of the pile in compression, tension, bending, buckling or shear; (vi) combined failure in the ground and in the pile foundation; (vii) combined failure in the ground and in the structure; (viii) excessive settlement; (ix) excessive heave; (x) excessive lateral movement of the ground; and (xi) unacceptable vibrations.

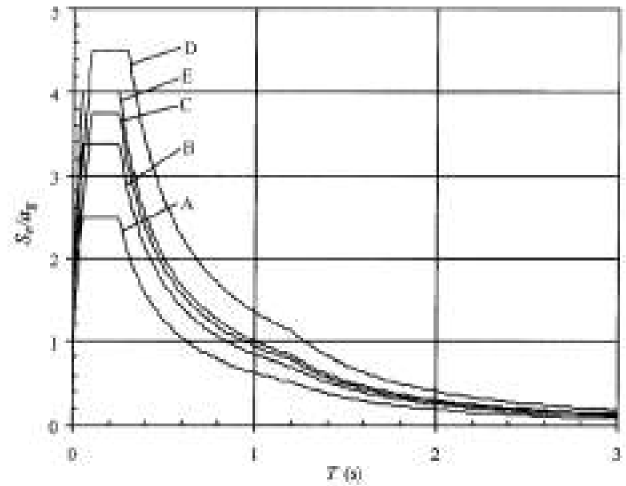

Figure 4 - Recommended Type 2 elastic response spectra (after EC8).

Table 3 - Recommended values of the parameters for the vertical elastic response spectra.

Spectrum	α_{vg}/α_g	T_B (s)	T_C (s)	T_D (s)
Type 1	0.9	0.05	0.15	1.0
Type 2	0.45	0.05	0.15	1.0

For the Soil-Structure Interaction (SSI) the design engineers ignore the kinematic component, considering a fixed base analysis of the structure, due to the following reasons: (i) in some cases the kinematic interaction may be neglected; (ii) aseismic building codes, with a few exceptions *e.g.* Eurocode 8 do not refer it; (iii) kinematic interaction effects are more difficult to assess than inertial forces.

For slender tall structures, structures founded in very soft soils and structures with deep foundations, the SSI plays an important role.

The Eurocode 8 states:" Bending moments developing due to kinematic interaction shall be computed only when two or more of the following conditions occur simultaneously: (i) the ground profile is of class D, S_1 or S_2, and contains consecutive layers with sharply differing stiffness; (ii) the zone is of moderate or high seismicity, $\alpha > 0.10$; (iii) the supported structure is of importance class I or II".

Piles and piers shall be designed to resist the following action effects: (i) inertia forces from the superstructure; and (ii) kinematic forces resulting from the deformation of the surrounding soil due to the propagation of seismic waves (Fig. 5). The decomposition of the problem in steps is shown in Fig. 5 (Gazetas & Mylonakis, 1998).

The complete solution is a very time consuming 3D analysis.

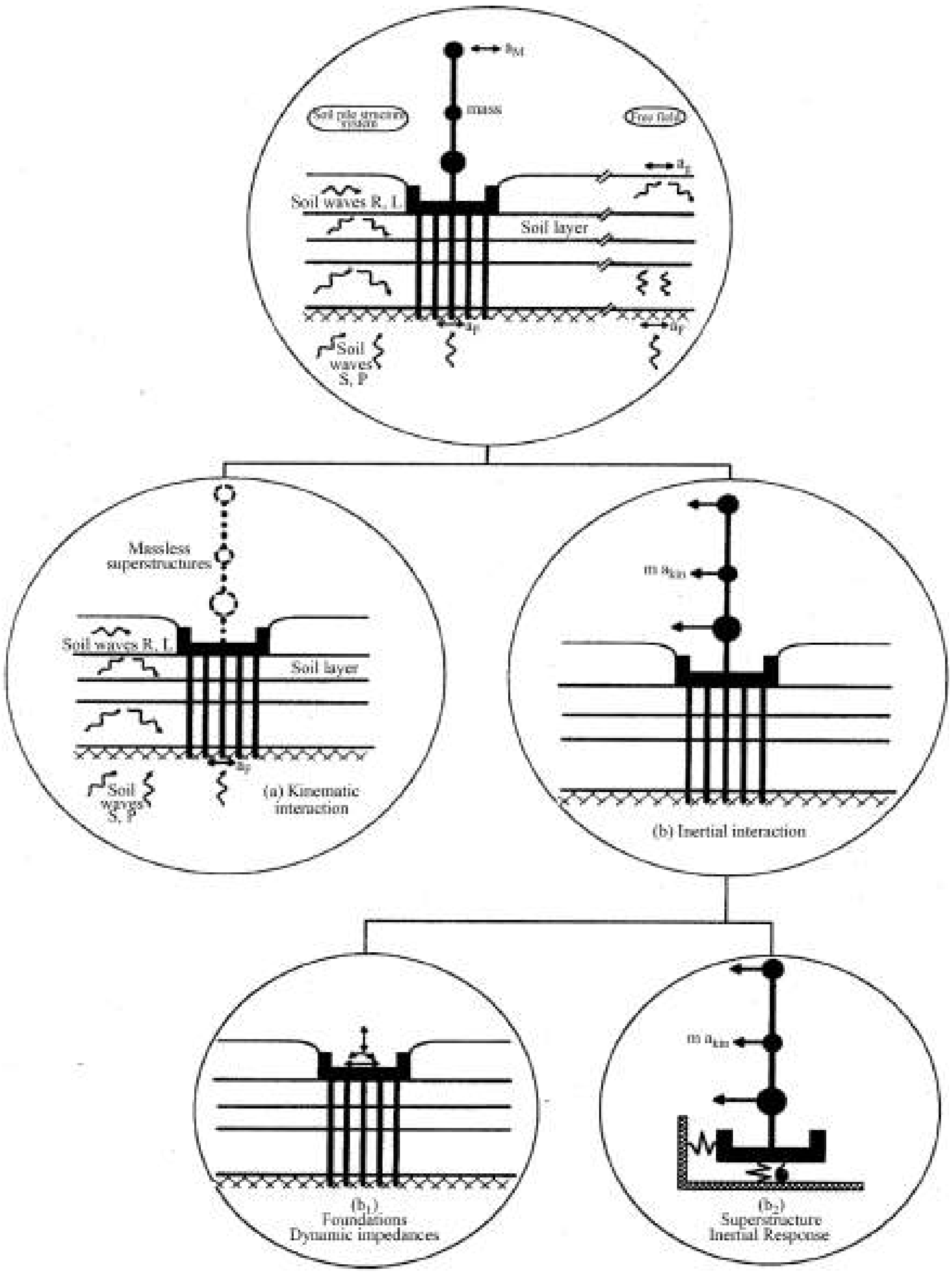

Figure 5 - Soil-structure interaction problem (after Gazetas & Mylonakis, 1998).

To analyze the internal forces along the pile, as well as the deflection and rotation at the pile head, discrete models (based in Winkler spring model) or continuum models can be used.

For simplicity a linear soil behaviour is assumed.

The following effects shall be included: (i) flexural stiffness of the pile; (ii) soil reactions along the pile; (iii) pile-group effects; and (iv) the connection between pile and structure.

4.2. Serviceability limit states

To prevent the occurrence of an ultimate limit state or a serviceability limit state the foundation movements shall not reach certain limit values (Sêco e Pinto & Sousa Coutinho, 1991).

Burland & Wroth (1974) proposed a consistent set of definitions based on the displacements, that are illustrated in Fig. 6:

- rotation (θ) is the change in gradient of a line joining two reference points;
- the angular strain (α), defined in Fig. (6a), is positive for upward concavity (sagging) and negative for downward concavity (hogging);
- relative deflection (Δ) is the displacement of a point relative to the line connecting two reference points on either side (see Fig. 6(b));

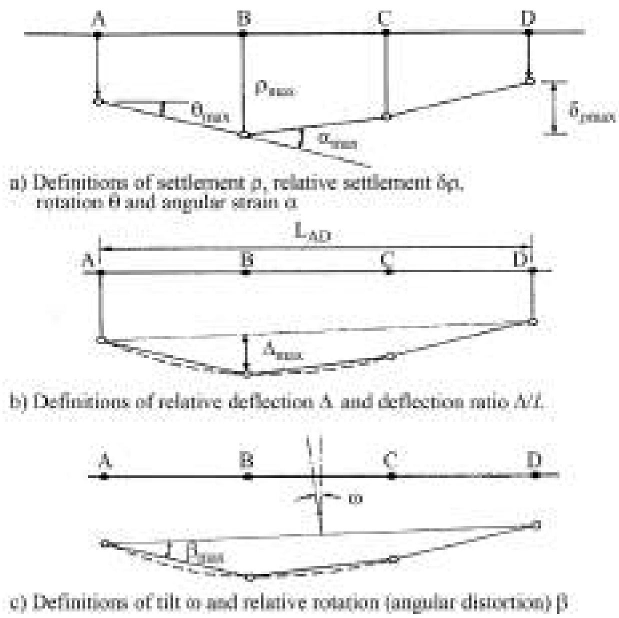

Figure 6 - Definition of foundation movements (after Burland & Wroth, 1974).

- relative rotation β - is the rotation of the line joining two points;
- average horizontal strain (e_n) is defined as the change of length δ_L over the length L.
- deflection rate Δ/L, where L is the distance between the two reference points defining Δ;
- tilt (w) describes the rigid body rotation.

Table 4 presents a summary of allowable deformations proposed by different authors and EC7.

Following EC7, the settlements for pile foundations for ultimate limit states and serviceability limit states shall include:

- the settlement of a single pile;
- the additional settlement due to group action.

The selection of design values for limiting movements shall take account of the following:

(i) the confidence to specify the acceptable value of the movement; (ii) the type of structure; (iii) the type of construction material; (iv) the type of foundation; (v) the type of ground; (vi) the mode of deformation; and (vii) the proposed use of the structure.

Bozozuk (1981), based on the observation of 150 cases related with the allowable displacemet in bridge foundation piles, has proposed the limits for vertical and horizontal settlement, S_V and S_H, defined in Table 5.

Moulton (1986) based on the analysis of 314 bridges located in the United States and Canada has confirmed the proposal of Bozozuk (1981).

Burland *et al.* (1977) have proposed 6 categories for damage in buildings shown in Table 6, where categories 0, 1 and 2 are related with esthetic damage, categories 3 and 4 are related with serviceability limit states and category 5 with ultimate limit states (stability).

Burland *et al.* (1977) have introduced the concept of limiting tensile strain, ε_{lim}, to define the ultimate limit state.

Boscardin & Cording (1989) develop the concept of differing levels of tensile strain and based on the analysis of 17 cases have proposed Table 7 to establish the relationship

Table 4 - Allowable deformations.

A - Concrete buildings and reinforced walls					
Allowable values for rotations	Skempton & MacDonald (1956)	Meyerhof (1956)	Polshin & Tokar (1957)	Bjerrum (1963)	EC7 (1994)
Structural damage & cracks on walls	1/150	1/250	1/200	1/150	1/150
	1/300	1/500	1/500	1/500	1/300
B - Wall without reinforcement					
Deflection ratio Δ/L	Meyerhof (1956)		Polshin & Tokar (1957)		Burland & Wroth (1975)
Deform. ∪	1/2500		$L/H < 3$ 1/3500 to 1/2500;		1/2500 $L/H = 1$
			$L/H > 5$ 1/2000 to 1/1500		1/1250 $L/H = 5$
Deform. ∩	-		-		1/5000 $L/H = 1$
					1/2500 $L/H = 5$

Table 5 - Limit values for bridge foundations (after Bozozuk, 1981).

Damage classification	Limit values
Allowable or acceptable	S_V < 50 mm
	S_H < 25 mm
With acceptable damages	50 mm = S_V = 100 mm
	25 mm = S_H = 50 mm
Non acceptable	S_V < 100 mm
	S_H > 50 mm

Table 7 - Categories of damages in buildings (after Boscarding & Cording, 1989).

Category of damage	Degree of severity	Limiting tensile strain (%)
0	Negligible	0-0.05
1	Very slight	0.05-0.075
2	Slight	0.075-0.15
3	Moderate	0.15-0.3
4 to 5	Severe to very severe	> 0.3

Table 6 - Damages categories in buildings (after Burland *et al.*, 1977).

Damage category	Degree of severity	Description of damage
0	Negligible	Hairline cracks 0.1 mm
1	Very light	Fine cracks easily treated
2	Light	Cracks easily filled
3	Moderate	Cracks required some opening
4	Severe	Extensive repair working involving breaking and replacement
5	Very severe	Major repair involving partial or complete rebuilding

between the category of damage and the limiting tensile strain.

Burland (1995) proposed three levels of risk for buildings: (i) preliminary evaluation; (ii) evaluation of second level; (iii) detailed evaluation.

The computation of the differential settlement shall take into consideration: (i) the variation of the ground properties; (ii) the distribution of loads; (iii) the construction methodology; (iv) the stiffness of the structure.

5. New Tagus Bridge

5.1. Introduction

The 18 km Tagus Bridge from Sacavém to Montijo (Lisbon, Portugal), integrates the North viaduct, the Expo viaduct, the cable stayed bridge, the central viaduct and the South viaduct (Fig. 7).

The bridge foundations are composed by bored and driven piles.

The central viaduct, 6.5 km long, is supported on 648 driven piles up to 60 m long. Related the central viaduct each pier is supported by eight piles with of 1.7 m diameter except in the vicinity of shipping channels.

Three channels cross the Tagus bridge: the main thoroughfare under the cable stayed bridge, and the piles supporting these piers are 2.2 m in diameter, to minimize possible ship impact; and two smaller channels under the central viaduct.

Driven piles were installed by large barge mounted cranes with a capacity around 58 ton.

For the foundations of the cable stayed bridge, with 0.83 km long, and the south viaduct, with 3.9 km long, bored piles were used. For the cable stayed 148 piles with 2.2 m diameter were used. For the south viaduct 60 piles with 2 m diameter and 280 piles with 1.8 m diameter were used.

For the north viaduct, 1.4 km long, and for the Expo viaduct 0.7 km long, bored piles, with 1.8 m diameter were used.

One of the most important key issues for design is the risk of earthquakes, as Lisbon was wiped out by an earthquake in 1755 with 8.5 of Richter magnitude. During a serious seismic event the new Tagus bridge will be the main access for emergency vehicles crossing the estuary.

5.2. Main geological conditions

Based on the geological data obtained by two implemented site investigation programmes, the ground is composed by the following two main units (Fig. 7), namely: a) Alluvial deposits (Al), aged Holocene and Pleistocene; and b) the bedrock under alluvial deposits, composed by Plio-Pleistocene materials.

The maximum observed thickness of Al is around 78 m and in average, its thickness varies between 60 and 70 m.

Five sub-units were identified, named a_0, a_1, a_{2a}, a_{2b} and a_3. The a_0 to a_{2b} units show the common geological structure of alluvial deposits, with lenticular or interstratified layers, with exhibiting lateral variations within each sub-unit.

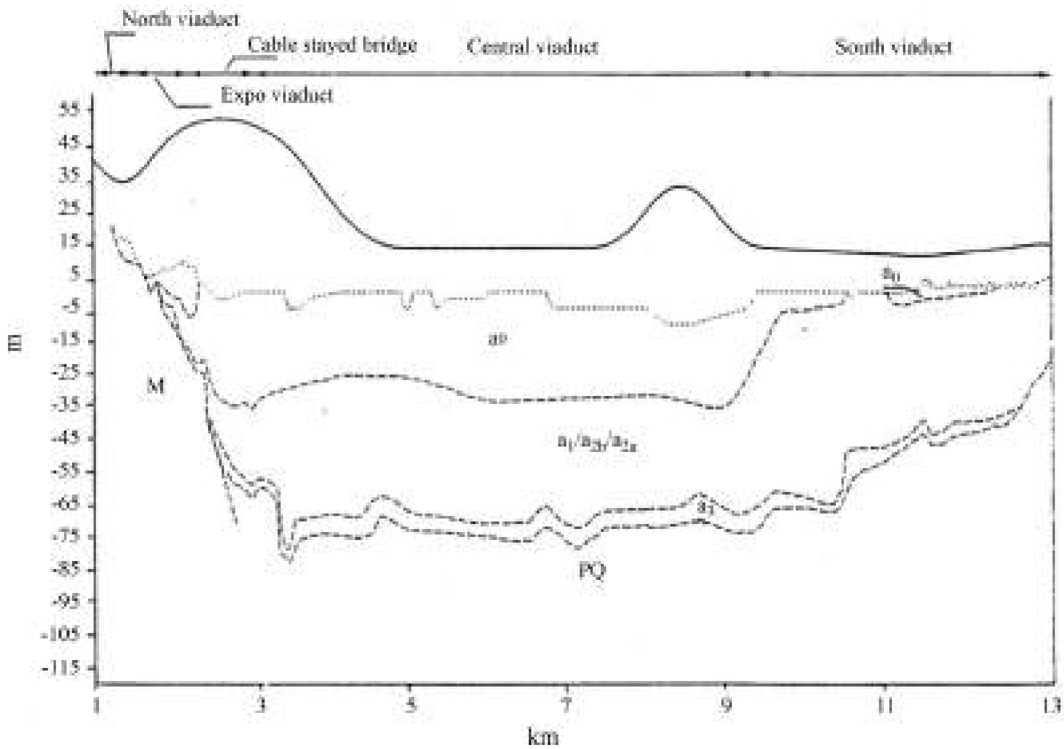

Figure 7 - Simplified geotechnical profile (after Oliveira, 1997).

At the bottom of the alluvial deposits occurs a gravel layer (a_3), integrating fine to coarse gravel, with sand, cobbles and occasionally boulders. The coarser elements (cobbles and occasionally boulders) occur scattered or concentrated in some zones, raising difficulties for the drilling equipment to cross the a_3 layer.

The general description of each type of the differentiated alluvial deposits is the following (Oliveira, 1997):

a_0: This unit is composed by silty to very silty clay (mud), dark grey, with a maximum thickness around 35 m.

a_1: Fine to medium sand with shells and shell fragments.

a_{2a}: Silty clay to clayey silt.

a_{2b}: Yellowish brown to grey medium to coarse (occasionally fine) sand.

a_3: Fine to coarse gravel, rounded to angular, with sand, cobbles and occasionally some boulders.

The bedrock under the alluvial deposits is composed by Plio-Pleistocene materials.

5.3. Pile load tests

5.3.1. Introduction

Pile load tests were performed with the following purposes:

i) to determine the response of a representative pile related the settlement and limit load;

ii) to verify the performance of individual piles and to extrapolate for the overall pile foundation behavior;

iii) to optimize the construction method.

Load tests were carried out on trial piles which were built for test purposes before the final design.

The results of load tests were used to calibrate the design parameters and to optimize pile lengths, based on the interpretation of site investigation and laboratory and situ tests (Sêco e Pinto & Oliveira, 1998).

5.3.2. Vertical pile load tests

Vertical load tests were performed on 3 piles located at main bridge (P8), central viaduct (P31) and South viaduct (P79).

The construction of bored piles has respected the following procedure:

(i) installation by vibro-driving, with a SOILMECH VTE 12000, of a permanent casing, with an exterior diameter of 1216 mm and a thickness of 8 mm, and 16 mm at the shoe level with a length of 40 m;

(ii) excavation of the soil inside the casing with a bucket of 1180 mm diameter and a SOILMECH rotary machine RT - 3ST;

(iii) boring below the bottom of the casing for a length higher than 19 m with a bucket using a polymeric drilling fluid GEOMUD - 15 mixed with salty Tagus water with the following composition: 2 kg of polymer per 1000 L of water. The mixture had a Marsh viscosity 40” and a density 1.035.

Load tests were carried out on several test piles and the test locations were representative of the pile where the most adverse ground conditions are believed to occur.

The following equipment for the vertical load tests was installed: 8 electrical displacement transducers, 2 mechanical dial gauges, 2 strips of LCPC removable extensometers, with a resolution of 10^{-6}, 1 temperature sensor, 1 high precision pressure transducer, 1 hydraulically operated pump, 4 hydraulic jacks and 1 optical level.

The loading program consisted in reaching 20000 kN with 8 load increments.

A general view for vertical pile load tests is presented in Fig. 8.

The load - settlement curves for piles P8, P31 and P 79 are shown in Fig. 9.

For the definition of the failure loads the criteria of settlement equal to 10 % of the pile diameter, *i.e.* at 120 mm settlement, was used. A comparison between the predicted failure loads, based from CPT tests, and the observed values is shown in Table 8.

Figure 8 - General view for vertical pile load tests.

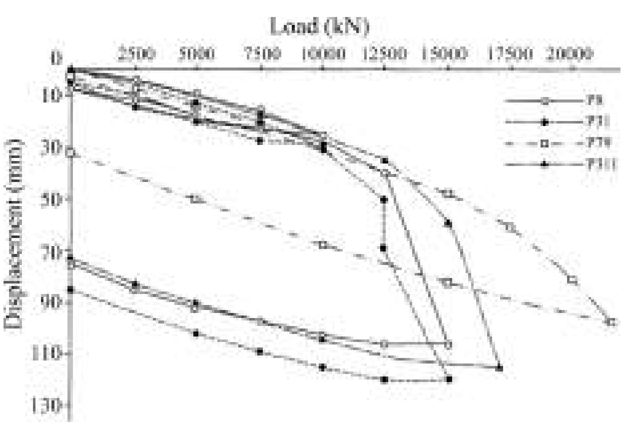

Figure 9 - Load settlement curves for vertical test.

Table 8 - Failure loads.

P8		P31		P79		P31i
m	p	m	p	m	p	m
15	20.3	15	21.4	> 21.15	> 22.7	> 17.5

m - measured. p - predicted loads in MN.

With the exception of P79 (the length of this pile was increased 10 m) the observed values are lower than the predicted loads and the difference were attributed to the lower shaft friction values. The results of P31i have shown an insufficient gain of the bearing capacity with soil grouting.

5.3.3. Horizontal pile load tests

Horizontal load tests were performed on 2 piles located at main bridge (P8) and south pylon.

The piles were constructed by the same procedure already described.

The installed equipment has integrated: (i) - horizontal displacement; (ii) - load cell; (iii) - strain along the shaft using strain gauges; (iv) - displacement along the vertical using inclinometer tubes; (v) - temperature.

The loading program consisted of: 10 load increments from 50 kN to 500 kN.

Figure 10 shows a general view for horizontal pile load tests.

To evaluate the effect of ship impact, a second series of load increments were applied, form 500 kN to 1 000 kN, for the south pylon, after 10 h.

The load displacement curve measured at 0.95 m below load level is shown in Fig. 11.

The computed values for pile displacements, bending moments and shear forces are shown in Fig. 12.

5.3.4. Dynamic pile tests

For a better characterization of the dynamic behaviour of the alluvial material for the bridge foundation a forced vibration test of a group of two piles was performed. The piles with 1.20 m of diameter and 60 m long were connected by a cap with 5.5 × 3.5 × 1.2 m.

Figure 10 - General view for horizontal pile load tests.

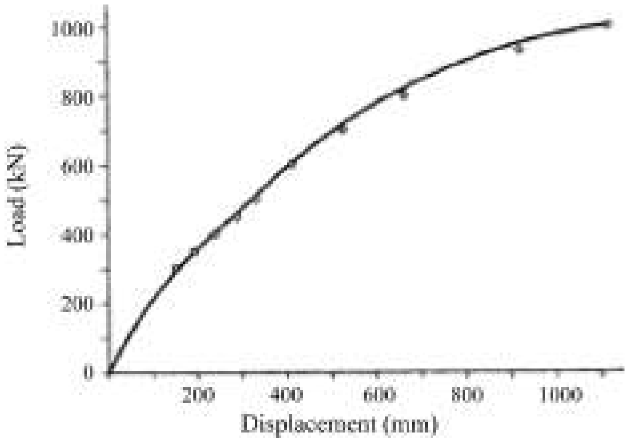

Figure 11 - Measured load displacement curve for horizontal tests.

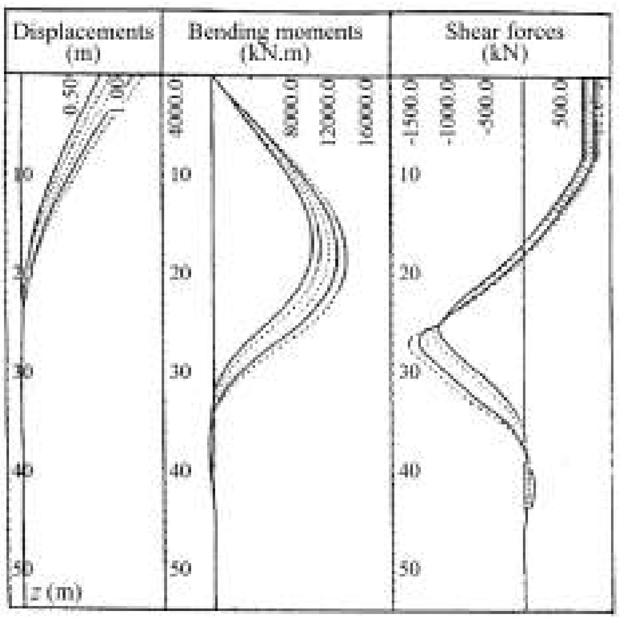

Figure 12 - Computed values for pile displacements, bending moments and shear forces.

A 3D finite element model was implemented for the interpretation of the observed behaviour. The soil - pile system was discretized with 3D finite elements of the second degree (cubic with 20 nodal points). The numerical results were compared with the observed values, in terms of displacement transfer functions.

To impose on the pile cap, harmonic horizontal loads, with different amplitudes and frequencies a shaker (Fig. 13), built in LNEC, was used.

The excitation frequencies were applied in steps of 0.1 Hz in the range from 0.5 to 20 Hz approximately.

Velocity transducers and accelerometers were installed to assess the dynamic response of the structure, for the various frequencies of excitation.

Figure 13 - General view of the shaker.

This equipment was placed in several points in order to monitoring the horizontal and vertical displacements (Fig. 14).

During the test time series of velocity were recorded on several points. The digital treatment of this time series was performed by a computer program developed at LNEC. Treated series are transported for frequency domain and the displacements were obtained by integration.

For the interpretation of the test results a 3D model was used, to represent the soil, the two piles and the cap.

For the material behavior a simplified model was adopted considering for the piles a continuous, homogenous and isotropic material with a linear and elastic behaviour. The soil was considered a continuous material, with elastic behaviour, and composed of various homogeneous layers.

Figure 15 shows the configuration of the two first modes of vibration and respective frequencies (observed and computed). The first vibration mode corresponds to the bending of both piles following a direction perpendicular to the vertical plan that encloses both of them. The second mode corresponds to the bending of both piles in the vertical plan that contains them.

Figure 14 - General view of the velocity transducers.

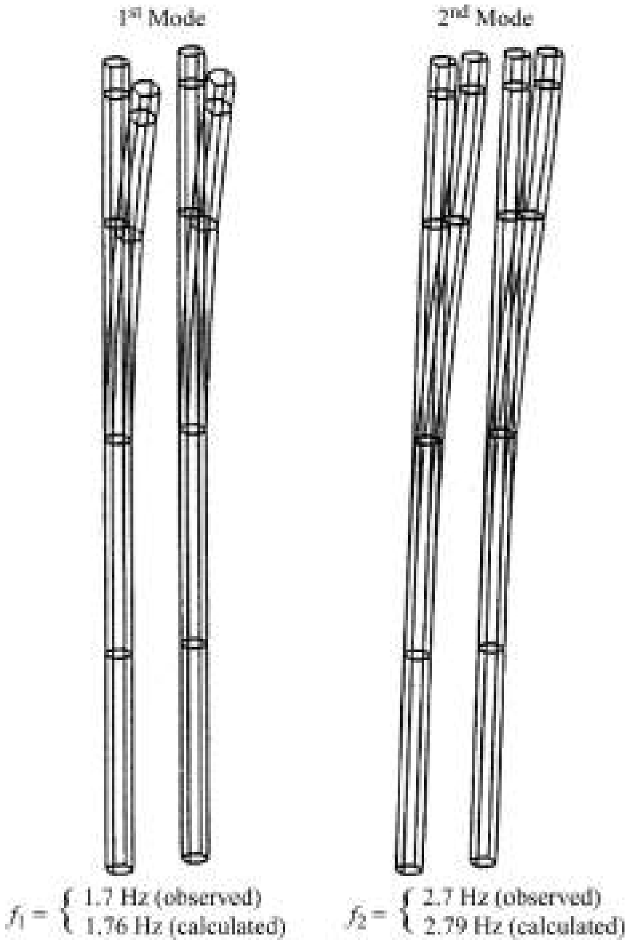

Figure 15 - Configuration of the two first vibration modes. Observed and computed frequencies (adapted from Oliveira *et al.*, 1996).

The modal damping values used in the mathematical model were based in the best adjustment to the transfer functions observed in the test. The adopted values are presented in Table 9.

The observed and calculated frequencies by the mathematical model are presented in Table 10. There is a good agreement for the two first vibration modes.

The displacement transfer functions of the force applied by the shaker are shown in Fig. 16.

Table 9 - Modal damping values adopted in the mathematical model.

Vibration modes	1	2	3
Damping modal in % of the critical damping	7	13	20

Table 10 - Frequencies of the first vibration modes.

Vibration modes	1	2	3	4
Observed frequencies	1.7	2.7	-	-
Calculated frequencies	1.76	2.29	8.78	11.70

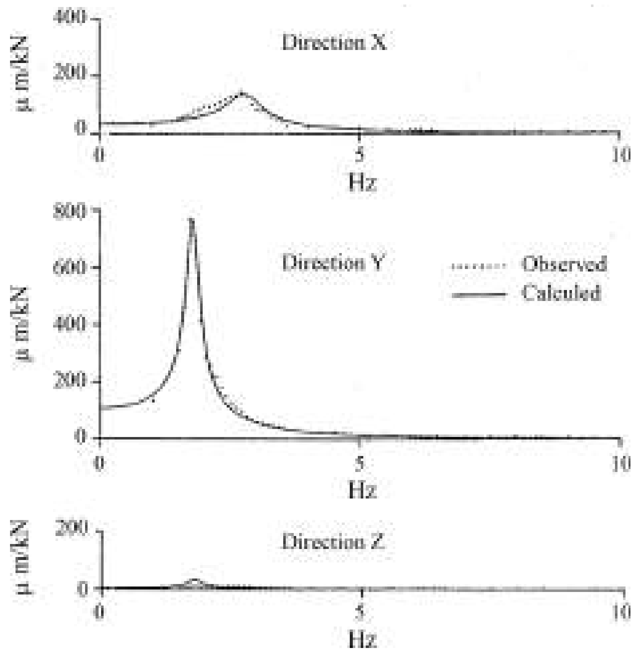

Figure 16 - Displacement transfer functions. Comparison between computed and observed values (adapted from Oliveira *et al.*, 1996).

The results observed in the test and those computed by the mathematical model in terms of displacement transfer functions of the force applied have shown that: (i) In order to improve the pile behaviour field tests instrumented piles are highly recommended for design purposes; (ii) The results of load tests performed in New Tagus bridge and Lezíria bridge for design purposes have shown how they should be used to calibrate the design parameters, to check the performance of individual piles,to allow judgement of the overall pile foundation, and to assess the suitability of the construction method.

The good agreement obtained shows that the mathematical model is well calibrated for simulation of the behaviour of the soil-pile system. The variation of pile maximum displacement with depth according to directions X and Y, as well as some displacement transfer functions computed at different depths, are shown in Fig. 17.

5.4. Reception tests for piles

Taking into account that the development and implementation of load tests is very costly and can only be performed in a small number of piles, non-destructive techniques, *e.g.* the use of core sampling and integrity tests to control the final quality of the piles, are getting more popular.

To assess the quality of piles sonic tests were performed. The involved costs are small, the execution is fast, it is possible to perform a great number of tests and the prin-

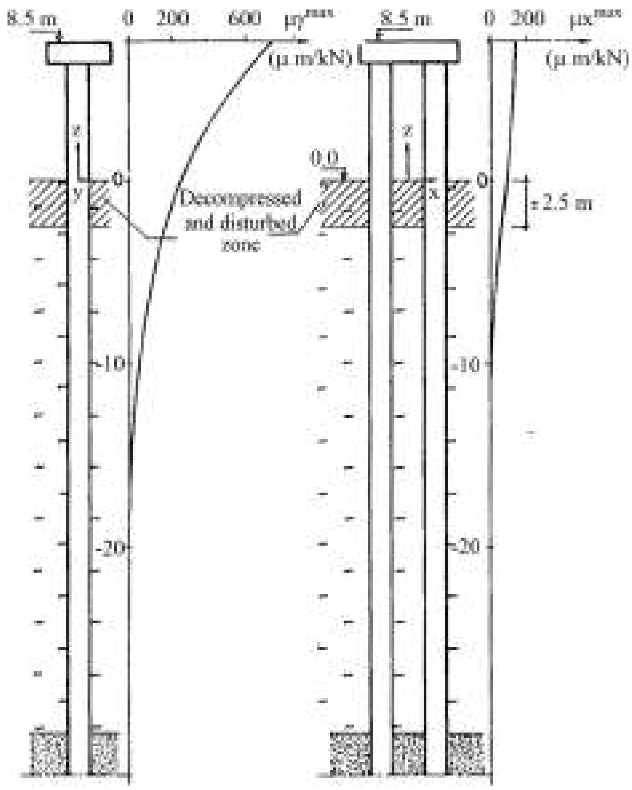

Figure 17 - Variation with depth of maximum displacement of piles. X and Y directions (adapted from Oliveira *et al.*, 1996).

cipal structural singularities of the piles can be detected. With this technique, a blow on the pile head is performed with a hammer and the response is recorded by an accelerometer.

Also sonic diagraph tests were done and a continuous recording was performed along the length of the pile of the velocity of sonic waves between the source and the geophones introduced in two pipes attached to the pile reinforcement.

5.5. Monitoring during construction and long term

5.5.1. Introduction

The designer faces always the difficult task to define the loads and to characterize the materials for the project. In spite of the great progress performed in these domains it is necessary to compare the model with the prototype response in order to assess the structural behaviour and to define the corrective actions to be implemented in case of an anomalous behaviour.

The following advantages of instrumentation of bridges are pointed out:

i) Validation of design criteria and calibration of the model.

ii) Analysis of bridge behaviour during his life.

iii) Definition of corrective measures for the rehabilitation of the structure, if needed.

iv) Cumulative experience that will be important for the design of more economic and safer bridges.

5.5.2. Quantities to be measured

For the superstructure, the measurement of the following quantities was proposed:

a) deck vertical displacement; b) pier cross-sections rotations; c) internal deck and piers deformation; d) internal deck deformation due to time-dependent effects; e) deck and stay temperatures; f) air temperature, relative humidity and wind speed; g) seismic and wind induced acceleration in the deck and piers; h) force in stays.

Related with the infrastructure the following measurements were proposed:

a) pile head displacements using electronic theodolites and appropriate reflectors; b) installation of inclinometers to measure horizontal displacements along the pile shaft; c) strain distribution of the piles using extensometers; d) recording of the accelerations, velocities and displacements along the piles and in selected points of the ground (to assess amplification effects) by 3D accelerographs.

5.5.3. Warning levels

Four warning levels were defined:

(i) warning level 1 - no interruption of traffic; (ii) warning level 2 - limitation of traffic; (iii) warning level 3 - interruption of traffic; (iv) warning level 4 - decision concerning the traffic.

For warning levels 1 to 3, the maintenance team can deal with the problem alone. For warning level 4, the decision will be taken by a specialist.

5.5.4. Inspections

To complement the data given by the instrumentation of the bridge regular inspections would be performed.

Four levels of inspection were proposed:

i) The reference situation corresponds to a detailed inspection of all parts of the structure (foundations, bearings and decks) and the measurement of all the instruments with the purpose to characterize the initial state of the bridge before opening to the traffic;

ii) The daily inspections aim at an efficient visual checking of the superstructure (drainage systems, road surface, expansion joints, handrail, gantries, safety barriers, lighting, etc.) to detect the need for small repairs;

iii) The annual inspections are related with the visual inspection of the foundations (measurements by sensors placed into the piles), supporting structures, bearings, expansion joints, superstructures and equipment.

iv) After the opening to traffic, the first detailed inspection will be done after two years. During bridge operation, the frequency of the inspections is five years.

v) After a ship impact or earthquake with a magnitude superior to 4, a detailed inspection is recommended.

6. Leziria Bridge

6.1. Brief description

BRISA awarded to a Construction Consortium the bridge Project that integrates the Conception, Design, and Construction of Tejo Crossing in Carregado.

The crossing (Fig. 18) is composed by the North Viaduct, the Main Bridge and the South Viaduct.

This 11.9 km long crossing of the Tagus river, is located 25 km upstream of the Vasco da Gama Bridge.

The river, 1 km wide, runs in Tagus valley filled with soft sediments that exhibits a thickness between 35 m and 55 m, with a maximum value of 62 m (Oliveira *et al.*, 2006).

The 1695 m North Viaduct has 33 m spans. The deck 23 m above the water level, is a concrete 2.0 m depth beam directed connected to 1.5 m diameter piers. There is a 62 m span to cross the railway (Fig. 19).

The cross-section of the Main Bridge is composed by (Portugal *et al.*, 2005):

- a 0.30 m width reserve;
- interior hard shoulder;
- 3 traffic lanes, each with 3.50 m with a total width of 10.50 m;
- 2.525 m exterior hard-shoulder.

The platform with a total width of 29.95 m includes a curb, on which rests a safety barrier, a maintenance foot walk and an edge beam with a total width of 1.15 m.

The deck is made of a pre- stressed cast in place concrete box-section 970 m long (Fig. 20). The individual spans are: 95 + 6 × 130 + 95 m. Piers P1 to P5 are monolithical with the deck and composed by two blades of reinforced concrete with 1.20 m thick spaced 5.0 m between axes. Piers P6 to P7 are similar with the blades spaced 7.40 m.

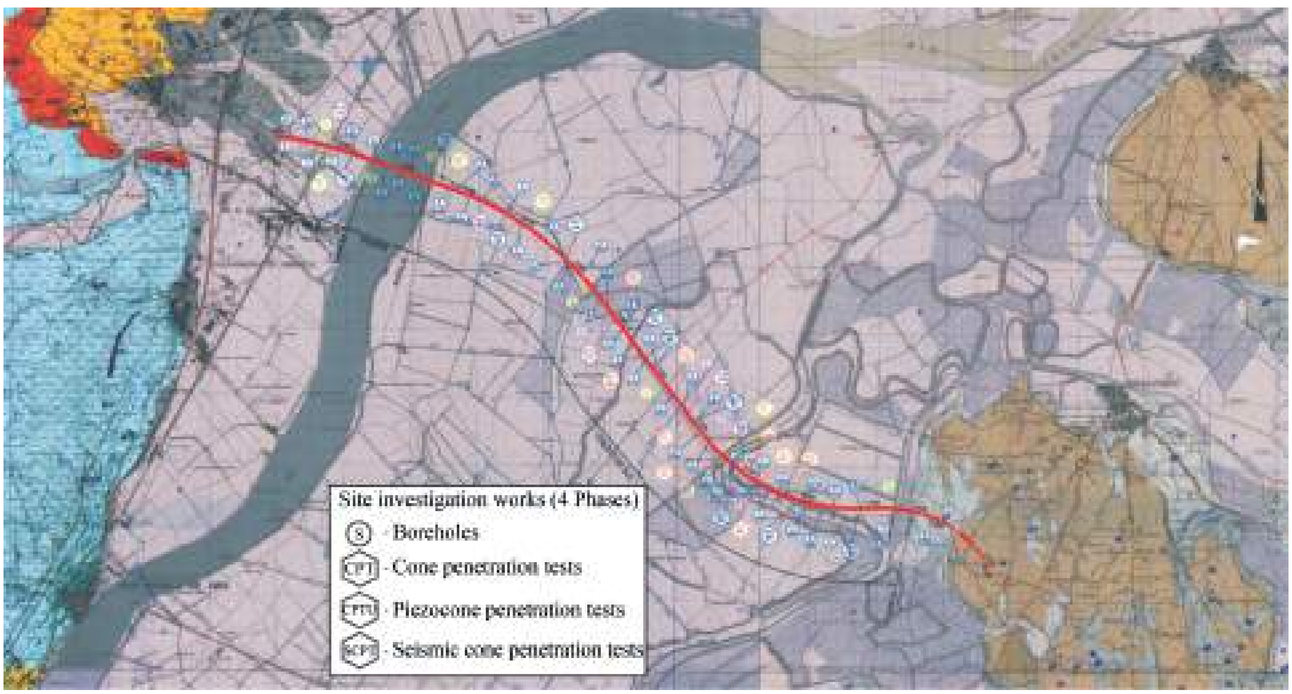

Figure 18 - Lezíria Tagus River Crossing site.

Figure 19 - North Viaduct (courtesy of Charles Lavigne).

Figure 20 - Main Bridge (courtesy of Charles Lavigne).

The bridge foundations are composed by 2.20 m diameter piles. The Piers P1 and P2 and the Piers P3 to P7 are supported by 10 piles and 8 piles, respectively. The piles were built by metallic casings 17 mm thick penetrating in the Miocene formations 1m to 5.5 m depending of the gravel materials thickness.

The sacrificial thickness of the casings varies between 7.2 mm and 5 mm to face corrosion effects.

The pile caps with 11.0 × 22.0 m and 8 m thick to support piers P1C and P2C, were designed to resist ship impact. For piers P3C to P7C pile cap with 11.0 × 16.0 m and 5.05 m thick were adopted.

The South Viaduct is composed by a set of 22 continuous viaducts, with a total length of 9230 m, with a concrete deck longitudinal pre-stressed with current spans of 36 m and 1.5 m of diameter piles.

One of the most important considerations for design is the risk of earthquakes since Lisbon was wiped out by an 8.5 Richter magnitude earthquake in 1755.

6.2. Main geological conditions

6.2.1. Regional geology

The new Tagus River crossing, located in the Cenozoic basin of the Tagus river, incorporates sedimentary materials of Miocene and Paleocene ages. Figure 21 illustrates a simplified geological profile.

6.2.2. Geomorphology

The morphology, at levels of 4 to 5 m, is flat and crossed by secondary water streams, water channels and protection dykes.

6.2.3.Geological structure

The tertiary formations, at regional scale, exhibit horizontal stratification with weak deformation.

6.2.4. Lithostratigraphy

The site is composed of recent superficial deposits, namely Holocene alluvial and quaternary fluvial terraces above the bedrock that integrates Miocene clay-grey materials. The visual aspect of materials is shown in Fig. 22.

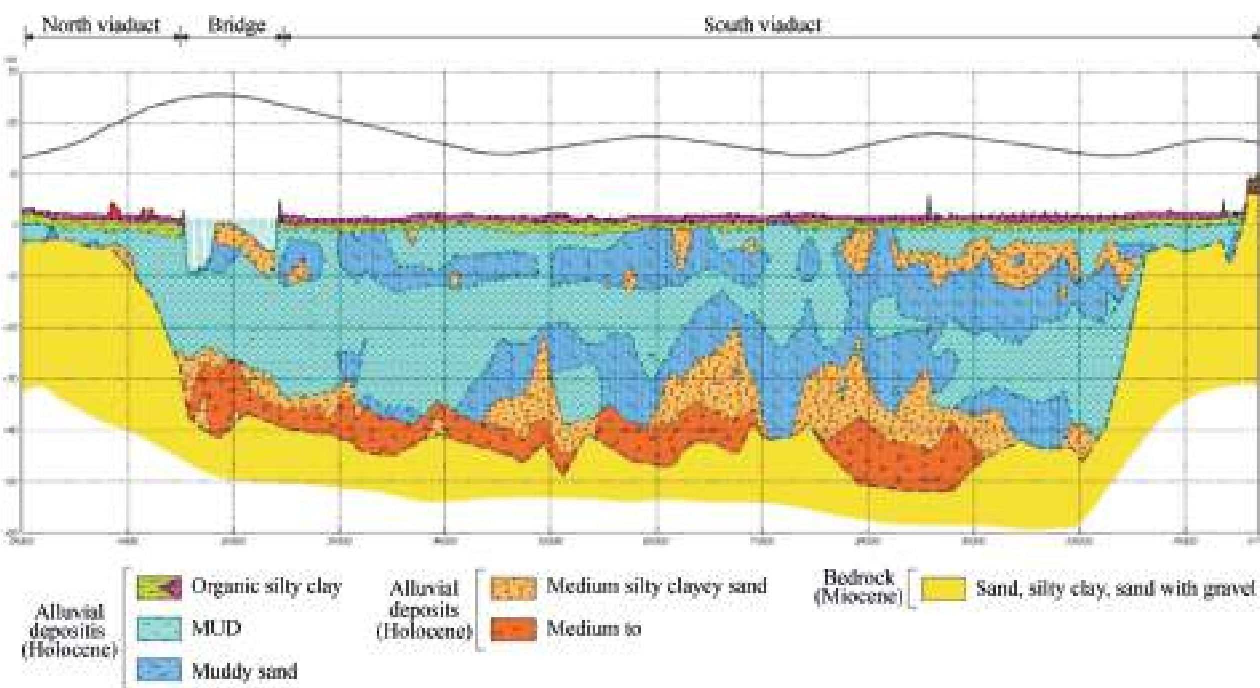

Figure 21 - Simplified geological profile.

Figure 22 - Visual aspect of the materials (courtesy of Virgílio Rebelo).

6.2.5. Hydrogeological conditions

The superficial layers, with characteristics of free aquifer, exhibit phreatic water level near the surface. The alluvial formations exhibit characteristics for the occurrence of suspended, half closed or closed aquifers. The Miocene formations show conditions for the occurrence of closed aquifers or semi closed artesian aquifers.

6.3. Field investigation

The field investigations have included 58 boreholes, namely 6 boreholes during the Preliminary Studies, followed by 49 boreholes and 3 additional boreholes during the complementary investigation program for the Basic Design. The boreholes were performed by Geocontrole.

In all boreholes, the disturbed samples were collected by a Terzaghi sampler, the water level was recorded and SPT tests were performed 1.5 m apart.

Thirty two undisturbed samples were collected using Shelbi and Proctor-Moran samplers.

Thirty-two cone penetration tests, namely 4 CPT tests during the Preliminary Studies, 20 CPT tests during the complementary investigation, 6 CPTu tests, and 2 seismic cones were performed by Geocontrole.

Nineteen vane shear tests, namely 3 tests during the Preliminary Studies and 16 tests during the complementary campaign by Geocontrole.

Nine seismic cross-hole tests were performed, namely 7 tests by GEOCISA and 2 tests by LNEC during the Preliminary Study. In addition, 7 downhole tests were performed.

During the Final Design the complementary geotechnical project has integrated:

i) 41 boreholes with SPT tests 1.5 m apart (Fig. 23);
ii) 10 vane shear tests;
iii) 25 undisturbed samples taken with Geobore S sampler (Fig. 24);
iv) 16 CPTU tests (Figs. 25 and 26);
v) 5 seismic cross-hole tests.

A summary of field tests is presented in Table 11.

The cross-hole tests have given the following results:

Figure 23 - Borehole equipment (after Oliveira *et al.*, 2006).

Figure 24 - Geobore S sampler (after Oliveira *et al.*, 2006).

Shear wave velocities, V_s, from 53 to 350 m/s

Longitudinal wave velocities, V_p, from 665 to 1526 m/s.

The variation of V_s with depth is shown in Fig. 27.

SPT results were between 0 and 4 blows, with 0 values for soft soils and the higher values related with silty materials.

Vane shear tests have given for undrained strength the following results:

Peak values - 12.5 to 51 kPa

Residual values - 4 to 26.3 kPa.

The variation of these values is shown in Fig. 28.

Figure 25 - CPTu equipment (after Oliveira *et al.*, 2006).

Figure 26 - CPTu tip (after Oliveira *et al.*, 2006).

Table 11 - Distribution of field tests.

Tests	Basic design	Final design	Total
Boreholes	58	60	118
Boreholes undisturbed sampling	0	3	3
Vane shear tests	19	7	26
Crosshole	9	6	15
CPTu/CPT	28	23	51
Seismic cone	2	4	6

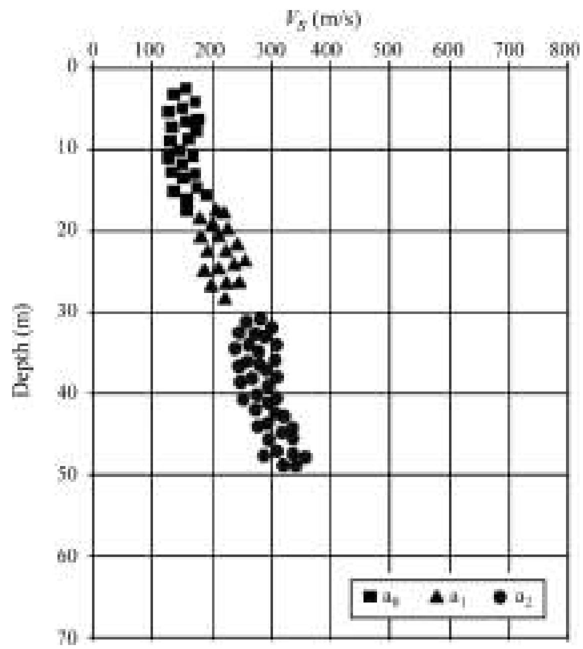

Figure 27 - Variation of V_s with depth.

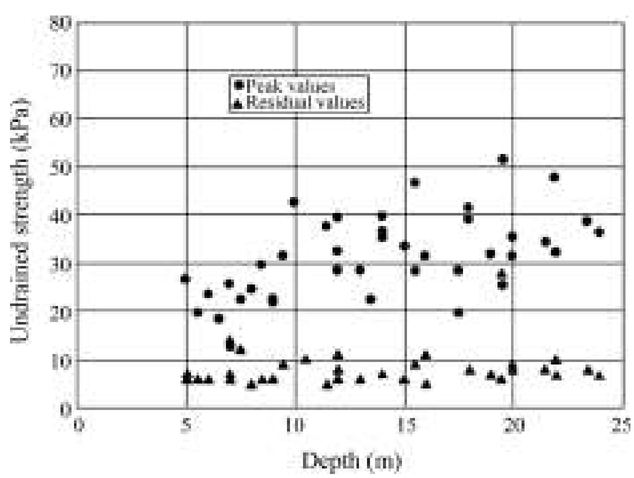

Figure 28 - Variation of undrained strength with depth.

PCPT tests, with measurement of pore pressures, have given point resistances between 0.15 and 1.2 MPa, with an increase with depth. This trend is illustrated in Fig. 29.

Pore pressures values have allowed the identification of zones with higher values related with mud materials.

6.4. Laboratory tests

During the Basic Design, 12 identification tests (sieve analyses and Atterberg limits) were performed by COBA.

During the Preliminary Studies. forty-three identification tests, consisting on sieve analyses as well as Atterberg limits, were performed. Determinations of natural water content, W_n, were also done.

Table 12 summarizes the results of laboratory tests.

In three water samples, pH tests, determination of alkalis, sulfate content, magnesium content and ammonia content were performed.

Nineteen direct shear tests for the definition of the strength in terms of cohesion (c) and friction angle (ϕ), were performed.

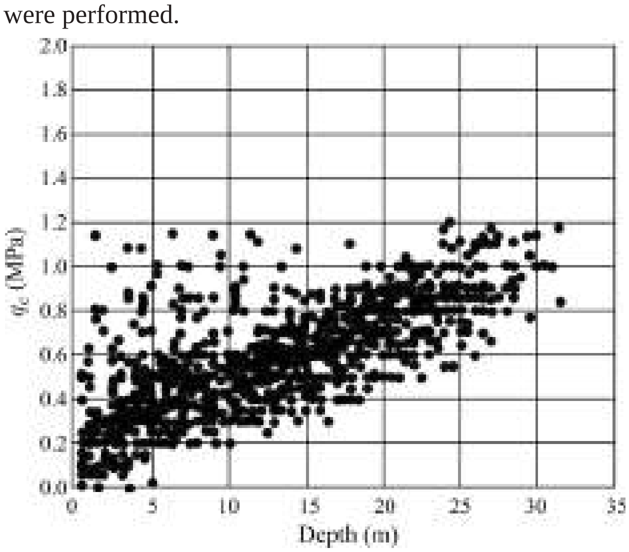

Figure 29 - Variation of q_c values with depth.

Table 12 - Distribution of laboratory tests.

Tests	Basic design	Final design	Total
Identification	55	180	235
Sieve curves	55	180	235
Oedometer	4	18	22
Triaxial	0	6	6
Direct shear	6	13	19
Permeability	6	18	24
Chemical	3	9	12
Resonant column	0	3	3
Cyclic torsional shear	0	3	3

Six triaxial tests for the definition of the strength in terms of cohesion (c) and friction angle (ϕ) were done.

The curves (σ_1 - σ_3) *vs.* axial strain (ε_1), σ_1/σ_3 *vs.* ε_1, variation of pore pressure (u) *vs.* ε_1, and volumetric variation *vs.* ε_1, as well as the stress path and the Mohr-Coulomb envelopes were obtained.

Twenty-two oedometer tests with the determination of the values of water content (W_n), degree of saturation (S_r), pressures, compressibility volumetric coefficients (a_v), consolidation coefficients (c_v) and permeability coefficients (k), were performed.

Twenty-four permeability tests were done.

Twelve chemical tests related with sulfate content, carbonate content and pH values were performed.

Also twenty-five particle density tests were performed.

Three cyclic torsional simple shear tests were done.

A view of cyclic torsional simple shear apparatus is presented in Fig. 30.

The curves G (shear modulus) *vs.* γ (shear strain), $\sqrt{G}$ *vs.* γ, ξ (damping ratio) *vs.* γ and γ *vs.* τ/σ_0 were obtained.

The results of cyclic torsional tests are shown in Fig. 31.

6.5. Geotechnical characteristics

The interpretation of the site investigation programme, namely in situ and laboratory tests, has allowed the identification of the following geotechnical units (Oliveira *et al.*, 2006): a_{0a}, a_0, a_1, a_2. a_3, M. Table 13 summarizes the geological and geotechnical characteristics of each unit.

A correlation between V_s and SPT values is shown in Fig. 32, following the proposal of some authors.

6.6. Pile load tests

6.6.1. Introduction

Pile design can be performed by (Eurocode 7, 1997):

- prescriptive measures and comparable experience;
- design models;

Figure 30 - View of cyclic torsional shear apparatus (IST).

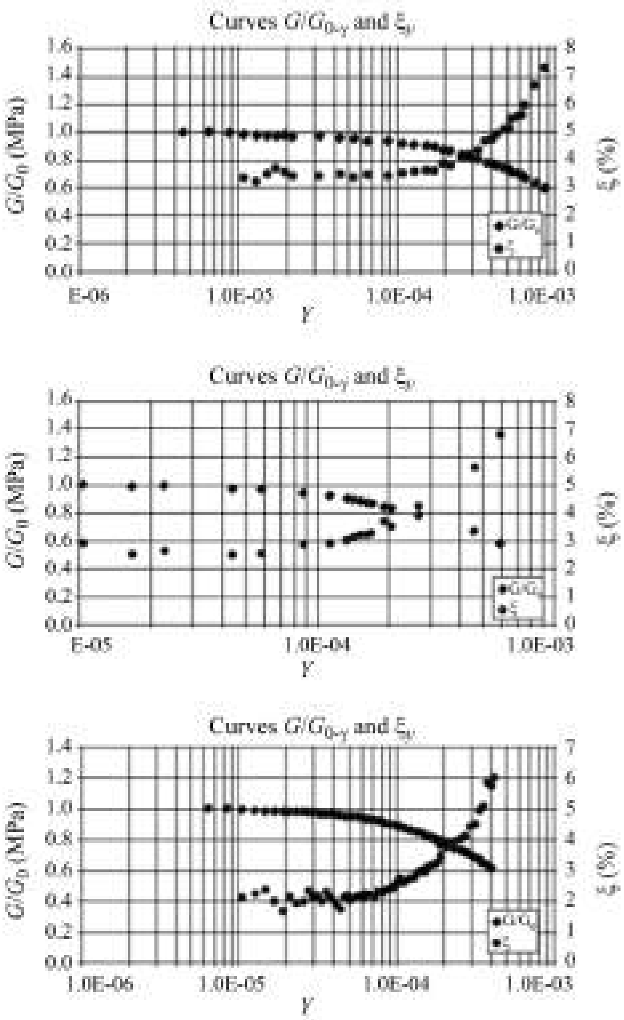

Figure 31 - Curves of shear modulus and damping ratio *vs.* shear stra–in (after IST, 2005).

- use of experimental models and load tests;
- observational method.

The piles of Lezíria bridge were designed by:

i) design models;

ii) pile load tests that have provided useful information about the characteristics of gravel materials and techniques of driving the metallic casings;

iii) comparable experience.

Pile load tests were performed with the following purposes:

i) to determine the response of a representative pile and the surrounding ground, related settlement and limit load;

ii) to verify the performance of individual piles as well the overall pile foundation;

iii) to assess the suitability of the construction method.

Load tests were carried out on trial piles that were built before the final design.

The results of load tests were used to calibrate the design parameters and so to optimize the preliminary values of pile lengths obtained by the interpretation of site investigation and laboratory and in situ test results.

The criteria to select pile tests has incorporated the following aspects:

- the geotechnical category of the structure;
- the ground condition and the spatial variation;
- past experience related the use of same type of piles in same ground conditions;
- planning of the works.

Due to spatial variation of foundations characteristics and to analyze the embedded effects, the experimental piles for static and dynamic tests were located at km 8 + 200 where the pile was embedded 1 diameter in the Miocene, at km 7 + 900 where the pile was embedded 3 diameters in the gravel materials, and at km 5 + 400 where the pile was embedded 3 diameters in the Miocene. Table 14 summarizes pile type and location.

For static tests in each selected place, one 800 mm diameter pile and two 1500 mm diameter reaction piles with were built, 3.5 m apart from the pile test, and, in addition, a fourth 800 mm diameter pile, 5.5 m apart from the first pile, for dynamic test.

To perform pile load tests, seven 1.5 m diameter piles and seven 0.8 m diameter piles were built.

6.6.2. Vertical pile load tests

The static vertical pile load tests have followed the “Axial Pile Loading Test, Suggested Method” protocol recommended by ISSMGE and published in ASTM D1143 (1981).

The purpose was to incorporate the contribution of all the ground layers and their influence in the deformations

Table 13 - Summary of geotechnical unit characteristics.

Material	W_L (%)	W_P (%)	V_s (m/s)	V_p (m/s)	E_{dyn} (MPa)	G_{dyn} (MPa)	SPT	CPT (MPa)
a_0 - Fine to medium sand	64	38	130-160	665-1526	50-150	20-100	2-6	1-2
a_1 - Sandy materials with silty clay	NP-40	NP-18	130-240	665-1526	100-300	30-100	2-20	2-8
a_2 - Fine sand with silt	NP	NP	140-300	665-1526	100-500	20-200	5-40	3-16
a3 - Sandy material with silt	NP	NP	320-400	665-1526	500-1100	200-400	40-60	
M - Miocene bedrock			400-500		500-1700	200-600, > 60		

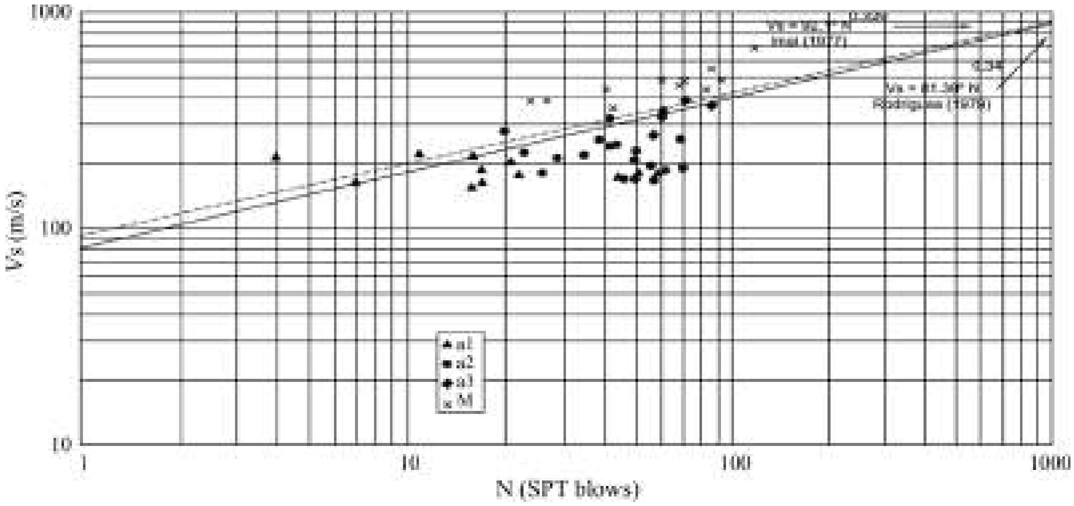

Figure 32 - A correlation between V_s and SPT values.

Table 14 - Summary of pile type and location.

Piles (km)	Diameter (m)	Pile embedding	Load test type
5+400	0.8	3Ø (M)	Vertical (Dynamic)
7+900	0.8	3Ø (a3)	Vertical (Dynamic)
8+200	0.8	1Ø (M)	Vertical (Dynamic)
4+750	1.5	3Ø (M)	Horizontal (Dynamic)

until a depth of 5 diameters, unless the bedrock was situated at upper level.

Vertical load tests were performed on 3 piles.

The following equipment was installed for the vertical pile load test: 2 mechanical dial gauges, electrical displacement transducers (Fig. 33) with removable extensometers (Fig. 34), with a resolution of 10^{-6} and anchors, 1 temperature sensor, 1 tilt meter, 1 hydraulically operated pump, 2 hydraulic jacks and 1 optical level.

A general view for vertical pile load tests is presented in Fig. 35.

Figure 33 - Displacement transducers.

For the vertical pile load tests, a maximum load of 9100 kN was applied, *i.e.* 3.25 times the service load. The loads were applied in two cycles of loading and unloading, with a maximum service load for the first cycle and loads were applied in 4 increments.

In the second cycle, the loads were applied in 19 increments. The number of load increments and the cycles of loading and unloading were carefully selected with the purpose of collecting information related to deformation, creep effects and ultimate load. Figure 36 illustrates the load-settlement curves for 3 pile tests.

To define the failure load, a criterion of settlement equal to 10 % of the pile diameter, *i.e.* 80 mm settlement, was adopted.

Figure 34 - Recovery extensometer.

Figure 35 - General view for vertical pile load tests (after Ferreira *et al.*, 2008).

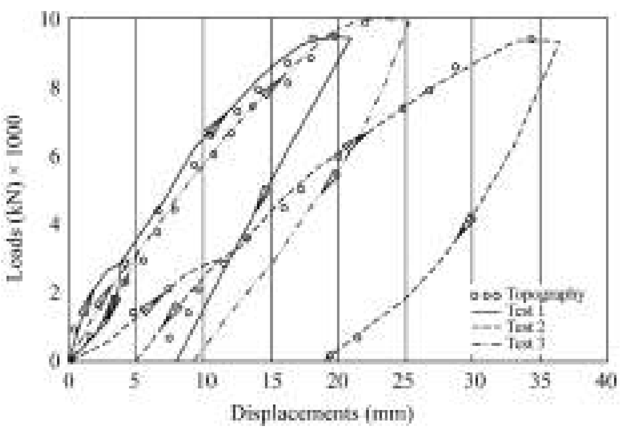

Figure 36 - Load settlement curves for vertical tests (after ICIST-IST, 2005).

6.6.3. Horizontal pile load tests

The horizontal load tests were performed in two piles of 800 mm and 1500 mm diameter located at km 5 + 400. The maximum load was 600 kN to mobilize a displacement of 8 cm and the loads were applied in steps of 75 kN.

For the horizontal load tests, the following equipment was installed:

- clinometers-vibrating wire transducers;
- load cells;
- retrieval extensometers;
- inclinometer tubes to measure horizontal displacements;
- temperature device.

The loading program consisted of 10 load increments, from 50 kN to 500 kN. The measured load-displacement curve is illustrated in Fig. 37. The measured loads *vs.* rotations values are shown in Fig. 38.

Figure 39 shows a comparison between the bending moments values computed from the tests results considering different k values (2500 kPa, 5000 kPa, and 10000 kPa).

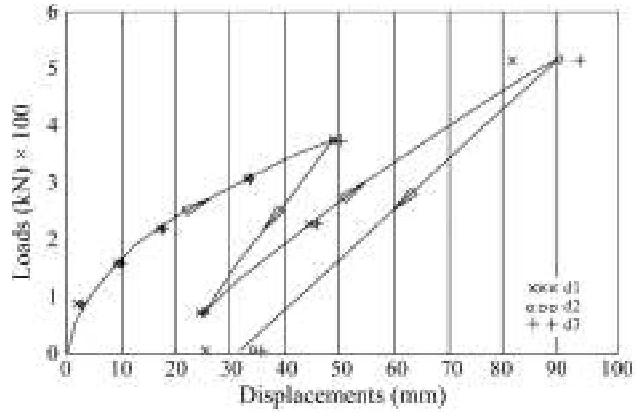

Figure 37 - Measured load displacement curve for horizontal tests (after ICIST-IST, 2005).

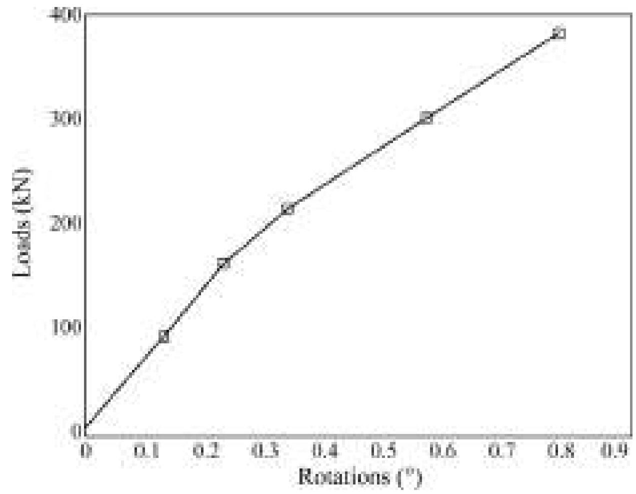

Figure 38 - Measured load rotations curve for horizontal tests (after ICIST-IST, 2005).

6.6.4. Dynamic pile tests

Dynamic pile tests were performed in 9 piles with diameters of 800 mm and 1500 mm. The piles were instrumented with 4 pairs of accelerometers (Fig. 40), 4 transducers and topographic equipment. Figure 41 illustrates a dynamic test view. During the tests, the height of the hammer fall was increased from 0.2 m to 3.0 m in steps of 0.2 m. The mobilized point resistance (R_b) and the lateral resistance (R_s) values for pile E 800-2 are shown in Fig. 42.

It is important to stress that the results of dynamic tests have confirmed the results of static tests, showing the high contribution of the lateral resistance in comparison with the point resistance.

6.7. Design surface spectra

6.7.1. Introduction

A very comprehensive analysis was performed to define the design free field surface spectra.

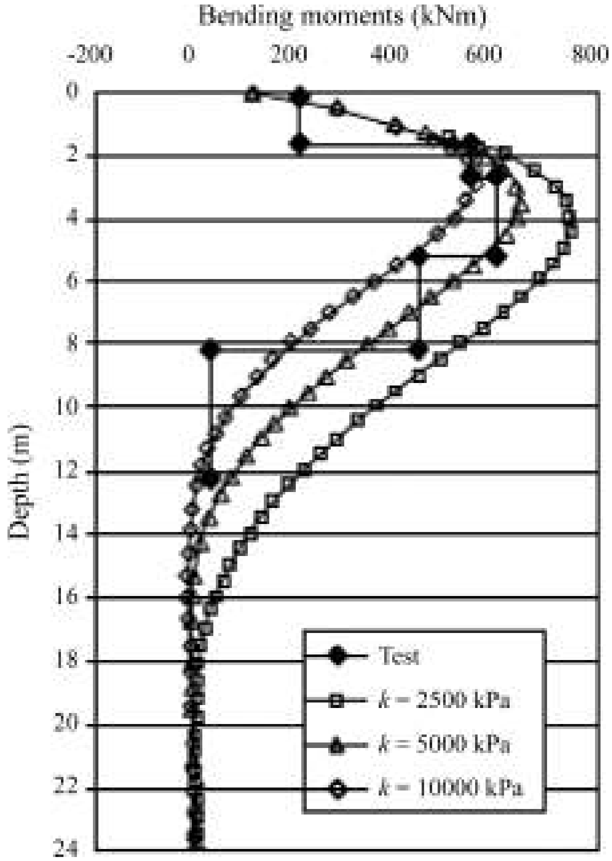

Figure 39 - Bending moments (after ICIST-IST, 2005).

Figure 40 - Transducers and accelerometers.

6.7.2. Seismic action

Following the Portuguese Code (RSA, 1983), the seismic action is defined by a stochastic Gaussian stationary vectorial process (two horizontal orthogonal components and one vertical component). For the Portuguese territory, it is important to consider two seism tectonic sources, namely: (i) a near source that represents a moderate magnitude earthquake at a short epicentral distance with a duration of 10 s; (ii) a distant source that represents a higher magnitude earthquake at a larger epicentral distance with a duration of 30 s.

Figure 41 - Dynamic test (after Ferreira *et al.*, 2008).

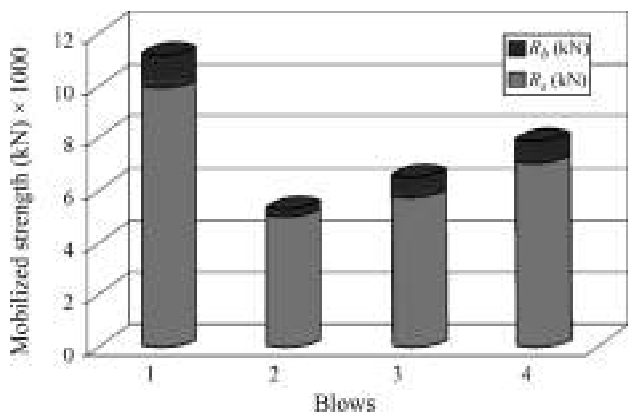

Figure 42 - Mobilized resistances (after ICIST-IST, 2005).

Five artificial time histories of acceleration were produced for seismic action type 1 and seismic action type 2 and for soil type A for the deterministic approach (IST, 2004). For the computation of these accelerograms, the validation criteria of EC8 (1998a) were considered (Fig. 43).

Based on RSA (1983), power spectral density functions were used for the stochastic approach.

In order to incorporate the spatial variation, taking into consideration the 12 km length of the bridge, 17 geotechnical profiles were selected to incorporate the variation of the geological and geotechnical characteristics.

Only the results obtained for the profile located between km 1 + 500 and km 1 + 800, where the main bridge is located, are presented, due to space limitations.

Figures 44 and 45 illustrate the results of the response spectra (IST, 2004), as well as the shear stress computed by the SHAKE 2000 code. The analyses were performed for seismic action type 1 and seismic action type 2, considering for the bedrock type A ground.

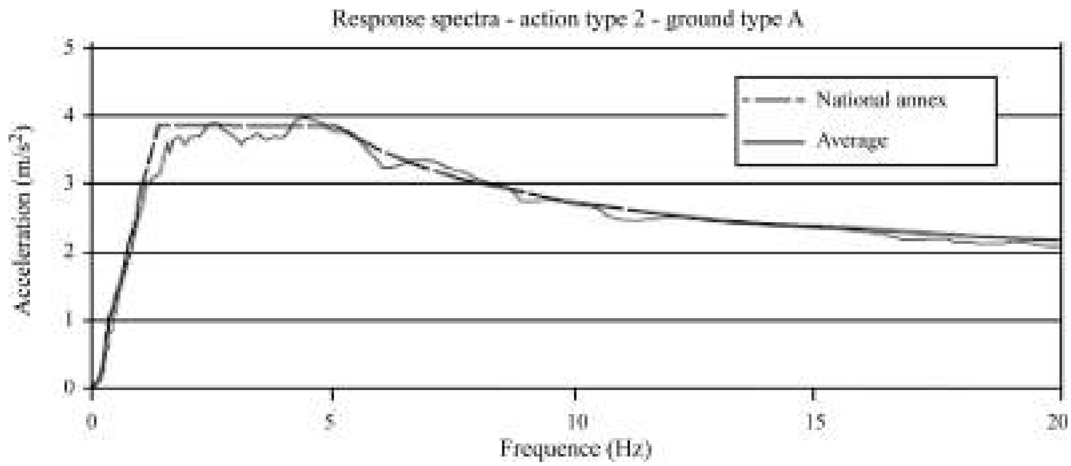

Figure 43 - Response spectra *vs.* code spectra (after IST, 2004).

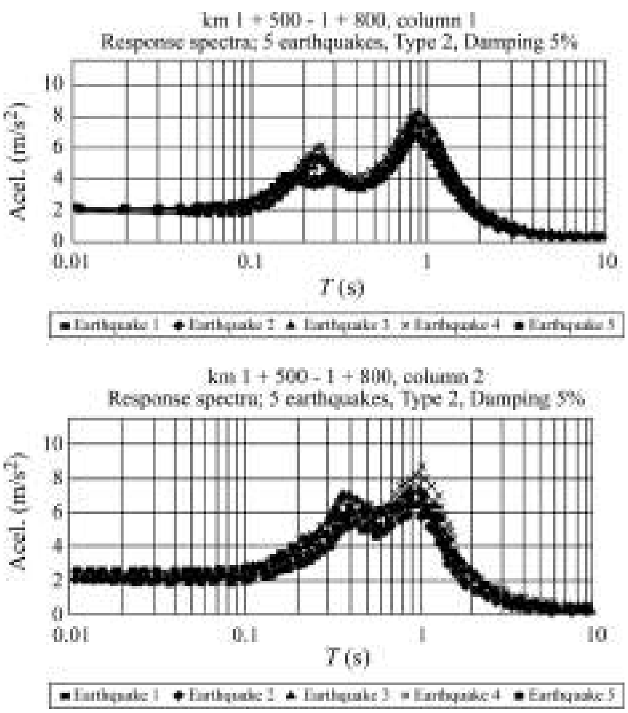

Figure 44 - Acceleration response spectra (km 1 + 500 - km 1 + 800 action type 2) (after IST, 2004).

6.8. Liquefaction assessment

Following Eurocode 8 - Part 5- 4.1.3. (2) (1998b), *"An evaluation of the liquefaction susceptibility shall be made when the foundation soils include extended layers or thick lenses of loose sand, with or without silt/clay fines, beneath the water level, and when such level is close to the ground surface"*.

The seismic shear stress τ_e can be estimated from the simplified expression:

$$\tau_e = 0.65\,\alpha_{gr}\gamma_f\,S\,\sigma_{v0} \tag{1}$$

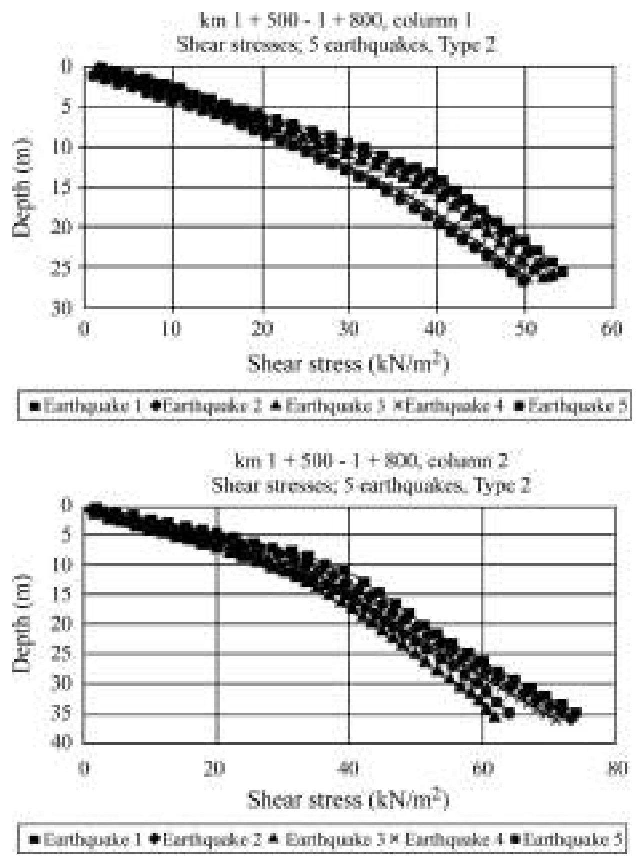

Figure 45 - Induced shear stress (km 1 + 500 - km 1 + 800, action type 2) (after IST, 2004).

where α_{gr} is the design ground acceleration ratio, γ_f is the importance factor, S is the soil parameter and σ_{v0} is the total overburden pressure. It is important to refer that this expression should not be applied for depths larger than 20 m. The shear level should be multiplied by a safety factor of 1.25.

For the magnitude correction factors, EC8 follows the Ambraseys (1988) proposal, which is different from the

NCEER (1997) factors. A comparison between the two proposals is shown in Table 15 and Fig. 46.

Cetin *et al.* (2001) have presented a new proposal for liquefaction analysis (see Fig. 47). It is considered advanced in relation to the previous ones, as it integrates: (i) data of recent earthquakes; (ii) corrections due to the existence of fines; (iii) experience that incorporates a better interpretation of SPT test; (iv) local effects; (v) cases histories that incorporate lessons of more than 200 earthquakes; (v) Bayesian theory.

For liquefaction evaluation of sandy materials, two methods are used, namely, based in laboratory tests or field tests. In general, the following laboratory tests are used: (i) cyclic triaxial tests; (ii) cyclic simple shear tests; and (iii) cyclic torsional shear tests. Due to the difficulties to obtain

Table 15 - Magnitude scaling factors.

Magnitude M	Seed & Idriss (1982)	NCEER (1997)	Ambraseys (1988)
5.5	1.43	2.20	2.86
6.0	1.32	1.76	2.20
6.5	1.19	1.44	1.69
7.0	1.08	1.19	1.30
7.5	1.00	1.00	1.00
8.0	0.94	0.84	0.67
8.5	0.89	0.72	0.44

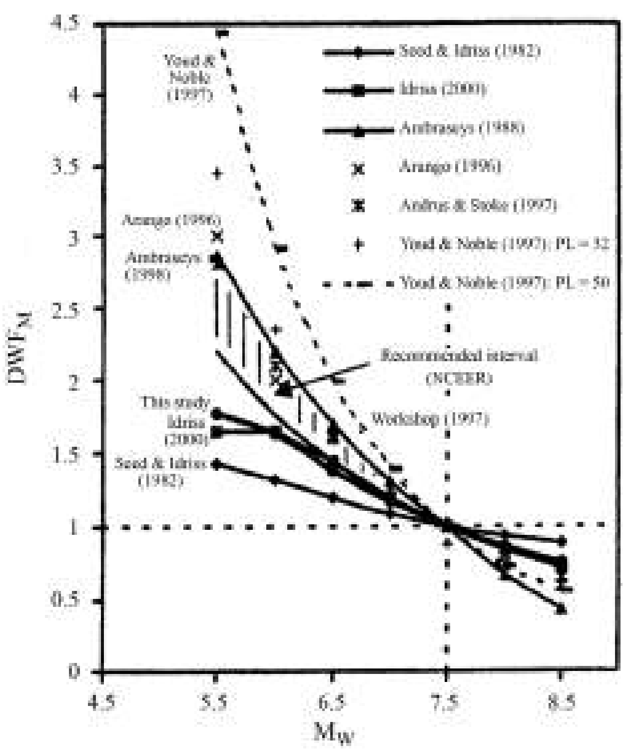

Figure 46 - Magnitude scaling factors.

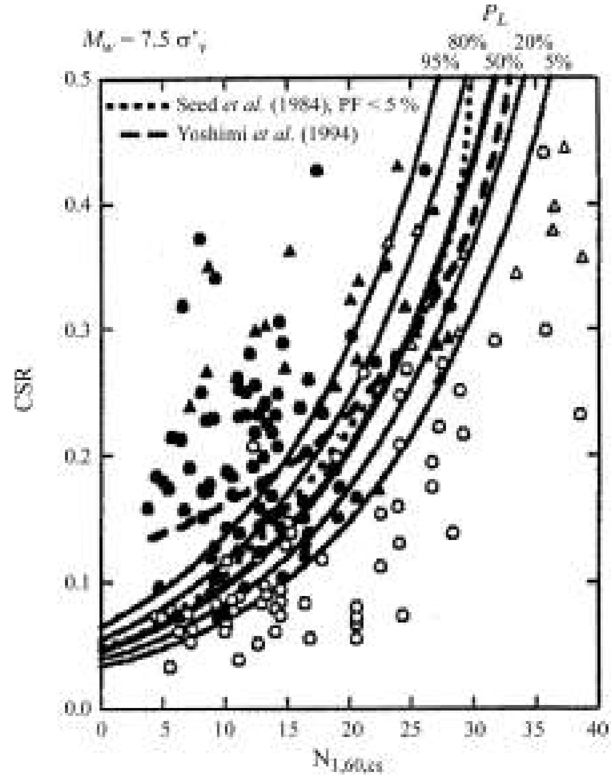

Figure 47 - Probabilistic approach for liquefaction analysis (after Cetin *et al.*, 2001).

high quality undisturbed samples, in general field tests are used: SPT, CPT, seismic cone tests, flat dilatometer tests and tests to assess electrical properties (Sêco e Pinto *et al.*, 1997).

For liquefaction assessment by shear wave velocity, two methodologies are used: (i) methods combining the shear wave velocities by laboratory tests on undisturbed samples obtained by tube samplers or by frozen samples (Tokimatsu *et al.*, 1991); (ii) methods measuring shear wave velocities and its correlation with liquefaction assessment by field observations (Stokoe *et al.*, 1999).

To overcome the difficulties of CPT and SPT tests in soils with gravel, some proposals to evaluate the susceptibility of liquefaction of these materials based in seismic tests with measurement of shear waves velocities V_s were made (Stokoe *et al.*, 1999).

Following Youd & Gilstrap (1999), the post-liquefaction strength of silty materials is less than that of sandy materials, but superficial silty materials with moderate density are dilatant and with higher strength than clean sands. The authors have concluded that loose soils with IP < 12 and $w_d/w_L > 0.85$ are susceptible to liquefy and loose soils with 12 < IP < 20 and $w_d/w_L > 0.85$ have higher strength to liquefaction and soils with IP > 20 are not liquefiable.

It is important to refer that Eurocode 8 (1998b) - Part 5 considers "*no risk of liquefaction when the ground acceleration is less than 0.15 g in addition with one of the following conditions: (i) sands with a clay content higher than*

20 % and a plasticity index > 10; (ii) sands with silt content higher than 10 % and $N_1(60) > 20$; and (iii) clean sands with $N_1(60) > 25$".

6.8.1. Settlement assessment

The susceptibility of foundation soils to densification and to exhibit excessive settlement is referred in EC8, but the assessment of expected liquefaction induced deformation is not adequately treated.

By combination of cyclic shear stress ratio and normalized SPT N-values, Tokimatsu & Seed (1987) have proposed relationships with shear strain (Fig. 48).

To assess the settlement of the ground due to the liquefaction of sand deposits based on the knowledge of the safety factor against liquefaction and the relative density converted to the value of N1, Ishihara (1993) has proposed a chart (Fig. 49).

6.8.2. Remedial measures

Following EC8, ground improvement against liquefaction should compact the soil or use drainage to reduce the pore water pressure. The use of pile foundations should be considered with caution due to the large forces induced in the piles.

The remedial measures against liquefaction can be classified in two categories (TC4 ISSMGE, 2001; INA, 2001): (i) prevention of liquefaction; and (ii) reduction of damage to facilities due to liquefaction.

The measures to prevent occurrence of liquefaction include the improvement of soil properties or improvement of conditions for stress, deformation and pore water pressure. In practice a combination of these two methods is adopted.

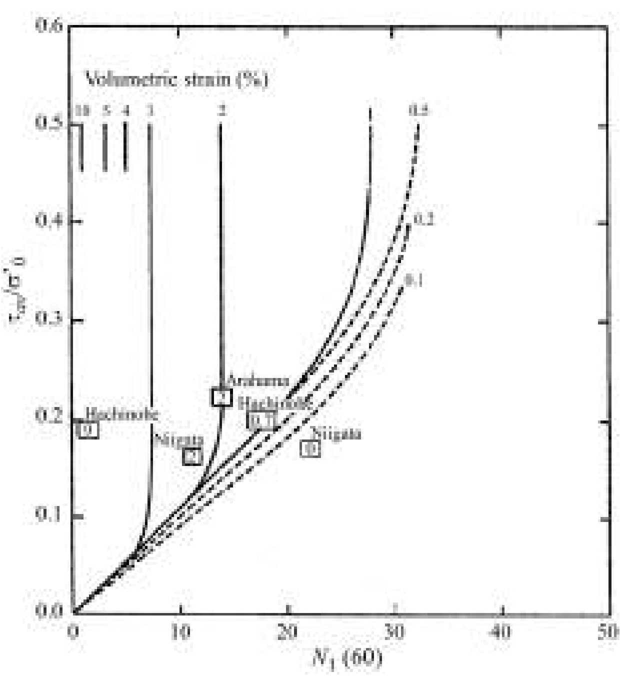

Figure 48 - Correlation between volumetric strain and SPT (after Tokimatsu & Seed, 1987).

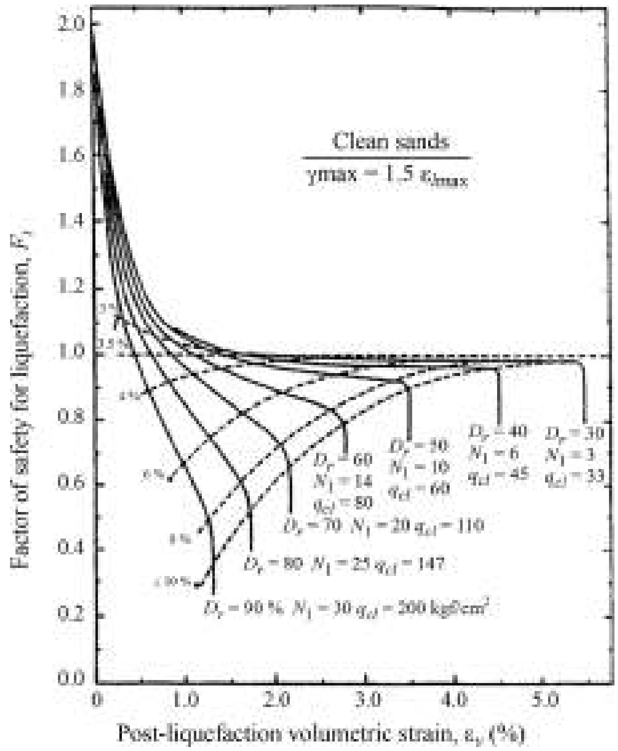

Figure 49 - Post cyclic liquefaction volumetric strain curves using CPT and SPT results (after Ishihara, 1993).

The measures to reduce liquefaction induced damage to facilities include: (1) to maintain stability by reinforcing the structure: reinforcement of pile foundation and reinforcement of soil deformation with sheet pile and underground wall; (2) to relieve external force by softening or modifying the structure: adjustment of bulk unit weight, anchorage of buried structures, flattening embankments.

6.9. Liquefaction evaluation

Due to the disturbance that occurs during sampling of sandy materials, the liquefaction potential evaluation was performed only by field tests.

Attention was drawn to SPT and CPT tests as the seismic tests have only been used when the soil contains gravel particles.

To compute the shear values a total stress model, the code "SHAKE 2000", was used and the obtained results are on the conservative side.

Just as an example, Fig. 50 compares the results obtained by the total stress model and the effective stress analysis using the computer program DYNAFLOW for the Vasco da Gama bridge in the Tagus river and with the same type of alluvial materials.

Corrections of SPT test results due to the depth effect and the equipment were performed, following the recommendations of EC8 (1998b).

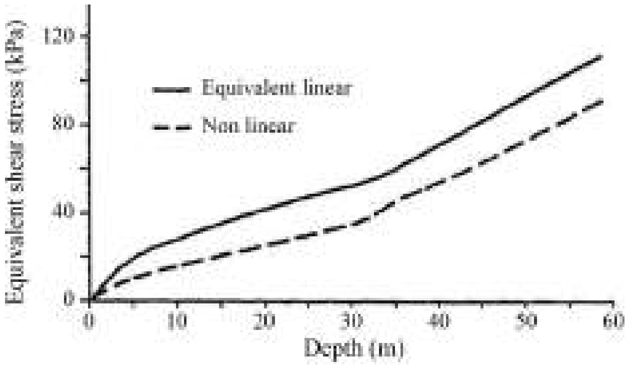

Figure 50 - Equivalent shear stresses computed from the SHAKE and DYNAFLOW codes (after Sêco e Pinto & Oliveira, 1998).

The sieve curves of materials a_1 and a_2 are shown in Figs. 51 and 52.

Taking into account that we are dealing with underwater materials, the sieve curves exhibit percentages of fines lower than the reality, as a consequence of the washing effect during sampling.

The liquefaction potential evaluation was given in tables and the columns have included the following data: (i) columns 1 to 4, reference to the pier, type of test (SPT or CPT), depth of the test and thickness of the layer; (ii) columns 5 and 6, values of N_m (SPT) and $(q_c)_m$ (CPT); (iii) columns 7 and 8, effective overburden pressure (σ'_0) and correction factor (C_N); (iv) columns 9 and 10, normalized values N_1 (60) (SPT) (for effects reduced C_N values were considered) and $(q_c)_1$ (CPT); (v) column 11, τ_{equiv} (equivalent shear stress value computed for action type 2 related with the highest magnitude 7.5); (vi) column 12 (τ/σ'_0 ratio value); (vii) column 13 (τ/σ'_0 ratio value with a safety factor of 1.1), column 14 (τ/σ'_0 ratio value with a safety factor of 1.25); (viii) column 15, Ref. (reference of the analyzed SPT or CPT value); (ix) column 16, liquefaction susceptibility analysis. Taking into account the dilatant behavior of the material observed in the CPT tests and the values of the pore pressures developed in the cyclic torsional shear tests, where the registered values of the pore pressure rarely reach 80 %, being frequently below 60 %, a safety factor of 1.1 can be considered sufficient. Nevertheless, in the present case, a conservative analysis was performed, with a safety factor of 1.25 being adopted, as recommended in EC8 - Part 5 (1998b).

Table 16 presents an application of liquefaction evaluation for materials a_1 and a_2. The liquefaction potential evaluation, by SPT and CPT tests, is shown in Figs. 53 and 54.

Taking into account Figs. 48 and 49, the estimated settlement of materials a_1 and a_2 are between 40 mm to 150 mm.

6.10. Construction aspects

The most important construction aspects are listed below:

i) After the temporary works through the execution of sheet piles the anchorage of the pontoon was done, in order to ensure stability during the driving of the casings. The system had the purpose of ensuring the verticality of the casings.

ii) Transportation of the metallic 2.2 m diameter and 17 mm thick casing. This casing was driven by a high capacity

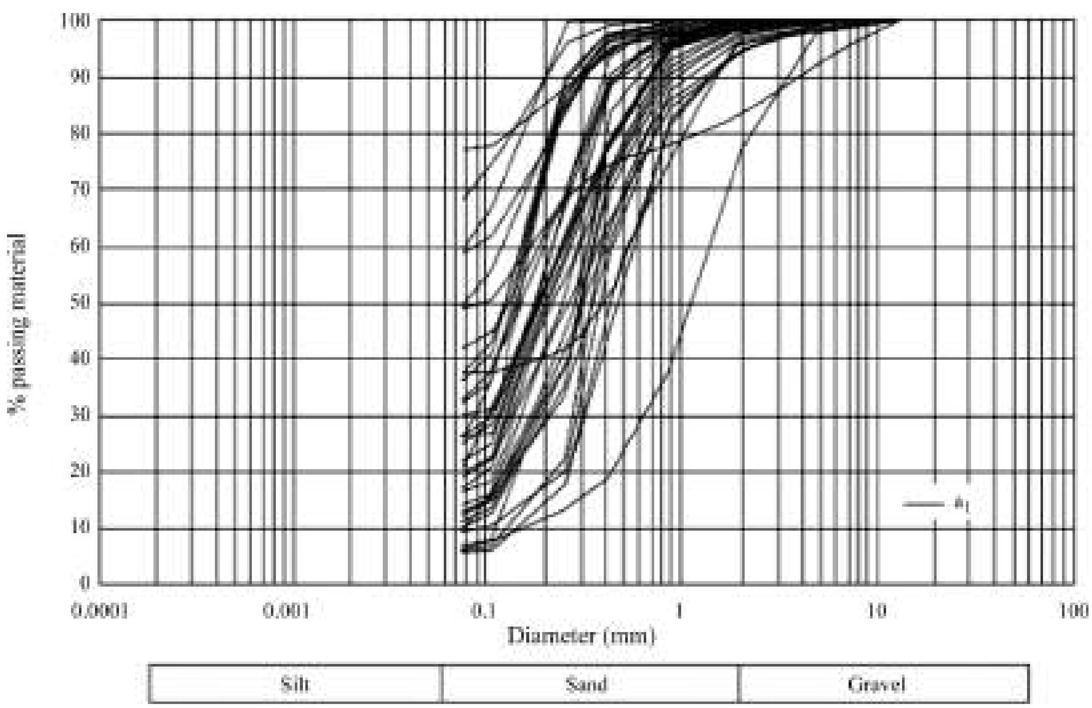

Figure 51 - Sieve curves for material a_1.

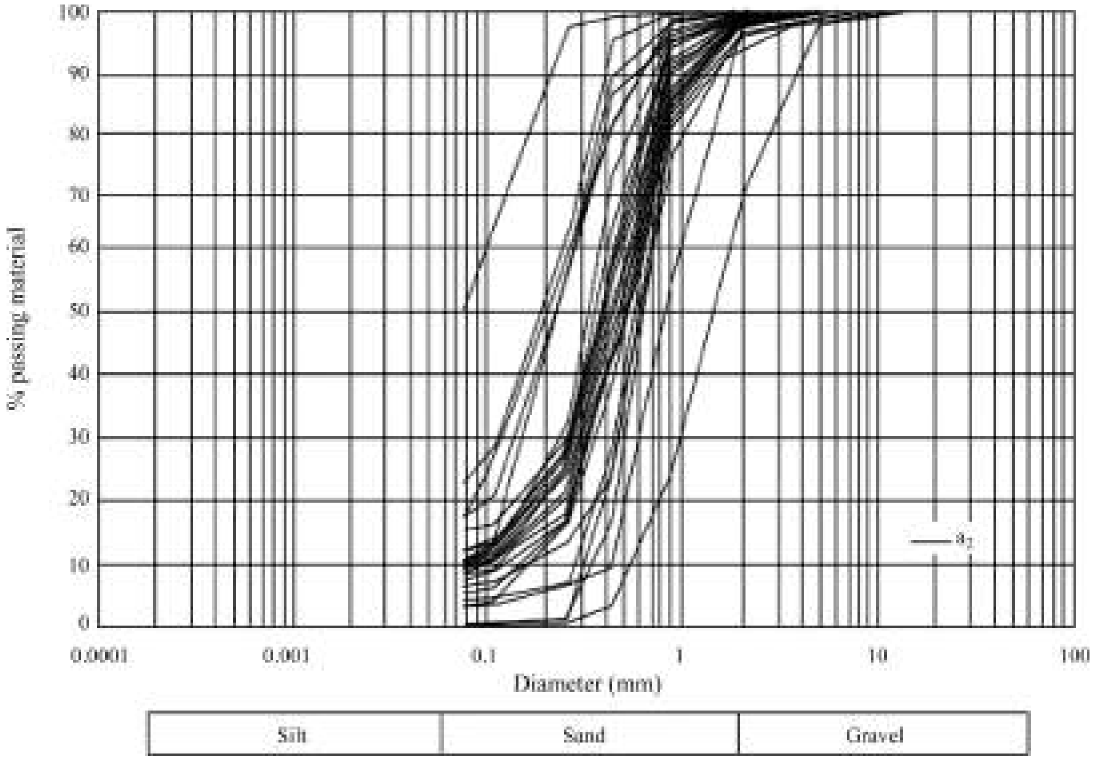

Figure 52 - Sieve curves for material a_2.

vibrator and a penetration of 1 to 2 m in geotechnical unit a_{0a} was ensured.

Driven piles were installed by joint venture subcontractor Volker Stevin - Ballast Nedam. Large barge mounted cranes were used to drive each pile as one piece. A handling capacity around 58 ton was necessary for the cranes and the hammer to drive the piles into position.

Subsequently a guidance system was used to drive the casing 1 diameter into gravel materials or into a compacted ground with a minimum SPT value of 10 blows.

iii) Progress of the excavation with a 2.2 m diameter "hammergrab" in order to reach the Miocene. For wall stabilization were used polymer materials manufactured in a central located in the left bank. For polymer control, pH tests, density and viscosity tests, as well sand content tests, were performed.

iv) After the excavation and the decantation of the polymer, the reinforcement with the pipes for the cross-hole tests was installed. To ensure a minimum cover of 12 mm centralizers were placed.

v) Concreting of the piles with the use of "tremie" and pumping was done at a rate of 50 m^3/h.

The duration of these 5 phases was 2.5 days.

In the construction procedure proposed in the Basic Design, the pile caps for piers P1 and P2 were performed within cofferdams constructed with sheet piles driven into the mud materials by equipment installed in barges. The voids under the casings were stabilized through the use of polymers.

For caps P3 to P7, the constructive procedure consisted in the construction of prefabricated caissons in dry dock. The caissons were transported from onshore casted *in situ* and subsequently the metallic casings were driven through the holes of the bottom slab, the openings under the casings being stabilized through the use of polymers.

During the Final Design, a solution of pre-fabricated caissons was developed with large caissons for piers P1C and P2C and small caissons for piers P3C to P7C.

A view of the North Viaduct construction is shown in Fig. 55.

To avoid excavations of the protection dykes, a parallel way (transient viaduct) was built (Fig. 56).

A view of the South Viaduct construction is shown in Fig. 57.

The placement of pile casing is shown in Fig. 58.

The placement of pile reinforcement and tremie pipes are shown in Figs. 59 and 60.

In Figs. 61 to 63 a caisson view, a pier under construction and a general view of the construction works are presented.

The pre-fabricated caissons were temporarily supported by the casings of the definitive piles. With the support of hydraulic cylinders, the temporary metallic structure was uplifted and subsequently the caisson was moved downward until the design level.

After the sealing of the joints between the piles and the bottom slab the water inside the caissons was removed by pumping.

Table 16 - Evaluation of liquefaction potential (material a_1 and material a_2).

(1)	(2)	(3)	(4)	(5)	(6)	(7)	(8)	(9)	(10)	(11)	(12)	(13)	(14)	(15)	(16)
Pier	Borehole no. or CPT	Depth (m)	Thickness (m)	N_m	$(q_c)_m$ (MPa)	σ'_0 (kPa)	C_N	N_1 (60)	$(q_c)_1$ (MPa)	$\tau_{equiv.}$ (kPa)	τ/σ'_0	τ/σ'_0 x 1.1	τ/σ'_0 x 1.25	Mat.	Remarks
	S1B	16.8-25.1	8.3	44	-	139.1	0.8	37	-	39	0.29		0.36	A2	N.L
	S2B-2	24.3-31.3	7.0	23	-	215.4	0.7	16	-	55	0.26		0.32	A2	L
“	S3B-1	0.0-4.2	4.2	3	0.5	33.9	1.0	3	0.5	7.6	0.22		0.28	A2	L
“	S3B-2	4.2-7.4	3.2	6	0.52	66.4	1.2	7	0.6	19.2	0.29		0.36	A1	L
“	S3B-3	7.4-9.6	2.2	12	0.65	89.4	1.1	13	0.71	26.3	0.29		0.37	A1	L
“	S3B-4	24.6-27.6	3.0	26	-	200.2	0.7	18	-	52.0	0.26		0.32	A2	L
“	S4B-1	0.0-3.6	3.6	4	0.5	31.2	1.0	4	0.5	6.6	0.21		0.26	A2	L
	S4B-2	3.6-6.2	2.6	3	0.52	58.5	1.0	3	0.52	16.5	0.28		0.35	A2	L
	S5B-1	0.0-4.5	4.5	3	0.5	20.3	1.0	3	0.5	8.3	0.41		0.51	A2	L
	S5B-2	26.0-28.8	2.8	31	-	191.1	0.7	22	-	55.1	0.29		0.36	A2	NL
	S6B-1	0-5.4	5.4	2	0.5	24.3	1.0	2	0.5	9.7	0.40		0.50	A2	L
	S6B-2	24.1-25.0	0.9	5	-	164.2	0.8	4	-	48.7	0.30		0.37	A2	L
	S6B-3	25.0-29.2	4.2	17	-	188.1	0.7	12	-	54.4	0.29		0.36	A2	L

N_m: SPT value, N_1(60): Normalized SPT value, $(q_c)_m$: CPT cone resistance value, $(q_c)_1$: Normalized CPT cone resistance, σ'_0: Effective overburden pressure, $\tau_{equiv.}$: Equivalent cyclic shear stress, C_N: Correction factor for overburden pressure, L: Liquefaction, NL: No Liquefaction.

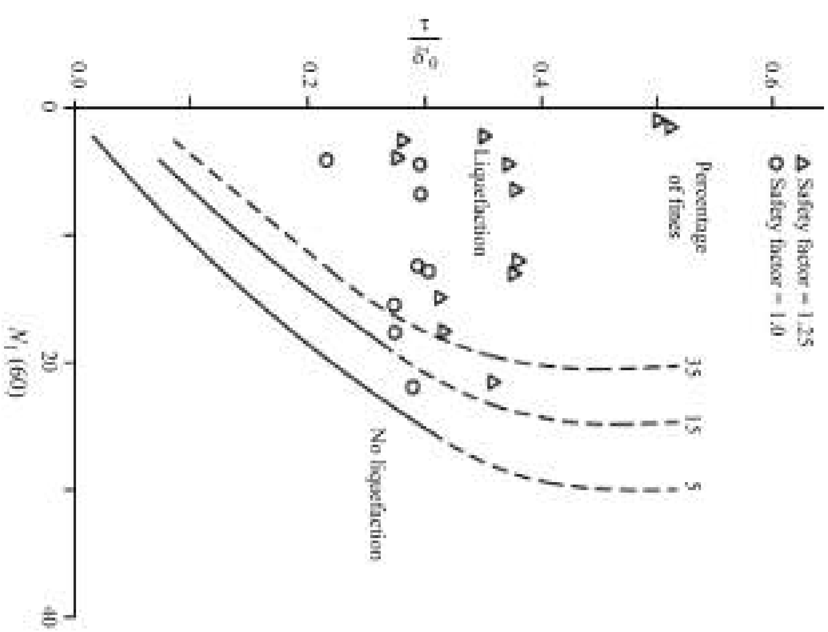

Figure 53 - Liquefaction potential evaluation by SPT tests.

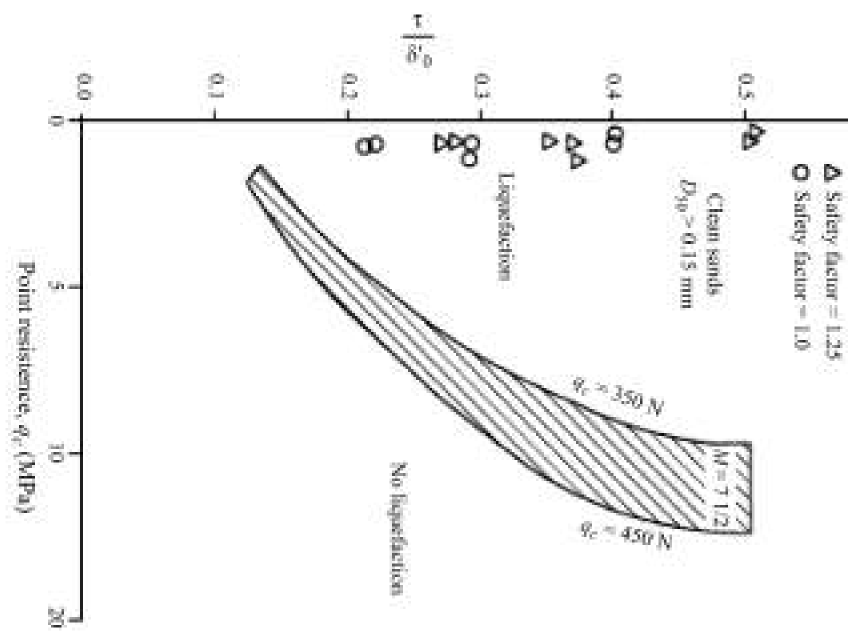

Figure 54 - Liquefaction potential evaluation from CPT tests.

Figure 55 - Construction of North Viaduct.

Figure 56 - Parallel Way.

Figure 57 - A view of South Viaduct construction.

Figure 58 - Placement of pile casing (courtesy Ferreira *et al.*, 2008).

Figure 59 - Placement of pile reinforcement (courtesy Ferreira *et al.*, 2008).

Figure 60 - Placement of tremie pipes (courtesy Ferreira *et al.*, 2008).

Figure 61 - View of caisson (courtesy of Perry da Câmara).

7. Conclusions

The following conclusions can be outlined:

For the Vasco de Gama bridge

1) For the pile foundations, each geotechnical design situation shall be verified that no relevant limit state is exceeded.

Figure 62 - Pier under construction (courtesy of Perry da Câmara).

Figure 63 - General view of the construction works (courtesy of Perry da Câmara).

2) For the verification of limit states, one or a combination of the following methods can be used: design by prescriptive measures, design by calculation, design by loads tests and experimental models and observational method.
3) For design purposes and for a better knowledge of pile behaviour, it is recommended to perform field tests with instrumented piles.
4) Field load tests performed in the New Tagus bridge and Lezíria bridge for design purposes have shown their importance to calibrate the design parameters, to check the performance of individual piles, to assess the overall pile foundation behavior and to analyze the suitability of the construction method.
5) For pile quality control, the use of non-destructive of pile test techniques is recommended.
6) Monitoring during construction and in the long term is important to assess bridge behavior.

For the Lezíria bridge

7) The geotechnical campaigns implemented during the Preliminary Study and Basic Design have allowed the definition of the geological and geotechnical model.
8) The geotechnical characteristics were obtained by a combination of field and laboratory test results.
9) The geotechnical study in the Basic Design was performed respecting the requirements of Eurocode 7, Specification 1536 Bored Piles prepared by CEN - Committee TC 288 and the Procedures and Specifications for Piles prepared by ICE (1978).
10) As the Lezíria bridge is located in zone A of Portugal seismic map, the seismic studies are important.
11) For pile design were used: i) design models; ii) pile load tests that have contributed for the characterization of gravel materials and techniques for driving the metallic casings; and iii) comparable experience.
12) To calibrate the design parameters and to optimize the pile length, static pile load tests (both vertical and horizontal) were carried out on trial piles. In addition, dynamic pile tests were performed for seismic design.
13) As sampling of sandy materials is always difficult, the liquefaction potential evaluation was based in *in situ* tests, namely CPT and SPT. The computation of shear stress in total and effective stress analyses was performed.

8. Lessons for tomorrow

Due to the complexity of bridge analysis, there is a need to work with multidisciplinary teams exploring the huge capacity of computers. Innovative methods and new solutions require highly reliable information and multidisciplinary teams integrating seismologists, geologists, geophysicists, geotechnical engineers and structural engineers.

The success of this challenge requires the joint effort of Owners, Decision Makers, Researchers, Consultants, Professors, Contractors and General Public.

The understanding of the vulnerability and resilience concepts is crucial. Vulnerability is associated with two dimensions, one is the degree of loss or the potential loss and the second integrates the range of opportunities that people face in recovery. This concept has received a great attention from Rousseau and Kant (1756). Resilience is a measure of the system`s capacity to absorb recovery from a hazardous event. It includes the speed with which a system returns to its original state after a perturbation. The capacity and opportunity to relocate or to change are also key dimensions of disaster resilience. The purpose of assessing resilience is to understand how a disaster can disturb a social system and the factors that can disturb the recovery and to improve it.

The education of engineers and Public with scientific methods for evaluating risks incorporating the unpredictable human behavior and human errors is crucial for disaster reduction.

The analysis of past bridge incidents and accidents occurred during earthquakes have shown that all the lessons have not deserved total consideration, in order to avoid repeating the same mistakes. We need to enhance a global conscience and to develop a sustainable strategy of global compensation to better serve our Society. The recognition of a better planning, early warning, that we should take for extreme events which will hit our civilization in the future, is important. Plato (428-348 BC) in the Timaeus stressed that destructive events that happened in the past can happen again, sometimes with large time intervals between and for prevention and protection we should follow the Egyptians example and preserve knowledge through writing.

We should never forget the 7 Pillars of Engineering Wisdom: Practice, Precedents, Principles, Prudence, Perspicacity, Professionalism and Prediction. Following Thomas Mann. we should enjoy the activities during the day, but only by performing those will allow us to sleep at the night.

Efforts should be done to narrow the gap between university education and professional practice, but we should not forget that Theory without Practice is a Waste, but Practice without Theory is a Trap. Kant has stated that *Nothing better than a good theory*, but, following Seneca, *Long is the way through the courses, but short through the example*. I will add through a careful analysis of Case Histories.

In dealing with this subject we should always have in mind:

All for Love
"Errors, like straws, upon the surface
flow;
He who would search for pearls must
dive below".
(John Dryden)

Acknowledgements

Special thanks are due to GATTEL and NOVAPONTE for the permission to publish the results of New Tagus bridge. It is important to refer the contributions of Ricardo Oliveira, Virgílio Rebelo and Vicente Rodrigues for geological studies. The role of LNEC for static and dynamic pile tests needs to be stressed. For the Lezíria Tagus River Bridge, several construction companies and experts were involved, namely Construction Consortium and Design Group. The studies carried out by them are greatly acknowledged. The contribution of Virgílio Rebelo for geological studies is important to refer. The field investigations were carried out by Geocontrole and LNEC, and the laboratory tests were performed by Geocontrole. Special thanks are due to TACE and particularly to Mr. Secundino Vilar and also to BRISA for the permission to publish this paper. It is important to refer the contributions of IST for the static

pile tests and also for the dynamic pile tests. The reception tests for piles were carried out by Geosolve.

References

Ambraseys, N.N. (1998). Engineering Seismology, Earthquake Engineering and Structural Dynamics, 17(1):1-105.

ASTM D1143 (1981). Standard Test Method for Piles Under Static Axial Compressive Load. Annual Book of Standards, Vol. 04.08, Philadelphia, P.A.

Bjerrum, L. (1963). Discussion Section VI - Interaction between structure and soil. Proc. European Conference Soil Me-chanics and Foundation Engineering, Wiesbaden v. 2, pp. 135-137.

Boscardin, M.D. & Cording, E.G. (1989). Building response to excavation induced settlement. Journal Geot. Eng. ASCE, 115(1):1-21.

Bozozuk, M. (1981). Tolerate movements of bridge foundations. Proc. 10th Int. Conference Soil Mechanics and Founda-tion Engineering, Stockholm. Balkema, Rotterdam, v. 1, pp. 699-700.

Burland, J.B. & Wroth, C.P. (1974). Settlement of buildings and associated damage. SOA Review. Conference Settle-ment of Structures. Pentech Press, London, pp. 611-654.

Burland, J.B.; Broms, B.B. & De Mello, V.F.B. (1977). Behaviour of foundations and structures. Proc. 9th Int. Conference Soil Mechanics and Foundations Engineering, Tokyo, Japan, v. 2, pp. 495-546.

Burland, J.B. (1995). Assessment of risk of damage to buildings due to tunneling and excavation. Special Lecture. First International Conference on Earthquake Geotechnical Engineering, Tokyo, Japan, v. 3, pp. 1189-1201.

Cetin, K.O.; Seed, R.B. & Kiureghian, A.D. (2001). Reliability based assessment of seismic soil liquefaction initiation. Proc. XV ICSMGE TC4 Satellite Conference on Lessons Learned from Recent Strong Earthquakes, Istanbul, Turkey, pp. 327-332.

EN 1997 Eurocode 7 (1997a). Geotechnical design. Part 1.

EN 1997 Eurocode 7 (1997b). Ground investigation and testing. Part 2.

EN 1998 Eurocode 8 (1998a). Design of structures for earthquake resistance.

EN 1998 Eurocode 8 (1998b). Design provisions for earthquake resistance of structures - Part 5 Foundations, Retaining Structures and Geotechnical Aspects.

Ferreira, S.; Rebelo, V. & Ribeiro, J. (2008). Pile foundations for Lezíria Bridge (in Portuguese), 11° Congresso Nacional de Geotecnia, Coimbra, v. 4, pp. 3-10,

Gazetas, G. & Mylonakis, G. (1998). Seismic soil structure interaction: New evidence and emerging issues. Geotechnical Earthquake Engineering and Soil Dynamics, ASCE II pp. 1119-1174.

ICIST-IST (2005). Experimental Pile Load Tests. Report. New Tagus River Crossing at Carregado, Lisboa, Portugal.

Institution of Civil Engineers (1978). Piling - Model Procedures and Specifications. Institution of Civil Engineers, London.

Imai, T. (1977). P and S wave velocities of the ground in Japan. Proc. 9th International Conference Soil Mechanics and Foundation Engineering, Tokyo, Japan, v. 2 , pp. 257-260.

INA (International Navigation Association) (2001). Seismic Design Guidelines for Port Structures. Working Group nº 34 of the Maritime Navigation, Commission International Navigation Association. A.A. Balkema Publishers, Rotterdam, 474 p.

Ishihara, K. (1993). Liquefaction and flow failure during earthquakes. 33rd Rankine Lecture. Géotechnique 43(3):351-415.

IST (2004). Generation of response and displacements spectra of alluvial soils of Carregado site, February (in Portu-guese), Report, Lisboa, Portugal.

IST (2005). Dynamic characterization of alluvial soils at Carregado site, May (in Portuguese), Report, Lisboa, Portugal.

Meyerhof, G.G. (1956). Discussion on Paper by Skempton, Peck & MacDonald - Settlements analysis of six structures in Chicago and London. Proc. Inst. Civ. Eng. 5, n. 1.

Moulton, L.K. (1986). Tolerable movement criteria for highway bridges. Report FHWA-TS-85-228, Federal Highway Administration, Washington, D.C., 86 pp.

NCEER (1997). Proc. NCCER Workshop on Evaluation of Liquefaction Resistance of Soils, Summary Report. Edited by Youd, T.L. & Idriss, I.M. National Center for Earthquake Engineering Research, University of Buffalo, Technical Report NCEER-97-0022.

Oliveira, J.B.; Gomes, J.P.; Sêco e Pinto, P.S. & Pina, C.A. (1996). Dynamic tests performed on large piles. Proc. 11 WCEE. Acapulco, Mexico. CD-Rom

Oliveira, R. (1997). Geological and geotechnical studies for the design of Vasco de Gama Bridge. Proc. 6th CNG, Lisboa, v. 3, pp. 1467-1500 (in Portuguese).

Oliveira, R.; Rebelo, V.; Jeremias, F., Coelho, A.G. & Sardinha, R. (2006). Geological and geotechnical studies for the basic design of a new bridge over the Tagus River, at Carregado. Proc. 10 CNG, Lisboa (in Portuguese), v. 1, pp133-144.

Polshin, D.E. & Tokar, R.A. (1957). Maximum allowable non-uniform settlement of structures. Proc. 4th Int. Conference Soil Mechanics and Foundation Engineering, Butterworths Scientific Publications, London, pp. 402-405.

Portugal, A.; Perry da Câmara, A.; Virtuoso, F. & Rebelo, V. (2005). New Crossing across Tagus river in Carregado. 4[as] Jornadas Portuguesas de Engenharia de Estruturas, Lisboa (in Portuguese).

Rodrigues, L.F. (1979). Methods for Seismic Site Investigation in Engineering Geology. The Importance of Shear Wave (in Portuguese). Research Thesis, LNEC, Lisboa.

RSA (1983). Portuguese Safety and Actions Code for Buildings and Bridges (in Portuguese), 96 p.

Sêco e Pinto, P.S. & Sousa Coutinho, A.G.F. (1991). Deformation of soils and displacements of structures. Proc. X ECSMFE, Florence, Italy, pp. 539-542.

Sêco e Pinto, P.S. & Oliveira, R. (1998). A recent difficult foundation problem: The case of the new Tagus Bridge. Proc. 4th International Conference on Case Histories in Geotechnical Engineering, St. Louis, USA. CD-Rom.

Sêco e Pinto, P.S.; Correia, J. & Vieira, A. (1997). Evaluation of liquefaction potential of a site located in the south of Portugal. Proc. of the Discussion Special Technical Session on Earthquake Geotechnical Engineering during 14th ICSMFE, Hamburg, Germany. Edited by Pedro S. Sêco e Pinto, Published by Balkema, Kalamazoo, pp. 113-124.

Sêco e Pinto, P.S. & Rodrigues, L.F. (1989). Pile integrity tests in Boinas Bridge. Proc. 3rd Portuguese Geotechnical Congress, Porto (in Portuguese), v. 2. pp. G-57-G65.

Seed, H.B. & Idriss, I.M. (1982). Ground Motions and Soil Liquefaction During Earthquakes. Earthquake Engineering Research Institute Monograph, Berkeley, p 12.

Skempton, A.W. & MacDonald, D.H. (1956). Allowable settlement of buildings. Proc. Institute of Civil Engineers, Part 3, n. 5, pp 727-768.

Stokoe II, K.H.; Darendeli, M.B.; Andrus, R.D. & Brown, L.T. (1999). Dynamic soil properties: laboratory, field and correlation studies. Theme Lecture. Proc. of 2nd International Conference on Earthquake Geotechnical Engineering, Lisboa, Portugal. Edited by Pedro Sêco e Pinto. Published by A. Balkema, Kalamazoo, v. 3, pp. 811-845.

TC4 (ISSMGE) (2001). Case Histories of Post-Liquefaction Remediation. Technical Committee on Earthquake Geotechnical Engineering, Tokyo, Japan, Editor Japanese Geotechnical Society, 117 pp.

TC4 (ISSMGE) (1993). Manual for Zonation of Seismic Geotechnical Hazards. Japanese Society of Soil Mechanics and Foundation Engineering, Tokyo, 209 p.

Tokimatsu, K. & Seed, H.B. (1984). Simplified Procedure for the Evaluation of Settlements in Clean Sands. Report UCB/EERC 84/16. University of California.

Tokimatsu, K.; Kuwayama, S. & Tamura, S. (1991). Liquefaction potential evaluation based on rayleigh wave investigation and its comparison with field behavior. Proc. 2nd Int. Conf. on Recent Advances in Geotech. Earthquake Eng. and Soil Dynamics, March 11-15, St. Louis, USA, v. I, pp. 357-364.

Tokimatsu, K & Seed, H.B. (1987). Evaluation of settlements in sands due to earthquake shaking. JGE, ASCE, Vol. 113, Nº 8, pp. 861-878.

Youd, T.L. & Gilstrap, S.D. (1999). Liquefaction and deformation of silty and fine-grained soils. General Report. Proc. of 2nd International Conference on Earthquake Geotechnical Engineering, Lisboa, Portugal. Edited by Pedro Sêco e Pinto, A. Balkema, Kalamazoo, v. 3, pp. 1013-1020.

Evaluation of Sample Quality and Correction of Compressibility and Strength Parameters-Experience with Brazil Soft Soils

M.I.M.C.V. Bello, R.Q. Coutinho, A.S. Norberto

Abstract. Sample quality has a direct influence on the results of geo-mechanical parameters obtained in laboratory and *in situ* tests, potentially causing serious technical and economic consequences. In the study of soft soil behavior using laboratory tests, it is important to evaluate, and be able to quantify sample quality, and if necessary and possible, to correct the effects of sample disturbance and to obtain geotechnical parameters appropriate and necessary for engineering projects. This paper presents and discusses the Brazilian results of sample quality evaluation and the correction of compressibility and strength parameter results to account for the effects of sample disturbance, as well as a review of several papers that address correction and sample quality issues. Proposals presented by Coutinho (2007) and Futai (2010) were used to evaluate sample quality. Proposals presented by Schmertmann (1955), Oliveira (2002), Coutinho (2007) and Futai (2010) were used for correction of compressibility parameters that were altered by the effects of sample disturbance. The results from these study areas were satisfactory for all the proposals. It was possible to obtain compression parameters corresponding to good quality samples using the proposals for correcting the effects of sample disturbance.

Keywords: compressibility parameters, oedometer test, sample quality.

1. Introduction

The qualitative study of soft clay samples is very important in order to be able to obtain the appropriate values for geotechnical parameters resulting from laboratory and *in situ* tests used in engineering projects and in empirical correlations. The quantitative effect of inappropriate sampling can bring serious consequences both technical and economic.

Efforts have been made during research projects to understand, quantify, minimize, and whenever possible, correct the geotechnical parameters resulting from sample disturbance of Recife soft clays (Coutinho, 1976; Ferreira, 1982; Ferreira & Coutinho, 1988; Coutinho *et al.*, 1998; Oliveira *et al.*, 2000, Oliveira, 2002; Coutinho, 2007; Bello, 2011; Coutinho & Bello, 2012). The studies cited above were carried out by the Geotechnical Research Group (GEGEP/UFPE) coordinated by the second author.

This article presents and discusses a review of the Brazilian results of sample quality evaluation, and correction of the effects of sample disturbance. Proposals presented by Coutinho (2007) and Futai (2010) were used to evaluate sample quality. Proposals presented by Schmertmann (1955), Oliveira (2002), Coutinho (2007) and Futai (2010) were used in order to correct compressibility parameters that were influenced by the effects of sample disturbance.

2. Analyses of the Sampling Process

Sample disturbance occurs in all sampling processes and, if sampling is carried out well, the effects of disturbance will hopefully be more subtle. Whatever its magnitude, sampling disturbance normally affects both undrained strength and compressibility. In addition, chemical effects may cause changes in the plasticity and sensitivity of the soil sample.

Hvorslev (1949) classified the sample disturbance according to five categories: (a) variations in the stress conditions; (b) variations in the water content and in the initial void ratio; (c) alteration of the soil structure; (d) chemical variations; and (e) mixture and separation of the soil constituents. The influence of the disturbance on the results of laboratory tests depends on the type and degree of disturbance, the soil characteristics, and the technique used in the tests.

Ladd & Lambe (1963) (see also Sandroni, 1977) defined that perfect sampling is correlated to the process where the disturbance is limited only to the effects caused by relieving field stress, however the real sampling presents additional disturbance. The sampling procedure varies the stress state and induces disturbance of the soil (Fig. 1).

Jamiolkowski *et al.* (1985) considered some of the factors that result in alterations during the sampling procedure and preparation of the sample specimens: (a) variations in stress caused by opening of the hole; (b) removal of

Maria Isabela Marques da Cunha V. Bello, D.Sc., Associate Professor, Universidade Federal de Pernambuco, Caruaru, PE, Brazil. e-mail: isabelamcvbello@hotmail.com.
Roberto Quental Coutinho, D.Sc., Full Professor, Universidade Federal de Pernambuco, Recife, PE, Brazil. e-mail: rqc@ufpe.br.
Alison de Souza Norberto, M.Sc., Ph.D. Student, Universidade Federal de Pernambuco, Recife, PE, Brazil. e-mail: alison_norberto@hotmail.com.
Submitted on October 9, 2018; Final Acceptance on August 1, 2019; Discussion open until December 31, 2019.
DOI: 10.28927/SR.423245

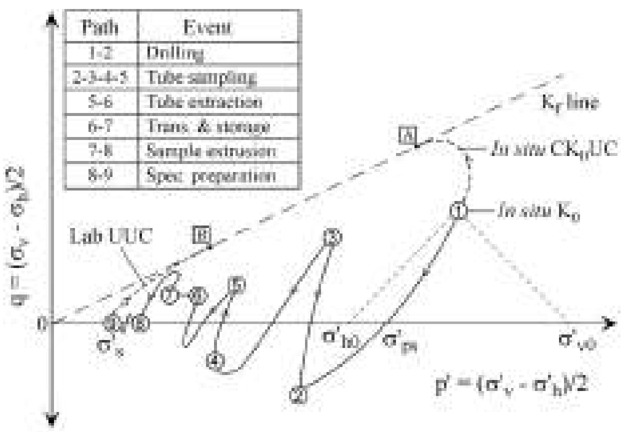

Figure 1 - Stress Paths during the tube sampling process (Ladd & Lambe, 1963).

the field strength stress; (c) geometry and type of the sample extraction equipment; (d) method used by the sample extraction equipment; (e) relation between diameter of the sample extraction equipment and the sample specimens; (f) transport, storage, and laboratory manipulation.

Leroueil & Jamiolkowski (1991) defined the disturbance as destruction of the agglutinate between the points of contact of the grains, and indicated that the two main causes of the disturbance are the distortion mechanics associated with the operation of sampling, and the relief of the total stress field.

Hight (2000) examined the effect of sampling on the behavior of soft clays, stiff clays and sands, and described improvements that have been made to the methods of sampling, which have enabled higher quality samples to be obtained.

Coutinho (2007) reported that in practical and research works in Brazil, sampling has normally been carried out by means of a thin walled stainless-steel tube (Shelby), or by using a stationary piston sampler, 800 to 1000 mm in length, with an internal diameter measuring 100 to 110 mm, and an area ratio of 7% respectively, in order to obtain samples of satisfactory quality. According to Coutinho (2008), complementary procedures in each case must be established by updating the knowledge base in the literature. Aspects of the disturbance process of the sample are inevitable, but the degree of disturbance can be minimized through improvements in sampling procedures in the field, along with proper manipulation in the laboratory.

Oliveira (2002) comments that better-quality samples can be obtained by adequately trained teams using Sherbrooke sampling. Tanaka (2008) concluded that it is possible to obtain high quality samples of soft clays to depths of 400 meters using standard sampling methods that follow technical recommendations.

Futai (2010) indicates that, the solutions adopted to eliminate the unwanted effects on samples often include the use of the method suggested by Ladd & Foot (1974): SHANSEP ("Stress History and Normalized Soil Engineering Properties").

Okumura (1971) listed some quantitative requirements for parameters to be used in evaluating sampling disturbance. Such parameters must be: (a) Easy to determine for perfectly undisturbed conditions; (b) Regularly variable with disturbance, regardless of the depth of extraction, the stress system experienced, and the soil type; (c) Sensitive to change due to disturbance; (d) Easily and accurately measured.

3. Influence of the Sample Quality on Strength Parameters

The sample quality has direct influence on the strength parameters obtained in laboratory testing. Many researchers have investigated ways to understand and avoid the disturbance processes. Santagata *et al.* (2006) present the discussion about the effect of the sampling tube in results of triaxial CIU-C tests. Hight (2000) presents the familiar results of a conventional soft clay site investigation, involving sampling and laboratory testing (Fig. 2a). It shows the results of unconsolidated undrained (UU) triaxial compression (TC) tests on samples of Singapore marine clay, the majority of which were taken with a thichwalled open drive sampler. There is a large scatter in the data, most of which falls below the best estimate of *in situ* shear strength in compression. Samples taken with a thin-walled piston sampler lead to higher strength. Figure 2b shows the comparison between the results of undrained strength obtained from UU-C e CIU-C triaxial tests and *in situ* field vane tests obtained by Teixeira (1972), Oliveira (1991) and Oliveira *et al.* (2000) in Clube Internacional of Recife. The lower S_u values, obtained by Teixeira (1972), were caused by the disturbance of samples (Shelby type samples with diameter of 60 mm) and test conditions (procedure and equipment). The reduction of S_u values was in the order of 50% in comparison with the results obtained by Oliveira (1991) and Oliveira *et al.* (2000).

Ortigão (1980) performed UU triaxial tests and registered the variation of S_u value with the diameter of samplers, using piston samplers with different diameters. This effect was studied theoretically by Baligh (1986), when was introduced the concept of stress path. Baligh (1986) showed that the disturbance increases when the relation between the thickness and diameter of the tube also increase. Tube sampling can be causing yielding by compression and shear because the cycles of compression-extension-compression can be causing the destructuring of the soil. These effects and the theoretical prediction of Baligh (1986) were confirmed experimentally by La Rochelle & Lefebvre (1971), Ortigão (1980), Tavenas & Leroueil (1987) and Hight *et al.* (1992).

Hight (2000) comments that the advantage of both UC and UU tests is that they show the full imprint of sam-

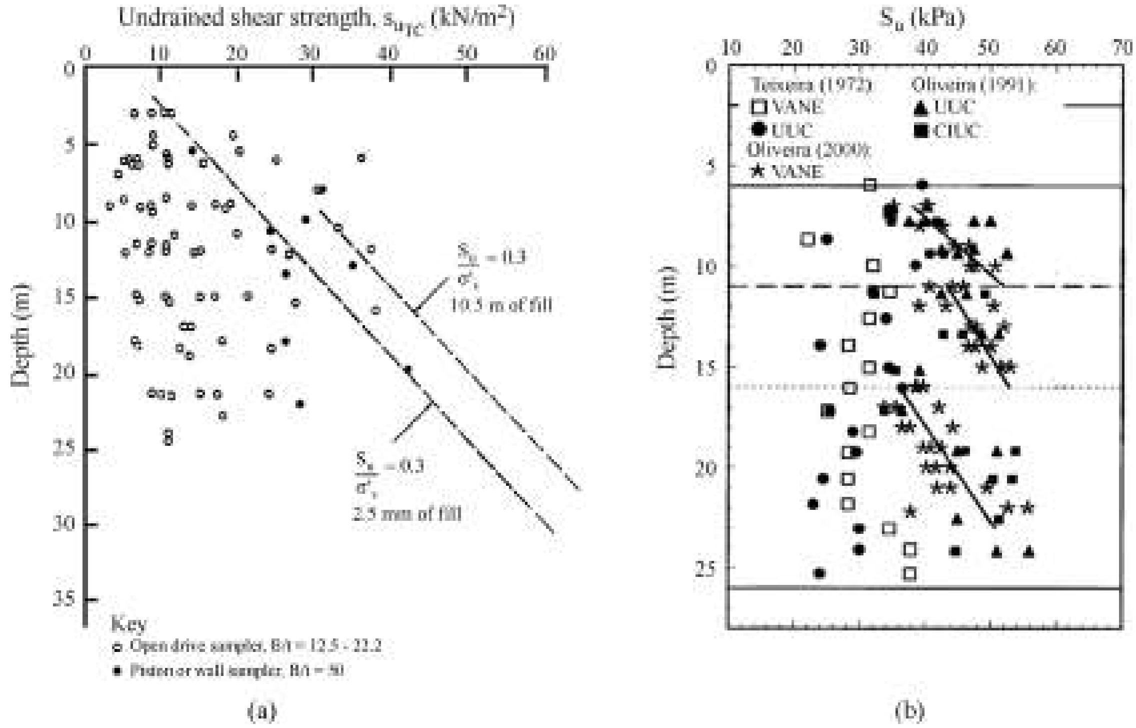

Figure 2 - (a) Results of unconsolidated undrained triaxial compression tests on thick-walled and thin-walled tube samples of Singapure marine clay (Hight, 2000); (b) Undrained strength profile of the Clube Internacional -Recife (Coutinho *et al.*, 1998).

pling effects, and the UC data in Fig. 3a confirms that "block" samples taken by rotary methods can be of higher quality than even the best tube samples. Between tube samples, there is a significant difference in measured strengths, and, therefore, in levels of sample disturbance.

Coutinho *et al.* (1998) show results of the stress-strength curve of UU triaxial tests performed in Recife soft clays (samples of good and bad quality). It can be observed the difference in the S_u and ε_f values obtained (Fig. 3b).

Figure 4 shows the influence of sample quality in the obtained S_u value. This influence is represented for difference between the sampler diameter and the relation of the sampler/specimen's diameters for Sarapuí-RJ deposit (Ortigão, 1980) and Clube Internacional - Recife deposit (Coutinho *et al.*, 1993).

For the Sarapuí deposit, the S_u values for 8.0 m depth, using sampler and specimens with diameters of 50 mm (S_u = 4.5 kPa), and sampler and specimens with diameters

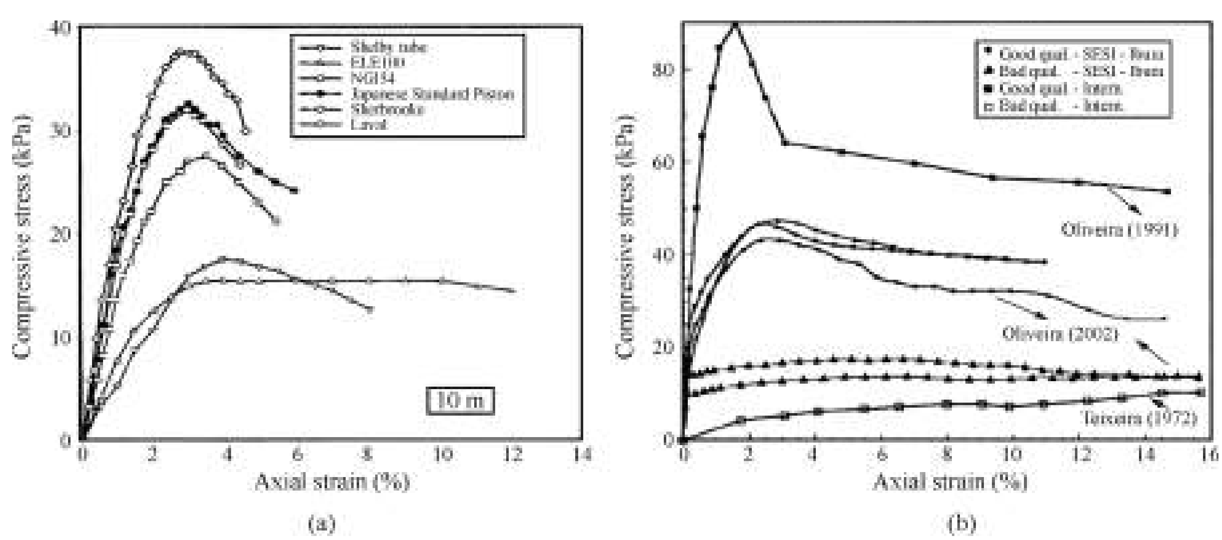

Figure 3 - (a) Unconfined compression tests on Ariake Clay (Hight, 2000); (b) Triaxial UU tests performed in poor and good samples - Recife (Coutinho *et al.*, 1998).

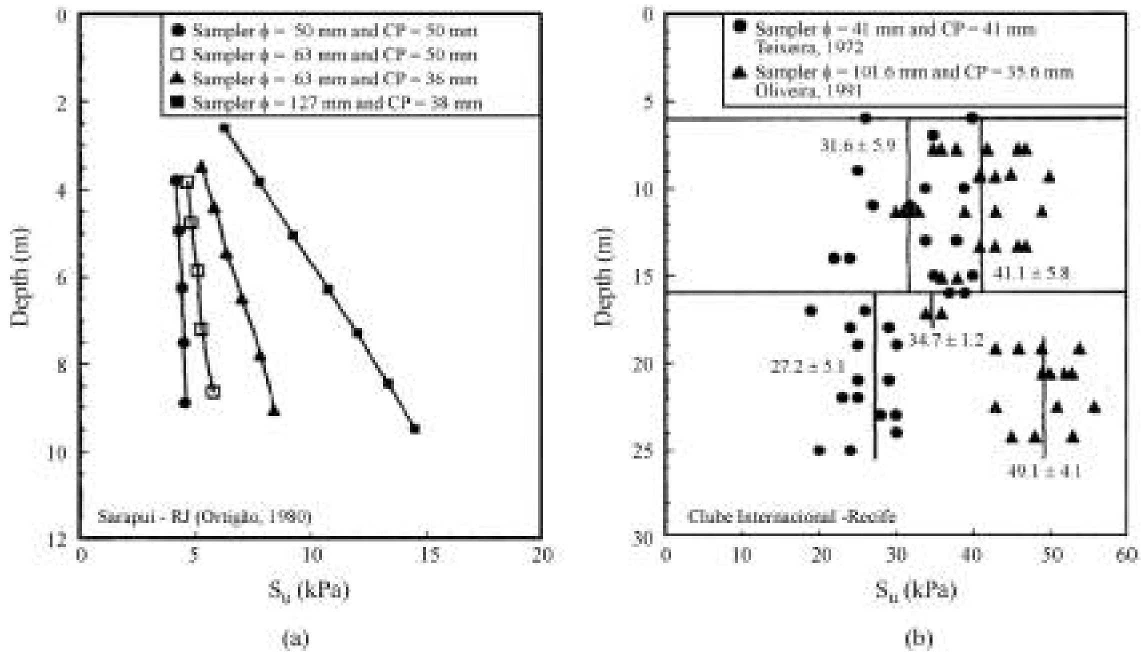

Figure 4 - UU Triaxial tests results: (a) Sarapuí (Ortigão, 1980); (b) Clube Internacional do Recife (Coutinho *et al.*, 1993).

of 125 mm and 38 mm, respectively (S_u = 13 kPa), provided the relation of $S_{u\phi127}/S_{u\phi50}$ = 2.9. For Clube Internacional, the relation for the second layer was equal to $S_{u\phi101.6}/S_{u\phi41}$ = 1.8 (sampler of 101.6 mm diameter and specimen of 35.6 mm; and sampler of = 41 mm and specimen of 41 mm). It is observed that the larger the diameter of the sampler and the relationship between the diameters of the sampler and the specimen, the greater the S_u value.

Clayton *et al.* (1992) show comparisons of stress paths of Bothkennar clay sampled in different ways (Sherbrook, Laval and piston samples) of Bothkennar clay. The authors found that provided tube sampling strain excursions were limited to ± 2% and that appropriate stress paths were used to reconsolidate the material back to its *in situ* stress state, the undrained strength of the Bothkennar clay would be within ± 10% of its undisturbed value. Strain path tests on high quality (Laval and Sherbrook) undisturbed samples of natural clay by Clayton *et al.* (1992) have confirmed that, in normally and lightly over-consolidated clays, stiffness is greatly affected by tube sampling, but undrained strength reductions are less significant and can, in any case, be recovered by good reconsolidation procedures.

Hight (2000) shows that the strength available around the critical potential failure surface A-B-C beneath an embankment constructed on this clay will vary by an amount reflecting the level of anisotropy of the soil (Fig. 5). The average mobilized strength is indicated as S_u. Experience has shown that S_u is often close to the average strength measured in simple shear, which in this case is similar to the strength measured in UU tests on poor quality samples, so that, when UUTC data is combined with a conventional factor of safety, a safe design results. An improvement in sample quality will lead to a higher UUTC strength profile, and if the same design procedure is adopted, *i.e.* using UUTC strengths to represent an average mobilised

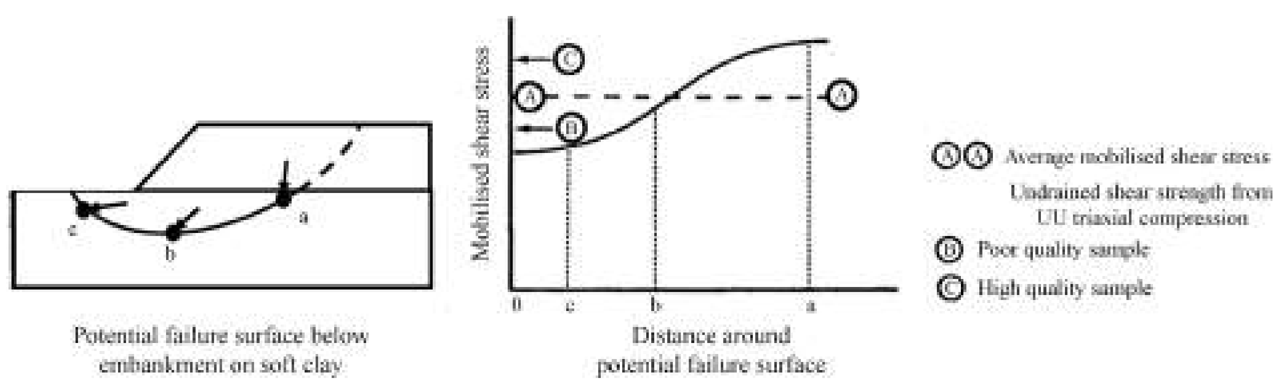

Figure 5 - Inherent dangers in improving sample quality while neglecting anisotropy (Hight, 2000).

strength, an unsafe design may result, unless the factor of safety is modified.

4. Influence of the Sample Quality on Compressibility Parameters

The quality of the sample directly influences the edometric compression test. Skempton & Sowa (1963) analyzed the compressibility through the relations between *in situ* void ratio subjected to the same vertical stress σ'_{vo} (usually consolidation) for more than 20 clays of different lithologies. The authors observed that the void ratio can be correlated with limits of liquidity, plasticity and depth, and concluded that: (a) the relationship between e_0 and log σ'_{vo} is essentially linear; (b) for a certain value of (σ'_{vo}, e_0) normally consolidation depends fundamentally on the nature and mineralogy of the clays and can be represented by the liquid limit; (c) the compressibility curves tend to converge; (d) the use of the liquidity index reduces dispersion.

Ladd (1973) listed the following structural disarrangement effects in the oedometer compression curve: (a) decrease of the void ratio (or increase in deformation) for a σ'_v value;

(b) difficulty in defining the point of smaller curvature; (c) reduction of the pre-consolidation pressure value; (d) increase of compressibility in the recompression region, and decrease in the compression region. Hight (2000) shows in Fig. 6a, the bounding surfaces found for Saint Louis clay, from East Canada, in block samplers, Laval samples and 50 mm diameter piston samples. Tests on the block and Laval samples define the same bounding surface, which sits well outside the equivalent surface defined on the basis of the poorer quality piston samples.

Coutinho (1976, 2007) presents a study with examples of comparative oedometer curves for samples taken by different samplers (Sherbrooke, Shelby 60 and 100 mm), and their corresponding properties (Fig. 6b).

Oedometer curves are also shown for a completely disturbed sample obtained from the laboratory. It is observed that the better-quality sample was obtained with Sherbrooke samplers (Coutinho *et al.*, 2000). The results confirmed all the effects caused by the disturbance described by Ladd (1973). It also shows that the normally consolidation range of a good quality curve is not linear, as usually described ("straight virgin"), but rather presents itself as a curve. The line recognized as a straight (virgin) line is in fact curved.

The void ratio relation *vs.* the effective pressure becomes linear with the disturbance. Compression curves are similar for effective pressures reaching high values. The relation between pre-consolidation pressures of good and poor-quality samples was found to be as high as 3, although initial void ratios do not seem to be significantly influenced by sampling quality. Significant reductions were also observed in the compression index C_c, in the permeability and in the coefficient of vertical consolidation c_v values as the soil was disturbed through poor quality sampling procedures (Table 1). In general, the swell index C_s showed a slight increase with sampling disturbance (Coutinho, 1976, 2007). These effects cause errors in the evaluation of the evolution of the settlements through time (the periods predicted for stabilization can be greater when based on sample disturbance).

The use of geotechnical parameters obtained from poor quality samples can lead to serious technical and economic consequences (Martins, 1983; Coutinho *et al.*, 1998; Oliveira, 2002; Coutinho, 2007, 2008; Almeida & Marques, 2010).

Figures 7a and 7b (Coutinho *et al.*, 1998) show the behavior of geotechnical parameters of depth compressibility for the SESI - Ibura (Recife) and Sarapuí (Rio de Janeiro) sites, respectively. For both sites, the values obtained for the compression index (C_c), the pre- consolidation stress

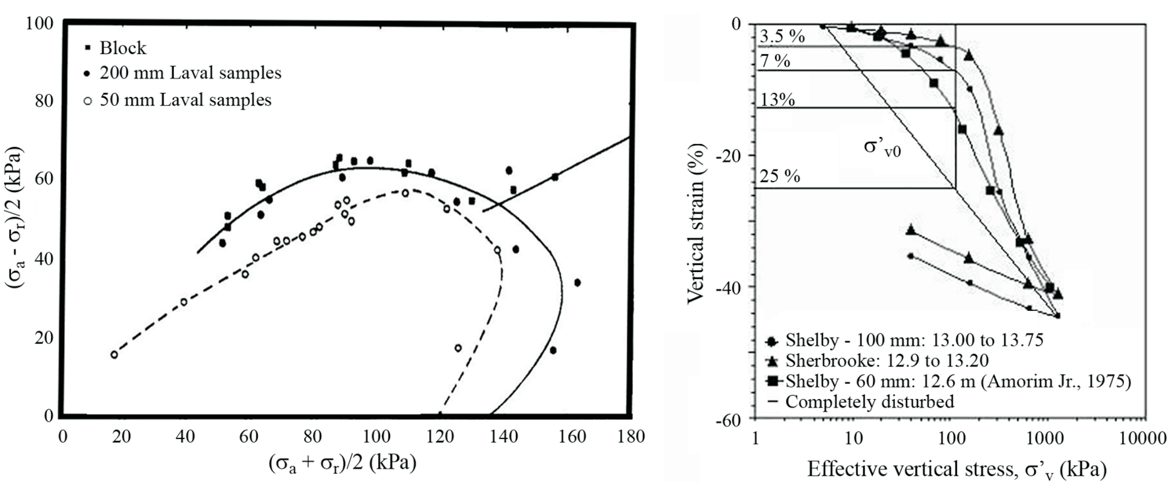

Figure 6 - (a) Shrinking of the bounding surface for Saint Clay as a result of disturbance during sampling (Hight, 2000); (b) Oedometer curves from samples taken using differing methods (Coutinho, 2007).

Table 1 - Effect of sampling on one-dimensional consolidation for Recife and Sarapuí-RJ clays (Coutinho *et al.*, 1998).

	Recife (International Club)		Sarapuí (Rio de Janeiro)	
Parameters	Good/poor	Good/disturbed	Good/poor	Good/disturbed
σ'_p	1.5-3.0	3.0-5.0	1.5-2.0	1.5-2.5
C_S	0.8-1.0	0.7-1.2	0.9-1.2	1.0-1.1
C_c	1.2-2.0	1.2-2.1	1.2-1.5	1.4-1.7
C_v (water level)	1.21	1.93	1.26	1.37

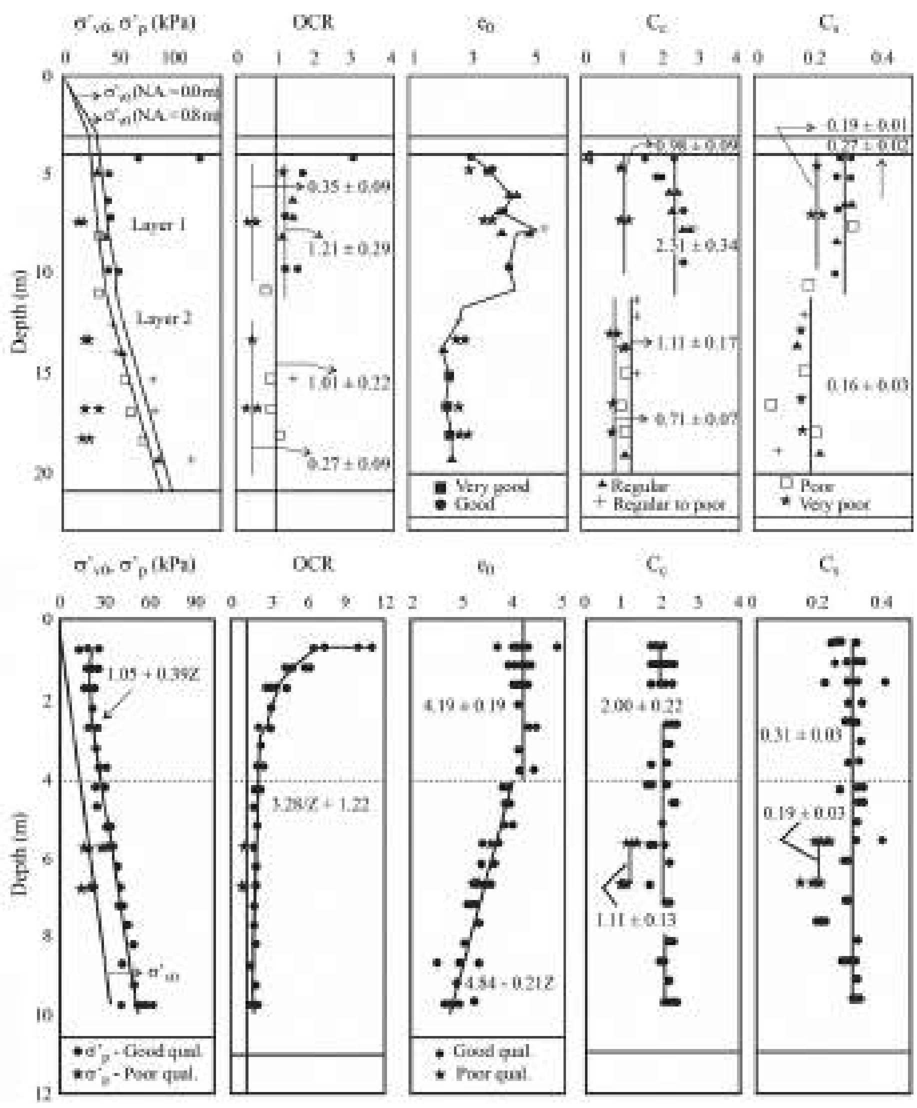

Figure 7 - Compressibility parameters *vs.* depth; (a) SESI-Ibura - Recife (b) Sarapuí-Rio de Janeiro (Oliveira, 2000).

(σ'_p) and OCR, for the samples of better quality were higher compared to the disturbed/poor quality samples. The relationships obtained were as follows: SESI - Ibura: (a) $C_{c\ satisfactory}/C_{c\ poor\ quality}$ = 2.4 for the 1st layer and 1.6 for the 2nd layer; (b) $OCR_{satisfactory}/OCR_{poor\ quality}$ = 3.6 (on average) for both layers; (c) $C_{s\ satisfactory}/C_{s\ poor\ quality}$ = 1.2 for the 1st layer, not varying for the 2nd layer; Sarapuí: (a) $C_{c\ \mathrm{satisfactory}}/C_{c\ poor\ quality}$ = 1.8; (b) $OCR_{satisfactory}/OCR_{poor\ quality}$ = 1.8. The initial void ratio (e_0), the influence of the disturbance is not significant, in both deposits.

Ferreira & Coutinho (1988) results show the influence of disturbance on the coefficient of consolidation (c_v), which causes a large drop in c_v values in the recompression region, and a lower quantitative effect in the virgin compression region (Ladd, 1973). In the normally consolidated region the ratios found for mean values of c_v for samples of good quality, poor quality and completely disturbed were for the International Club, 2.3/1.9/1.0; and for Sarapuí, 1.7/1.4/1.0, respectively.

Figure 8 shows correlations between C_C and e_0, considering the sample quality, for the SESI - Ibura and Internacional Club sites. The samples were classified as Very Good to Excellent (VG), Good (G), Regular (R), Transition range between Regular and Poor (T), Poor (P) and Very Poor (VP). In this way, we attempted to perform correlations with all samples obtained, separating what is called satisfactory / adequate quality (VG, G and R) from what is called inadequate quality (T, P and VP). It was also sought to verify the quantitative effect of the transition band (T) on the correlation of samples with satisfactory quality.

It is easily observed in Fig. 8 the effect of sample disturbance in obtaining the C_c. Considering e_0 = 3.0, C_c values of 1.67 (SESI - Ibura) and 2.43 (International Club) are obtained for samples of satisfactory quality (VG + G + R) and for very poor samples, values of C_c of 0.88 (SESI - Ibura) and 1.44 (International Club). There was a decrease in the value of C_c of 90% for SESI-Ibura and 70% for the International Club, due to the poor quality of the samples.

Table 2 presents the results of the statistical correlations performed for the two sites of Recife. As can be observed, the correlation coefficients (r^2) are larger for the SESI-Ibura deposit than the International Club results, as the standard deviations are smaller. The quantitative effect of the transition range (T) on the correlation of samples with satisfactory quality was higher for the International Club deposit.

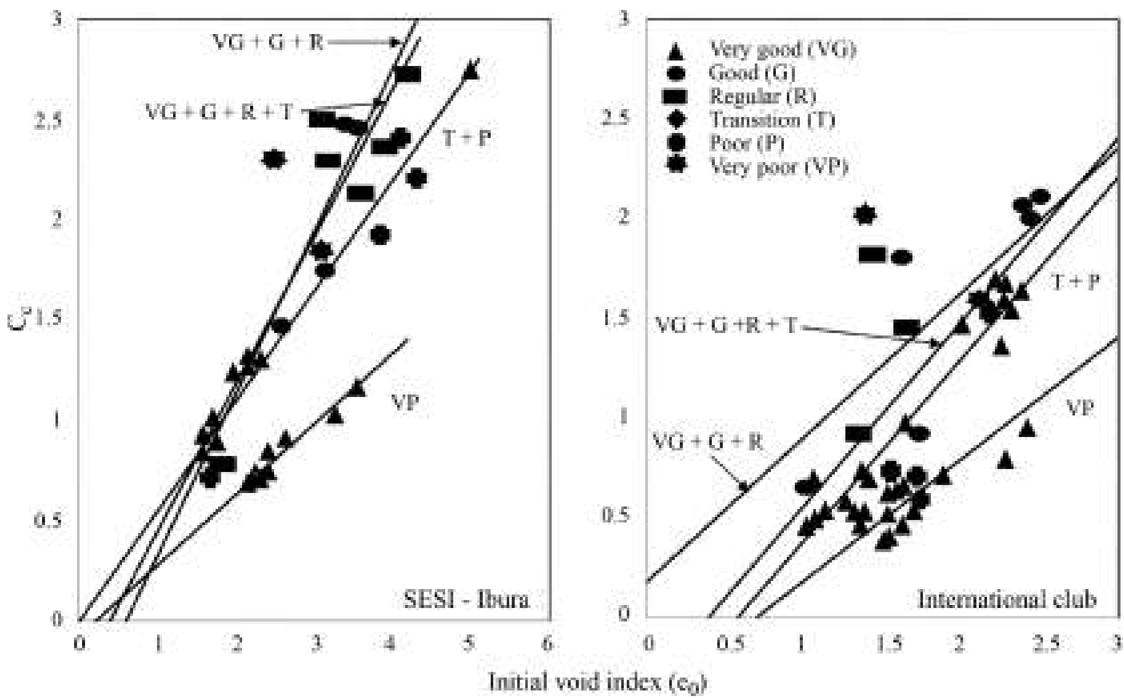

Figure 8 - Statistical correlation between C_c and e_0: SESI-Ibura and International Club - Recife (Coutinho *et al.*, 1998).

Table 2 - Results of statistical correlations for the deposits studied in Recife (Coutinho *et al.*, 1998).

Site	Correlation C_C *vs.* e_0	Equation	r^2	Standard deviation
SESI - Ibura	VG + G + R	$C_C = 0.695\ (e_0 - 0.604)$	0.92	0.18
	VG + G + R + T	$C_C = 0.638\ (e_0 - 0.373)$	0.95	0.16
	T + P	$C_C = 0.520\ (e_0 - 0.011)$	0.96	0.13
	VP	$C_C = 0.308\ (e_0 - 0.127)$	0.88	0.06
International Club	VB + G + R	$C_C = 0.757\ (e_0 + 0.210)$	0.61	0.29
	VG + G + R + T	$C_C = 0.947\ (e_0 - 0.388)$	0.77	0.27
	T + P	$C_C = 0.923\ (e_0 - 0.557)$	0.86	0.17
	VP	$C_C = 0\ 620\ (e_0 - 0\ 668)$	0.64	0.18

5. Evaluation of Sample Quality

5.1. Proposal of Coutinho (2007) from Lunne *et al.* (1997)

A quantitative procedure for evaluation of the quality of samples has been defined by NGI-the Norwegian Geotechnical Institute (Lacasse, 1988). This procedure uses volumetric deformation (ε_{vo}) corresponding to the initial effective vertical stress (σ'_{vo}) (Eq. 1). This criterion was later modified using the ratio $\Delta e/e_0$ by Lunne *et al.* (1997) (Table 3). Lunne *et al.* (1997) justify that a variation in void ratio (Δe) is more detrimental to the soil structure the lower the initial void ratio (e_0). In accordance with the proposal, the relation $\Delta e/e_0$ is used as criterion for evaluating sample disturbance, with Δe being the void ratio variation, and e_0 being the initial void ratio.

$$\varepsilon_{\sigma'_{v0}} = \frac{e_0 - e_{\sigma'_{v0}}}{1 + e_0} \qquad (1)$$

Coutinho (2007), from Coutinho *et al.* (1998) and Oliveira (2002), based in Lunne *et al.* (1997) presented a proposal for Brazilian clays (Table 3).

The proposal presents four groups used for the classification of samples: very good to excellent, good to regular, poor, and very poor. Figure 9 shows the volumetric (ε_{vo}) to σ'_{vo} profile obtained in oedometric tests in the two research areas of UFPE (Internacional Club and SESI-Ibura). Results of Sherbrooke samples and completely dented samples were included. The straight vertical line presented corresponds to the limits suggested by Lunne *et al.* (1997), separating the samples in satisfactory to unsatisfactory, for the material investigated.

5.2. Proposal of Futai (2010)

Futai (2010) presented a proposal for evaluation of sample quality through application of a normalized compression curve using data from Brazilian deposits (Fig. 10a). According to this proposal, the normalized curve (ID x $(e_y - e)/e_y$) allows direct evaluation of sample quality, distinguishing between good quality samples, and those remolded or disturbed, for ID > 1 (clays that are normally consolidated).

The restructuring index (ID) is presented in Eq. 2, while Eqs. 3 and 4 make it possible to evaluate sample quality, and make comparisons using the results of compression tests to adopt ID values, or classify them by direct use of the curve limit presented in Fig. 10a.

$$\mathrm{ID} = \sigma'_v / \sigma'_{vy} \qquad (2)$$

where σ'_v is the effective pressure, σ'_{vy} is the pressure of the oedometer tests, and e_y is the void ratio in the effective procedure.

Good quality samples must present:

$$0.22 < (e_y - e)/e_y < 0.32 \text{ (for ID = 3)}; \qquad (3)$$

$$0.48 < (e_y - e)/e_y < 0.58 \text{ (for ID = 10)}. \qquad (4)$$

Table 4 presents values of (ID x $(e_y - e)/e_y$) for Recife and Sarapuí clays taking into account different sample conditions. Good quality samples are situated in the range of recommended values (Eqs. 3 and 4).

The proposals presented by Coutinho (2007) and Futai (2010) were used to classify the soft clay samples from the Suape study areas (Bello, 2011). In the AE-1 and AE-2 study areas, 43% and 62% of the samples, respectively, were classified as being of satisfactory quality according to the Coutinho (2007) proposal (Table 5).

In spite of all the care taken during sampling and handling procedures used for laboratory and field samples, many were still classified as poor and very poor (unsatisfactory). The presence of decomposing material in the study area, as well as the difficulties encountered when dealing with this type and consistency of soil, causes greater difficulty when attempting to obtain good quality samples.

6. Correction of compression parameters to account for sample disturbance

Three proposals for correction of the effects from disturbance of the samples are presented and discussed in this study: (a) Schmertmann (1955)-construction of the field curve; (b) Oliveira (2002) - construction of new laboratory compression curves (c) Coutinho (2007) - correction of compression ratio (CR) and overconsolidation ratios (OCR) or σ'_{vm} parameters.

Table 3 - Proposed criteria for evaluation of sample disturbance by Coutinho (2007) and Lunne *et al.* (1997).

Overconsolidation ratio	$\Delta e/e_0$ (Coutinho 2007)			
(OCR)	Very good to excellent	Good to regular	Poor	Very poor
1-2.5	< 0.05	0.05-0.08	0.08-0.14	> 0.14
	$\Delta e/e_0$ (Lunne *et al.* 1997)			
(OCR)	Very good to excellent	Good to regular	Poor	Very poor
1-2	< 0.04	0.04-0.07	0.07-0.14	> 0.14
2-4	< 0.03	0.03-0.05	0.05-0.10	> 0.10

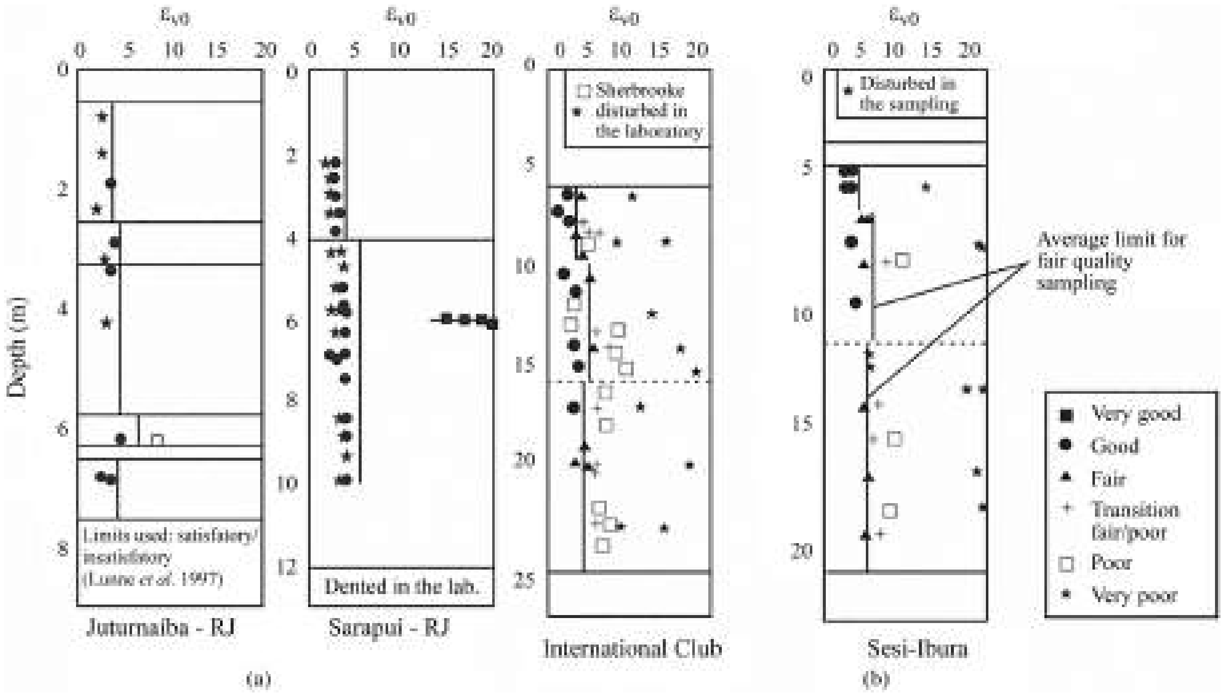

Figure 9 - Sample quality classification: (a) Rio de Janeiro deposits; (b) research areas of Recife (from Coutinho *et al.*, 1998; Oliveira, 2002).

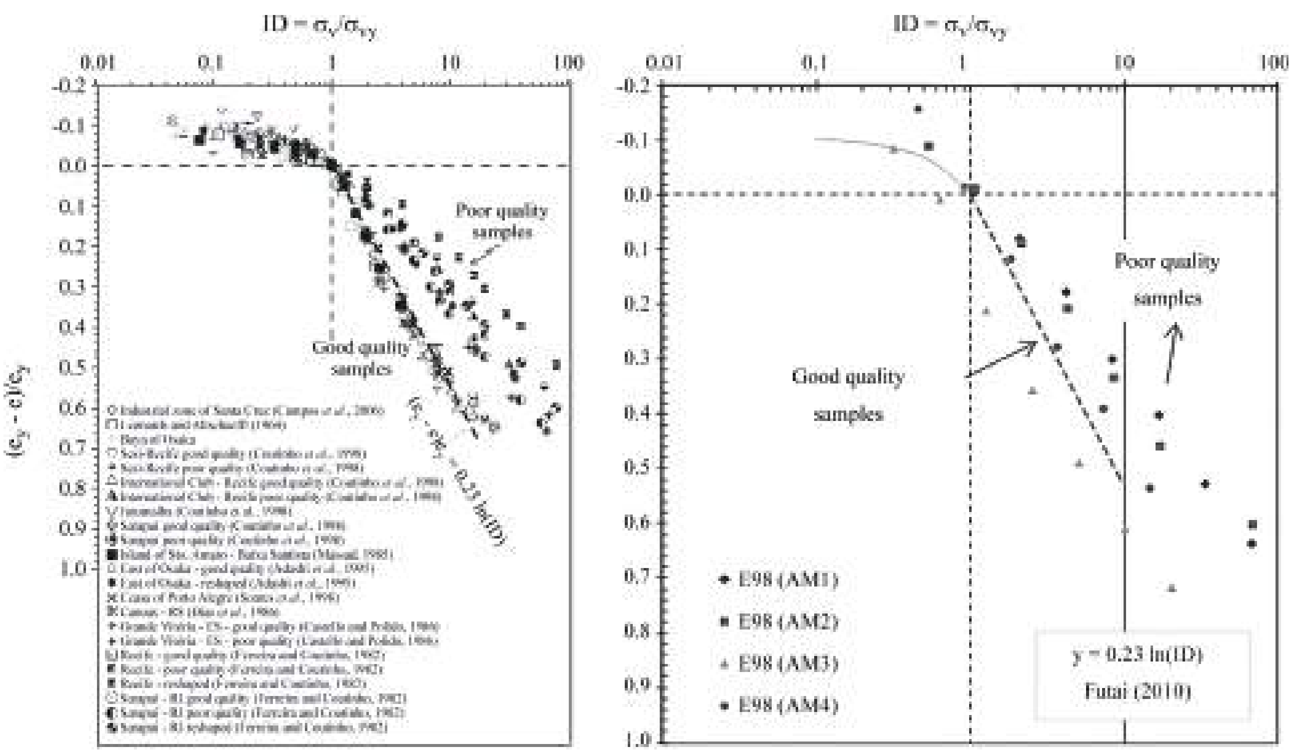

Figure 10 - (a) Standard compression curves of good and poor quality curves (Futai, 2010); (b) Evaluation of sample quality, proposal Futai (2010): Suape study area AE-1 - E98 (Bello, 2011).

Table 4 - Evaluation of sample quality (Futai, 2010).

Local and reference	Sample quality	$(e_y - e)/e_y$	
		ID = 3	ID = 10
Recife (Ferreira & Coutinho, 1988)	Completely disturbed	0.07	0.20
	Poor quality	0.12	0.31
	Good quality	0.25	-
Rio de Janeiro (Ferreira & Coutinho, 1988)	Completely disturbed	0.10	0.30
	Poor quality	0.16	0.37
	Good quality	0.25	0.50

Table 5 - Classification of sample quality according to Coutinho (2007) proposal: results of Suape (Bello, 2011).

Areas	Classification	Samples	(%)
AE-1 30 samples	Very good to excellent	4	13.3
	Good to regular	9	30.0
	Poor	13	43.3
	Very poor	4	13.3
AE-2 50 samples	Very good to excellent	5	10.0
	Good to regular	26	52.0
	Poor	15	30.0
	Very poor	4	8.0

A comparative study was performed with the objective of verifying the efficiency of corrections for geotechnical parameters/compression curves. The results obtained were then compared with experimental values/curves from good quality samples.

6.1. Schmertmann proposal (1955)

The Schmertmann (1955) proposal made it possible to predict the curve for field compression. The pre-consolidation pressure (σ'_{vm}) can be corrected in an interactive manner, using the void ratio (e_0) in the oedometer curve as a base for differentiation between the corrected and laboratory curves for different pre-consolidation pressure values. The symmetry point of the curve e_0 supposedly represents the actual preconsolidation pressure (without disturbance).

Oliveira (2002) evaluated the effect of the Schmertmann (1955) correction on the good, poor quality curves constructed through the abacus for the three clays (Sarapuí, Ibura and Juturnaíba) by estimating the relationship between the other pre-consolidation curves and the preconsolidation stress of the good quality curve corrected by Schmertmann (1955), which was taken as a reference (Table 6). The same was done for the compression ratio of the first straight stretch (C_{C1}). By analyzing the data in this ta-

Table 6 - Geotechnical parameters obtained from the curves corrected by the Schmertmann (1955) methodology (good and poor quality experimental and built by the abacus) (Oliveira, 2002).

Clay	Curve	σ'_{vm}	C_{c1}	C_r	Relation of C_{c1}/C_{c1} good quality	C_r/C_r good quality
Sarapuí (e_0 = 3.54)	Good quality	42	2.9	0.33	1	1
	Poor quality	25	1.64	-	0.75	0.59
	Built by abacus	40	1.94	0.33	0.95	0.67
SESI-Ibura (e_0 = 3.84)	Good quality	55	2.75	0.20	1	1
	Poor quality	42	1.96	0.22	0.76	0.71
	Built by abacus	40	2.14	0.20	0.72	0.78
Juturnaíba (e_0 = 4.24)	Good quality	40	2.24	0.23	1	1
	Built by abacus	32	2.49	0.23	0.80	1.11

ble, it can be seen that the σ'_{vm} and C_{C1} ratios of the abacus-constructed curves corrected by Schmertmann (1955) range from 0.72 to 0.95 for σ'_{vm} and from 0.67 to 1.11 for C_{C1}. This means that the curves constructed by the abacus and corrected by the Schmertmann (1955) methodology, can reproduce these parameters in at least 67% of their value corrected from good quality experimental curves, the results being well above a poor sample quality. The correction still approximates the curves of good quality and built by the abacus.

By removing the poor quality samples, the mean corrections and ranges of variation for each parameter are: (a) Pre-consolidation pressure σ'_{vm}: average of 25% for more and range of 8-39%; (b) Compression index C_{C1}: average of 16% for more and range of 8-26%; (c) C_r recompression index: mean of 20% for less and range of -68 to + 50%.

Jamiolkowski *et al.* (1985) state that the correction typically increases between 10 and 20% the value of the compression index C_c for samples of good quality of soft and medium clays. In the clays studied by Oliveira (2002), the results obtained for good quality samples are within this range (8-16%). Oliveira (2002) also comments that some authors recommend that Schmertmann (1955) correction be made, as Jamiolkowski *et al.* (1985), while Lunne *et al.* (1997) only cite its existence without detailing or recommending its use. Recently, Almeida & Marques (2010) indicate the correction of Schmertmann (1955) in the compression curves.

Bello (2011) presents in Figs. 11a and 11b the experimental oedometer curves representing good and poor quality samples, together with the corrected curves according to the proposal from Schmertmann (1955). In good quality samples, a small correction is observed in the compressibility parameters, however in poor quality samples significant correction of these parameters is noted. The curves corrected by the Schmertmann methodology (1955) are always above the good quality curves.

6.2. Oliveira proposal (2002)

Oliveira (2002) suggested a simple method for construction of a proper oedometer curve, using the results of oedometer tests performed in Sherbrooke soft clay samples from Rio de Janeiro and Recife. These curves are compared with the experimental curves, and can be used to estimate the first calculations. The method adopts the initial void ratio for use as input data, since its value is approximately constant, and does not depend on disturbance. A calculation method was developed for the curves considering the final and initial void ratio (e_f/e_0) *vs.* the initial void ratio (e_0) for each stress normally used in the laboratory (Fig. 12).

The following steps describe the methodology needed to construct the curve: (a) identify the void ratio of the sample; (b) enter the void ratio into the calculations in order to determine the e_f/e_o relation for each stress normally used in the oedometer tests; (c) calculate the final void ratio for each load period; (d) construct a new oedometer curve.

The abacus proposed by Oliveira (2000) has the objective of constructing curves equivalent to those of good experimental quality, which are not free of even slight denting. The compressibility parameters are corrected by rereading the oedometric curve.

In order to evaluate this proposal, Oliveira (2000) selected samples from three Brazilian clays: Sarapuí-RJ, Ibura-PE and Juturnaíba-RJ. The constructed curves are shown in Figs. 13 (a), (b) and (c), together with experimentally obtained oedometric curves.

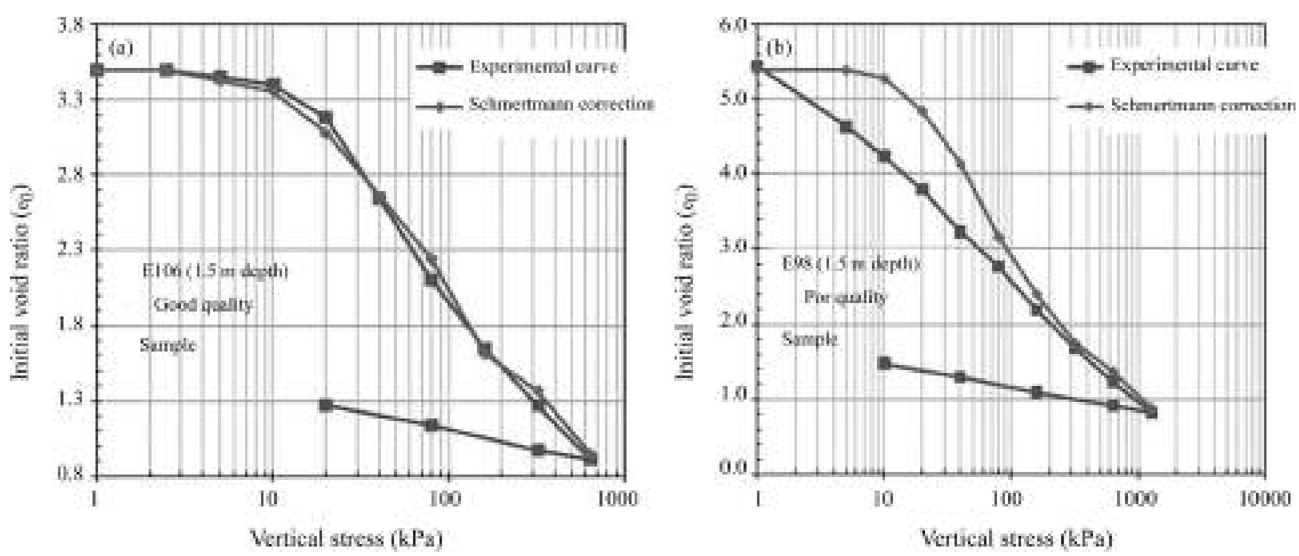

Figure 11 - Experimental oedometer curves, and curves constructed by Oliveira (2002) calculations: (a) good quality, AE-1 study area; (b) poor quality, AE-2 study area (Bello, 2011).

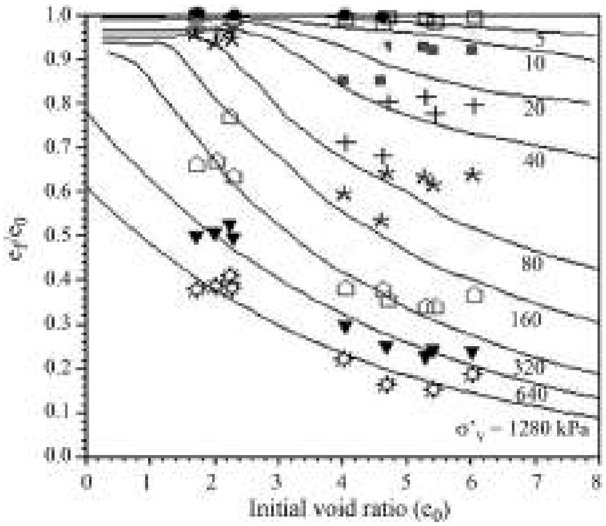

Figure 12 - Calculations used to construct the oedometer curve (Oliveira, 2002).

The curves constructed from the proposed abacus approximated the experimental curves of good quality. In the case of Sarapuí clay, the agreement between the good quality curves and those built by the abacus is very good at low stress, up to about 100 kPa; from this value the agreement reduces, presenting a smaller setback. In the Ibura clay, the curve constructed by the abacus lies below the experimental curve up to about 160 kPa, when the curves meet. Despite this fact, the curves have good agreement. In both cases, the shape of the curves is similar and distinct from the poor quality curve. In the Juturnaíba clay, the curves are practically parallel from the stress of 20 kPa, with a final void ratio difference for each pressure, approximately equal to 0.3 (or 7% of the initial void ratio e_0 = 4.24), in the sense of greater (see results in Table 7).

Figure 14 presents curves constructed by using the calculations based on experimental oedometer curves obtained in good and poor-quality samples from the Suape study areas (Bello, 2011; Coutinho & Bello, 2012). The curves produced from the calculations feature characteristics of curves from good quality samples. The compressibility parameters are obtained from the corrected curve.

Table 8 presents geotechnical parameters obtained from the experimental curves, and the curves constructed from the Oliveira (2002) calculations. The experimental recompression index (C_s) is greater than that of the constructed curve. The experimental preconsolidation stress and the compression index (C_c) are smaller than that of the constructed curve. In the AE-1 study area, the C_s, σ'_{vm}, C_c relations (experimental curves / curves constructed) varied from 1.25 to 3.17 for C_s, from 0.23 to 0.94 for σ'_{vm} and from 0.55 to 0.97 for C_c. In the AE-2 study area, the C_s, σ'_{vm}, C_c relations varied from 1.80 to 3.89 for C_s, from 0.19 to 0.80 for σ'_{vm}, and from 0.51 to 0.99 for C_c. The results show an improvement in the constructed curve, particularly for those relating to poor quality samples. Considering the previous studies performed by Oliveira (2002) and the results obtained for Suape soft clays, the potential can be seen for this methodology, along with its usefulness in correcting the oedometer curves, and obtaining compressibility parameters that correspond to good quality samples.

6.3. Proposal of Coutinho (2007)

Coutinho (2007) presented a correction proposal based on the relation involving the compression ratio (CR) and the overconsolidation ratio (OCR) with specific defor-

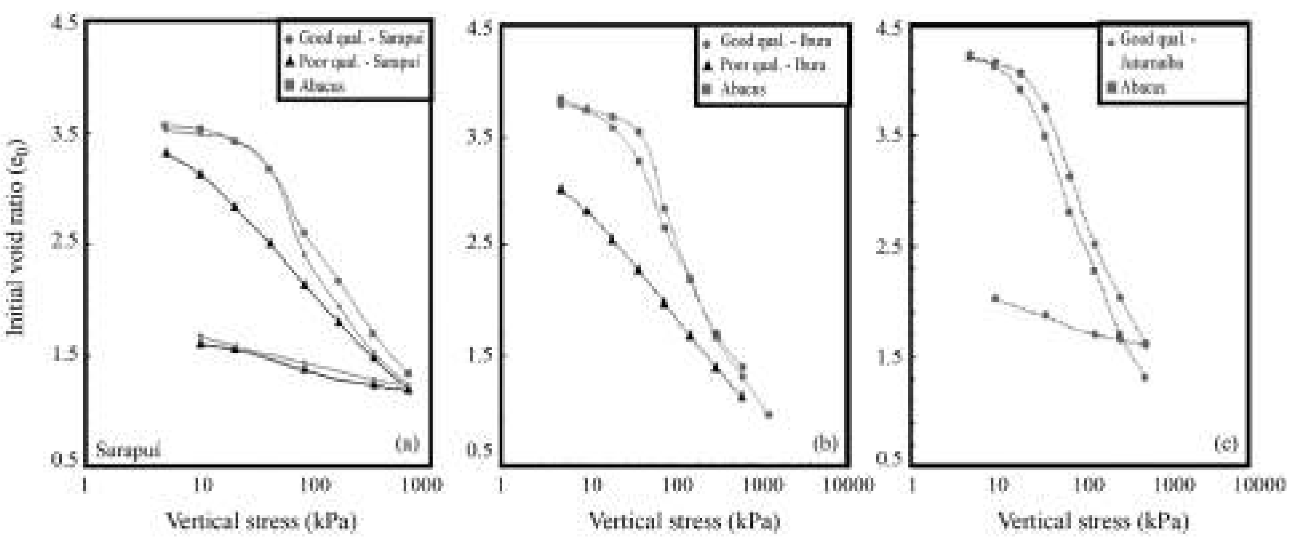

Figure 13 - Experimental oedometer curves (Coutinho *et al.* (1998) and constructed by the abacus (good and poor quality): (a) (e_0 = 3.54), Sarapuí; (b) (e_0 = 3.84), SESI-Ibura; (c) (e_0 = 4.24), Juturnaíba (Oliveira, 2002).

Table 7 - Geotechnical parameters obtained from the experimental oedometric curves and constructed by the abacus (Oliveira, 2002).

Clay	Curve	σ'_{vo}	C_{c1}	C_r (beginning of the curve)	Relation of to σ'_{vo} good quality	Relation of to C_{c1} good quality	C_r/C_r good quality
Sarapuí (e_0 = 3.54)	Good quality	39	2.5	0.12	1	1	1
	Poor quality	21	1.12	0.63	0.54	0.45	5.25
	Built by abacus	30	1.6	0.22	0.77	0.64	1.83
SESI-Ibura (e_0 = 3.84)	Good quality	43	2.55	0.16	1	1	1
	Poor quality	11	0.95	0.68	0.26	0.37	4.25
	Built by abacus	32	1.84	0.50	0.74	0.72	3.12
Juturnaíba (e_0 = 4.24)	Good quality	33	2.03	0.27	1	1	1
	Built by abacus	23	1.98	0.48	0.70	0.98	1.78

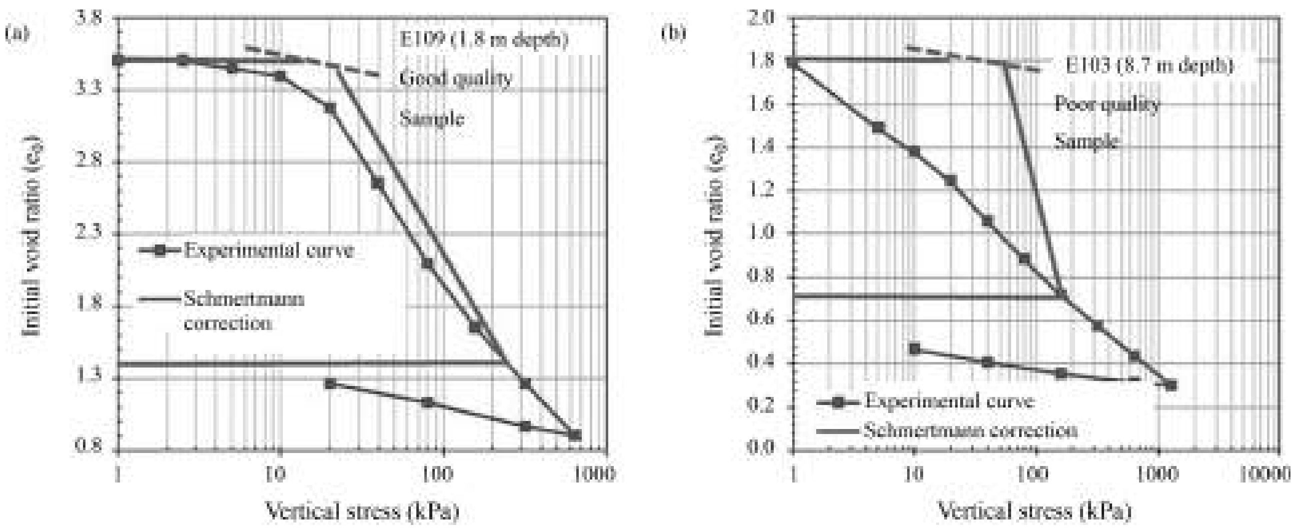

Figure 14 - Experimental curves and curves constructed by use of the Schmertmann proposal (1955): (a) good quality, study area AE-2; (b) poor quality, study area AE-1 (Bello, 2011).

Table 8 - Corrected compressibility parameters values from Oliveira (2002) proposal: AE-2 study area, Suape (Bello, 2011).

Vertical	Depth (m)	σ'_{vo}	Classification Coutinho (2007)	Parameters							
				Experimentals				Corrected (Oliveira, 2002)			
				σ'_{vm}	OCR	C_c	C_s	σ'_{vm}	OCR	C_c	C_s
SP102	1.5	6.2	Good to regular	20.0	3.2	0.8	3.1	30.0	4.84	0.81	1.80
	6.0	15.2	Good to regular	9.0	0.6	1.3	0.2	12.0	0.79	1.31	0.17
SP105	5.5	27.3	Poor	6.0	0.2	1.1	0.1	14.0	0.51	1.25	0.08
SP106	4.5	19.5	Good to regular	6.0	0.3	1.4	0.2	32.0	1.64	1.51	0.18
SP109	6.3	30.0	Very poor	16.0	0.5	2.1	0.4	18.0	0.60	2.50	0.09
SP123	1.7	6.1	Poor	12.0	2.0	0.6	0.1	26.0	4.26	0.86	0.10
SP121	2.5	19.6	Poor	16.0	0.8	1.6	0.2	45.0	2.30	2.45	0.19
SP128	3.5	10.5	Poor	13.0	1.2	0.9	0.2	20.0	1.90	1.10	0.17
SP137	0.4	5.5	Poor	8.0	1.5	1.8	0.2	20.0	3.64	3.60	0.07
SP138	2.9	5.7	Good to regular	10.0	1.8	2.0	0.4	20.0	3.51	3.80	0.22
	3.9	11.1	Very poor	20.0	1.8	2.2	0.2	25.0	2.25	2.30	0.12

mation (ε_{vo}), that represents the quality of the sample. A greater decrease can be verified in the CR and OCR values when ε_{vo} increases and a minimum limit exists where the samples are almost totally disturbed.

Figures 15a and 15b show, respectively, the compression ratio (CR) and overconsolidation ratio (OCR) *vs.* ε_{vo} for the SESI-Ibura deposit. Coutinho *et al.* (1998) and Coutinho *et al.* (2000) comment that, as expected, CR and OCR values decrease strongly when ε_{vo} increases. There is a minimum limit for CR values (20%) and for OCR values (0.25), where the samples are almost completely dented. This type of correlation may be useful for an approximate correction of CR and OCR values, considering the quality of sampling in practical projects. In this type of work, the sampling process often does not utilize the recommended procedures and field teams with adequate training.

Figures 16 (a) and 16 (b) present the correlations between CR and σ'_{vm} *vs.* ε_{vo}, respectively, for the AE-2 study area (SUB-AREA A). Each layer is represented by a curve correlating to soft soil deposits containing different compressibility layers (different CR and σ'_{vm} values for each layer). Results found in SUB-AREA A seem consistent with the observations of Coutinho (2007) on the behavior of soft clays of Recife. The relation between the value of σ'_{vm} obtained in samples of good quality and in samples of poor quality was in the order of 3 (considered high), however e_o does not appear to be significantly influenced by the quality of the sample.

The results obtained in the Suape areas showed reasonable correlations of CR and σ'_{vm} *vs.* ε_{vo} for soft layers, allowing for correction of the CR and σ'_{vm} values by considering ε_{vo} values corresponding to very good - excellent quality samples. The correction can be particularly important when considering poor quality samples in practical projects.

6.4. Proposal of the normalized oedometric curve presented by Futai (2010)

Futai (2010) proposed to use normalization of the compression curves in calculations of repression. The

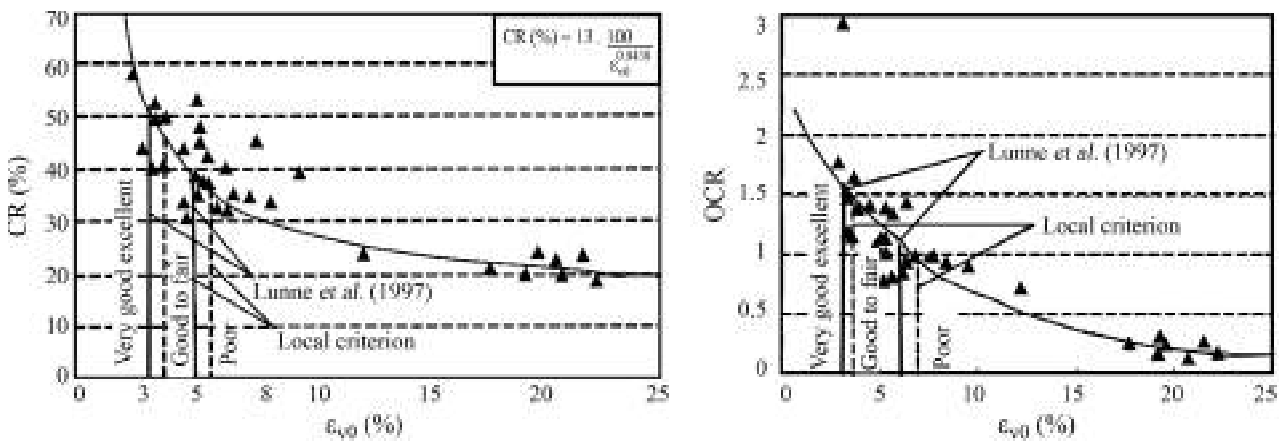

Figure 15 - (a) Curve CR *vs.* ε_{vo} ; (b) Curve OCR *vs.* ε_{vo} for the SESI-Ibura deposit -PE (Coutinho *et al.*, 1998).

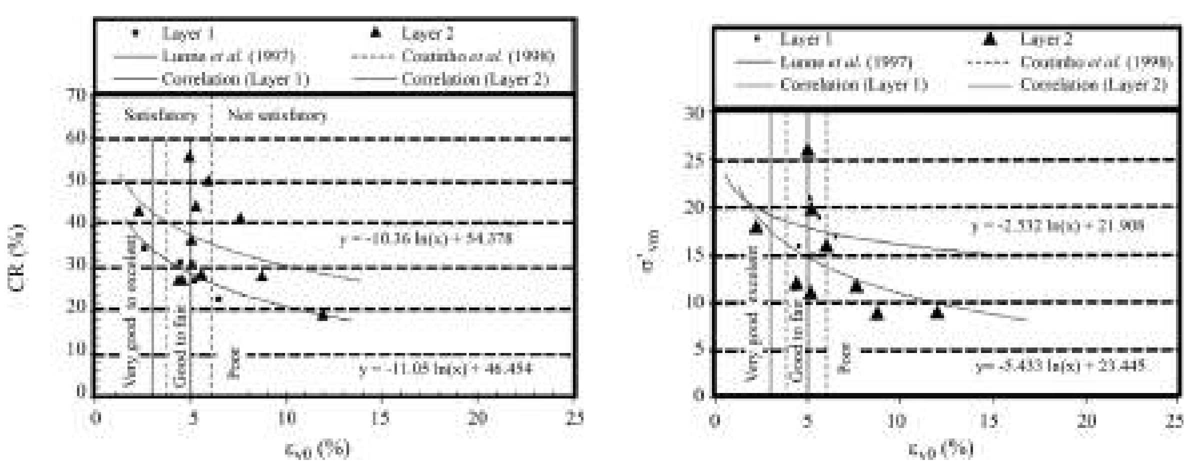

Figure 16 - Evaluation of sample quality, study area AE-2, SUB-AREA A: (a) Curves CR *vs.* ε_{vo}; (b) Curves σ'_{vm} *vs.* ε_{vo} (Bello 2011, from Coutinho *et al.*, 1998; Coutinho, 2007).

equations to estimate settlements do not require the values of C_c ou $C_c/(1 + e_0)$ and nor of correlations. It is only necessary to know the initial void ratio, the history of stress and the loading. Therefore, the author believes that this is a more rational way of calculating settlements, and emphasizes the need to verify if the normalized compression curve of the soil falls within the classification range of good quality sample before applying the proposed calculation of setbacks. However, the author does not comment on the correction of sample curves classified as poor quality for use in the calculation of settlements.

From the data of tests in clays of different Brazilian localities and collected in the international literature, Futai (2010) applied the normalization of oedometric compression curves to evaluate the sample quality.

In the proposal, two sections were considered: ID > 1 (usually consolidation), and ID > 1 (final vertical stress greater than the yield stress). The normalized compression curve, for ID > 1, can be represented by a logarithmic function (Eq. 5). In the section ID < 1, the relation is linear, and the field void ratio is used as reference (Eq. 6).

$$e = e_y \,.\, (1 - \xi .\, \ln(\mathrm{ID})) \tag{5}$$

$$\frac{e_y - e}{e_y} = \chi .(\mathrm{ID}_0 - 1) \tag{6}$$

where ξ is an adjustment coefficient equal to 0.23, and χ is the angular coefficient of the line equal to 0.06.

And so it is possible to calculate the void ratio for yielding (Eq. 7).

$$e_y = \frac{e_0}{1.06 - (0.06\mathrm{ID}_0)} \tag{7}$$

where ID_0 equals the relation of the effective vertical field stress (σ'_{vo}) with the yield stress (σ'_{vy}).

Based on these criteria, it is suggested that samples that were not included in the good quality bands proposed by Futai (2010), be corrected to obtain a new value of the yield stress (σ'_{vy}). In Eq. 7, the parameters e_0, ID_o and σ'_{vo} are known, as well as σ'_{vy} obtained directly from the test, thus obtaining e_y in a simple way. In the second stage of the procedure, Eq. 5 would be used, since it is a reference for samples of good quality. The void ratio used would correspond to the final loading pressure, where it coincides with the reference line. By developing the equation, we arrive at the value of the yield stress.

Table 9 shows the results of the σ'_{vm} correction by the proposed Futai standard curve (2010) obtained in the AE-1 study area (E98 and E137) and in the AE-2 study area (E109 and E138, together with the results of the correction proposed by Oliveira (2002).

Table 9 - Correction of the preconsolidation stress according to criteria of Futai (2010)-Suape (Bello, 2011).

Stake	Sample	Quality Coutinho (2007)	Pre-consolidation stress σ'_p (kPa)		
			Oedometric	Futai (2010)	Oliveira (2002)
E98	AM1	Poor	9.0	20.4	27.0
	AM2	Very poor	7.0	37.8	30.0
	AM3	Good to regular	4.0	8.9	15.0
	AM4	Very good	6.0	16.8	19.0
E137	AM1	Good to regular	21.0	19.91	22.0
	AM2	Poor	22.0	23.34	26.0
	AM3	Very good	9.0	14.91	13.0
	AM4	Good to regular	35.0	40.47	36.0
	AM5	Good to regular	30.0	42.23	31.0
E109	AM1	Good to regular	19.0	25.9	21.0
	AM2	Good to regular	16.0	17.97	17.0
	AM3	Good to regular	20.0	21.02	22.0
	AM4	Good to regular	26.0	25.37	26.0
	AM5	Very poor	16.0	26.51	18.0
E138	AM1	Good to regular	8.0	15.12	12.0
	AM2	Very poor	10.0	16.47	20.0
	AM3	Good to regular	14.0	25.26	17.0
	AM4	Very poor	20.0	22.30	23.0
	AM5	Good to regular	28.0	30.10	28.0

In samples of good quality the proposal reached values of σ'$_{vm}$ higher than the values obtained experimentally. In samples of poor quality the values of σ'$_{vm}$ corrected by the proposal were significantly higher than the values obtained experimentally. Comparing the proposed correction of σ'$_{vm}$ with the Futai (2010) normalized curve and the proposal for the construction of new oedometric curves suggested by Oliveira (2002), the results of σ'$_{vm}$ were alternated in each sample tested, concluding that in the application of the two corrections satisfactory results can be obtained.

The proposed correction of σ'$_{vm}$ by the normalized curve of Futai (2010) constitutes a tool of simple application to obtain values of σ'$_{vm}$ not influenced by the molding. In general the results of the application of the σ'$_{vm}$ correction by the normalized curve were stimulating in Suape soft clays. It is suggested to use in other Brazilian clays reported in the literature.

The initial proposal of Futai (2010) had as objective to use air standard curves to evaluate samples and calculate settlements. It is only necessary to know the initial void ratio, the stress history and the loading. Apparently there was no interest in constructing the curves to obtain other parameters. In this work, it is suggested to construct the corrected oedometric curves from this proposal to obtain the parameters.

Bello (2011) and Coutinho & Bello (2012) comparing the results of the correction proposal for Suape soft clay samples, made some observations:

(a) The Oliveira (2002) proposal amounts to a simple procedure, where only the initial void ratio and the oedometer test pressures are needed. All of the curve's corresponding points must be determined. Considering the studies carried out by Oliveira (2002) applied in the clays of Recife, Juturnaíba and Sarapuí, and the results found in the clays of Suape, the potential of the proposal for correction of the oedomometric curves is verified.

(b) The σ'$_{vm}$ value obtained by the Schmertmann (1955) proposal was practically unmodified when considering good quality samples. A significant difference was observed in the σ'$_{vm}$ corrected value when dealing with poor quality samples.

(c) In the Coutinho (2007) proposal, it was possible to obtain corrected CR and OCR values by considering the ε_{vo} value corresponding to very good and excellent quality samples. Correlations for each soft soil layer of the deposit must be constructed.

Figure 17 for the AE-1 Suape study area shows a comparison between the experimental oedometer curve (poor quality samples), and the curves constructed by the Oliveira (2002) calculations and Schmertmann proposal (1955) (Coutinho & Bello, 2012). It can be observed that the corrected curve for good quality experimental samples approximates the Schmertmann (1955) curve (field curve). The σ'$_{vm}$ values obtained from the two corrected curves are similar (around 24 kPa), and the recompression ratio is slightly greater in the Schmertmann curve.

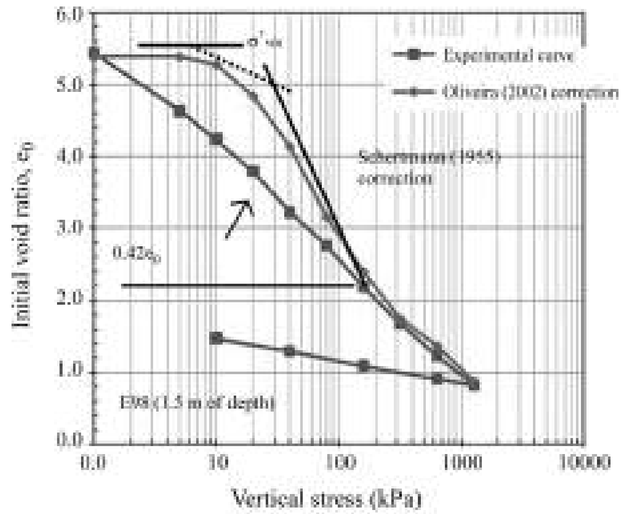

Figure 17 - Oedometer curve and curves constructed by Oliveira (2002) and Schmertmann (1955) proposals (Coutinho & Bello, 2012).

7. Correction of Strength Parameters to Account for Sample Disturbance

For correction of the value of S_u is proposed the use of the relationship of resistance (S_u/σ'$_{vm}$) *vs.* the IP plasticity index. The values of σ'$_{vm}$ are considered corrected for the effect of the sample's denting (see Schmertmann, 1955; Oliveira, 2000; Coutinho, 2007; Futai, 2010).

Figure 18 shows the relation $S_{u\,vane}$/σ'$_{vm}$ *vs.* IP proposed by Mesri (1975), Coutinho *et al.* (2000) modified from Skempton (1957), Larsson (1980) and Mayne & Mitchell (1988), together with the mean values of various Brazilian clays, including Recife and Suape (SUB-AREAS A and C). For Recife and Suape clays, the points fall between the correlations of Larsson (1980) and Mesri (1975), forming upper and lower limits respectively. The proposal from Coutinho *et al.* (2000) represents clays from Recife, Juturnaíba-RJ, Sarapuí-RJ and satisfactorily for Suape. The poor quality samples had the σ'$_{vm}$ value corrected (see Coutinho & Bello, 2012; Bello, 2011).

The equation of the resistance relationship obtained by Coutinho *et al.* (2000) modified from Skempton (1957) is proposed in this work to be used as a criterion for correcting the value of S_u. Table 10 presents a summary of the results of the S_u correction of Suape's AE-1 study area. The corrected S_u values were around ± 16% higher in relation to the S_u values obtained in the field vane tests.

This new proposal constitutes an efficient tool and easy to apply to obtain the S_u value, indicative of samples of good quality.

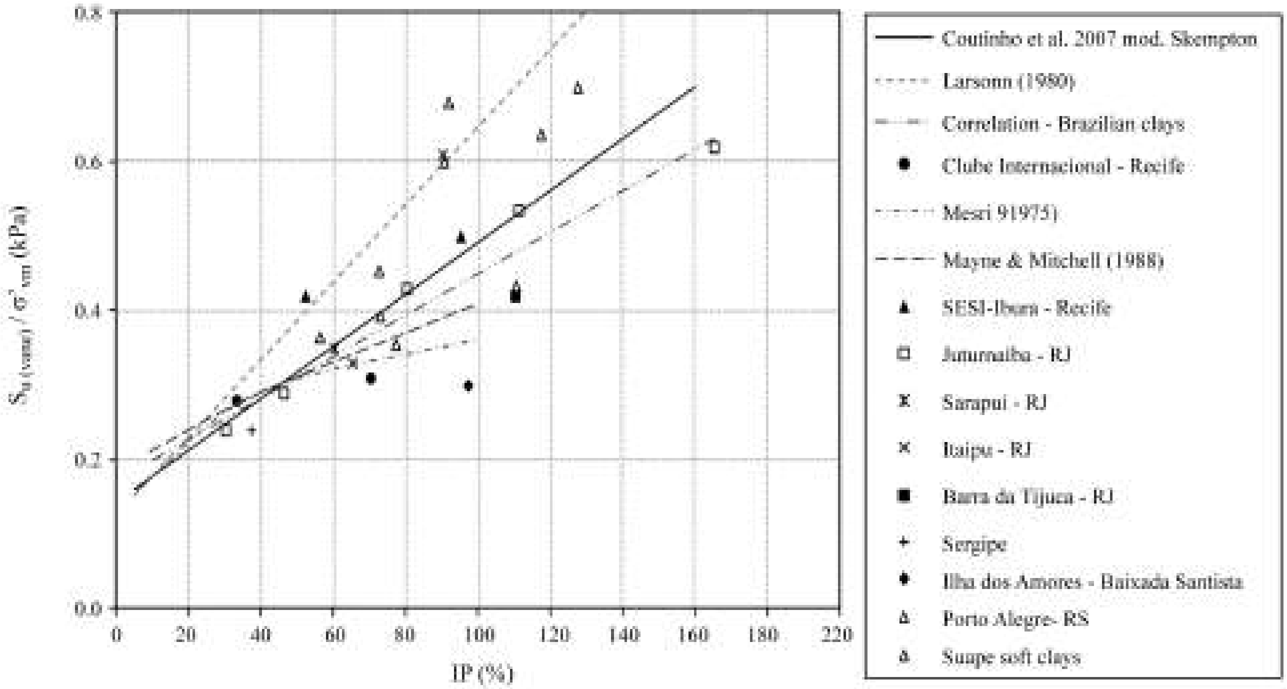

Figure 18 - Resistance ratio several brazilian soft clays: $S_{u\ vane}/\sigma'_{vm}$ and IP (Coutinho *et al.*, 2000; Coutinho & Bello, 2012).

Table 10 - Summary of S_u values corrected according to Coutinho *et al.* (2000) modified from Skempton (area of study AE-1 - Suape).

	$S_{u\ vane}/\sigma'_{vm}$	Equation (Coutinho *et al.*, 2000 apud Skempton, 1957)	σ'_{vm}	IP	$S_{u\ vane}$	$S_{u\ corr}$
1st stretch	0.30	0.539	27.0	116.04	8.20	14.56
	0.73	0.546	20.0	117.72	14.60	18.91
	0.27	0.469	17.0	96.92	4.53	7.97
	0.26	0.391	30.0	75.91	7.90	11.73
	0.15	0.421	29.2	83.98	8.00	12.29
	0.27	0.373	33.0	71.11	8.82	12.31
2nd stretch	0.34	0.557	31.0	120.93	10.51	17.28
	0.47	0.535	25.8	114.83	12.04	13.80
	0.69	0.527	28.4	112.65	14.71	14.96
	0.43	0.495	22.0	104.15	9.40	10.90
	0.28	0.591	21.0	130.00	6.00	12.41

8. Conclusions

This study presented and discussed results from sample quality evaluations, and correction of the effects of sample disturbance of Brazilian soft clays.

Results from the Coutinho (2007) and Futai (2010) proposals were similar, and may be considered satisfactory for evaluating and quantifying the quality of Suape soft clay samples. Overall, within this study, more than 50% of the samples were classified as being of satisfactory quality (very good to excellent, and good to regular).

The Schmertmann (1955), Oliveira (2002) and Coutinho (2007) proposals were used for correcting the compressibility parameters from samples whose quality was classified as unsatisfactory. The proposals studied for correction use produced parameters corresponding to very good / excellent field curves. The corrections can be particularly important for use with poor quality samples. For use in project, the corrections must be utilized for all of the important parameters, or simply throughout the complete curve.

In a study of sample quality, it is very important to make use of a regional / local data base in order to obtain proper correlations, and to be able to verify standard behavior.

Acknowledgments

The authors acknowledge support from specific research projects: PRONEX (CNPq/FACEPE) and INCT - REAGEO (CNPq), and from the CNPq for the financial support (fellowship) in research involving Bello (2011).

References

Almeida, M.S.S. & Marques, M.E.S. (2010). Aterros Sobre Solos Moles: Projeto e Desempenho. Coleção Huesker: Engenharia com Geossintéticos. Oficina de Textos. São Paulo.

Baligh, M.M. (1986). Undrained deep penetration II: Pore pressure. Géotechnique, 36(4):486-501.

Bello, M.I.M.C.V. (2011). Parâmetros Geotécnicos e Banco de Dados de Argilas Moles: O Caso de Suape. D.Sc. Thesis, Universidade Federal de Pernambuco, 320 p.

Bello, M.I.M.C.V. & Coutinho, R.Q. (2012). Piezocone testing for use in the classification of soil behavior and flow characteristics - An experience carried out in Suape, Pernambuco. Proc. 4th International Conference on Site Characterization ISC'4, Recife. Brazil.

Clayton, C.R.I.; Hight, D.W. & Hopper, R.J. (1992). Progressive destructuring of Bothkennar clay: implications for sampling and reconsolidation procedures. Géotechnique, 42(2):219-239.

Coutinho, R.Q. (1976). Características de Adensamento com Drenagem Vertical e Radial em Argila Mole na Baixada Fluminense. M.Sc. Dissertation, COPPE, UFRJ, 206 p.

Coutinho, R.Q.; Oliveira, J.T.R & Danziger, F.A.B. (1993). Geotechnical characterization of a Recife soft clay. Soils and Rocks, 16(4):255-266.

Coutinho, R.Q.; Oliveira, J.T.R. & Oliveira, A.T.J. (1998). Estudo quantitativo da qualidade de amostras de argilas moles brasileiras - Recife e Rio de Janeiro. Proc. XI Cong. Brasileiro de Mecânica dos Solos e Engenharia Geotécnica, ABMS, Brasília, v. 2. pp. 927-936.

Coutinho, R.Q.; Oliveira, A.T.J. & Oliveira, J.T.R. (2000). Conferência Palheta: Experiência, Tradição e Inovação. Seminar on Special Foundation Engineering and Geotechnics, SEFE IV, São Paulo, Brazil, v. 3, pp. 53-79.

Coutinho, R.Q. (2007). Characterization and engineering properties of Recife soft clays-Brazil. Proc. 2nd Int. Workshop on Charac. and Eng. Properties of Natural Soils. Tan, Phoon, Higth and Leroueil (eds). Singapore, pp. 2049-2100.

Coutinho, R.Q. (2008). Investigação geotécnica de campo e avanços para a prática. Proc. XIV Congresso Brasileiro de Mecânica de Solos e Engenharia Geotécnica, ABMS, Búzios, v. 1. pp. 201-230.

Coutinho, R.Q. & Bello, M.I.M.C.V. (2012). Evaluation of sample quality and correction of compressibility parameters results to account for the effects of sample disturbance-experience at Suape in Pernambuco. Proc. 4th International Conf. on Site Characterization ISC'4, Recife, Brazil.

Ferreira S.R.M. (1982). Característica de Compressibilidade de uma Argila Orgânica Mole do Recife. M.Sc. Thesis, COPPE/UFRJ.

Ferreira, S.R.M. & Coutinho, R.Q. (1988). Quantificação do efeito do amolgamento nas características de compressibilidade de argila mole - Rio de Janeiro e Recife. Proc. Simp. Depósitos Quaternários das Baixadas Litorâneas Brasileiras, SIDEQUA, v. 1. pp. 3.55-3.69.

Futai, M.M. (2010). Theoretical and Practical Concepts on Behavior Analysis of Some Rio de Janeiro Clays. D.Sc. Seminar, COPPE/UFRJ, 133 p.

Hight, D.W.; Boese, R.; Butcher, A.P.; Clayton, C.R.I. & Smith, P.R. (1992). Disturbance of the Bothkennar clay prior to laboratory testing. Géotechnique, 42(2):199-217.

Hight, D.W. (2000). Sampling methods: evaluation of disturbance and new practical techniques for high quality sampling in soils. Proc. VII Congresso Nacional de Geotecnia, Porto, v. 3, pp. 1275-1309.

Hvorslev, M.J. (1949). Surface Exploration and Sampling of Soils for Civil Engineering Purposes. Waterways Experiment Station, Vicksburg, 521 p.

Jamiolkowski M.; Ladd, C.; Germaine, J.T. & Lancellota, R. (1985). New Developments in field and laboratory testing of soils. Proc. Proc. 11th ICSMFE, San Francisco, v. 1, pp. 57-153.

Lacasse, S. (1988). Design Parameters of Clays from *in Situ* and Laboratory Tests. Simpósio sobre Novos Conceitos em Ensaios de Campo e Laboratório em Geotecnia. COPPE–UFRJ/ABGE/ABMS/Clube de Engenharia, Rio de Janeiro, v. 3, p. 51-95.

Ladd, C.C. & Lambe, T.W. (1963). The Strength of Undisturbed Clays Determined from Undrained Tests. ASTM STP361, Laborat. Shear Tests of Soils, pp. 342-371.

Ladd, C.C. (1973) Estimating Settlements of Structures Supported on Cohesive Soils. Filecopy ASCE, Massachussets, 99 p.

Ladd, C.C. & Foott, R. (1974). New design procedure for stability of soft clays. Journal of the Geot. Engineering Division, ASCE, 100(GT7):763-786.

La Rochelle, P. & Lefebvre, G. (1971). Sampling disturbance in champlain clays. ASTM Conf. on Sampling in Soil and Rocks, STP 483:143-163.

Larsson R. (1980). Undrained shear strength in stability calculation of embankments and foundations on soft clays. Canadian Geotechnical Journal, 17(4):591-602.

Leroueil, S. & Jamiolkowski, M. (1991). Exploration of soft soil and determination of design parameters. General Report-Session 1, Int. Conf. on Geotech. Engin. for Coastal Development, Yokohama, pp. 1-41.

Lunne, T.; Berre, T. & Strandvik, S. (1997). Sample disturbance effects in soft low plastic norwegian clay. In: Recent Develop. in Soil and Pavement Mechanics. COPPE/UFRJ, Rio de Janeiro, p. 81-102.

Martins, I.S.M. (1983). Sobre uma Nova Relação Índice de Vazios Tensões em Solos. M.Sc. Dissertation, COPPE/UFRJ, Rio de Janeiro, Brasil.

Mayne, P.W. & Mitchell, J.K (1988). Profiling of overconsolidation ratio in clays by field vane. Canadian Geotechnical Journal, 25:150-157.

Mesri, G. (1975). New design procedure for stability of soft clays. Discussion. Journal of Geotechnical Engineering Division, ASCE, 101:409-412.

Oliveira, J.T.R. (1991). Ensaios de Piezocone em um Depósito de Argila Mole da Cidade do Recife. Tese de Mestrado, COPPE/UFRJ.

Oliveira J.T.R.; Danziger, F.A.B. & Coutinho, R.Q. (2000). Amostragem em Bloco nas Argilas Moles Brasileiras. SEFE-BIC, São Paulo, v. 3, pp. 199-208.

Oliveira J.T.R. (2002). Influência da Qualidade da Amostragem no Comportamento Tensão-Deformação-Tempo das Argilas Moles. Tese de Doutorado, COPPE/UFRJ-DEC-UFPE.

Okumura, T. (1971). The variation of mechanical properties of clay samples depending on the degree of disturbance. Proc. Spl. Session, Quality in Soil Sampling. Fourth Asian Conf. Int. Soc. Soil Mech and Found. Engg., Bangkok, pp. 73-81.

Ortigão, J.A.R. (1980) Aterro Experimental Levado à Ruptura Sobre Argila Cinza do Rio de Janeiro. Tese D.Sc., COPPE/UFRJ, 715 p.

Santagata, M.; Sinfield, J.V. & Germaine, J.T. (2006) Laboratory simulation of field sampling: comparison with ideal sampling and field data. Journal of Geotechnical l and Geonvironmental Engineering, ASCE: 351-362.

Sandroni, S.S. (1977). Amostragem indeformada em argilas moles. 1° Simpósio ABMS/NE - Prospecção do subsolo- Recife, pp. 81-106.

Schmertmann, J.H. (1955). The undisturbed consolidation behavior of clay. Transactions, ASCE, 120:1201-1233.

Skempton, A.W. & Sowa, V.A. (1963). The behaviour of saturated clays during sampling and testing. Géotechnique, 13(4):269-290.

Skempton, A.W. (1957). Discussion: Further data on the c/p ratio in normally consolidated clays. Proceedings of the Institution of Civil Engineers, v. 7, pp. 305-307;

Tanaka, H. (2008). Sampling and sample quality of soft clays. Proc. of the 3rd International Conference on Site Characterization, (ISC3), Taipei, pp. 139-157.

Tavenas, F. & Leroueil, S. (1987) State-of-the-Art report: Laboratory and *in situ* stress strain-time behaviour of soft clays. International Symposium on Geotechnical Engineering of Soft Soils, Mexico City, v. 2, pp. 3-48.

Teixeira, D.C.L. (1972) Características Geotécnicas dos Depósitos de Argilas Orgânicas Moles do Recife e a Infuência da Matéria Orgânica. Dissertação M.Sc., COPPE/UFRJ.

Performance Evaluation of Rigid Inclusion Foundations in the Reduction of Settlements

J.F.R. Rebolledo, R.F.P. León, J. Camapum De Carvalho

Abstract. In this study, numerical modeling is used to evaluate the performance of rigid inclusion foundations for settlement control considering the characteristic soils of the city of Brasília, Federal District, Brazil. Two- and three-dimensional (2D and 3D) PLAXIS software models were used considering the Hardening Soil constitutive model parameters previously obtained, calibrated and validated by the authors. First, the general concepts regarding systems with rigid inclusions are presented. Then, parametric 2D axisymmetric numerical modeling is shown, where the spacing between inclusions, the height of the distribution layer and the soil conditions were varied. The load transfer mechanisms were analyzed, including the performance of rigid inclusions for settlement control. Finally, 3D modeling was performed with the information from a real project located in the Federal District. In the 3D modeling, the performance of the rigid inclusion foundation was compared with that of a slab foundation solution; then, the obtained settlements and angular distortions were compared with the serviceability limit states indicated in the literature. The results show that for the analyzed conditions, rigid inclusion foundations can be considered to be reliable foundation solutions. However, feedback from instrumentation cases in the city of Brasilia is required to further validate the design considerations.
Keywords: 3D model, angular distortion, numerical modeling, rigid inclusions, settlement control performance.

1. Introduction

The region of the Federal District of Brazil is covered by a detritus-laterite soil mantle from the Tertiary-Quaternary age called “porous clay”. This superficial clay layer presents a porous and highly unstable structure, with high void ratio and low shear strength resistance; therefore, deep foundations are widely used. In this study, numerical modeling is used to evaluate the performance of rigid inclusion foundations for settlement control.

Inclusions have been commonly used all over the world as foundation solutions, primarily for road and railway embankments (Zanziger & Gartung 2002; Quigley *et al.*, 2003; Wood 2003; Almeida *et al.*, 2011; Okyay *et al.*, 2014; Fonseca & Palmeira, 2018). Since the late twentieth century, in North America (López *et al.*, 1999; Santoyo & Ovando, 2006; Rodríguez, 2001, 2010; Rodríguez & Auvinet, 2006; Auvinet & Rodríguez, 2006) and in Europe (Combarieu, 1990; Pecker, 2004; Simon & Schlosser, 2006; ASIRI, 2011; Briançon *et al.*, 2015), this solution has been studied and employed for settlement control and to lower the costs of deep foundations for buildings on difficult soil conditions. Currently, the use of inclusions is one of the most employed deep foundation techniques under these conditions due to good performance (Briançon *et al.*, 2015) and low cost compared to other solutions (Rodríguez & Auvinet, 2006). Therefore, the objective of this paper is to evaluate the use of this type of foundation for situations involving superficial layers of collapsible porous soils, such as those present in the stratigraphy of the city of Brasilia in the Federal District of Brazil.

The settlement reduction obtained with the use of rigid inclusions is due to the transfer of a significant load supported by the soil to these elements.

In this study, the performance of rigid inclusion foundations in settlement control is evaluated through numerical modeling. Two- and three-dimensional (2D and 3D) PLAXIS software models were used considering the mechanical parameters of the characteristic soils of the city of Brasília, obtained, calibrated and validated (Rebolledo *et al.*, 2019) for the Hardening Soil (HS) model based on laboratory and field test results obtained in previous studies conducted in the Experimental Field of the University of Brasília (CEGUnB).

To evaluate the influence of the main geometric variables of the foundation on settlement control, parametric 2D axisymmetric modeling was performed. The analyses were performed using the soil stratigraphy and properties of the CEGUnB for natural moisture conditions and with the first 3.5 m of the saturated soil. The latter condition was investigated to consider the significant increase in the soil moisture in this active zone during the rainy season.

Additionally, 3D modeling was done with information from a real project located in the Federal District. The

Juan Félix Rodríguez Rebolledo, Dr., Associate Professor, Programa de Pós-Graduação em Geotecnia, Universidade de Brasília, Brasília, DF, Brazil. e-mail: jrodriguezr72@hotmail.com.
Raimundo Francisco Pérez León, Ph.D. Student, Programa de Pós-Graduação em Geotecnia, Universidade de Brasília, Brasília, DF, Brazil. e-mail: rai88mundo@gmail.com.
José Camapum De Carvalho, Ph.D., Professor, Programa de Pós-Graduação em Geotecnia, Universidade de Brasília, Brasília, DF, Brazil. e-mail: camapumdecarvalho@gmail.com.
Submitted on November 28, 2018; Final Acceptance on August 1, 2019; Discussion open until April 30, 2020.
DOI: 10.28927/SR.423265

performance of the rigid inclusion foundation was compared with that of a single-slab foundation solution; then, the settlements and angular distortions obtained were compared with the serviceability limit states indicated in the literature.

2. Rigid Inclusions

2.1. Main characteristics

A foundation with rigid inclusions has five components that interact with each other, as shown in Fig. 1: the foundation (slab or footing), the distribution layer or load transfer platform, the rigid inclusions, the column caps (optional), and the surrounding soil. A rigid inclusion foundation solution should incorporate all of these components.

Commonly, in embankment projects, the distribution layer is composed of granular soils reinforced with geosynthetics, but for building foundation projects, the distribution layer is commonly composed of compacted soils. To increase the shear strength and stiffness of the distribution layer, the material of this layer can be mixed with cement, lime or another chemical or physical additives.

Inclusions are cylindrical or prismatic elements with no direct contact with the foundation (slab or footing) that can be placed in the ground using different techniques, such as bored piles, jacked piles, precast-concrete pile driving, steel pipe pile driving, micropiles, continuous flight augers, low-pressure grouting, jet grouting, and stone columns, i.e., any type of deep foundation that has a rigidity considerably greater than that of the ground the foundation reinforces. According to the Soil Improvements through the use of Rigid Inclusions (ASIRI) National Project (2011), the concept of rigid inclusions is based on the hypothesis that the structural stability of an element is guaranteed without the lateral confinement of the soil.

In this study, we assumed that the rigid inclusions were constructed using the continuous flight auger technique because, compared with other techniques, the flight auger technique produces small disturbances in the excavated soil, has relatively high performance and is widely used in Brazil; however, any of the methods mentioned above can be used.

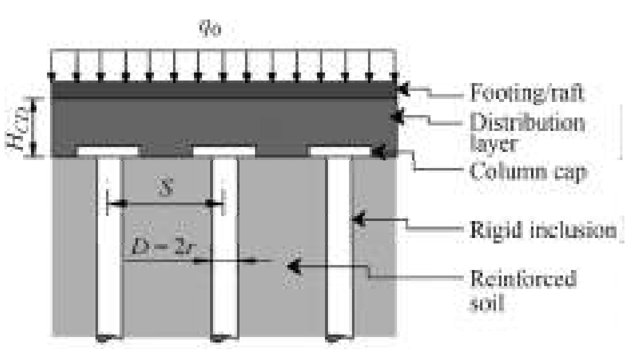

Figure 1 - General scheme of a rigid inclusion foundation.

2.2. Load transfer mechanism

The settlement reduction obtained with the use of rigid inclusions is due to the transfer of a significant load supported by the soil to these elements. A complex interaction develops between the reinforced soil, the inclusions and the distribution layer, as shown in Fig. 2a. To understand the inclusion-soil and soil-inclusion load transfer, we can use concepts similar to those accepted for piles, as shown in Fig. 2b (Vesic, 1970; Rodríguez, 2010; Combarieu, 1990; Rodríguez *et al.*, 2015; Briançon *et al.*, 2015). Initially (Fig. 2a), the distribution layer transfers the load of the structure to the inclusion cap (q_c) and to the reinforced soil (q_s); then, the reinforced soil transfers the load to the upper inclusion shaft as negative skin friction ($f^{(-)}$); finally, the inclusion transfers the load through the inclusion tip (q_p) and through the lower inclusion shaft as positive skin friction ($f^{(+)}$). Both negative and positive friction are separated by a neutral point (z_0), where no relative displacement occurs between the inclusion and soil.

The distribution layer or load transfer platform is intended to transfer most of the load from the structure to the rigid inclusions, q_c. The geotechnical and geometric characteristics of this layer influence the efficiency of the transfer because these characteristics can increase the stresses at the heads of the inclusions (q_c, Fig. 2a) and reduce the stresses in the soil to be reinforced (q_s). Additionally, the distribution layer absorbs the loads transferred by the inclusion heads (column caps or top of the piles, according to the case), which prevents the inclusion heads from punching the foundation slab, and homogenizes the settlements, ensuring efficient foundation performance. The parameters that have the most influence on this efficiency are the friction angle of the compacted material, the spacing and head diameter of the inclusions and the thickness of the distribution layer (BSI, 2010). According to Fonseca & Palmeira (2018), to obtain the load transfer efficiency of geosynthetic reinforced piled embankments, analytical methods are commonly used, but the results obtained are significantly different. Generally, methods based on arching stresses such as the British Standard BS 8006 (BSI, 2010) showed satisfactory results.

According to Rodríguez (2010), the use of rigid inclusion systems is more economical than the use of other deep foundation solutions, mainly because:

1) inclusions do not require steel reinforcement (Fig. 2) because only small compressive loads develop in the element,
2) the foundation slab or footing does not require steel reinforcement (Fig. 2) to transfer load to the inclusions, since the top of the inclusions are located at a depth sufficient to prevent the inclusions from reacting as point load to the foundation slab or footing, and
3) the magnitudes of the loads transmitted by the inclusions are low, so a concrete with low resistance can com-

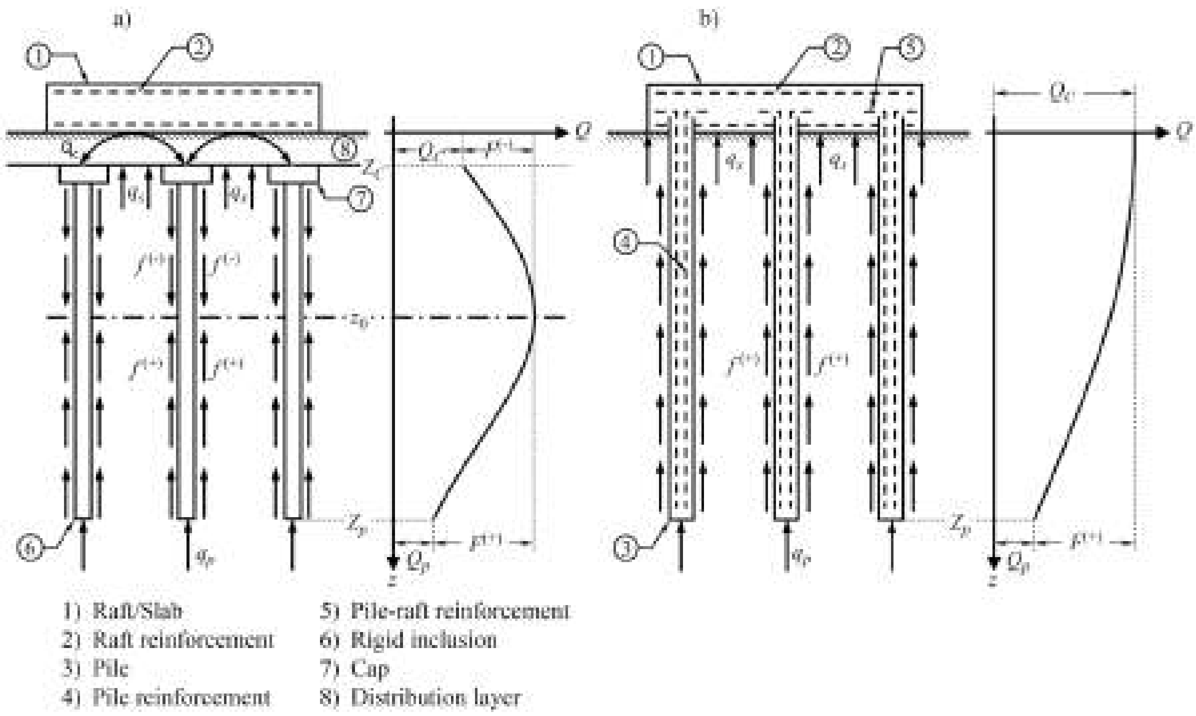

Figure 2 - Load transfer mechanism and axial load (Q) developed along a) rigid inclusion foundation and b) piled raft foundation.

monly be used (compressive strength of the order of 10 MPa).

3. Aspects of the Numerical Modeling

3.1. Stratigraphy used in the modeling

For this study, the stratigraphy of CEGUnB, shown in Fig. 3, was considered. This program provides valuable geotechnical information obtained from surveys, in situ tests, laboratory tests and loading tests on superficial and deep foundations (Pérez, 2017; Jardim, 1998; Sales, 2000; Guimarães, 2002; Mota, 2003; Coelho, 2013; Sales *et al.*, 2015). According to this information and the tropical soil profiles proposed by Cruz (1987) and Cardoso (2002), Rebolledo *et al.* (2019) defined the typical stratigraphic profile of the CEGUnB, as shown in Fig. 3.

For the numerical simulation of soil behavior based on the information from the CEGUnB, the HS model (Schanz *et al.*, 1999; Brinkgreve *et al.*, 2014, 2015) of the software PLAXIS was used. The HS model is one of the most complete constitutive models of PLAXIS and is capable of:

1) calculating the total strains using a stress-dependent stiffness that is different for loading and unloading/reloading conditions, and
2) modeling irreversible strains due to primary deviatoric loading (shear hardening) and modeling irreversible plastic strains due to primary compression under oedometric and isotropic loading (compression hardening).

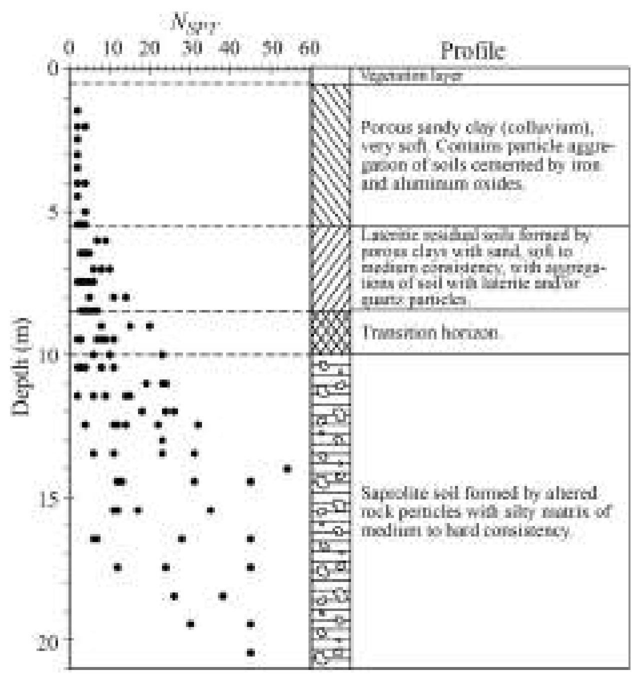

Figure 3 - CEGUnB profile used in the model (Rebolledo *et al.*, 2019).

Rebolledo *et al.* (2019) developed a methodology to obtain, adjust and validate the mechanical parameters of characteristic soils of the city of Brasília for the HS model, making use of laboratory and field test results obtained in previous studies conducted in the CEGUnB. The methodology presented began with the evaluation of the strength and compressibility parameters of triaxial CU tests (with isotropic and anisotropic consolidation) and one-dimensional consolidation tests, respectively (Guimarães, 2002). Then, the parameters obtained for the HS model were calibrated through the explicit numerical modeling of the tests using the finite element method (FEM) and the *SoilTest* module of the PLAXIS software. Based on the evaluation and calibration of these parameters and the proposed soil profile (Fig. 3), a geotechnical model based on the natural moisture state of the CEGUnB was proposed for the HS model, shown in Table 1. This geotechnical model was validated through numerical modeling of the load testing of footings and piles conducted in the CEGUnB (Sales, 2000; Guimarães, 2002).

Using the same methodology and with the triaxial and consolidation tests performed by Guimarães (2002), Pérez (2017) determined the HS model parameters for the first 3.5 m in depth of porous clay from Brasília in the saturated moisture state, as shown in Table 2.

3.2. Definition of the problem geometry

To define the diameter of the inclusions, the studies by ASIRI (2011) and Guimarães (2002) were considered. According to ASIRI (2011), for nonreinforced concrete inclusions constructed on site that do not rely on a micropile-type technique, the typical minimum diameter is 25 cm. According to Guimarães (2002), mechanically excavated piles, which are of great use and versatility in the Federal District of Brazil, can reach 25 m in depth, with diameters varying from 30 to 110 cm.

In this study, the inclusions were modeled with a diameter of 30 cm and placed at a depth of 9.5 m, thus penetrating 1 m into the noncollapsible soil layer to ensure the load transfer from the inclusions to a more competent stratum. For the load distribution layer, thicknesses ranging from 0.5 to 2.5 m were considered, according to the recommendations of ASIRI (2011). The slab was considered flexible with a thickness of 0.20 m with the properties described in 3.3.

According to ASIRI (2011), the minimum center-to-center spacing between inclusions is three times the diameter of the element (3*D*) if the inclusions are constructed on a site with minimum soil disturbance. Hence, the minimum inclusion spacing considered in the parametric analysis was 1 m ($\approx 3D$).

Table 1 - Geotechnical model proposed by the CEGUnB for the natural moisture state for the HS model (Rebolledo *et al.*, 2019).

Parameters	Layer number					
	1	2	3	4	5	6
	Porous sandy clay			Lateritic residual soil		Saprolitic soil
Depth (m)	0 - 1.5	1.5 - 3.5	3.5 - 5.0	5.0 - 7.0	7.0 - 8.5	8.5 - 20.0
γ (kN/m^3)	13.1	12.8	13.9	14.3	16.0	18.2
c (kPa)	5	5	5	20	75	20
ϕ' (°)	25	25	26	32	20	22
ψ (°)	0	0	0	0	0	0
E_{50}^{ref} (MPa)	3.2	2.5	4.0	12.0	13.2	12.2
E_{oed}^{ref} (MPa)	4.9	1.45	2.2	6.9	7.0	5.7
E_{ur}^{ref} (MPa)	14.0	14.0	36.9	37.5	54.0	54.0
m	0.5	0.5	0.5	0.5	0.5	0.7
ν_{ur}	0.2	0.2	0.2	0.2	0.2	0.2
p^{ref} (kPa)	100	100	100	100	100	100
R_f	0.8	0.8	0.9	0.9	0.9	0.8
POP (kPa)	65.7	31.8	0	31.4	0	0
K_0^{nc}	0.58	0.58	0.56	0.47	0.66	0.63
K_0	1.37	0.77	0.56	0.56	0.66	0.63

γ: unit weight of moist soil, c' and ϕ': the effective shear strength parameters, ψ: dilatancy angle, E_{50}^{ref}: the reference secant stiffness modulus for the drained triaxial test, E_{oed}^{ref}: the reference tangent stiffness modulus for oedometric loading, E_{ur}^{ref}: the reference stiffness modulus for unloading and reloading conditions, m: the exponent that defines the strain dependence of the stress state, ν_{ur}: unloading/reloading Poisson's ratio, p^{ref}: the reference isotropic stress, R_f: the failure ratio, POP: the preoverburden pressure, K_0^{nc}: the coefficient of the earth pressure at rest for normal consolidation, and K_0: coefficient of earth pressure at rest.

Table 2 - Geotechnical model proposed for the CEGUnB for the first 3.5 m in depth in the saturated moisture state for the HS model (modified from Pérez 2017).

Parameters	Layer number	
	1	2
	Porous sandy clay	
Depth (m)	0-1.5	1.5-3.5
γ (kN/m^3)	16.5	16.4
c (kPa)	0	0
ϕ' (°)	26	26
ψ (°)	0	0
E_{50}^{ref} (MPa)	2.2	2.1
E_{oed}^{ref} (MPa)	0.96	0.83
E_{ur}^{ref} (MPa)	13.0	13.0
m	0.65	0.80
ν_{ur}	0.2	0.2
p^{ref} (kPa)	50	50
R_f	0.75	0.75
POP (kPa)	16.1	6.59
K_0^{nc}	0.56	0.56
K_0	0.75	0.75

3.3. Properties considered for concrete elements

For the modeling of slab and inclusions, both in concrete, the linear elastic constitutive model was assumed because the stiffness and the strength of this material are considerably higher than those of the reinforced soil. Table 3 presents the parameters of the constitutive model adopted for each concrete element.

The concrete Young's modulus was calculated according to the equation proposed in Brazilian standard NBR 6118 (ABNT, 2014) as a function of the strength characteristics of the concrete subjected to simple compression. Therefore, a compressive strength of 20 MPa was assumed for the slab and 10 MPa for the inclusions.

As proposed in NBR 6118 (ABNT, 2014) and by ASIRI (2011), a Poisson's ratio for concrete equal to 0.2 was adopted for both elements.

Table 3 - Parameters of the slab and the rigid inclusions.

Parameters	Slab	Inclusions
Unit weight of concrete, γ (kN/m^3)	24.0	23.0
Young's modulus of concrete, E (GPa)	25.0	17.7
Normal stiffness, EA (kN/m)	5.0×10^6	-
Bending stiffness, EI (kN/m^2/m)	1.67×10^4	-
Poisson's ratio, ν	0.20	0.20

3.4. Properties considered in the distribution layer

For the distribution layer (improved soil), the Mohr-Coulomb model was adopted. Research performed by Otálvaro (2013) at the Geotechnics Laboratory of the University of Brasília (UnB) provided the estimates of the parameters for tropical soil improved by compaction that were used in this study, and these parameters are presented in Table 4. The compacted tropical soil, of the laterite type and highly weathered, was collected in the Brazilian Cerrado region in the city of Brasília. The material was classified as ML (low plasticity silt) according to the Unified Soil Classification System (USCS). The γ value was obtained from the results of Proctor Standard testing (compaction energy of 600 kN-m/m3), from values of w_{opt} = 24 % and γ_{dmax} = 15 kN/m^3. Parameters E, ϕ' and c' were obtained from CD (consolidated-drained) triaxial tests performed on the same compacted soil. Echevarría (2006) obtained similar parameters for numerical simulation of tropical porous compacted soil.

3.5. Analysis steps

The analysis steps of the numerical models were established according to the construction process of foundations with rigid inclusions. Initially, five steps were defined: Step I consists of the excavation of the natural soil, upon which the distribution layer will be built; in Step II, the rigid inclusions are installed; in Step III, the distribution layer is built; in Step IV, the slab is built; in Step V, the load is applied to the foundation.

4. Parametric Modeling of Rigid Inclusions

4.1. General considerations

An infinite group of rigid inclusions over an infinitely large distribution layer and slab was considered (Fig. 4a). The area of influence, or influence cell, of each internal inclusion (Schlosser *et al.*, 1984) is hexagonal but can be idealized as a circular unit cell (Rodríguez *et al.*, 2015); the problem then becomes axisymmetric (Fig. 4b). The radius R of this area, corresponding to the radius of a finite element axisymmetric mesh, is approximately equal to half the spacing between inclusions ($S \approx 2R$). For the inclusions located in the periphery, the conditions are no longer axisymmetric, and the results obtained by such a model are less

Table 4 - Estimated parameters for soil improved by compaction.

Parameter	Value
Unit weight, γ (kN/m^3)	18.6
Young's modulus, E (MPa)	60
Cohesion, c' (kPa)	80
Friction angle, ϕ' (°)	38
Poisson's ratio, ν	0.25

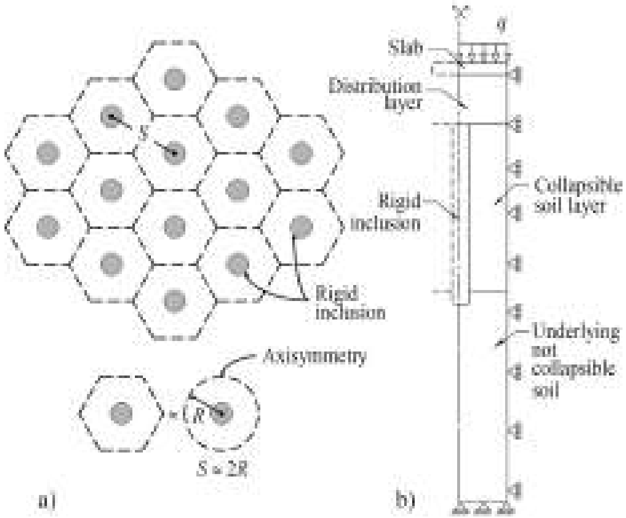

Figure 4 - a) Distribution of an infinite group of inclusions arranged as a grid and b) axisymmetric model representing the area of influence or cell inside the grid (modified from Rodríguez *et al.*, 2015).

representative. However, according to Schlosser *et al.* (1984), for large groups of inclusions where the boundary conditions become less important, the influence cell model can capture the essence of the physical phenomena.

The centerline of the axisymmetric model coincides with the axis of the rigid inclusion. The right boundary was placed halfway between the inclusions. The lower boundary was established at a depth of 20 m, beyond which the N_{SPT} was larger than 40 blows, and the soil was classified as very compact, according to the Brazilian standard NBR 6484 (ABNT, 2001). Therefore, the lower boundary was considered 10.5 m below the tip of the inclusion.

The parametric modeling of the rigid inclusions was carried out using PLAXIS 2D software (Brinkgreve *et al.*, 2014). The problem was discretized using a finite element mesh with more than 6,700 15-node triangular elements. A mesh densification was considered around the inclusions. The slab was modeled using 5-node beam elements. The lateral boundaries were fixed in the horizontal direction, and the bottom boundary was fixed in both directions. The sensitivity studies showed that the mesh was dense enough to provide accurate results. To adequately consider the interaction between the inclusion surface and the soil, five pairs of node interface elements were added.

4.2. Cases analyzed

To evaluate the performance of the rigid inclusion foundation for settlement control, the case of a single-slab foundation (without inclusions) was analyzed, and the results obtained from both cases were compared. Parametric analyses were performed considering the stratigraphy previously presented in two situations: with the soil at natural moisture conditions (Case 1) and with the first 3.5 m of the soil saturated (Case 2). The influence of two parameters was considered: the spacing between inclusions (1, 1.5, 2, 2.5, and 3 m) and the distribution layer thickness (0.5, 1, 1.5, 2, and 2.5 m). In each model, the results for loads on the slab (q_0) equal to 10, 20, 40, 60, 80, 100 and 120 kPa were obtained. The base of inclusion was placed at a depth of 9.5 m, and the slab thickness was 0.2 m.

4.3. Loads developed on the inclusions

As part of the results, Fig. 5a shows the axial load developed in the inclusions for spacing between elements (*S*) of 1 to 3 m, distribution layer thickness (H_{DL}) equals to 1.5 m, and load (q_0) of 60 kPa. As explained previously (Fig. 2a), the model highlights the development of the cap and tip forces and those due to negative and positive skin friction. Similar behavior was observed by Briançon *et al.* (2015) in instrumented rigid inclusions that were part of the foundation of an industrial structure. The author notes that the shape of the strain curve inside both instrumented rigid inclusions indicates an evolution of the strain during the construction of the building, indicating the interval where the neutral point between the negative and positive friction was located.

Figure 5a shows that the magnitudes of the cap, negative friction and positive friction loads significantly increase when *S* increases. The load on tip does not increase with increasing *S*, probably because the tip bearing capacity has been reached at this point; therefore, the inclusions respond mainly by lateral friction, as in the case of friction piles.

Figure 5b shows the axial load in the inclusion for different H_{DL} values; when H_{DL} increases, the maximum axial load increases because the unit weight of the distribution layer is 18.6 kN/m^3 and that of the substituted superficial soil is approximately 13 kN/m^3, which gives an overload of 5.6 kN/m^2 for each meter of thickness. Then, when H_{DL} increases, the overload is transferred to the inclusions mainly by the caps, with the negative skin friction almost constant; hence, the positive skin friction increases. The increase in positive skin friction means that additional settlements can occur. Due to the above and for economic reasons, the thickness of the distribution layer cannot be large; this layer has to enable partial load transfer to the inclusion cap, surface settlement reduction and homogenization, thereby guaranteeing the durability and functionality of the surface structure.

Figure 6 shows that when the first 3.5 m of the soil saturate, the load on the inclusion cap increases, the negative friction load decreases, and both positive skin friction and tip load remain constant. These results indicate that saturated soil is less resistant and more compressible than the soil at natural moisture condition and thus is not able to transmit the same load to the shaft of the inclusion (negative friction); therefore, the load transferred by the distribution layer to the inclusion tip increases, and no additional

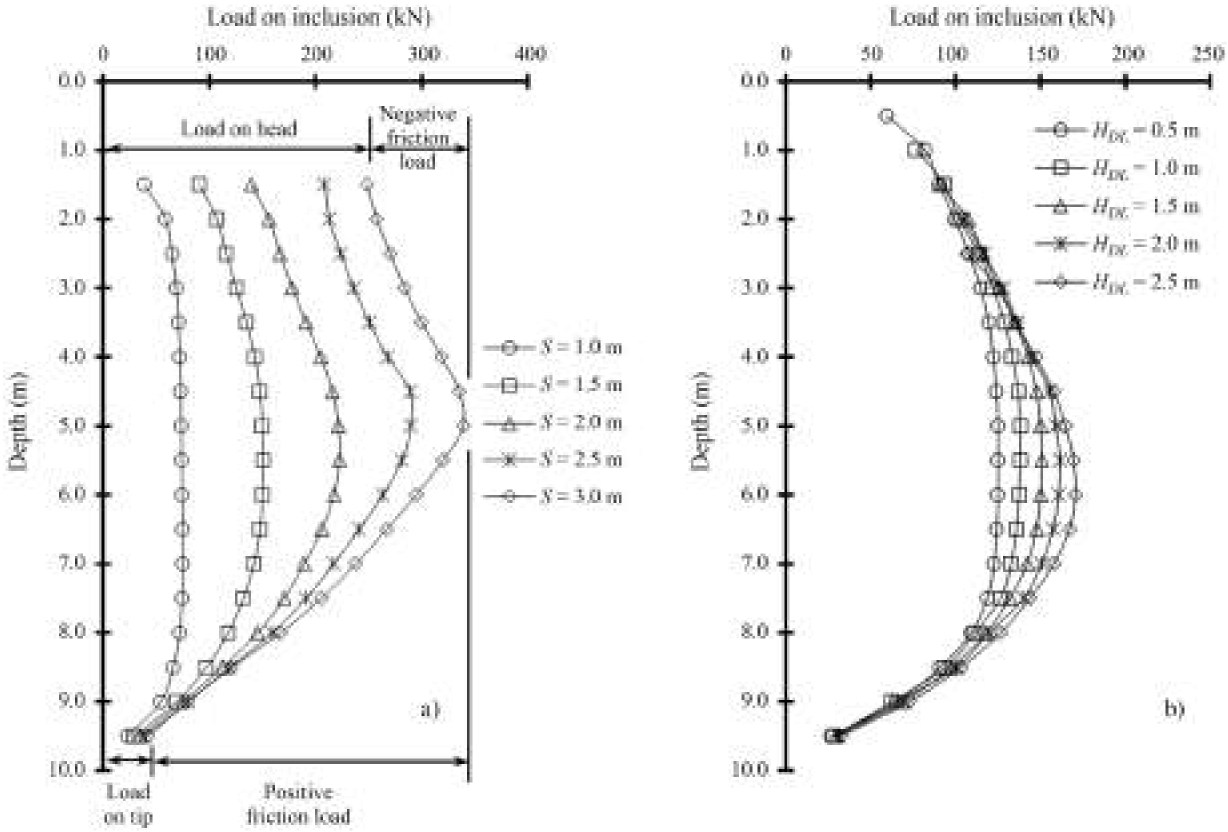

Figure 5 - Axial loads developed in the inclusion body, for a) different spacing between elements (S), H_{DL} = 1.5 m and q_0 = 60 kPa and b) different distribution layer thickness (H_{DL}), S = 1.5 m and q_0 = 60 kPa.

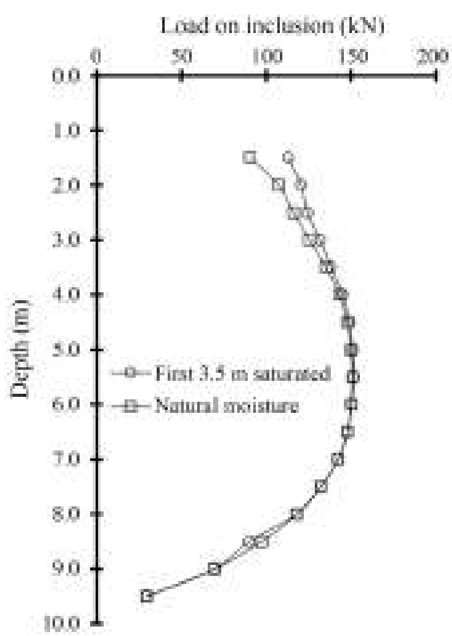

Figure 6 - Load developed along the inclusion for natural and saturated moisture conditions, S = 1.5 m, H_{DL} = 1.5 m and q_0 = 60 kPa.

load is transferred to the reinforced soil, which means that inclusions can work properly for both natural and saturated conditions.

4.4. Settlement control

The performance of the rigid inclusion foundation in controlling surface settlement was determined using the proposed settlement reduction factor (SRF):

$$SRF = 1 - \frac{\delta_s^+}{\delta^*} \qquad (1)$$

where δ_S^+ is the settlement of the soil reinforced by rigid inclusions and δ^* is the settlement of the soil without reinforcement, both obtained at the center of the slab. When SRF = 1, the settlement is fully reduced, and the performance of the inclusion system is at the maximum; when SRF = 0, the settlement reduction is null, and the performance of the system is at the minimum.

The analyses were performed for several values of spacing between inclusions (S), distribution layer thicknesses (H_{DL}) and load levels (q_0), considering cases of stratigraphy with natural moisture (Case 1) and with the first 3.5 m of the soil saturated (Case 2).

Figure 7 shows graphs of settlement *versus* q_0 at the center of the slab, for H_{DL} = 1.5 m, for different S values and for Cases 1 and 2 (Figs. 7a and 7b, respectively). The results for δ_S^+ are presented by continuous lines, and those for δ^* are presented by dashed lines.

For Case 1, δ^* varies from 2.7 to 40.2 cm and for Case 2, from 4.2 to 57.4 cm; an increment of 43 to 56 % of the total settlement is obtained from one case to the other. When inclusions are added for both cases (Figs. 7a and 7b), very similar values of δ_S^+ are obtained for the different *S* values; a maximum difference of 16 % is calculated for q_0 = 120 kPa and *S* = 3 m. This result means that, as shown in Fig. 8, the performance of rigid inclusions for settlement control (*SRF* values) significantly increase from Case 1 (Fig. 8a) to Case 2 (Fig. 8b). As mentioned before, rigid inclusion foundations are more efficient when the soil to be reinforced is more compressible and less resistant because the distribution layer transfers more load to the head of the element and less load to the reinforced soil.

Figures 7 and 8 show that very similar results are obtained for *S* = 1.0 m and 1.5 m. For *S* values greater than 1.5 m, the *SRF* passes from a maximum value of 0.6 to 0.35 for Case 1 and from 0.75 to 0.48 for Case 2. On the other hand, as demonstrated in Fig. 9, when *S* is held constant (*S* = 1.5 m) the settlement reduction achieved with the inclusions for different H_{DL} values is practically constant for q_0 values greater than 40 kPa. For q_0 < 40 kPa, the overload generated by the distribution layer influences the inclusion performance for H_{DL} > 1.5 m; inclusive negative *SRF* values can be obtained.

The axisymmetric analyses show high performance for the rigid inclusions regarding settlement control for the two cases analyzed. According to the research developed by Briançon *et al.* (2015) related to the monitoring and numerical investigation of rigid inclusion-reinforced industrial buildings, the settlement measured both at the pile head and the soil surface showed that the supporting system can significantly reduce settlements.

According to the results obtained, a thickness of 1.5 m for the distribution layer and an *S* value close to 1.5 m were proposed for the following 3D analyses.

5. 3D Modeling

5.1. General considerations

The 3D modeling was based on a real project located in the Meireles Sector in the city of Santa Maria, DF, as presented by Castillo (2013). Lot 401, chosen for the study, encompasses three types of residential blocks with pile group and single-pile foundations; the Type II block was chosen for these analyses. Type II block consists of four floors (ground floor plus three decks), with two two-bedroom

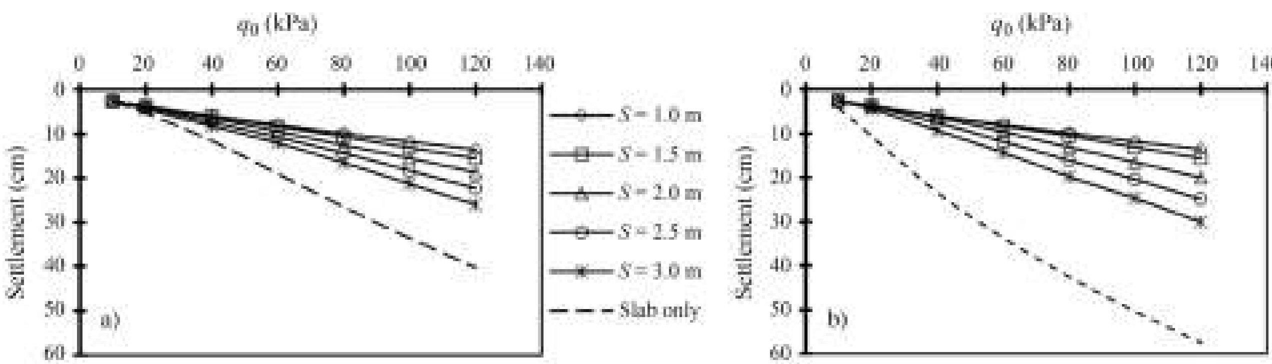

Figure 7 - Settlement as a function of q_0, for H_{DL} = 1.5 m, different *S* values, and a) Case 1: stratigraphy with natural moisture conditions and b) Case 2: stratigraphy with the first 3.5 m of the soil saturated.

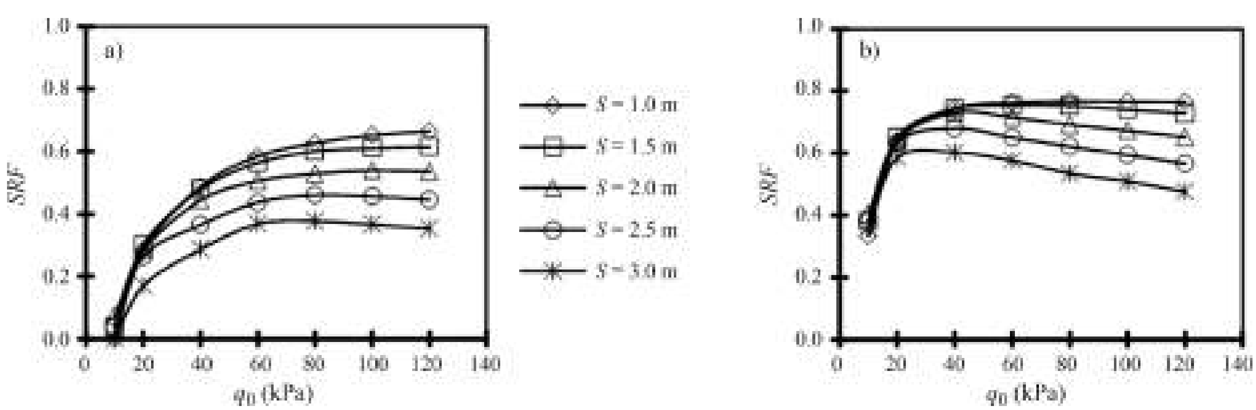

Figure 8 - Settlement reduction factor (*SRF*) as a function of q_0, for H_{DL} = 1.5 m, different *S* values, and a) Case 1: stratigraphy with natural moisture conditions and b) Case 2: stratigraphy with the first 3.5 m of the soil saturated.

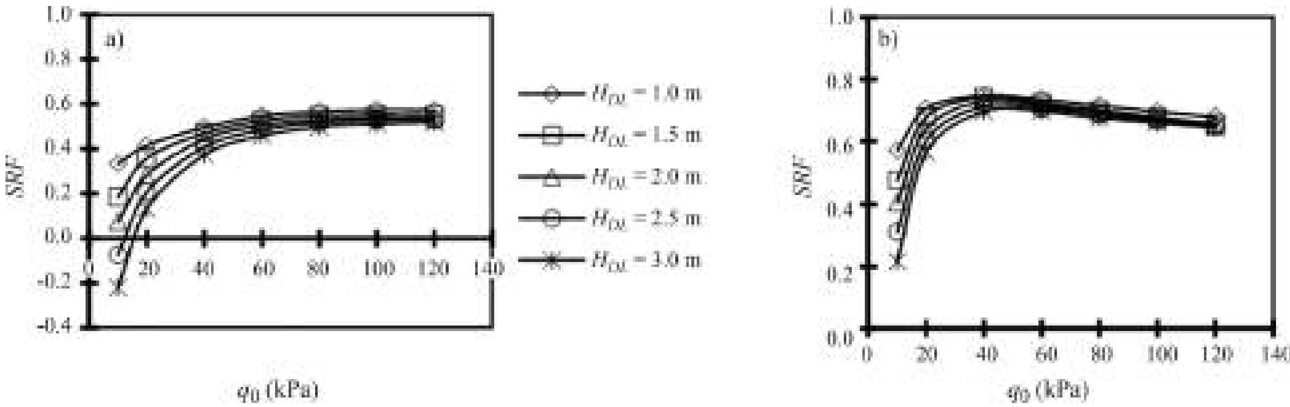

Figure 9 - Settlement reduction factor (*SRF*) as a function of q_0, for S = 1.5 m, different H_{DL} values, and a) Case 1: stratigraphy with natural moisture conditions and b) Case 2: stratigraphy with the first 3.5 m of the soil saturated.

housings per floor. The original project foundation was formed by a total of 32 bored concrete piles with diameters from 30 to 50 cm and depths of 12 to 17 m, arranged as shown in Fig. 10.

For practical purposes and as a demonstrative example only, the stratigraphy and properties considered for this analysis were those described in section 3.1.

Figure 10 shows the floor plan for the locations of the columns and the load acting on each (serviceability state load combination). To simplify the simulation, the total load imposed by the superstructure (9,740 kN) was obtained through the sum of loads of all columns (Fig. 10). This total load was divided by the total area of the slab (202.4 m^2) and by the number of floors (five), and then, a distributed load of the same value (9.7 kN/m^2) was applied directly to each slab.

To obtain the magnitudes of the settlements that needed to be minimized and to evaluate the performance of the rigid inclusion system, the foundation was initially modeled considering only a single-slab foundation. Subsequently, analysis was performed considering the rigid inclusion system.

The numerical simulation presented below was performed using PLAXIS 3D (Brinkgreve *et al.*, 2015).

5.2. Modeling of the foundation with a single-slab foundation

As shown in Fig. 11, for modeling a single-slab foundation, the symmetry conditions of the problem were considered. The medium was discretized by a finite element mesh with more than 112,200 10-node tetrahedral elements, the foundation and floor slabs were discretized by

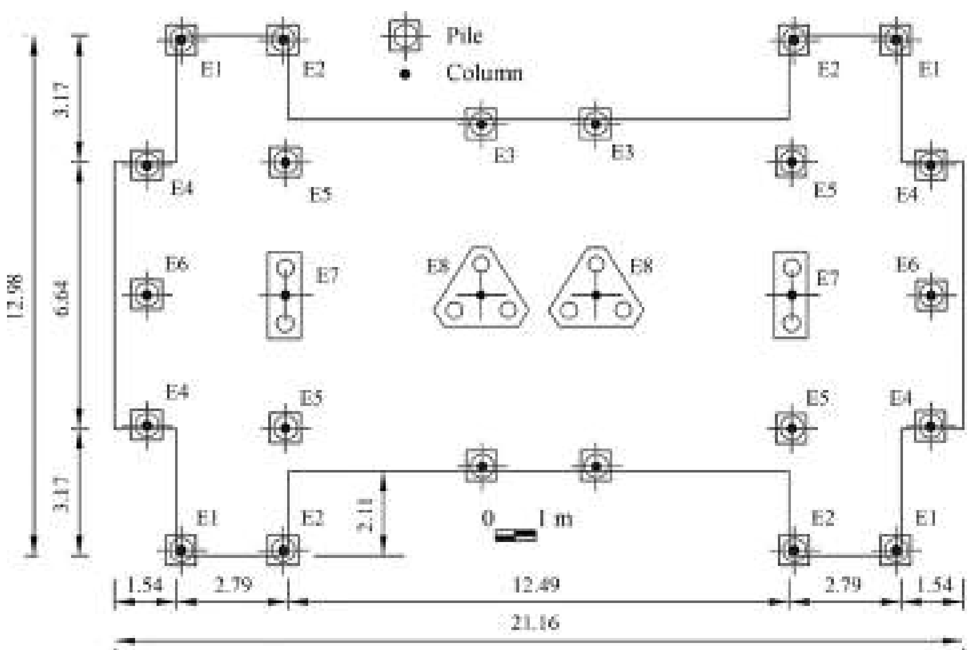

Pile details	
Pile	Acting load (kN)
E1	140
E2	150
E3	470
E4	280
E5	470
E6	400
E7	580
E8	880

Concrete strength (MPa)	
Block	25
Piles	15

Figure 10 - Floor plan for locations of piles and columns in the type II block (Castillo, 2013).

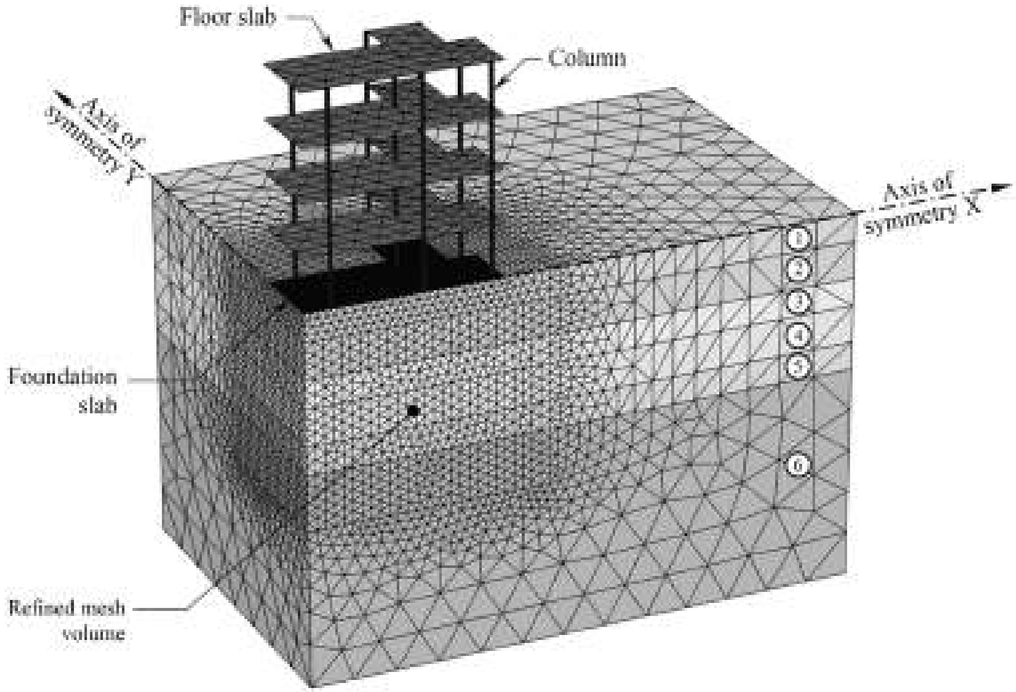

Figure 11 - 3D model of the single-slab foundation.

six-node triangular plate elements (0.2 m thick) and the columns with three-node beam elements. The densification of the mesh around (14 m along the x-axis and 10 m along the y-axis) and under (12 m in z-axis) the footing was considered. The lateral boundary conditions were fixed in the horizontal direction, and the bottom boundary conditions were fixed in both directions. The sensitivity analyses showed that the mesh density was sufficient for accurate results.

5.3. Modeling of the foundation with rigid inclusions

As for the single-slab foundation, for the modeling of the foundation with rigid inclusions, the symmetry conditions of the problem were considered, as shown in Figs. 12 and 13.

In all the models, the following characteristics were considered: a slab thickness of 0.20 m, a distribution layer 1.5 m thick, an inclusion diameter of 0.3 m, and spacing between inclusions of 1.8 m (6 times the diameter of the inclusion). The inclusion tips were placed at 9.5 m and 12 m in depth, and stratigraphies were analyzed with natural moisture conditions (Case 1) and with the first 3.5 m of the saturated soil (Case 2).

The medium was discretized by a finite element mesh with more than 109,200 10-node tetrahedral elements, the foundation and floor slabs were discretized by six-node triangular plate elements (0.2 m thick), the columns with three-node beam elements, and the rigid inclusions with three-node embedded pile elements. The densification of the mesh around (14 m along the x-axis and 10 m along the y-axis) and under (12 m in z-axis) the footing and the rigid inclusions was considered. The lateral boundary conditions were fixed in the horizontal direction, and the bottom boundary conditions were fixed in both directions. The sensitivity analyses showed that the mesh density was sufficient for accurate results. A general view of the mesh employed for the structure and foundation is shown in Fig. 13.

5.4. Analysis of the results

According to the Brazilian standard NBR 6122 (ABNT, 2010), the maximum allowable displacements supported by the structure, without prejudice to the serviceability limit states, shall comply with the requirements of NBR 8681 (ABNT, 2003). These displacements, both in absolute terms (total settlements) and in relative terms (differential settlements), must be established by the designer according to the importance of the construction work. As shown in Table 5, several publications propose reference values; in this study, the admissible settlement value adopted was 50 mm.

Figures 14 and 15 show the settlements obtained in the slab for Cases 1 and 2, respectively, and Table 6 shows the maximum values. For Case 1, the maximum total settlement obtained was 127.8 mm, and that for Case 2 was 318 mm. The foundation does not meet the maximum admissible settlement criterion, requiring the use of rigid inclusions to minimize the total surface settlements. On the other hand, Fig. 16 shows the settlements obtained for the foundation with rigid inclusions, considering: a) Case 1 and inclusions at a depth of 9.5 m, b) Case 2 and inclusions at a depth of 9.5 m, c) Case 1 and inclusions at a depth of 12 m, and d) Case 2 and inclusions at a depth of 12 m. Table 6 in-

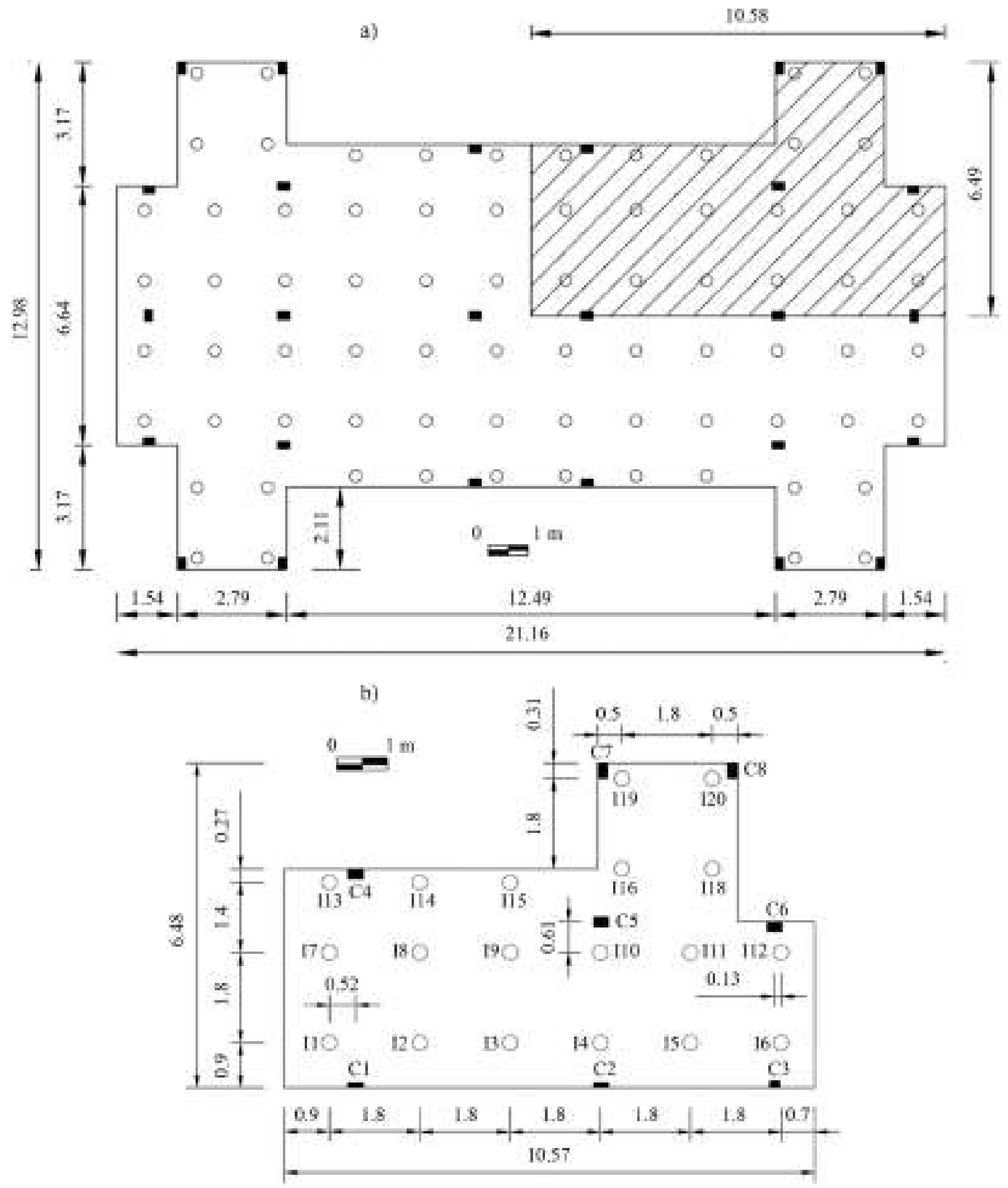

Figure 12 - a) Floor plan of the original project highlighting the area considered in the numerical modeling and b) details of the distribution of the rigid inclusions.

cludes the maximum values obtained for all the cases analyzed.

For Case 1 (Fig. 16a), the use of rigid inclusions placed at a depth of 9.5 m yields a settlement reduction of 62.5 % compared with the foundation with the single-slab, for inclusions placed at 12 m (Fig. 16c), the reduction was 71.8 %, and for Case 2 (9.5 m in depth, Fig. 16b, and 12 m in depth, Fig. 16d), the settlement reductions were 83.0 and 87.1 %, respectively.

To control the angular distortion, a limit of 1/500 was adopted, according to those proposed by Bjerrum (1963), as shown in Table 7. The angular distortion value was calculated from Figs. 14, 15 and 16 as the ratio of the differential settlement between two neighboring columns (Fig. 12) and the distance between axes.

Table 8 summarizes the maximum angular distortion for all the cases analyzed. For the single-slab foundation in Case 1 (Fig. 14), the maximum angular distortion was 1/396, and that for Case 2 (Fig. 15) was 1/1000. According to these results, the single-slab foundation does not meet the angular distortion limit in Case 1, and therefore, the use of rigid inclusions is required. With rigid inclusions, as shown in Table 8 and Fig. 16, all the cases analyzed meet the maximum angular distortion limit (1/500).

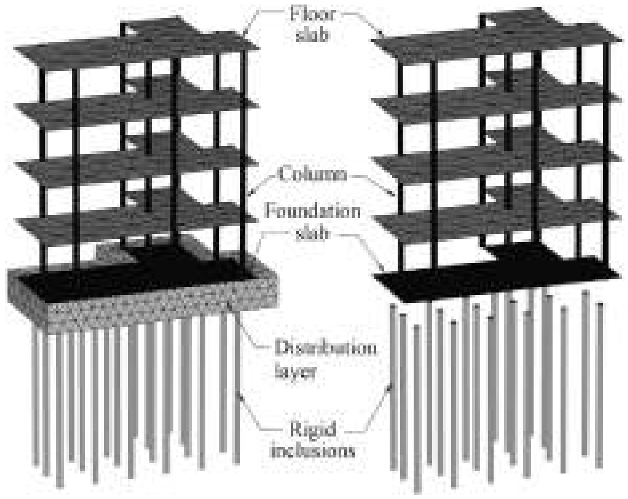

Figure 13 - Isometric projections of the foundation with rigid inclusions and the structure.

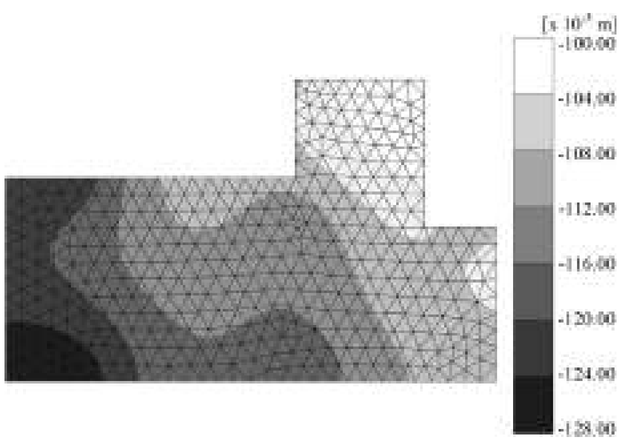

Figure 14 - Vertical displacements for the single-slab foundation, Case 1.

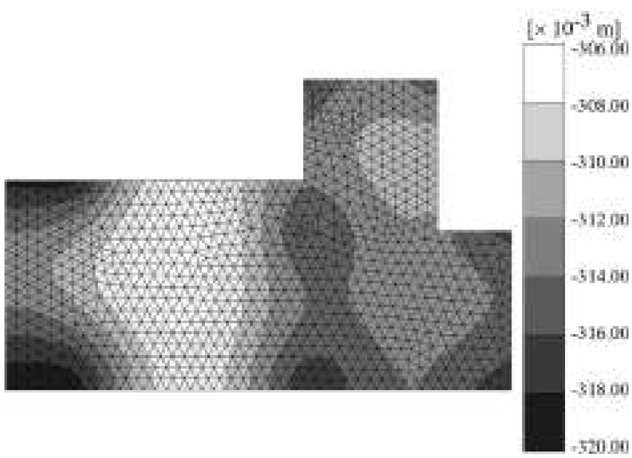

Figure 15 - Vertical displacements for the single-slab foundation, Case 2.

In general, for the cases analyzed, the rigid inclusions perform well, reducing the settlement by more than 80 % and homogenizing the vertical displacements at tolerable values meeting with the serviceability limit states.

Based on measurements performed one year after construction at superficial benchmarks located at eight points around the perimeter of three five-floor buildings with rigid inclusion foundation systems in soft soils, Rodri-

Table 5 - Maximum allowable settlements (Castillo, 2013).

Publication	δ_{max} (mm)
Eurocode 7	< 50
Eurocode 1 (1993)	50
Teixeira & Godoy (1998)	90
Burland *et al.* (1977)	65-100
Bowles (1977)	64
Terzaghi & Peck (1967)	50
Skempton & MacDonald (1956)	90

Table 6 - Maximum total settlements (mm).

Single-slab		Inclusions up to 9.5 m		Inclusions up to 12 m	
Case 1	Case 2	Case 1	Case 2	Case 1	Case 2
128	318	48	54	36	41

Table 7 - Values of angular distortion limits proposed by Bjerrum (1963).

Damage category	η
Danger to settlement-sensitive machines	1/750
Danger to landmarks with diagonal cracks	1/600
Safe limit for cracks not occurring in buildings*	1/500
First cracks on walls	1/300
Problems with overhead crane	1/300
Slant of tall buildings becomes visible	1/250
Considerable cracking of brick walls and panels	1/150
Risk of structural damage to general buildings	1/150
Safe boundary for flexible brick walls, L/H > 4 *	1/150

*The safe limits include a safety factor.

Table 8 - Maximum angular distortion values.

Slab-only		Inclusions up to 9.5 m		Inclusions up to 12 m	
Case 1	Case 2	Case 1	Case 2	Case 1	Case 2
1/396	1/1000	1/616	1/616	1/821	1/593

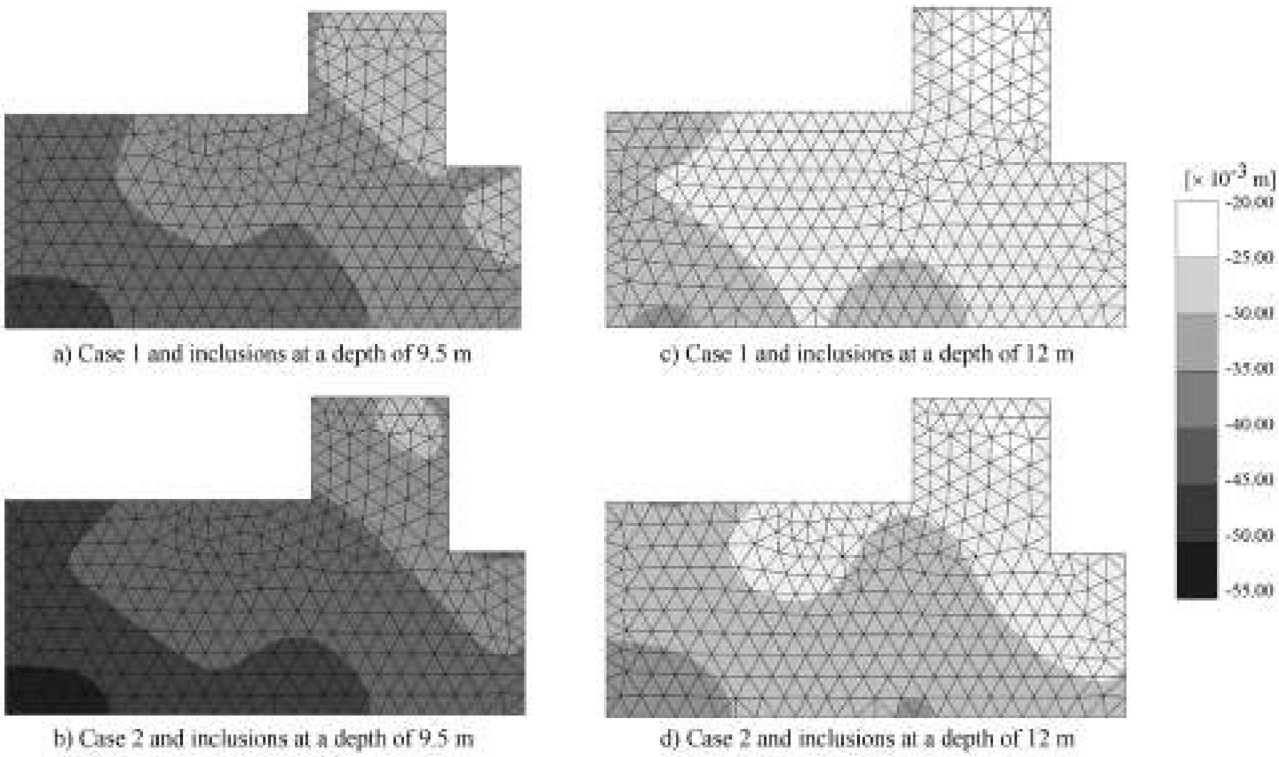

Figure 16 - Vertical displacements for all the cases analyzed with rigid inclusion foundations.

guez & Auvinet (2006) concluded that the mean differential settlement was approximately 0.5 cm, and hence, the behavior of the buildings was adequate during that period.

6. Conclusions

In this study, numerical modeling was used to evaluate the performance of rigid inclusion foundations for settlement control considering the characteristic soils of the city of Brasília in the Federal District of Brazil. PLAXIS 2D and 3D software was used considering the Hardening Soil constitutive model parameters previously obtained, calibrated and validated by the authors.

The settlement reduction obtained with the use of rigid inclusions is due to the transfer of a significant load from the soil to these elements. Complex interactions develop between the reinforced soil, the inclusions and the distribution layer.

To evaluate the performance of a rigid inclusion foundation for settlement control, the case of a single-slab foundation (without inclusions) was analyzed, and the results obtained for both cases were compared.

The numerical modeling highlights the development of forces in the cap and inclusion tip, and those due to negative and positive skin friction. Similar behavior was observed in instrumented rigid inclusions that were part of the foundation of an industrial structure.

The magnitudes of the cap, negative friction and positive friction loads increased significantly when the inclusion spacing increased. However, the tip load does not increase in this case, probably because the tip bearing capacity had been reached at this point; therefore, for the cases analyzed, the inclusions mainly responded by lateral friction, as in the case of friction piles.

When the thickness of the distribution layer increased, an overload was generated and was transferred to the inclusion mainly by the cap, while the negative skin friction was almost constant, and hence, the positive skin friction increased. Thus, additional settlements could occur. Due to the above results and economic reasons, the distribution layer cannot be large in thickness; this layer has to enable: i) partial load transfer to the cap, ii) surface settlement reduction, and iii) homogenization; thereby guaranteeing the durability and functionality of the surface structure.

When the first 3.5 m of the soil was considered to be saturated, the load on the inclusion cap increased, the negative skin friction load decreased, and both positive skin friction and tip load remained almost constant. These results indicated that saturated soil is less resistant and more compressible than soil at natural moisture conditions and thus is not able to bear the same load to the shaft of the inclusion (negative friction); therefore, the load transferred by the distribution layer to the inclusion tip increases, and no additional load is transmitted to the reinforced soil. This effect means that inclusions can work properly for both natural and saturated conditions without a significant increase in settlement.

The performance of the rigid inclusion foundation for controlling surface settlement was determined using the proposed Settlement Reduction Factor. Rigid inclusion foundations are more efficient when the soil to be reinforced is more compressible and less resistant because the distribution layer transfers more load to the head of the element and less load to the reinforced soil.

In general, for the 3D cases analyzed, the rigid inclusions perform well, reducing the settlement by more than 80 % and homogenizing the vertical displacements at tolerable values that meet the serviceability limit states. However, feedback from instrumentation cases in the city of Brasilia is required to further validate the design considerations.

Acknowledgments

The authors acknowledge the Coordination for the Improvement of Higher Education (CAPES), the National Council for Scientific and Technological Development (CNPq) and the Federal District Development Support Fund (FAPDF) for their support and partnership.

References

ABNT (2001). Solo - Sondagens de Simples Reconhecimento com SPT - Método de Ensaio - NBR 6484. Associação Brasileira de Normas Técnicas, Rio de Janeiro, RJ, Brazil, 17 p.

ABNT (2003). Ações e Segurança nas Estruturas - Procedimento - NBR 8681. Associação Brasileira de Normas Técnicas, Rio de Janeiro, RJ, Brazil, 15 p.

ABNT (2010). Projeto e Execução de Fundações - NBR 6122. Associação Brasileira de Normas Técnicas, Rio de Janeiro, RJ, Brazil, 33 p.

ABNT (2014). Projeto de Estruturas de Concreto - Procedimento - NBR 6118. Associação Brasileira de Normas Técnicas, Rio de Janeiro, RJ, Brazil, 256 p.

Almeida, M.S.S.; Magnani, H.O.; Dias, D. & Deotti, L.O.G. (2011). Behaviour of three test embankments taken to failure on soft clay. Soil and Rocks, 34(4):389-404.

ASIRI (2011). Recommendations for Design, Construction and Control of Rigid Inclusion Ground Improvements. ASIRI National Project. Institute for Applied Research and Experimentation in Civil Engineering (IREX), Presses des Ponts, France, 317 p.

Auvinet, G. & Rodríguez, J.F. (2006). Modelling of rigid inclusions in consolidating soils. Proc. Int. Symp. Rigid Inclusions in Difficult Soft Soil Conditions, Mexico City, v. 1, pp. 83-93.

Bjerrum, L. (1963). Allowable Settlement of Structures. Proc. ECSMFE, Wiesbaden, v. 3, pp. 135-137.

Briançon, L.; Dias, D. & Simon C. (2015). Monitoring and numerical investigation of a rigid inclusions-reinforced industrial building. Can. Geotech. J., 52(10):1592-1604.

Brinkgreve, R.B.J.; Engin E. & Swolfs W.M. (2014). Plaxis 2D Anniversary Edition, Plaxis bv.

Brinkgreve, R.B.J.; Kamarswamy S. & Swolfs W.M. (2015). Plaxis 3D Anniversary Edition, Plaxis bv.

BSI (2010). Code of Practice for Strengthened/Reinforced Soils and Others Fills - BS 8006-1. British Standards Institution, London, UK, 249 p.

Cardoso, F.B.F. (2002). Propriedades e Comportamento Mecânico de Solos do Planalto Central Brasileiro. Doctorate Degree Thesis, Civil Engineering and Environmental Department, University of Brasília, Brasília, 357 p.

Castillo, D.J.A. (2013). Uso da Técnica de Radier Estaqueado para Pequenos Edifícios Assentes Sobre Solo Colapsível. Master Degree Dissertation, Civil Engineering and Environmental Department, University of Brasília, Brasília, 154 p.

Coelho, R.S. (2013). Relatório das Sondagens Executadas na Área Destinada à Construção da Obra Casa do Professor. FUNDEX, Brasília, 11 p.

Combarieu, O. (1990). Fondations superficielles sur sol amélioré par inclusions rigides verticales. Rev. Franç. Géotech., 53:33-44, DOI: 10.1051/geotech/1990053033

Cruz, P.T. (1987). Solos residuais: algumas hipóteses de formulações teóricas de comportamento. Proc. Seminário em Geotecnia de Solos Tropicais, Brasília, v. 1, pp. 79-111.

Echevarría, S.P. (2006). Efeitos de Arqueamento em Aterros sobre Solo Estaqueado. Master Degree Dissertation, Civil Engineering and Environmental Department, University of Brasília, Brasília, 136 p.

Fonseca, E.C.; & Palmeira, E.M. (2018). An evaluation of the accuracy of design methods for geosynthetic reinforced piled enbankments. Can. Geotech. J., 56(6):761-773.

Guimarães, R.C. (2002). Análise das Propiedades e Comportamento de um Perfil de Solo Laterítico Aplicada ao Estudo do Desempenho de Estacas Escavadas. Master Degree Dissertation, Civil Engineering and Environmental Department, University of Brasília, Brasília, 183 p.

Jardim, N.A. (1998). Metodologia de Previsão de Capacidade de Carga Vertical e Horizontal com o Dilatômetro de Marchetti. Master Degree Dissertation, Civil Engineering and Environmental Department, University of Brasília, Brasília, 141 p.

López, R.; Shao, L.; Lam Po, I.; & Gularte, F. (1999). Composite ground reinforcement foundation system for large capacity grain domes under static and seismic loads. Proc. XI PCSMGE, Foz do Iguaçu, v. 1, pp. 1-16.

Mota, N.M.B. (2003). Ensaios Avançados de Campo na Argila Porosa Não Saturada de Brasília: Interpretação e Aplicação em Projetos de Fundação. Doctorate Degree

Thesis, Civil Engineering and Environmental Department, University of Brasília, Brasília, 335 p.

Okyay, U.S.; Dias, D.; Thorel, L.; & Rault, G. (2014). Centrifuge modelling of a pile supported granular earth platform. Journal Geotecn Engrg ASCE, 140(2), DOI: 10.1061/(ASCE)GT.1943-5606.0001004

Otálvaro, I.F. (2013). Comportamento Hidromecânico de um Solo Tropical Compactado. Doctorate Degree Thesis, Civil Engineering and Environmental Department, University of Brasília, Brasília, 112 p.

Pecker, A (2004). Le pont de Rion Antirion en Grèce, le défi sismique. 550 conférence, Prononcée à l'Université de Tous les savoirs.

Pérez, R.F. (2017). Inclusões Rígidas para o Controle de Recalques nos Solos Colapsáveis do Distrito Federal. Master Degree Dissertation, Civil Engineering and Environmental Department, University of Brasília, Brasília, 156 p.

Quigley, P.; O'Malley, J. & Rodgers, M. (2003). Performance of a trial embankment constructed on soft compressible estuarine deposits at Shannon, Ireland. Proc of the Int. Workshop on Geotechnics of Soft Soils, Theory and Practice. Noordwijkerhout, pp. 619-624.

Rebolledo, J.F.; León, R.F.; Camapum De Carvalho, J. (2019). Obtaining the mechanical parameters for the hardening soil model of Tropical soils in the city of Brasília. Soils and Rocks, 42(1):61-74.

Rodríguez, J.F. (2001). Uso de Inclusiones Rígidas para el Control de Asentamientos en Suelos Blandos. Master Degree Dissertation, Engineering Faculty, UNAM, Mexico City, 154 p.

Rodríguez, J.F. (2010). Modelado del Comportamiento de Pilotes e Inclusiones Sometidos a Consolidación Regional, en la Zona Lacustre de la Ciudad de México. Doctorate Degree Thesis, Engineering Faculty, UNAM, Mexico City, 244 p.

Rodríguez, J.F. & Auvinet, G. (2006). Rigid inclusions in Mexico City soft soils. Proc. Int. Symp. Rigid Inclusions in Difficult Soft Soil Conditions, Mexico City, v. 1, pp. 197-206.

Rodríguez, J.F.; Auvinent G. & Martínez H.E. (2015). Settlement analysis of friction piles in consolidating soft soils. DYNA, 82(192):211-220.

Sales, M.M. (2000). Análise do Comportamento de Sapatas Estaqueadas. Doctorate Degree Thesis, Civil Engineering and Environmental Department, University of Brasília, Brasília, 229 p.

Sales, M.M.; Vilar, O.M.; Mascarenha, M.M.A.; Silva, C.M.; Pereira, J.H.F & Camapum De Carvalho, J. (2015). Fundações em solos não saturados. Camapum De Carvalho, J.; Gitirana Jr, G.; Machado, S.; Mascarenha, M.M. & Filho, F. (eds.), Solos Não Saturados no Contexto Geotécnico. ABMS, São Paulo, pp. 651-685.

Santoyo, E. & Ovando, E. (2006). Geotechnical considerations for hardening the subsoil in Mexico City's Metropolitan Cathedral. Proc. Int. Symp. Rigid Inclusions in Difficult Soft Soil Conditions, Mexico City, v. 1, pp. 171-178.

Schanz, T.; Vermeer, A. & Bonnier, P. (1999). The hardening soil model: formulation and verification. Proc. Int. Symp. beyond 2000 Comput. Geotech. 10 years PLAXIS, The Netherlands, v. 1, pp. 281-296.

Schlosser, F.; Jacobsen, H.M; & Juran, I. (1984). Le renforcement des sols. Revue Française de Géotechnique, 29:7-33.

Simon, B. & Schlosser, F. (2006). Soil reinforcement by vertical stiff inclusions in France. Proc. Int. Symp. Rigid Inclusions in Difficult Soft Soil Conditions, Mexico City, v. 1, pp. 3-23.

Vesic, A.S. (1970). Load Transfer in Pile-Soil Systems. School of Engineering, Duke University, Soil Mechanics Series, v. 23.

Wood, H.J. (2003). The design and construction of pile-supported embankments for the A63 Selby Bypass. Proc. of Foundations: Innovations, Design and Practice, Dundee, pp. 941-950.

Zanziger, H. & Gartung, E. (2002). Performance of a geogrid reinforced railway embankment on piles. Proc. of the 7th Int. Conf. on Geosynthetics, Nice, pp. 381-386.

Microstructural Characterization of Siltstone and Sandstone Pore Space by X-Ray Microtomography

J.S. Fernandes, C.R. Appoloni, C.P. Fernandes

Abstract. Microstructural parameter assessment of reservoir rocks is extremely important for oil companies. In this regard, computerized X-ray microtomography (μ-CT) has proven to be an exceptionally useful methodology for the analysis of these rocks, since it provides significant microstructural parameters, such as porosity, permeability, and pore distribution. X-ray microtomography is a relatively novel non-destructive technique in the petroleum area which, besides enabling the reuse of already measured samples, also provides 2-D and 3-D images, as well as a 3-D mathematical model of the sample. This technique has the great advantage that it does not require sample preparation, allowing the reuse of the sample and also reducing the measurement time. A Skyscan model 1172 microtomograph was used for the acquisition of microtomographic data from the reservoir rocks. This work presents results of porosity and pore size distribution of six sandstones and two siltstones. Most of the analyzed samples from the Tibagi River basin had porosity below 10 %, except for the PG6 and PG8 samples, which presented 12 % and 13 %, respectively. Maximum pore radius ranged from 8 to 59 μm for sandstones and from 5 to 6 μm for siltstones.

Keywords: pore size distribution, porosity, sandstone, siltstone, X-ray microtomography.

1. Introduction

X-ray computerized microtomography (μ-CT) is a non-destructive methodology that measures density variations of the material. This technique uses a set of two-dimensional projections of an object to reconstruct its three-dimensional structure (Landis & Keane, 2010), using a mathematical algorithm (Cormack, 1963, 1964; Wellington and Vinegar, 1987; Flannery *et al.*, 1987). It requires the employment of adequate software for the treatment and analysis of images that enables the determination of important microstructure parameters, thus providing a better knowledge of the analyzed material. A schematic illustration of the acquisition, reconstruction, and generation of 3-D images and models is shown in Fig. 1 (Fernandes *et al.*, 2016).

The application of X-ray microtomography and image analysis enabled the determination of some microstructural parameters for analyzing five samples of sandstone and two of siltstone from various geological formations in Brazil, which are or may become reservoir rocks for some type of fluid. Additionally, a sample of Australian sandstone was also analyzed. Microcomputed tomography (μ-CT) provides two-dimensional (2-D) and three-dimensional (3-D) images, from which various characteristics, such as porosity, permeability, and phase size distribution (pores or solids) can be obtained. Furthermore, it permits the creation of a 3-D volume of the sample, allowing the visualization of the actual structure of the porous network present in the scanned volume and also for mathematical simulations. As X-ray beams pass through the object being scanned, the signal is attenuated by scattering and absorption. The basic equation for attenuation of a monoenergetic beam by a homogeneous material is given by the law of radiation absorption (Siegbahn, 1979):

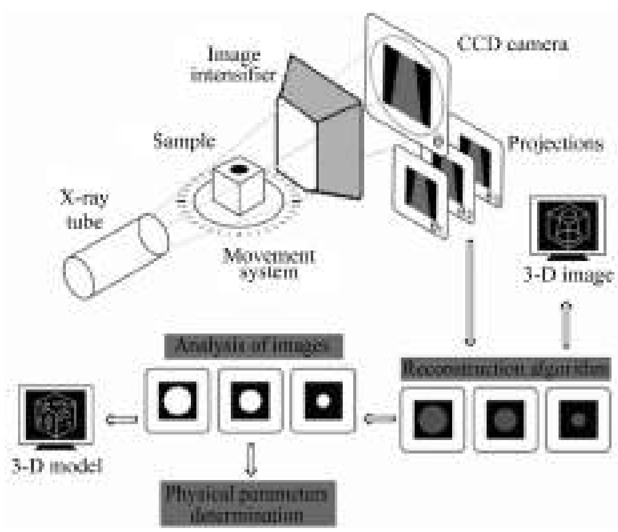

Figure 1 - Representation of the acquisition, reconstruction, and generation of three-dimensional images and models (Fernandes *et al.*, 2016).

Jaquiel S. Fernandes, Ph.D., Associate Professor, Instituto Federal Catarinense, Campus Videira, Videira, SC, Brazil. e-mail: jaquiel.fernandes@ifc.edu.br.
Carlos R. Appoloni, Ph.D., Senior Researcher, Laboratório de Física Nuclear Aplicada, Departamento de Física, Universidade Estadual de Londrina, Campus Universitário, Londrina, PR, Brazil. e-mail: appoloni@uel.br.
Celso P. Fernandes, Ph.D., Full Professor, Laboratório de Meios Porosos e Propriedades Termofísicas, Departamento de Engenharia Mecânica, Universidade Federal de Santa Catarina, Florianópolis, SC, Brazil. e-mail: celso@lmpt.ufsc.br.
Submitted on March 12, 2019; Final Acceptance on September 27, 2019; Discussion open until April 30, 2020.
DOI: 10.28927/SR.423281

$$I = I_0 e^{-\mu x} \quad (1)$$

where I_0 and I are the intensity of incident and transmitted X-ray beams, respectively, μ is the linear attenuation coefficient for the material being scanned, and x is the thickness of the sample through which the beam will traverse. As in most cases the scanned object is composed of a different number of materials and the energy of the X-ray beam tube is polyenergetic, this equation is rewritten as (Kalender, 2011):

$$I = \int_0^{E_{max}} I_0(E) \exp\left(-\int_0^x \mu(E,x)dx\right) \quad (2)$$

The petroleum industry commonly uses other methods to determine porosity and permeability, among which the most widespread is mercury intrusion porosimetry. The principle of this technique is based on the fact that mercury does not wet most substances and, therefore, will not penetrate pores by capillary action, unless it is forced to do so. Liquid mercury has a high surface tension and also exhibits a high contact angle against most solids. Entry into pore spaces requires applying pressure in inverse proportion to the pore diameter (Lowell & Shields, 1991; Webb & Orr, 1997; Johnson *et al.*, 1999). However, due to their destructive nature, this method often prevents the use of the samples for future analysis. Besides enabling future analyses of the sample already measured, the μ-CT also provides internal visualization of the sample through three-dimensional images (Fernandes *et al.*, 2016).

Through the most widespread methods such as mercury intrusion porosimetry, a sample may exhibit porosity lower than that it actually possesses, resulting therefore in a lower estimate for the rock storage capacity. This can be due to the lack of connection between the pores of the rock, which through the 3-D images obtained by microtomography, is verified and quantified.

The importance of not destroying the sample is justified when there is a need for future analysis, or by evolution of measurement techniques, or archiving of samples in their natural state.

The determination of the porosity of reservoir rocks through X-ray microtomography is quite widespread (Appoloni *et al.*, 2007; Flukiger and Bernard, 2009; Tsakiroglou *et al.*, 2009; Izgec *et al.*, 2010), however, for the rocks of the Tibagi River basin such analyzes are pioneering.

After being microphotographed, the samples were submitted to mercury porosimetry analyses to obtain the total porosity for comparison of the achieved microCT results.

2. Materials and Methods

2.1. Rocks analyzed

Except for the sample from the Tumblagooda Formation, which was collected from an outcrop of the Kalbarri National Park in Australia and provided by CENPES / PETROBRAS, all other rock specimens were taken from the Tibagi River Basin located in the central region of the Paraná State, Brazil. Table 1 shows a description summary of the rock samples analyzed, indicating their collection site, group, and formation. Such samples were selected to represent rocks of easy analysis (with larger pores and without clay) and rocks of difficult analysis (smaller pores and often with clay).

Figure 2 shows scale images of the analyzed samples with parallelepipedic shapes with diameters ranging from 5 to 8 mm and height from 10 to 20 mm to facilitate visualization of their dimensions.

Table 2 shows information about some of the most significant acquisition parameters. The number of projec-

Table 1 - Main characteristics of the samples analyzed.

Sample	Geological group	Formation	Collection site (city/state)	Description
107	São Bento	Botucatu	Faxinal-PR	Silicified sandstone.
108	Passa Dois	Rio do Rastro	Mauá da Serra-PR	Silty sandstone.
403	Passa Dois	Teresina	Sapopema-PR	Silty sandstone. Very thin lamination, orange gray.
MC16	Guatá	Rio Bonito	Figueira-PR	Siltstone.
PG6	Itararé	Rio do Sul	Curiúva-PR	Yellow siltstone with rounded embedded pebbles.
PG8	Paraná	Furnas	Tibagi-PR	Coarse sandstone with a low degree of granulometric selection and presence of muscovite.
PG19	Paraná	Furnas	Tibagi-PR	Coarse sandstone with a low degree of granulometric selection.
Tumblagooda	Dirk Hartog	Tumblagooda	Australia	Coarse sandstone.

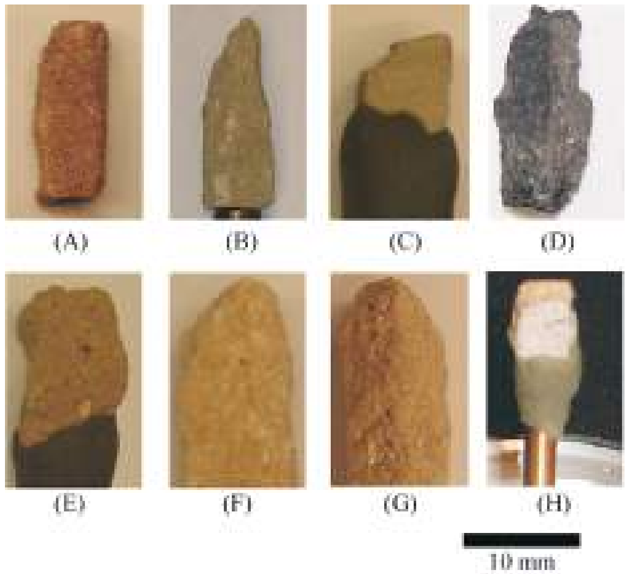

Figure 2 - Images of rock samples analyzed in this work. (A) Sandstone 107; (B) Sandstone 108; (C) Sandstone 403; (D) Siltstone MC16; (E) Siltstone PG6; (F) Sandstone PG8; (G) Sandstone PG19; (H) Sandstone Tumblagooda.

tions for each sample can be obtained dividing the total rotation by the angular step.

For the acquisition of the above data, a 1 mm thick aluminum filter was used, aiming to reduce beam hardening effects on the sample images (Ketcham and Carlson, 2001).

2.2. Equipment and software used

A microtochromograph Skyscan model 1172, installed at the Research and Development Center (CENPES) of PETROBRAS, Rio de Janeiro, RJ, Brazil, was used. The microtomographic images (projections) were reconstructed by the NRecon software (Skyscan, 2018). The porosities of the samples were obtained through the Imago software (Imago, 2018) developed in the Laboratory of Porous Media and Thermophysical Properties of Materials (LMPT) of the Department of Mechanical Engineering of the Federal University of Santa Catarina, Florianópolis, SC, Brazil, in association with the Brazilian software company ESSS (Engineering Simulation and Scientific Software). Other software used was the CTan (Skyscan, 2018), with which the 3-D reconstructions of the samples were performed. Figure 3 (Fernandes *et al.*, 2016) shows a photo of the Skyscan 1172 microtomograph installed at CENPES.

This microtomograph is provided with an X-ray tube with tungsten anode (W), 10 W maximum power, 20-100 kV voltage, and 0-250 μA current. A CCD camera of 10 Mp (megapixel) was used to detect the X-rays. The maximum spatial resolution obtained by this equipment is 1 μm for samples with 5 mm maximum diameter and 80 mm height (Fernandes *et al.*, 2016). To determine sample porosity for comparison purposes, a commercial porosimeter, PoreSizer model 9320 of Micromeritics was applied. However, it was not possible to perform the intrusion into one of the samples, since it had pores of very small dimensions, thus precluding the measurements.

Figure 3 - Microtomograph Skyscan 1172, 20 - 100 kV X-ray source, 10 W maximum power (Fernandes *et al.*, 2016).

Table 2 - Key parameters used for the μ-CT image acquisition.

Sample	Tension (kV)	Total rotation (°)	Angular step (°)	Spatial resolution (μm)	Exposure time for each projection (ms)	No. of frames	Total acquisition time
Sandstone 107	70	0 to 360	0.25	2.9	3245	5	6 h 28 min
Sandstone 108	70	0 to 180	0.25	2.9	9735	4	8 h 5 min
Sandstone 403	70	0 to 360	0.25	1.4	2655	3	3 h
Siltstone MC16	70	0 to 180	0.25	2.5	632	5	59 min
Siltstone PG6	70	0 to 180	0.25	2.9	2655	5	2 h 45 min
Sandstone PG8	80	0 to 180	0.25	5.0	1180	5	1 h 30 min
Sandstone PG19	70	0 to 180	0.25	1.4	8260	2	3 h 30 min
Sandstone Tumblagooda	50	0 to 180	0.5	2.9	4425	5	2 h 18 min

2.3. Image processing

Figure 4 shows two projections, 0° and 180°, acquired by the CCD chamber of sandstone sample 107. The projections were reconstructed by the NRecon software using a cone-beam reconstruction algorithm (Feldkamp *et al.*, 1984), resulting in 2-D grayscale images of a sandstone and a siltstone, as shown in Figs. 5a and 6a, respectively. After generation, the 2-D images are analyzed by the Imago software. In this step a region of interest (ROI) is defined and binarization (segmentation) (Imago, 2002) is performed, transforming the grayscale image into black and white, where black is the solid phase, and white, the porous phase, as shown in Figs. 5b and 6b (Fernandes *et al.*, 2016).

From the projection of 2-D images, it was reconstructed 3-D images using the CTan software, to reconstruct the actual volume of the rocks analyzed. As the 3-D reconstruction process is very limited and requires a large computational capacity, it was necessary to investigate the representative elementary volume (REV) of these samples, which must be large enough to represent the characteristics of the sample and the smallest possible when compared to its total volume. This scaling was analyzed, and it was concluded that the REV should be 1400 × 1400 × 1400 μm (Fernandes *et al.*, 2012). For a better view of the internal structure of sandstone 107, a subvolume of 1500 × 1001 × 300 μm was reconstructed, as shown in Fig. 7.

Figure 8 (Fernandes *et al.*, 2012) shows the 3-D image of the PG8 sandstone sample: in yellow, the porous networks with relatively large diameters and few isolated pores; in gray, the solid phase.

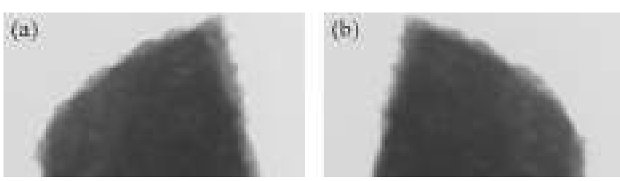

Figure 4 - Projections of sandstone107; (a) image acquired at the 0° position; (b) image acquired at the 180° position.

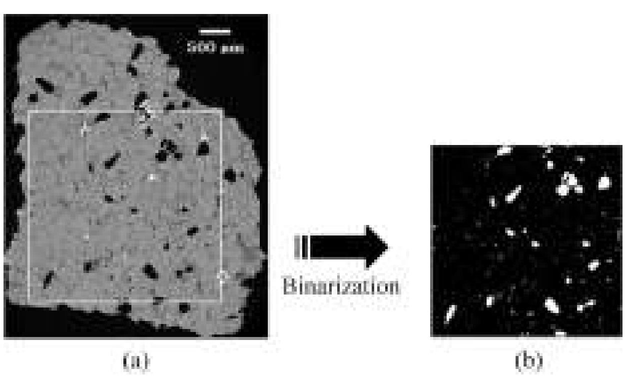

Figure 5 - Images of sandstone sample 107 reconstructed by the NRecon software; (a) 2-D grayscale image; (b) 2-D binarized image, where black represents the solid phase and white, the porous phase.

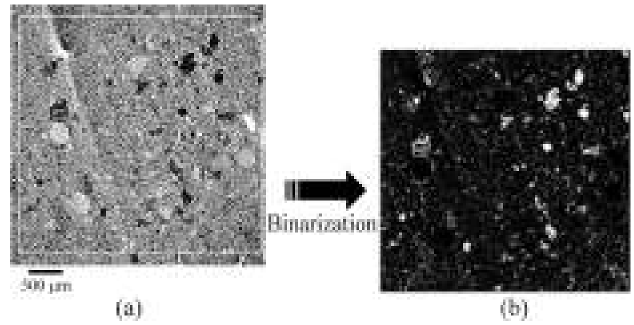

Figure 6 - Images of siltstone PG6 reconstructed by the NRecon software; (a) 2-D grayscale image; (b) 2-D binarized image, where black represents the solid phase and white, the porous phase.

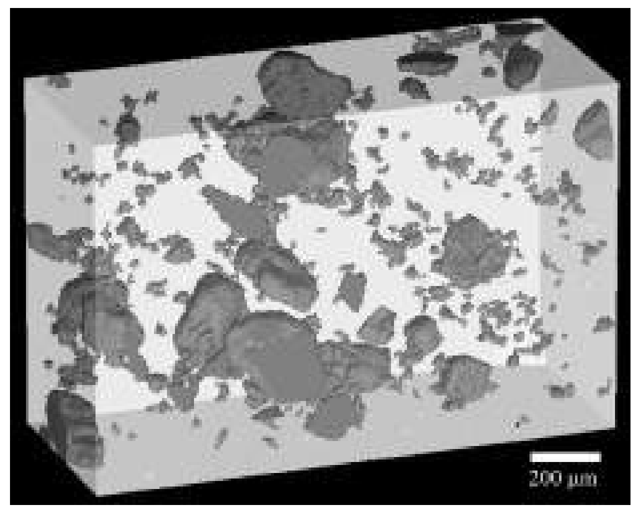

Figure 7 - 3-D image reconstructed from the sample 107 (1500 × 1001 × 300 μm): dark gray represents the porous phase and light gray, the solid phase.

3. Results

Figure 7 clearly shows that the pores of sandstone sample 107 are isolated, having no connection among them, thereby preventing the flow of any fluid through the rock, thus providing virtually no permeability. This same figure reveals that there are relatively large, but few pores, reflecting the low porosity of the sample. The porosity (ϕ) for this subvolume is 5.4 ± 0.2 %, and even with a relatively small subvolume, this value is very close to the mean value of the porosity determined from all analyzed 2-D sections ($\phi = 6.1 \pm 0.2$ %).

Table 3 shows the results of the average porosity of all 2-D sections, the porosity of the 3-D images based on the representative elementary volume, and the porosity obtained with the mercury porosimetry for all samples analyzed. In addition, the pore radius with the highest frequency in the pore size distribution histogram is also presented.

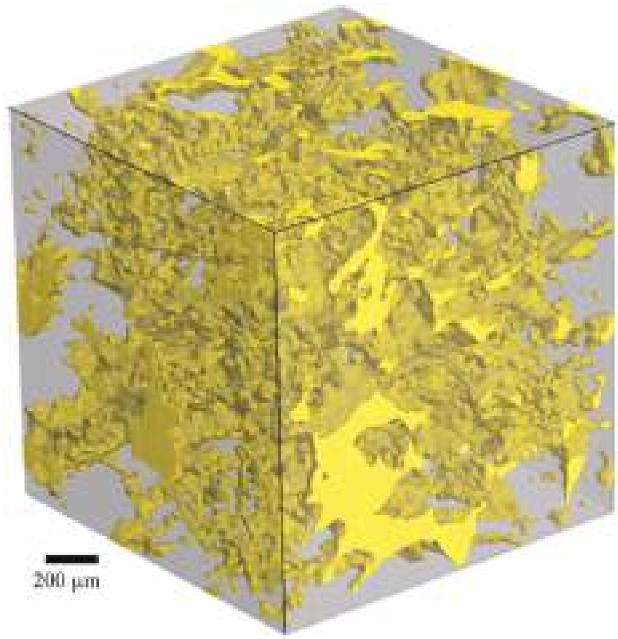

Figure 8 - 3-D image reconstructed from the sample PG8 (1400 × 1400 × 1400 μm): gray represents the solid phase, and yellow, the porous phase (Fernandes *et al.*, 2012).

The results of Table 3 show that the porosity found by X-ray microtomography is systematically lower than that achieved by mercury porosimetry, except for sample 107. Regarding this sample, it is conceivable that mercury did not completely fill its pores. In fact, the outcomes of the microtomographic image analysis reveal that the pores of sample 107 are isolated. In this connection, these findings may explain the impossibility of mercury infiltration into some of its pores, thus impairing a good performance of this methodology to determine the absolute porosity of the sample.

For the other samples, the porosity obtained by the μ-CT was smaller. Therefore, it was concluded that there are pores smaller than the resolution used by the microtomograph. Since the porosimeter can measure pores up to 6 nm in diameter, the microtomograph did not detect a portion of the pores with smaller diameters and indicated lower porosity values for those samples.

The porosity value for all 2-D images compared to the porosity of the 3-D images obtained using the representative elementary volume can also be observed from Table 3. These values are statistically the same for most of the samples. This demonstrates the great advantage in determining REV for the generation of representative 3-D images.

Figures 9 to 16 show the pore size distributions for the analyzed samples. In these figures, it can also be observed that the histogram for sandstone 107 presents two distributions: one around the pores with a radius of 5.8 μm and another for pores with a radius of 58.7 μm, and that 95 % of the pore of this sample are comprised between 2.9 μm and 108 μm.

For sandstone 108, approximately 92 % of the porous phase refers to pores with radii between 2.9 and 20.6 μm and there is a distribution around a value of 11.7 μm.

From the sandstone 403 histogram, it can be observed that approximately 97 % of the porous phase refers to pores with radii between 3.9 and 11.9 μm. The frequency of 37.5 % for pores with a radius of 3.9 μm (spatial resolution used) is considered very high, indicating that there are pores with smaller radii.

The histogram for siltstone MC16 reveals that nearly 95 % of the porous phase refers to pores with radii between 2.5 and 10.2 μm. Likewise, for sample 403, the 25 % frequency for pores with a radius of 2.5 μm (spatial resolution used) is considered very high, revealing that there are pores with smaller radii. Notwithstanding, when analyzing the 2-D and 3-D images of this sample, we observed the pres-

Table 3 - Summary of the microstructural properties of the analyzed samples.

Sample	ϕ^1 sections 2-D (%)	ϕ^2 image 3-D (%)	ϕ porosimetry Hg (%)	Pore[3] radius (μm)
Sandstone107	6.1 ± 0.2	5.4 ± 0.2	3.1	5.8-58.7
Sandstone 108	4.2 ± 0.1	4.0 ± 0.1	-	11.7
Sandstone 403	9.3 ± 0.2	7.6 ± 0.2	12.9	7.9
Siltstone MC16	7.0 ± 0.2	7.0 ± 0.2	13.4	5.1
Siltstone PG6	12.0 ± 0.3	11.5 ± 0.2	18.5	2.4-5.9
Sandstone PG8	13.0 ± 0.2	12.6 ± 0.2	15.8	20
Sandstone PG19	4.9 ± 0.1	5.1 ± 0.1	8.4	10
Sandstone Tumblagooda	15.3 ± 0.5	13.4 ± 0.4	-	11.7-23.5

[1]Average total porosity with 95 % confidence.
[2]REV porosity with 95 % confidence.
[3]Most frequent value.

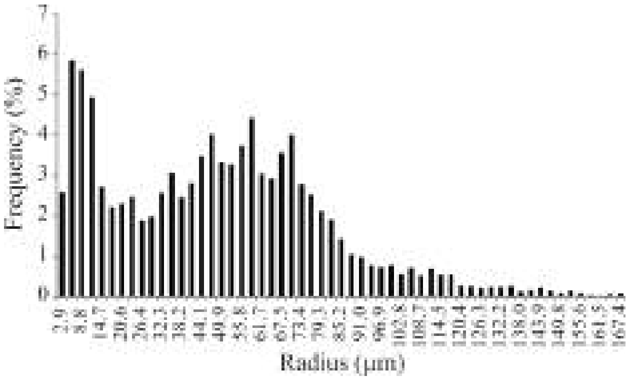

Figure 9 - Distribution of pore sizes for sandstone 107.

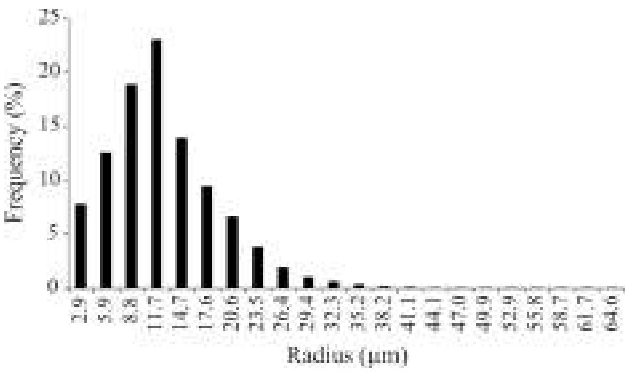

Figure 10 - Distribution of pore sizes for sandstone 108.

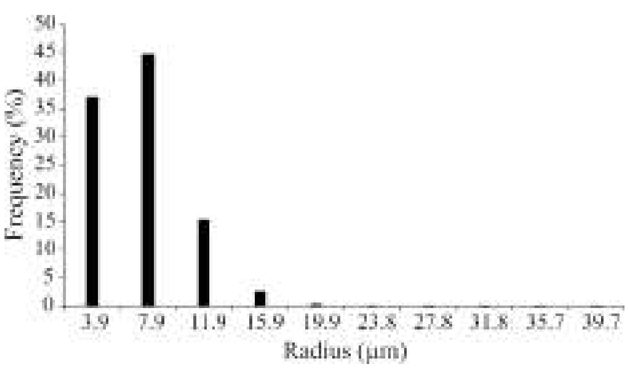

Figure 11 - Average pore size distribution for sandstone 403.

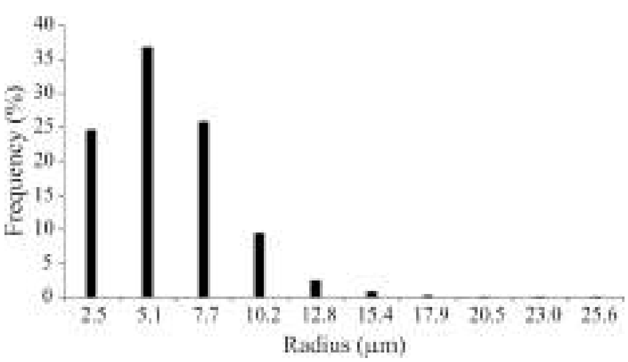

Figure 12 - Average pore size distribution for siltstone MC16.

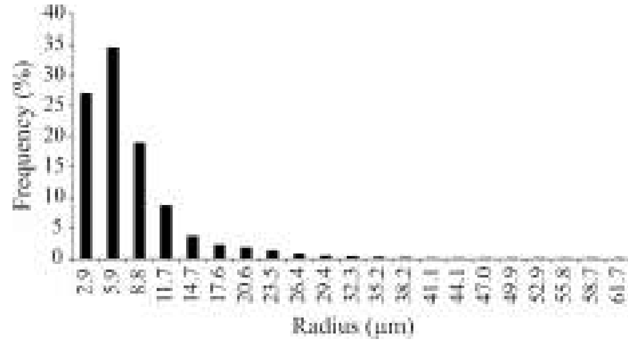

Figure 13 - Average pore size distribution for siltstone PG6.

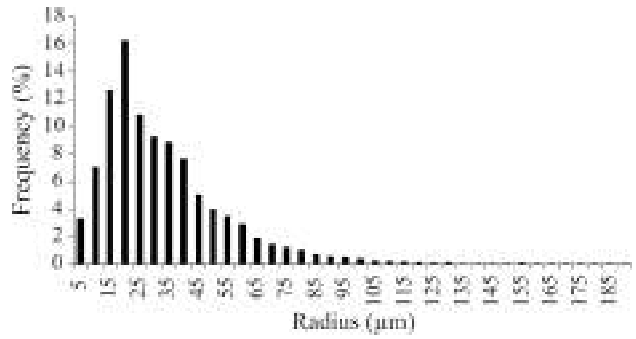

Figure 14 - Average pore size distribution for sandstone PG8.

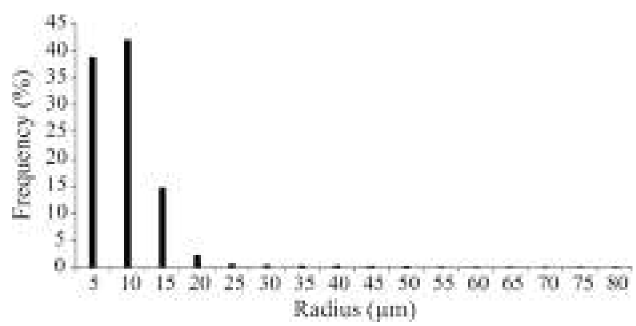

Figure 15 - Average pore size distribution for sandstone PG19.

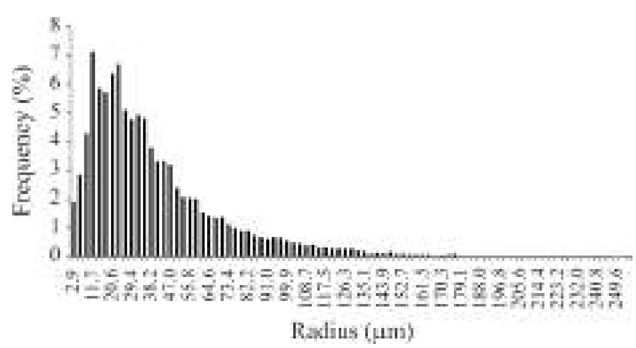

Figure 16 - Average pore size distribution for sandstone Tumblagooda.

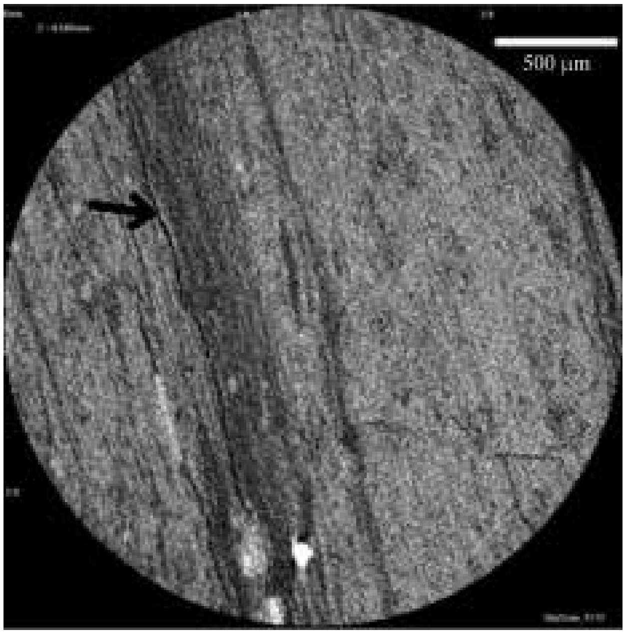

Figure 17 - 2-D image of siltstone MC16 sample. The arrow indicates one of the fissures mentioned in the text.

ence of cracks with a diameter of approximately 5-10 μm caused by the laminated part of the sample. Those fissures can be seen in Fig. 17 and are repeatedly found throughout the sample, justifying, in part, the high frequency at pores with smaller radii.

The histogram of siltstone PG6 shows that approximately 90 % of the porous phase refers to pores with radii between 2.9 and 11.7 μm. As for samples 403 and MC16, the 27 % frequency for pores with a radius of 2.9 μm (spatial resolution used) is considered very high, providing indications that there are pores with smaller radii.

Regarding sandstone PG8, it can be observed that approximately 91 % of the porous phase refers to pores with radii between 5 and 60 μm. The highest frequency refers to pores with radii equal to 20 μm.

Sandstone PG19 presented approximately 95 % of the porous phase with pores with radii between 5 and 15 μm. The 38 % frequency for pores with a radius of 5 μm (spatial resolution used) is considered very high, indicating that there are pores with smaller radii.

From the histogram of the Tumblagooda sandstone, it can be observed that approximately 90 % of the porous phase refers to pores with radii between 2.9 and 76.4 μm. This sandstone has a very heterogeneous distribution and does not present pores with high frequencies.

4. Conclusions

We observed that most of the analyzed samples from the Tibagi River basin had porosity below 10 %, except for the PG6 and PG8 samples, which presented 12 % and 13 %, respectively. If we consider the size of the Tibagi River basin, the number of samples analyzed is relatively small. However, since all samples had a porosity value about 10 %, we can ascertain that the sandstones and siltstones of the basin have low porosity.

The highest average pore radius frequency of these samples was about 10 μm. However, sample 107 presented mean radius between 5.8 and 58.7 μm. The largest pores are easily identified in Fig. 7. Nevertheless, as previously mentioned, apparently, they are not connected due to the silicification process that precludes the withdrawal of any fluid from the interior of the rock.

X-ray microtomography technique provides a detailed characterization of sample geometry, such as porosity and pore size distribution. The pore interconnectivity can be visualized and characterized by analyzing the 3-D images. Several software tools for image analysis allow scanning the internal structure of samples and enable visualization of pore distribution, thus providing data to determine whether they are connected or isolated and measuring the amount of open and closed porosity.

Acknowledgments

The authors of this paper are grateful for the support provided by CAPES, CNPq, CENPES / PETROBRAS, Federal University of Santa Catarina and State University of Londrina.

References

Appoloni, C.R.; Fernandes, C.P. & Rodrigues, C.R.O. (2007). X-ray microtomography of a sandstone reservoir rock. Nuclear Instruments and Methods in Physics Research, 580(1):629-632.

Cormack, A.M. (1963). Representation of a function by its line integrals, with some radiological applications, Part I. J. Appl. Phys., 34(9):2722-2727.

Cormack, A.M. (1964). Representation of a function by its line integrals, with some radiological applications, Part II. J. Appl. Phys., 35(10):2908-2913.

Feldkamp, L.A.; Davis, L.C. & Kress, J.W. (1984). Practical cone-beam algorithm. J. Opt. Soc. Am. A. 1(6):612-619.

Fernandes, J.S.; Appoloni, C.R. & Fernandes, P.C. (2012). Determination of the representative elementary volume for the study of sandstones and siltstones by X-ray microtomography. Materials Research, 15(4):662-670.

Fernandes, J.S.; Appoloni, C.R. & Fernandes, P.C. (2016). Accuracy evaluation of an X-ray microtomography system. Micron, 85(1):34-38.

Flannery, B.P.; Deckman, H.W.; Roberge, W.G. & D'Amico, K.L. (1987). Threedimensional X-ray microtomography. Science, 237(4821):1439-1444.

Flukiger, F. & Bernard, D. (2009). A new numerical model for pore scale dissolution of calcite due to CO_2 satured water flow in 3D realistic geometry: principles and first results. Chemical Geology, 265(1-2):171-180.

IMAGO. (2002). Manual do Usuário, Versão 2.1.4., ESSS - Engineering Simulation and Scientific Software Ltda. Copyright ©, 88 p.

IMAGO. (2018). Images analysis software. https://www.esss.com.br/index.php?pg=viewprojeto&idProject = 9 (accessed in November 2018).

Izgec, O.; Zhu, D. & Hill, A.D. (2010). Numerical and experimental investigation of acid wormholing during acidization of vuggy carbonate rocks. Journal of Petroleum Science and Engineering, 74(1-2):51-66.

Johnson, R.; Abrams, L. & Maynard, R.B. (1999). Use of mercury porosimetry to characterize pore structure and model end-use properties of coated papers. Tappi Journal, 82(1):239-251.

Kalender, W.A. (2011). Computed Tomography - Fundamentals, System Technology, Image Quality, Applications. 3rd ed., Publicis Corporate Publishing, Germany, 372 p.

Ketcham, R.A. & Carlson, W.D. (2001). Acquisition, optimization and interpretation of X-ray computed tomographic imagery: applications to the geosciences. Computers & Geosciences, 27(4):381-400.

Landis, E.N. & Keane, D.T. (2010). X-ray microtomography. Materials Characterization, 61(12):1305-1316.

Lowell, S. & Shields, J.E. (1991). Powder Surface Area and Porosimetry. 2nd ed., Chapman and Hall, London, 252 p.

Siegbahn, K. (1979). Alpha-, Beta- And Gamma-Ray Spectroscopy, North-Holland Publishing Company. Amsterdam, pp. 37-76.

Skyscan. (2018). Two-dimensional and three-dimensional reconstruction software. http://www.skyscan.be/products/downloads.htm (accessed in November 2018).

Tsakiroglou, C.D.; Loannidis, M.; Amirtharaj, E. & Vizika, O. (2009). A new approach for the characterization of the pore structure of dual porosity rocks. Chemical Engineering Science, 64(5):847-859.

Webb, P.A. & Orr, C. (1997). Analytical Methods in Fine Particle Technology. Ed. Micromeritics Instrument Corporation, Norcross, GA, 301 p.

Wellington, S.L. & Vinegar, H.J. (1987). X-ray computed tomography. J. Pet. Technol. 39(8):885-898.

An Alternative Approach to the Executive Control of Root Piles

F.F. Monteiro, A.S. Moura, M.F.P. Aguiar

Abstract. A root pile is an injected type of pile (cast-in-place with pressure, with very distinct construction aspects from the known micropile type). Those piles are installed by using distinct injection pressures up to 500 kPa during the mortar shaft formation. The executive control of root piles is usually carried out by static load tests, requiring a costly and time-consuming assessment method. To study root pile performance, static load tests were performed on eight monitored piles with diameters of 350 and 410 mm. This paper proposes an alternative methodology for confirming the root pile performance based on the use of a speedometer attached to the rotatory head of the drill rig. The methodology consists in monitoring variables that are related to the pile bearing capacity, thus, proposing empirical equations with simple and applicable use to estimate root pile bearing capacity during installation. The results obtained by the proposed equations were in agreement with the values obtained from static load tests for the tested piles. Therefore, the results show that the methodology proposed presents itself as a viable alternative for the executive control of root piles.

Keywords: foundations, micropiles, piles, root piles, static load test.

1. Introduction

The recent increase in the size of construction works has boosted advances in foundation engineering. Pile foundations are one of the most important foundation techniques and are widely used in foundation engineering (Zhou *et al.*, 2018). With the technological evolution of equipment used in the construction of foundations, as well as the development of new types of foundations, the use of bored piles has become widely spread in great urban centers of Brazil. In this context, the growth of root piles as a foundation solution for construction works is notorious. The root pile is an injected type of pile (cast-in-place with pressure, with very distinct construction aspects from the known micro-pile type). Those piles are performed by using distinct injection pressures up to 500 kPa during the mortar shaft formation.

The performance assessment of deep foundations varies according to the pile type. In the case of root piles, the performance assessment is usually performed after pile execution, by carrying out static load tests. The static load test to failure is by far the most reliable method to determine both the bearing capacity and the load–settlement relationship of a pile. Consequently, the most significant progresses in the field of pile design have been obtained just by collecting and interpreting data from load tests (Russo, 2012). Although the static load test is easy to perform and interpret, it is expensive, slow to implement, and cannot be used systematically because it can destroy the micro-pile (Calvente *et al.*, 2017). Therefore, a shortage of alternatives that assist in performance assessment of root piles is identified. In order to overcome these disadvantages, this paper proposes an alternative methodology for confirming root pile erformance based on the use of a speedometer attached to the rotatory head of the drill rig. The methodology consists in monitoring variables that are related to the pile bearing capacity, thus, proposing empirical equations that are simple and can be used for estimating root pile bearing capacity during their installation. Then the methodology is tested and calibrated on real-scale root piles at several experimental sites where five root piles with lengths ranging from 7.7 to 26 m were installed. Finally, to validate the methodology, the results of the proposed equations are compared with static load tests carried out on three real-scale root piles. Many researchers have investigated root pile performance, and several significant conclusions have been made (Cadden *et al.*, 2004; Huang *et al.*, 2007; Moura *et al.*, 2015; Lima & Moura, 2016; Melchior Filho, 2018). Similar researches were carried out regarding different types of piles (Lin *et al.*, 2004; Herrera *et al.*, 2009; Basu *et al.*, 2010; Silva *et al.*, 2012; Silva *et al.*, 2014).

This research aims to propose a methodology for root pile installation control. For that purpose, three equations were proposed to estimate the pile bearing capacity (Q_{ult}), which allows to control the root pile execution process. The pile bearing capacity (Q_{ult}) is necessary to carry out perfor-

Fernando Feitosa Monteiro, Ph.D. Student, Departamento de Engenharia Civil e Ambiental, Campus Darcy Ribeiro, Universidade de Brasília, Brasília, DF, Brazil. e-mail: engffmonteiro@gmail.com.
Alfran Sampaio Moura, D.Sc., Associate Professor, Centro de Tecnologia, Campus do Pici, Universidade Federal do Ceará, Fortaleza, CE, Brazil. e-mail: alfransampaio@ufc.br.
Marcos Fábio Porto de Aguiar, D.Sc., Associate Professor, Instituto Federal de Educação, Ciência e Tecnologia do Ceará, Fortaleza, CE, Brazil. e-mail: marcosporto@ifce.edu.br.
Submitted on March 17, 2019; Final Acceptance on August 1, 2019; Discussion open until April 30, 2020.
DOI: 10.28927/SR.423289

mance control of the execution process. Thus, it is necessary to use an expression, or more than one that allow, Q_{ult} estimation, in order to verify the minimum pile length during pile installation. In the specific case of the equations proposed in this research, the procedure is performed with measurements of N_{SPT}, pile geometry, drill bit advance velocity and drill bit linear velocity.

2. Root Pile Installation Process

The root pile installation process is presented in Fig. 1. A rotary drilling technique was used to install the test root piles. First, the drill casing was attached to the rotary head, which rotates to advance the drilling into the soil or rock (Fig. 1a). After that, a drilling rod (inner rod) was attached to the same rotary head to perform the drilling inside the drill casing. The drilling rod advanced ahead of the tip of the casing. High pressure water jets were used to clear the cuttings as drilling advanced (Fig. 1b). At the final depth, the base was cleaned using high pressure water jets until no soil or rock cuttings were observed. After reaching the desired depth, the inner rod was removed, whereas the outer steel casing was left permanently in the ground. A rebar was then installed into the drilling hole (Fig. 1c). The casing was then filled with grout (0.6 water–cement ratio) until grout was flowing through the annulus between the drilled hole and the outer casing (Fig. 1d). A plug is installed at the drill casing upper end and pressure (compressed air) is applied while the drill case is removed. The diameter of the drilling bit used to drill the test piles is equal to 0.31 m (Fig. 2).

3. Proposed Methodology

The methodology proposed is based on the use of a digital speedometer to monitor variables during pile installation. First, the monitoring equipment is set up on the rotary head of the drill rig as shown in Fig. 3.

The drill rotator diameter is digitally inserted in the speedometer, in such a way that the sensor records each complete lap performed by the drill rotor (magnet). This procedure allows recording the linear distance traveled by the drill rotor for a determinate period of time. The drilling rod used to drill the last meter length of the pile was then, marked with sections of 10, 20 and 20 cm as seen in Fig. 4.

The elapsed time to drill the length between 2 marked sections was recorded in order to determine the advance velocity (V_a). The other measured variable is the drill rotator linear velocity (V_b), which is measured for the same section. The linear distance traveled by the drill rotor between 2 marked sections is divided by the circumferential length of the drill rotor, thus, obtaining the number of rotations performed by the drill rotor during the drilling of the mentioned section. From the elapsed time during the drilling of this section and the number of rotations performed by the drill rotator, it is possible to determine the number of rotations per minute, that is, the frequency (f) of the drill rotor. The drill rotor angular velocity (ω_r) is then, obtained from the following relation:

$$\omega_r = 2\pi f \quad (1)$$

Since the drill rotor is connected by the drilling rod to the drill bit at the bottom of drilling hole while the drilling is performed (Fig. 4), it can be assumed that the drill bit angular velocity (ω_b) is equal to the drill rotor angular velocity (ω_r).

$$\omega_r = \omega_b \quad (2)$$

The drill bit linear velocity (V_b) is then determined from the following equation:

$$V_b = \omega_b R_b \quad (3)$$

Figure 1 - (a) Drill case drilling, (b) drill rod drilling, (c) reinforcement bar installation, (d) grouting.

Figure 2 - Drill bit.

Figure 3 - Monitoring equipment. (a) Magnet, (b) Sensor, (c) speedometer.

Figure 4 - Drilling rod marked sections.

where: V_b is the drill bit linear velocity; ω_b is the drill bit angular velocity and R_b is the drill bit radius.

Then, the drill bit linear velocity and the drill bit advance velocity are associated with the pile bearing capacity. The formulation of equations for executive control of the monitored test piles was initiated by choosing variables that would be used in the equation and considering that the formulation is intended to contribute to the development of an empirical approach with simple application in the executive control of root piles. Two variables obtained during monitoring were selected for correlating to pile bearing capacity: the drill bit linear velocity (V_b) and the drill bit advance velocity (V_a), the first one being associated to the skin friction resistance (Q_s) and the second to the tip resistance (Q_{tip}). In addition to the drill bit linear velocity (V_b) and drill bit advance velocity (V_a), the following variables were considered: tip resistance index ($N_{SPT,\ tip}$), average shaft resistance index ($N_{SPT,\ shaft}$), pile diameter (D), pile length (L), pile perimeter (U) and tip cross sectional area (A_p). The average shaft resistance index ($N_{SPT,\ shaft}$) is determined from the average N_{SPT} values along the pile shaft indicated in the standard penetration test results. The tip resistance index ($N_{SPT,\ tip}$) is determined by the average of the N_{SPT} values at the pile final depth indicated in the standard penetration test results.

Static load tests were carried out to determine the bearing capacity of the test piles. On most occasions, a distinct plunging ultimate load (Q_u) was not obtained in the test, and therefore, the Van der Veen extrapolation method was applied to obtain the ultimate load of the test piles (Van der Veen, 1953). In order to correlate the monitored variables and the pile ultimate load, it was necessary to estimate the load distribution along the pile shaft and tip. The Brazilian standard (ABNT, 2010) states that for bored piles, the load distribution must occur as 80 % to the pile shaft and 20 % to the pile tip. Since the static load tests were not instrumented, three distinct scenarios were proposed. In the first scenario, the load distribution would occur with 80 % along the pile shaft and 20 % at the pile tip. In the second scenario, the load distribution would occur with 90 % along the pile shaft and 10 % at the tip. Finally, in the third scenario, the load distribution would only occur along the pile shaft, that is, with 100 % along the shaft. In this way, the mentioned scenarios are presented as alternatives for use in practical cases. The definition of the expression to be adopted in real situations will depend on the user's own judgment, who may even apply the three equations to simulate possible real case scenarios.

For the development of the proposed equations in this paper, a multiple linear regression analysis method was used to explain the relationship between a dependent variable and several independent variables, so that:

$$Y = a_0 + a_1 X_1 + a_2 X_2 + \ldots + a_n X_n \quad (4)$$

where Y is the dependent variable (in this case, Q_{tip} or Q_s); X_1, X_2, ..., X_n are the independent variables; a_1, a_2, ..., a_n are the coefficients of the respective independent variables, known as regression coefficients and a_0 is a constant whose purpose is to represent the portion of Y that was not explained by the independent variables. By this approach and using the least squares method, the desired expression is adjusted based on the smallest deviation between the observed real values of the variable and the estimated value. Thus, considering a multiple linear function with three variables, the following system must be solved:

$$\sum Y = na_0 + a_1 \sum X_1 + a_2 \sum X_2 + a_3 \sum X_3 \tag{5}$$

$$\sum YX_1 = a_0 \sum X_1 + a_1 \sum X_1^2 + a_2 \sum X_1 X_2 + a_3 \sum X_1 X_3 \tag{6}$$

$$\sum YX_2 = a_0 \sum X_2 + a_1 \sum X_2 X_1 + a_2 \sum X_2^2 + a_3 \sum X_2 X_3 \tag{7}$$

$$\sum YX_3 = a_0 \sum X_3 + a_1 \sum X_3 X_1 + a_2 \sum X_3 X_2 + a_3 \sum X_3^2 \tag{8}$$

Using this system, the values of a_0, a_1, a_2 and a_3 are calculated using the current data of Y, X_1, X_2, X_3. As the relations between the variables are not linear in methods of bearing capacity estimation, it was necessary to use a logarithmic transformation of variables to create an exponential model. The following equations illustrate the procedure:

$$Y = a_0 \times X_1^{a_1} \times X_2^{a_2} \times \ldots \times X_n^{a_n} \tag{9}$$

$$\ln(Y) = \ln(a_0) + a_1 \times \ln(X_1) + a_2 \times \ln(X_2) + \ldots + a_n \times \ln(X_n) \tag{10}$$

Therefore, considering the new variables as ln (X_i) and solving the system of Eqs. 5 to 8, it is possible to use the logarithmic transformation of variables, then, apply the multiple linear regression model and obtain the values of the coefficients a_i.

Hence,

$$Q_u = Q_s + Q_{tip} \tag{11}$$

$$Q_{tip} = a_0' A_p^{a_1} V_a^{a_2} N_{SPT,tip}^{a_3} \tag{12}$$

$$Q_s = a_0'' V_b^{a_4} (UL)^{a_5} \overline{N}_{SPT,shaft}^{a_6} \tag{13}$$

where A_p is the tip cross sectional area; V_a drill bit advance velocity; ($N_{SPT,\,tip}$) is the tip resistance index; V_b is the drill bit linear velocity; U is the pile perimeter, L is the pile length; ($N_{SPT,\,shaft}$) is the average shaft resistance index; a_1, a_2, a_3, a_4, a_5, a_6 are linear regression coefficients; a_0' and a_0'' are regression constants.

4. Soil Profile and Site Description

Five construction sites were selected for this research; in all those sites, root pile foundations were built. In Fig. 5, the location of the selected sites for the development of the research is presented. The construction sites are located in the city of Fortaleza, Brazil.

SPTs and rock core borings were performed at five construction sites before installation of the root piles. In site 1, the groundwater level was found at a depth of 3 m. From the ground surface to 5 m, a clayey silt layer was encoun-

Figure 5 - Construction sites location.

tered, with N values ranging between 16 and 60. Below this layer, a sandstone layer with RQD varying from 43 to 54 % was encountered to a depth of 15 m; the N values, ranged from 58 to 60. In site 2, from the ground surface to 11 m, a clayey sand layer was encountered, with N values ranging between 3 and 60. Below this layer, a silty clay layer was encountered to a depth of 16 m; the N values ranged from 29 to 60. The bedrock is 16 m below the ground surface. The groundwater level was found at a depth of 1.2 m.

In site 3, the first layer with a total thickness of 2 m consists of silty sand soil, with N values ranging between 12 and 25. Below this layer, a silty clay layer was encountered to a depth of 11 m; the N values ranged from 38 to 60. Finally, a magmatic gneiss layer with RQD varying from 54 to 100 % was found to a depth of 26 m; the N values along this layer are equal to 60. The groundwater level was at a depth of 2 m.

In site 4, the groundwater level was found at a depth of 6.7-7.4 m. From the ground surface to 4 m, a silty sand layer was encountered with N values ranging between 2 and 4. Below this layer, a clayey sand layer was encountered to a depth of 12 m; the N values, ranged from 4 to 9. Finally, a sandy clay layer with N values varying from 9 to 42 was encountered to a depth of 22 m.

In site 5, the first layer with a total thickness of 11 m consists of silty sand soil, with N values ranging between 6 and 60. Finally, a clayey silt layer with N values varying from 7 to 59 was encountered to a depth of 19 m. The groundwater level was at a depth of 3.85 - 4 m.

Figures 6, 7, 8, 9, 10 and 11 present the geometry of the test root piles and the subsurface profile at the construction site locations.

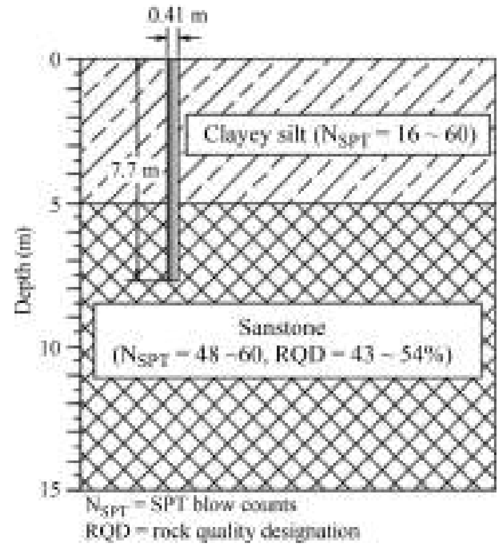

Figure 6 - Subsurface profile and test piles 1 and 2.

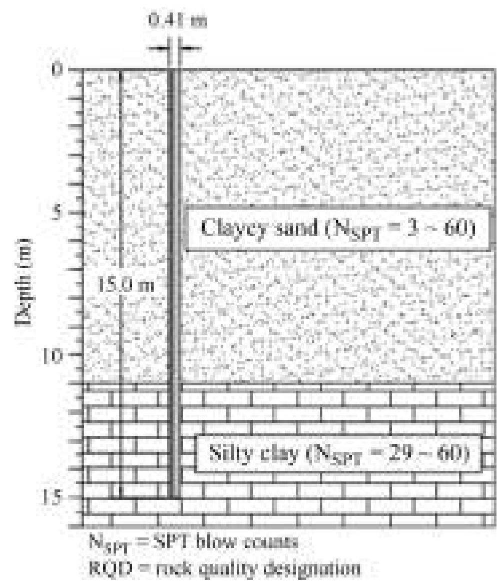

Figure 7 - Subsurface profile and test piles 3 and 4.

5. Load-Displacement Test Results and Procedures

Static load tests were performed on the test piles 10 days after installation. The vertical settlement of the pile head was measured by four dial gauges (two on each side of the pile) attached to two reference beams. The load was applied in increments of 20 % of the final test load and maintained until the settlement rate from two consecutive settlement readings at the pile head was less than 5 %. After reaching the maximum load, the pile was unloaded in five load stages, with the exception of pile 6. In Table 1, the geometry of the tested piles, the maximum applied load, injection pressure and maximum recorded displacement are summarized. Figs. 12 and 13 show the applied load at the pile head *vs.* pile head settlement curves obtained from the static load tests.

The curves show that the tests on piles 6 and 8 fully mobilized the shaft friction, showing a sudden increase in the settlement at about the maximum applied load. The other tests were executed on piles with the same diameter (d = 0.41 m) but with different lengths: the piles are far from failure and exhibit similar behavior mainly governed by the shaft friction along the shaft. On most tests, a distinct plunging ultimate load (Q_u) was not obtained, and therefore, the Van der Veen extrapolation method was applied to obtain the ultimate load of the test piles. The extrapolated ultimate load (Q_u) values are presented in Table 2.

6. Monitoring Results

The monitoring process was performed during test pile installation. The data acquisition system (speedometer) recorded the drill bit linear velocity (V_b) and drill bit advance velocity (V_a) during the drilling of the marked sections on the drill rod. In Table 3, the monitoring results are presented. However, due to unforeseen events that occurred during field monitoring, it was necessary to perform changes in the lengths of the marked sections in some test piles.

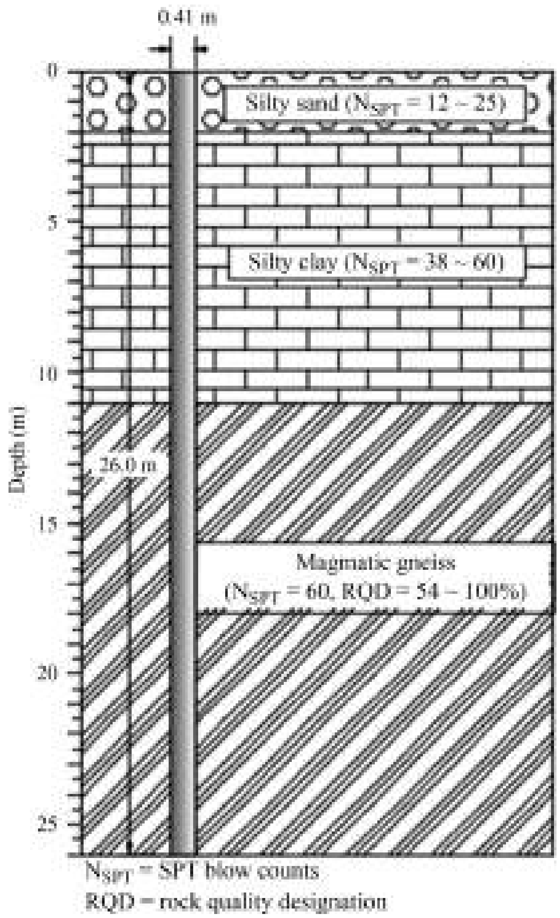

Figure 8 - Subsurface profile and test pile 5.

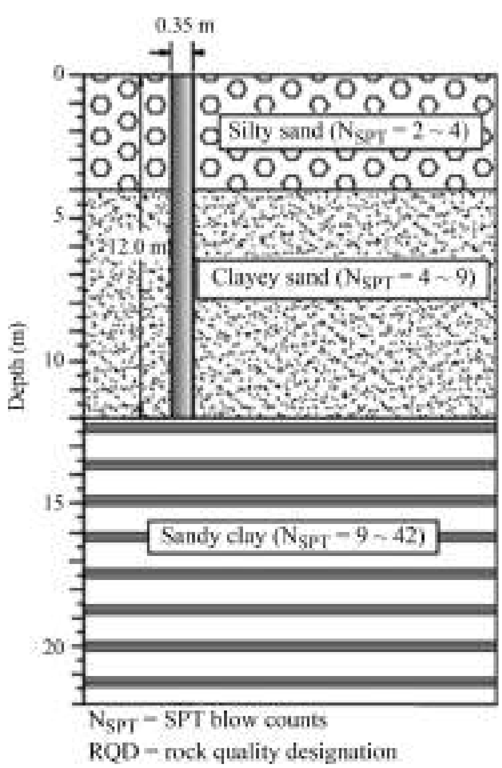

Figure 9 - Subsurface profile and test pile 6.

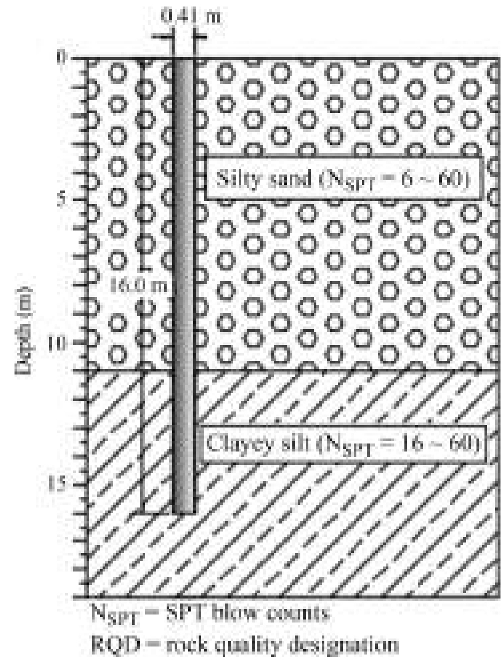

Figure 10 - Subsurface profile and test pile 7.

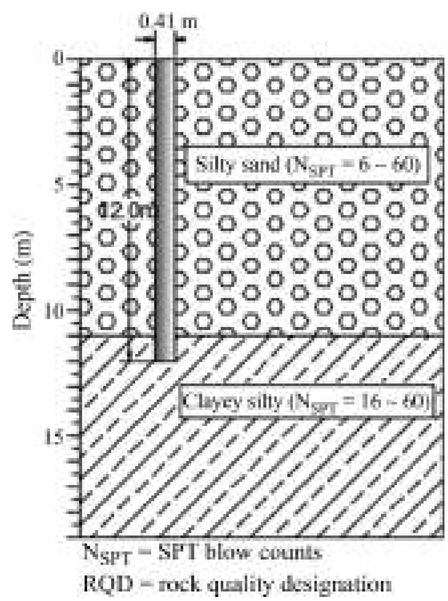

Figure 11 - Subsurface profile and test pile 8.

The penetration resistance index value (N_{SPT}) was limited to 60, in depths that presented high *N* values, in which the pile execution continued without additional difficulties.

For piles 1 and 2, executed in similar stratigraphic profiles (site 1), higher excavation times are observed when compared to the other piles, which is attributed to the pile tip being seated on a rock profile. Thus, for these piles, lower advance velocities are verified. However, the drill rotor frequency, which is directly associated with the drill bit

Table 1 - Summary of load test data.

Site	Test pile	*L* (m)	*D* (m)	Applied load (kN)	Settlement (mm)	Injection pressure (kPa)
1	1	7.7	0.41	2000	2.24	400
2	7.7	0.41	2000	4.32	400	
2	3	15	0.41	2400	11.24	300
4	15	0.41	2400	10.38	300	
3	5	26	0.41	2240	8.04	300
4	6	12	0.35	1620	15.61	300
5	7	16	0.41	2400	13.85	300
8	12	0.41	2400	25.04	300	

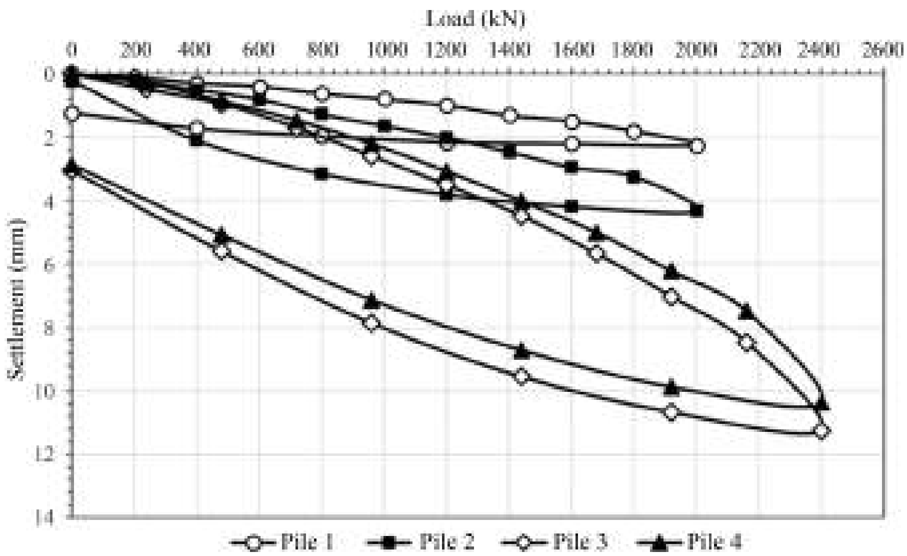

Figure 12 - Results from static load tests on piles 1, 2, 3 and 4.

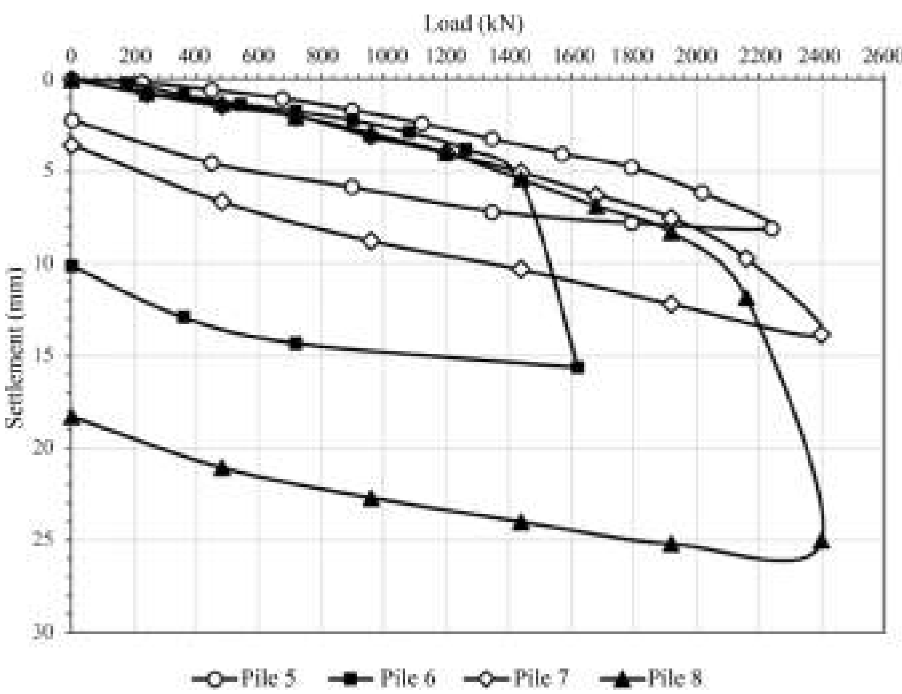

Figure 13 - Results from static load tests on piles 5, 6, 7 and 8.

Table 2 - Extrapolated ultimate load (Q_u) values.

Site	Pile	Q_u (kN)
1	1	3000
	2	3200
2	3	3100
	4	2900
3	5	2800
4	6	1550
5	7	2450
	8	2150

linear velocity, presents similar values when compared with values for piles 4 and 5.

Pile 5 (site 3), which has the tip supported in magmatic gneiss, presents an average penetration resistance index along the shaft similar to piles 1 and 2, which also have the tip supported on rock. In site 4, where pile 6 was executed, a reasonable compliance with pile 8 is verified when advance velocity is evaluated. Piles 6 and 8 are embedded in soils whose stratigraphy alternates between clayey silt, silty sand, clayey sand and sandy clay. These piles present a 7.4 % variation when compared to the respective advance velocities, which is smaller for pile 8. This is due to the fact that the penetration resistance index at the tip of pile 8 is higher than for pile 6. Thus, a correlation between these two variables is observed, in such a way that the higher the penetration resistance index, the lower the advance velocity, noting an inversely proportional ratio. High frequency values were observed during installation of piles 6, 7 and 8, which were already expected due to the direct frequency relationship with the drill bit linear velocity (V_b). Thus, it is possible to observe, that the higher the frequency, the greater the drill bit linear velocity and the smaller the soil N value. Based on the above, it is possible to infer that pile load capacity is inversely proportional to the drill bit linear velocity (V_b) and the frequency. Table 4 shows the average values of the monitored variables and the ultimate load for each test pile.

Table 3 - Monitoring results.

Pile	Drilled length (m)	Time (s)	V_a 10^{-3} (m/s)	Frequency (Hz)	ω_b (rad/s)	V_b (m/s)	$N_{SPT, tip}$	$N_{SPT, shaft}$
1	0.1	38.00	2.63	2.01	12.60	1.95	60	50
	0.2	51.00	3.92	2.50	15.72	2.44		
	0.2	78.00	2.56	2.15	13.50	2.09		
	0.2	72.00	2.78	2.25	14.13	2.19		
2	0.1	27.00	3.70	1.76	11.08	1.72	60	52
	0.2	50.00	4.00	2.67	16.76	2.60		
	0.2	56.00	3.57	1.36	8.55	1.33		
	0.2	54.00	3.70	2.65	16.62	2.58		
3	0.1	11.22	8.91	2.55	16.00	2.48	60	33
	0.1	8.27	12.10	1.15	7.24	1.12		
	0.2	19.28	10.40	0.99	6.21	0.96		
4	0.1	4.76	21.00	2.00	12.57	1.95	60	32
	0.2	9.78	20.40	1.95	12.24	1.90		
	0.2	15.84	12.60	1.20	7.56	1.17		
5	0.1	18.59	5.38	1.54	9.66	1.50	60	52
	0.2	34.30	5.83	1.94	12.21	1.89		
	0.2	43.19	4.63	1.76	11.08	1.72		
6	0.15	29.00	5.20	3.99	25.10	3.89	10	6
	0.2	43.00	4.70	4.06	25.48	3.95		
7	0.3	30.00	1.00	2.05	12.86	1.99	39	22
	0.2	27.00	7.40	2.44	15.32	2.37		
8	0.3	38.00	7.90	1.61	10.14	1.57	22	22
	0.2	44.00	4.50	4.38	27.52	4.27		

7. Equations Proposal and Validation

For the development of the equations, a multiple linear regression analysis method was used. Initially, piles 3, 4, 6, 7 and 8 were chosen for the development of the expression (calibration), then piles 1, 2 and 5 were chosen for validation. The selection of the piles for the calibration and validation of the equations was carried out randomly. As mentioned on a previous section, three distinct scenarios were proposed. In the first scenario, the load distribution would occur with 80 % along the pile shaft and 20 % on the pile tip. In the second scenario, the load distribution would occur with 90 % along the pile shaft and 10 % on the tip. Finally, in the third scenario, the load distribution would only occur along the pile shaft, that is, with 100 % along the shaft. The equations for the proposed scenarios are now, presented:

$$Q_{u,80/20} = \frac{81{,}61 A_p^{0,015} N_{SPT,tip}^{0,404}}{V_a^{0,08}} + \frac{1615{,}33 (UL)^{0,0058} \overline{N}_{SPT,shaft}^{0,168}}{V_b^{0,44}} \quad (14)$$

$$Q_{u,90/10} = \frac{40{,}80 A_p^{0,015} N_{SPT,tip}^{0,404}}{V_a^{0,08}} + \frac{1817{,}25 (UL)^{0,0058} \overline{N}_{SPT,shaft}^{0,168}}{V_b^{0,44}} \quad (15)$$

$$Q_{u,100/0} = \frac{2019{,}17 (UL)^{0,0058} \overline{N}_{SPT,shaft}^{0,168}}{V_b^{0,44}} \quad (16)$$

where A_p is the tip cross sectional area; V_a is the drill bit advance velocity; ($N_{SPT,\ tip}$) is the tip resistance index; V_b is the drill bit linear velocity; U is the pile perimeter, L is the pile length; ($N_{SPT,\ shaft}$) is the average shaft resistance index.

Analyzing the equations, it is verified that the regression coefficients did not change, whereas the regression constants changed; this occurred for both the skin friction bearing capacity and the tip bearing capacity. The regression constant of skin friction bearing capacity gradually increased when moving from one scenario to the other. The coefficient of determination (R^2) of the equations is 0.99.

It is noteworthy that the equations proposed for the executive control present physical sense for the pile ultimate load capacity, and the variables that have a positive regression coefficient, are directly proportional to the pile bearing capacity. Thus, for example, the greater the pile perimeter (U), pile length (L) or average shaft resistance index ($N_{SPT,\ shaft}$), the greater the pile skin friction bearing capacity. On the other hand, the greater the drill bit linear velocity (V_b), the lower the pile skin friction bearing capacity. The methodology proposed was verified on root piles monitoring data that were not part of the universe used for the development of the equations by comparing the results obtained from load tests performed on these piles and values obtained from the proposed equations. Piles 1, 2 and 5 were randomly selected to carry out the validation. The proposed equations did not consider the injection pressure. However, Melchior Filho (2018) observed the small influence of this variable in the evaluation of Q_{ult}. More details are presented in Melchior Filho (2018). It is also important to point out that the injection pressure of all the piles chosen for the development of the expression (calibration) was about 300 kPa. Table 5 shows the load capacity estimates from the proposed expressions, as well as those obtained from the load tests.

Considering the presented scenarios, it is observed that the percentage error between the estimated values and the reference values considered was at least 2.8 % and at most 13.3 %. When comparing the estimated pile bearing capacity values and the reference values for pile 1, an absolute error of 4.6 % is verified. It is worth mentioning that all bearing capacity estimates for pile 1 presented values slightly lower than the reference value (ultimate load obtained from the load test). For pile 2, an absolute error of

Table 4 - Average monitoring variables values.

Pile	Drilled length (m)	Time (s)	V_a 10^{-3} (m/s)	Frequency (Hz)	ω_b (rad/s)	V_b (m/s)	$N_{SPT,\ tip}$	$N_{SPT,\ shaft}$	Q_u (kN)
1	0.175	59.75	2.97	2.23	13.99	2.17	60	50	3000
2	0.175	46.75	3.74	2.11	13.25	2.05	60	52	3200
3	0.133	12.92	10.50	1.56	9.81	1.52	60	33	3100
4	0.167	10.13	18.00	1.72	10.79	1.67	60	32	2900
5	0.167	32.03	5.28	1.75	10.98	1.70	60	52	2800
6	0.175	36.00	4.95	4.03	25.29	3.92	10	7	1550
7	0.25	28.50	8.70	2.24	14.09	2.18	39	22	2450
8	0.25	41.00	6.20	3.00	18.83	2.92	22	22	2150

Table 5 - Methodology validation.

Method	Pile 1			Pile 2			Pile 5		
	Q_s (kN)	Q_{tip} (kN)	Q_u (kN)	Q_s (kN)	Q_{tip} (kN)	Q_u (kN)	Q_s (kN)	Q_{tip} (kN)	Q_u (kN)
Q_u, 80/20	2244	671	2915	2314	658	2972	2533	639	3173
Q_u, 90/10	2525	335	2860	2603	329	2932	2850	319	3170
Q_u, 100	2805	0	2805	2893	0	2893	3167	0	3167
Load test Q_u (kN)		3000			3200			2800	

8.3 % is observed when comparing the pile bearing capacity values with the reference values. As for pile 1, it is found that the bearing capacity values predicted for pile 2 are lower than the reference values; this occurs for all load distribution scenarios. A distinct trend is verified for pile 5, with the greater absolute error (average of 13.2 %). The pile bearing capacity values predicted for pile 5 were higher than the reference value.

It is important to mention that the use of the SPT on fine soils has some limitations, due to the characteristics of the test, in which a great disturbance of the soil structure is observed. Eurocode 7 states that the use of the SPT should be restricted to a qualitative evaluation of the soil profile as there is no general agreement on the use of SPT results in clayey soil (BS, 2007). The soil profiles analyzed to develop the proposed methodology consist, mostly, of coarse soils. Therefore, the application of this methodology to clayey soils has to be performed with proper evaluation. It is worth mentioning that the use of the proposed equations is restricted to soils with similar characteristics to those of this research. In this sense, the use of the proposed expressions in fine soil profiles should be preceded by further research, in order to contemplate a wider range of soil types.

In general, the bearing capacity values estimated by the proposed equations were in agreement with the reference values. Therefore, a correlation between the pile bearing capacity and the suggested variables is observed. It is worth mentioning that the proposal of this work is to present a simplified procedure for the executive control of root piles, helping in the decision-making during field execution, in relation to the definition of the pile length to be executed.

8. Conclusions

In this research, simplified methodologies and equations for the executive control of root piles were proposed, providing a useful tool to assist in the decision-making during field execution. The methodology is based on the monitoring of execution variables (advance velocity and drill bit linear velocity), determined from fundamentals of classical physics with measurements made during field testing. Based on these equations, it became possible to establish a monitoring methodology for root piles. The measured execution variables during monitoring are correlated with ultimate load values obtained from load tests.

This methodology is easy to carry out and provides an immediate interpretation. The methodology allows a systematic control without disturbing root piles. It is also adapted to the real conditions of root pile construction sites and is therefore a technically and economically feasible methodology. At present, the methodology is limited to root piles having a length lower than 30 m and maximum bearing capacity of 3500 kN. This methodology can provide the ultimate bearing capacity of the pile with a reasonable accuracy.

This alternative and original methodology has the advantage of estimating the root pile bearing capacity during pile installation with a non-destructive approach. This means that in the absence of a static load test, the methodology can become an alternative for the root pile executive control. The monitoring protocol and the processing and treatment of the acquired data show that the methodology proposed can provide results with great similarity when compared to static load test results.

Acknowledgments

This research was carried out under the auspices of the Foundation Group (M.Sc., Professors and Technicians) of the Geotechnical Post-Graduation Program of the University of Ceará-UFC (POSDEHA/UFC). The authors would like to express their gratitude to the engineering contractors FUNDAÇÕES GEOBRASIL and TECNORD for the field support, and to the Governmental sponsorship organization CAPES for the scholarship provided to the first author.

References

ABNT, Brazilian Association of Technical Standards (2010). Foundation Design and Execution. NBR 6122-2010. Rio de Janeiro, Brazil, 91 p.

Basu P.; Prezzi M. & Basu D. (2010). Drilled displacement piles – Current practice and design. DFI Journal, 4(1):3-20.

BS, British Standard (2007). Eurocode 7 – Geotechnical Design – Part 2: Ground Investigation and Testing. British Standard Institution. London, England, 199 p.

Cadden, A.; Gomez J. & Bruce D. (2004). Micropiles: recent advances and future trends. Proc. Current practices and future trends in deep foundations, ASCE. Los Angeles, pp. 140-165.

Calvente, R.; Breul P.; Benz M.; Bacconet C. & Gourves R. (2017). Methodology for confirming the micropiles service performance based on dynamic tests. Journal of Geotechnical and Geoenvironmental Engineering, 143(5):040161231-040161238.

Herrera, R.; Jones L.E. & Lai P. (2009). Driven concrete pile foundation monitoring with embedded data collector system. Proc. International Foundation Congress and Equipment Expo, ASCE. Orlando, pp. 78-84.

Huang, Y.; Hajduk E.L.; Lipka D.S. & Adams J.C. (2007). Micropile load testing and installation monitoring at the CATS vehicle maintenance facility. Proc. Geo-Denver. Denver, ASCE, pp. 28-38.

Lin, G.; Hajduk E.L.; Lipka D.S. & NeSmith W. (2004). Design, monitoring, and integrity testing of drilled soil displacement piles (DSDP) for a gas-fired power plant. Proc. GeoSupport Conference. Orlando, pp. 17-29.

Lima, D.R.; & Moura, A.S. (2016). Executive control of root piles from field measurements. Ciência & Engenharia, 25:95-104 (In Portuguese).

Melchior Filho, J. (2018). Improvements Development for the Root Piles Executive Control Procedure of the Post-Graduation Program in Civil Engineering of the Federal University of Ceara. Masters Dissertation, Hydraulic and Environmental Engineering Department, Federal University of Ceará Fortaleza, 114 p. (In Portuguese).

Moura, A.; Lima, R. & Monteiro, F. (2015). A preliminary proposal: Executive control of root piles. The Electronic Journal of Geotechnical Engineering, 20(26):12906-12920.

Russo, G. (2012). Experimental investigations and analysis on different pile load testing procedures. Acta Geotechnica, 8(1):17-31.

Silva, C.M.; Brasil A.L. & Camapum de Carvalho, J. (2012). On modelling coninuous flight auger pilings by means of energy. International Journal of Science and Engineering Investigations, 1:11-16.

Silva, C.M.; Camapum de Carvalho, J. & Brasil, A.L. (2014). The SCCAP methodology applied to design continuous flight auger pilings. The Electronic Journal of Geotechnical Engineering, 19(4):16909-16919.

Van der Veen, C. (1953). The bearing capacity of a pile. Proc. Third International Conference on Soil Mechanics and Foundation Engineering, Zurich, v. II, pp. 84-90.

Zhou, J.; Gong, X.; Wang, K. & Zhang, R. (2018). Shaft capacity of the pre-bored grouted planted pile in dense sand. Acta Geotechnica, 13(5):1227-1239.

Evaluating the Adsorptive Capacity of Aluminoferric Red Oxisol in Reducing the Availability of 2,4-Dichlorofenoxiacetic Acid

D.P. Baldissarelli, D.P. Siqueira, A. Dervanoski, M. Morais, L. Galon, E.P. Korf, G.D.L.P. Vargas

Abstract. Increased food production results in the development and application of agrochemicals to control weeds, which can affect agricultural production. Pesticides contaminate the environment and change soil and water quality. Therefore, to improve the understanding of the adsorption mechanism of 2,4-dichlorophenoxyacetic acid (2,4-D) in aluminoferric red oxisol we have conducted an adsorption study using Langmuir and Freundlich isotherms, treating kinetic data using pseudo first-order, pseudo second-order, and intraparticle diffusion models. The results showed the Freundlich isotherm fits the experimental data best, revealing favorable adsorption and a strong attraction between adsorbent molecules, considering the n_F and k_F model parameters of 3.7 and 34.21 L/g, respectively. The kinetic model with the best fit was the pseudo second-order model. The intraparticle diffusion model indicated the second step as the process controlling step, revealing k_D of 12.36 and 4.42 mg/g for the concentrations of 6352.80 mg/L and 1087.20 mg/L, respectively. Higher k_D represents lower transport resistance and higher motive power for mass transfer.

Keywords: adsorption isotherms, adsorption kinetics, agrochemicals, intraparticle diffusion model, pseudo second-order model.

1. Introduction

Global demand for food has grown considerably in recent decades due to population increase, which has resulted in increased food production. Weeds are prevalent in monoculture agriculture, causing the widespread use of pesticides (Martins *et al.*, 2014). Some farmers adopt a pre-established control system to apply pesticides that does not consider local conditions, such as soil type, climate, agricultural management, type of cultivar, or cropping system (Mancuso *et al.*, 2011). Thus, in soil it is estimated a concentration increase every year and therefore being able to exceed the limits permitted by environmental standards (Cotillas *et al.*, 2018). Consequently, high concentrations have been identified in several environmental compartments and can be spreading easily due the solubility of many pesticides, increasing he extension of the contaminated area (Pavlovic *et al.*, 2005; Piaia *et al.*, 2017).

The southern region of Brazil, more specifically, Rio Grande do Sul state, is known as agricultural, with its main crops being soy, corn and wheat. Among different types of herbicides used in agriculture, stand out the selective ones, such as 2,4-dichlorophenoxyacetic acid, also called 2,4-D, used for post-emergence application on weeds, for various crops such as soybeans and wheat. Its use intended to eliminate the presence of these weeds that may end up compromising production. This herbicide presents short to medium persistence in the soil, being maintained for prolonged periods and can reach up to 4 weeks in regions with tropical characteristic; in cold and dry regions its decomposition becomes very reduced (Silva & Silva, 2007), which can come to affect this ecosystem, as well as, to compromise subsequent plantations, reducing production.

The degradation of agricultural soils by 2,4-D has recently become a concern for researchers (Risco *et al.*, 2016; Souza *et al.*, 2016a). It is commercially distributed in amine formulations, salts, and esters (Amarante Jr. *et al.*, 2003; Sbano *et al.*, 2013). Amines were adsorbed more effectively in the soil than those of ester, therefore, more leachable, while those of ester are poorly soluble, therefore they present less movement (Silva & Silva, 2007). The active element of 2,4-D is widely used in the chemical industry, and due to the specific characteristics of this agrochemical, such as high water solubility (620 mg/L) (Pavlovic *et al.*, 2005; Souza *et al.*, 2016b), low biodegradability (Brillas *et al.*, 2003; Nethaji & Sivasamy, 2017), and low soil adsorption coefficient, it is commonly found in groundwater because it percolates through the soil (Prado *et al.*, 2016).

Considered moderately toxic by the World Health Organization (WHO, 2004), this long-lasting herbicide damages the nervous system of living beings (humans and ani-

Daiane Paula Baldissarelli, Undergraduate Student, Universidade Federal da Fronteira Sul, Erechim, RS, Brazil. e-mail: daianebaldissarelli.db@gmail.com.
Diego Pereira Siqueira, M.Sc., Researcher, Universidade Federal de Goiás, Goiânia, GO, Brazil, e-mail: diegopdq@gmail.com.
Adriana Dervanoski, Ph.D., Associate Professor, Universidade Federal da Fronteira Sul, Erechim, RS, Brazil. e-mail: dervanoa@gmail.com.
Manuella de Morais, M.Sc. Student, Universidade Federal da Fronteira Sul, Erechim, RS, Brazil. e-mail: manuellademorais@gmail.com.
Leandro Galon, Ph.D., Associate Professor, Universidade Federal da Fronteira Sul, Erechim, RS, Brazil. e-mail: leandro.galon@uffs.edu.br.
Eduardo Pavan Korf, Ph.D., Associate Professor, Universidade Federal da Fronteira Sul, Erechim, RS, Brazil. e-mail: eduardokorf@gmail.com.
Gean Delise Leal Pasquali Vargas, Ph.D., Associate Professor, Universidade Federal da Fronteira Sul, Erechim, RS, Brazil. e-mail: geandelise@uffs.edu.br.
Submitted on March 18, 2019; Final Acceptance on August 2, 2019; Discussion open until April 30, 2020.
DOI: 10.28927/SR.423301

mals). Its oral and dermal lethal dose (LD50) is 370 mg/kg (in rabbits) and 1400 mg/kg (in mice), respectively (Vieira *et al.*, 1999). From this perspective, it is important to understand the adsorption mechanisms of pesticides in the soil, as different processes are also affected by this dynamic, such as degradation, bioaccumulation, transport, and mobility (Long *et al.*, 2015).

Adsorption is a multi-step process involving the transport of adsorbate molecules (2,4-D) from the aqueous phase to the surface of the solid (soil) particles, followed by the diffusion of solute molecules into the pore interiors. If the experiment is a batch system with rapid shaking, there is a possibility that the transport of adsorbate from the solution into pores (bulk) is the step that controls the speed of the process (McKay, 1982). This process is described by a graphical relationship, that shows the amount of adsorbed 2,4-D varying with the square root of time (Weber & Morris, 1963).

Numerous studies have been conducted to clarify the behavior and adsorption of herbicides, such as terbuthylazine, prometryne, metribuzin, hexazinone, metolachlor, chlorotoluron, trifluralin, azoxystrobin, fipronil, chlormequat chloride (Kodeová *et al.*, 2011), and atrazine (Yue *et al.*, 2017), in soil. Regarding 2,4-D, research has demonstrated that in soils with a higher amount of organic matter, whether natural or derived from residues, the adsorption of pesticides by soil particles is higher (Amarante Jr. *et al.*, 2003; Bekbölet *et al.*, 1999; Spadotto *et al.*, 2003; Vieira *et al.*, 1999; Rodriguez-Rubio *et al.*, 2006).

Although 2,4-D is classified as an extremely toxic product in Brazil, its use is permitted and therefore there are many concerns about the effects on human health and the environment. Therefore, knowledge is essential about the mechanisms of retention and mobility of this contaminant in the soil. There have been numerous studies about the adsorption of this pesticide in Brazilian soil, however, there is a lack of research on the use of latosol with low organic matter as adsorbent material. To increase knowledge about the capacity and mechanisms of the adsorption of the 2,4-D agrotoxic in aluminoferric red oxisol, this study evaluates its adsorption capacity, adsorption processes, and interactions that occur between adsorbent particles and adsorbate compounds.

2. Methodology

2.1. Solutions and adsorbent

2,4-D pesticide was used in the amine formulation of 720 g/L. The solutions required for the study were prepared with ultrapure water from the Millipore Milli-Q system. The investigated soil was collected in the experimental area on the Erechim campus of the Federal University of Fronteira Sul (UFFS) in Rio Grande do Sul, Brazil. This soil is residual basalt material with a pedological classification of aluminoferric red oxisol (Erechim unit) (Streck *et al.*, 2008).

Samples were taken from the surficial layer of horizon A soil (from 0 to 10 cm) of a site that never received agrochemicals in order to avoid interference from other contaminating sources. Physical and physico-chemical characterization was performed for different attributes, such as: pH, micronutrients (iron, copper, zinc and manganese), soil density and organic matter content; these analyses were performed based on methodology described by Embrapa (2009); and moisture content and granulometric analysis, through the Brazilian Standards NBR 6457 and NBR 7181, respectively (ABNT, 2016; ABNT, 1984).

2.2. Evaluation of adsorption capacity and kinetic study

Under unsteady environment temperature (23 °C ± 1 °C) and pH 5.5, the mass of 2.5 g of soil was added to 50 mL of aqueous solution (1:20), and then, soil adsorption capacity was evaluated using a static method by American Society for Testing and Materials (ASTM, 2016). All the adsorption tests were conducted in triplicate, and the variables evaluated were the concentration of 2,4-D in the liquid phase at equilibrium (C_e), and through mass balance (Eq. 1), the amount of 2,4-D adsorbed on the solid phase (q_e) per unit mass of soil used as adsorbent was obtained.

Initially, a kinetic study was performed in which two initial concentrations of the 2,4-D contaminant (1087.20 and 6352.80 mg/L) were used, resulting from the used volumes of 0.25 and 1.30 liters per hectare, which are extreme values for application of 2,4-D, normally used in the field. These tested volumes are close to those recommended for agronomic application and the purpose of using these concentrations was to obtain the time at which the system reaches equilibrium. Monitoring time was 480 min, however, pre-tests verified that the highest adsorption rates occurred during the first hour of the study. Based on these results, it was determined that in the adsorption kinetic assays the aliquots would be withdrawn at shorter time intervals at the beginning of the kinetic study (5, 15, 30, and 45 min), with the experiment ending after eight hours. This study was used to perform the kinetic modeling of the process, which will be described later. Table 1 shows the experimental conditions used in the preliminary tests and in the kinetic study.

Subsequently, the adsorption study was carried out in triplicate, using initial concentrations of the 2,4-D contaminant of 0.0, 1668.80, 4734.40, 8318.40, 10176.00, and 17920.00 mg/L resulting from 2,4-D applications of 0.0, 0.50, 1.00, 1.50, 2.00, and 3.50 L per hectare of soil used in the field to obtain adsorption isotherm models, with the 2,4-D adsorbate concentration at equilibrium (C_e). Aliquots resulting from the kinetic study and the adsorption study were used to determine the amount of 2,4-D.

Table 1 - Experimental conditions used and kinetic study.

	Experi-ment	Concentration 2,4-D (mg/L)	Time (min)
Kinetic study	1	1087.20	480
	2	6352.80	
Equilibrium study	1	0.0	45
	2	1668.80	
	3	4734.40	
	4	8318.40	
	5	10176.00	
	6	17920.00	

2.3. Chromatographic analysis of 2,4-D

To determine the liquid phase 2,4-D adsorbate concentration at equilibrium (C_e), aliquots were centrifuged at 3000 rpm (Sigma Equipment 3-16 L) for 10 min. Thereafter, a syringe filter (0.45 μm) was used to separate the soil from the liquid phase. The resulting extract was then subjected to chromatographic analysis. Identification was achieved using a high-performance liquid chromatography system (HPLC) (Shimadzu, Prominence UFLC with PDA detector) using the standard curve of the analyte (2,4-D). Data processing was performed using LabSolutions software, version 5.75. The amount of solute adsorbed per unit mass of adsorbent (soil), q_e (mg/g), was determined using Eq. 1:

$$q_e = (C_0 - C_e)\frac{V}{W} \tag{1}$$

where C_0 is the initial adsorbate concentration (mg/L), C_e is the adsorbate concentration at equilibrium (mg/L), V is the solution volume (L), and W is the weight of the solid (g).

2.4. Adsorption process modeling

After determining the adsorbed concentrations, adsorption isotherms were traced and mathematical modeling was applied to determine the adsorption mechanisms of 2,4-D in soil particles.

2.5. Adsorption isotherms

Langmuir and Freundlich isotherm models were employed in the study. The Langmuir isotherm model, presented in Eq. 2, assumes uniform adsorption energy on the surface and in the transmigration of the adsorbate between sites (McKay *et al.*, 1982).

$$q_e = \frac{q_{\max} b_L C_e}{1 + b_L C_e} \tag{2}$$

q_e is the amount of solute adsorbed per unit mass of adsorbent (mg/g), C_e is the adsorbate concentration at equilibrium (mg/L), and q_{max} (mg/g) and b_L (L/g) are Langmuir parameters representing the maximum adsorption capacity and the adsorbate/adsorbent interaction constant, respectively.

The Freundlich isotherm is described by Eq. 3. The empirical model considers multilayer adsorption and can be applied on highly heterogeneous surfaces. In many cases it provides better representation of adsorption equilibrium of a single solute compared to a Langmuir isotherm (Merk *et al.*, 1981), where the heat of adsorption depends on the concentration in the solid phase.

$$q_e = k_F C_e^{\frac{1}{n_F}} \tag{3}$$

q_e is the amount of solute adsorbed per unit mass of adsorbent (mg/g), k_F is the equilibrium constant of the Freundlich model related to adsorption capacity (L/g), C_e is the adsorbate concentration at equilibrium (mg/L), and n_F is a dimensionless exponent of the Freundlich equation related to the intensity of adsorption.

2.6. Kinetic adsorption

Adsorption kinetics describe the rate of solute removal in the fluid phase over time and are dependent on the physical and chemical characteristics of the adsorbate, the adsorbent, and the experimental system. The adsorption mechanism in adsorbents may involve the following steps: the transfer of adsorbate molecules from the solution to the external surface of the adsorbent (boundary layer); the adsorption of the adsorbate molecules into the external surface of the particle through molecular interactions; the diffusion of adsorbate molecules from the external surface to the interior of the particle (effective diffusion); and the adsorption inside the particle (Ruthven, 1984). According to Sun & Xiangjing (1997), the first stage of adsorption can be affected by increased adsorbate concentration and shaking, accelerating diffusion of the adsorbate to the solid surface. The second stage is dependent on the nature of adsorbate molecules. The third stage is generally considered the determining step, especially in the case of microporous adsorbents.

Kinetic adsorption models can be used to determinate the mechanisms and adsorbent efficiency in the removal of contaminants. In this study, data relating to the adsorption of 2,4-D by soil has been treated using three kinetic models - the pseudo first-order, pseudo second-order, and intraparticle diffusion models.

Pseudo first-order Lagergren model (Khaled *et al.*, 2009; Xu *et al.*, 2013; Ho & McKay, 1998; Roy *et al.*, 2013; Gulnaz *et al.*, 2005) is the first known equation to describe the adsorption rate based on adsorption capacity. According to some authors, the pseudo first-order model may be related to the occurrence of physical adsorption, which can control the reaction rate (Ho & McKay, 1999).

The linear equation of Lagergren or pseudo first-order equation is expressed in Eq. 4:

$$\log(q_e - q_t) = \log q_e - \frac{k_1}{2.303} t \quad (4)$$

where q_e is the adsorption capacity at equilibrium (mg/g), q_t is the adsorption capacity in time t (mg/g), k_1 is the constant of the adsorption rate of pseudo first order (1/min), and t is the time of reaction (min).

Another kinetic model evaluated was the pseudo second-order model (Roy *et al.*, 2013; Gulnaz *et al.*, 2005; Khaled *et al.*, 2009; Ho & McKay, 1999; Xu *et al.*, 2013), being a linear model represented by Eq. 5:

$$\frac{t}{q_t} = \frac{1}{k_2 q_e^2} + \frac{1}{q_e} t \quad (5)$$

where t is the time of reaction (min), q_t is the adsorption capacity in time t (mg/g), k_2 is the constant of the adsorption rate of pseudo second order (g/mg.min), and q_e is the adsorption capacity at equilibrium (mg/g).

The intraparticle diffusion model is commonly expressed by Eq. 6 (Roy *et al.*, 2013; Ho e McKay, 1998):

$$q_t = k_D t^{\frac{1}{2}} \quad (6)$$

where q_t is the adsorption capacity in time t (mg/g), k_D is the velocity constant of intraparticle diffusion (mg/g.min) and t is the time of reaction (min).

Based on the assumption that 2,4-D is transported from the aqueous solution to the adsorbent by intraparticle diffusion, this is another kinetic model that must be used to study the adsorption of this contaminant in soil. The intraparticle diffusion velocity constant (k_D), also known as the Weber and Morris constant, is obtained by the linearization of Eq. 6 corresponding to the angular coefficient of the line, which can present two or more linear steps that can limit the adsorption, as follows:

a) Linear stage that begins with a rapid diffusion on the outer surface of the particle;
b) Linear stage that begins with gradual adsorption, where intraparticle diffusion is the limiting rate; and
c) The equilibrium stage in which the intraparticle diffusion begins to decay due to the low solute concentration in the solution and the lower availability of adsorption sites (Chen *et al.*, 2003).

All the experimental results for the adsorption equilibrium of the 2,4-D compounds were adjusted using the least squares method with version 7.0 STATISTICA software, applying the Langmuir and Freundlich models. The statistical significance adopted for fitting the experimental data to the models was 95 %.

3. Results and Discussion

3.1. Soil characterization

Table 2 shows pH, moisture content, density, micronutrients and organic matter content of the soil sample.

High moisture content of the superficial soil layer (0-10 cm) is due to pluviometric precipitations that occurred in the days prior to the collection of the material. According to Streck *et al.* (2008), the latosols have low nutrient content and high acidity, with pH below 4.9 in the superficial layer and, at greater depths, values close to 5.5 (Brazil, 1973).

Fig. 1 shows the particle size distribution of the soil sample, with clay, silt and fine sand contents, corresponding to 38,26 %, 12,83 % and 47,33 %, respectively.

3.2. Equilibrium studies

Langmuir and Freundlich adsorption isotherms were obtained using the adsorption tests with different initial concentrations of 2,4-D. Fig. 2 shows the results of experimental adsorption isotherms for 2,4-D, adjusted using the Langmuir and Freundlich models.

Adsorption isotherms for 2,4-D in soil were described as type L, according to Giles *et al.* (1960) classification. Fig. 2 indicates that for lower concentrations of agrochemicals added to the soil, adsorption occurs with greater intensity, indicating the affinity of the adsorbent with 2,4-D. This is confirmed by Pavlovic *et al.* (2005), who showed that in this isothermal shape (L) monofunctional adsorbate is strongly attracted to an adsorbent, mainly via electrostatic or ion-ion interactions, thus reaching the saturation value. By means of the experimental results, it was still possible to observe that when the lowest concentration of 2,4-D (1668.80 mg/L) was used, a removal of approximately 25.00 % was obtained, and as the concentration of the contaminant was increased (17920.00 mg/L), there was a decrease in removal to 4.50 %.

The parameters obtained by the Langmuir and Freundlich models are shown in Table 3. Considering the parameters of the models presented in Table 3, calculated with the experimental data obtained by the chromatographic analysis of 2,4-D, it is possible to verify that the Freundlich model showed better adjustment for the adsorption process

Table 2 - Soil characteristics: pH, moisture content, micronutrients and organic matter.

pH	Moisture content (%)	Density (g/cm^3)	Micronutrients (mg/dm^3)				Organic matter content (%)
			Fe	Cu	Mn	Zn	
4.21 ± 0.11	50.85 ± 4.88	1.22 ± 0.50	7.580.50	1.52 ± 0.20	1.47 ± 0.01	0.36 ± 0.03	3.17 ± 0.71

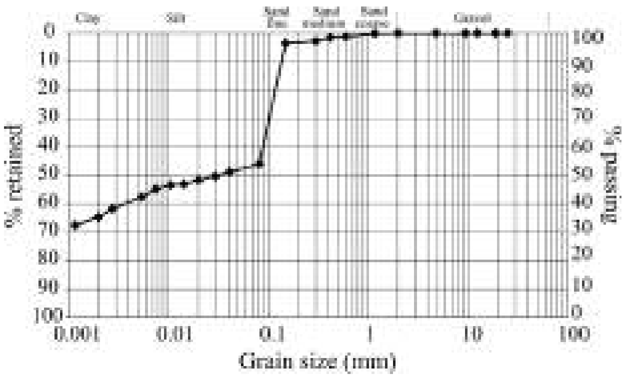

Figure 1 - Particle size distribution of the soil sample.

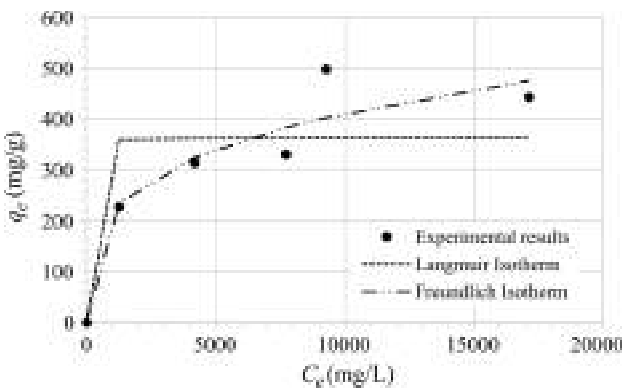

Figure 2 - Langmuir and Freundlich adsorption isotherms for 2,4-D (0.0, 1668.8, 4734.4, 8318.4, 10176.0, and 17920.0 mg/L); adsorbate weight, 2.5 g; volume, 50 mL; temperature, 23 °C ± 1 °C.

Table 3 - Parameters of the Langmuir and Freundlich models, adjusted to experimental data.

Langmuir isotherm model - Eq. 2			Freundlich isotherm model - Eq. 3		
q_{max} (mg/g)	b_L (L/g)	R^2	n_F	k_F (L/g)	R^2
363.00	0.09	0.86	3.70	34.21	0.96

of 2,4-D in the soil, based on the value of the determination coefficient (R^2). Considering the model, it can be assumed that the soil studied has heterogeneous sites and that the adsorption process occurs in multiple layers.

In adsorption studies of 2,4-D (25 °C) in adsorbents such as illite, sand, and humic acid, Haque & Sexton (1968) obtained values of 1.02, 1.454, and 1,09 L/mg, respectively, for the equilibrium constant of the Freundlich model (k_F). Delle Site (2000) reports that for values of $n_F > 1$ it is possible to have L-shaped isotherms and that the lower this ratio, the greater the interaction between adsorbate and adsorbent. This shows that due to the high n_F determined in the present study, the ratio becomes smaller when compared to studies cited above, and therefore there is a high interaction between adsorbate and adsorbent.

More information can be gathered using the equilibrium constant of the Freundlich model. Alfonso *et al.* (2017) evaluated the adsorption of four organophosphorus pesticides (diazinon, dimethoate, methyl parathion, and sulfotep) in different soils from Yucatán, Mexico. Their results indicate that all agrochemicals had low adsorption in the soil studied and therefore high mobility. The Freundlich model provided the best correlations, with k_F in the range of 1.62-2.35 L/mg for sulfotep, 2.43-3.25 L/mg for dimethoate, 5.54-9.27 L/mg for parathion, and 3.22-5.17 L/mg for diazinon.

These values, found by Alfonso *et al.* (2017), are much lower than the values observed in this research, indicating a good adsorption capacity and a higher affinity of 2,4-D for the aluminoferric red oxisol. The increased values for the two constants of the Freundlich model (n_F and k_F) are related due to the presence of a higher clay and silt content in the studied soil, being 38,26 % and 12,83 %, respectively. According to Bekbölet *et al.* (1999), who investigated the adsorption of 2,4-D in soils with low organic matter and neutral pH, it has been also verified that the adsorption process is positively correlated with the organic matter content and the amount of clay and silt. This is also confirmed by Alfonso *et al.* (2017), who obtained the lowest and highest values of n_F and k_F, respectively, for soil with higher clay content.

3.3. Adsorption kinetics

Fig. 3 shows the behavior of 2,4-D adsorption kinetics using two different initial concentrations (6352.80 mg/L and 1087.20 mg/L), in order to evaluate the equilibrium time between the adsorbent and the adsorbate used . This equilibrium time was also used to construct the adsorption isotherms. Fig. 3 shows that the equilibrium time decreases as the concentration of the contaminant increases. Based on this result and other preliminary results, the equilibrium time chosen for the other tests concerning the adsorption isotherms was 45 min.

Through the results obtained and analyzing the studied soil, it is verified that this soil does not present micro-

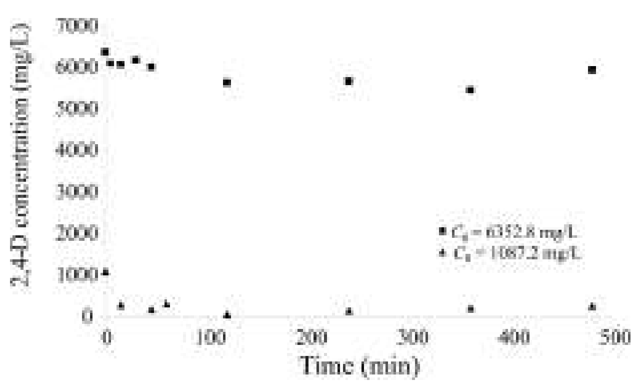

Figure 3 - Behavior of different 2,4-D concentrations in the adsorption process as a function of the reaction time.

porosity characteristics, being that the adsorption occurs more effectively on the surface, reaching equilibrium more quickly compared to microporous adsorbents, such as activated carbon, for example. The clay soil used in this study favors the adsorption process of the contaminant, as it presents a larger surface area when compared to sandy soils. Thus, by knowing the adsorption kinetics it is possible to determine the process control steps and the adsorption behavior of 2,4-D in the studied soil. Table 4 presents the kinetic parameters of pseudo first-order and pseudo second-order Lagergren models. These parameters were determined by establishing a linear relationship from the experimental results.

Considering the kinetic pseudo first-order and pseudo second-order models, if the q_e of the linearization is not equal to q_e obtained experimentally, then the reaction will probably not be of the analyzed order, even though this plot has high correlation with the experimental data (Khaled *et al.*, 2009; Crini *et al.*, 2007). Analyzing the data presented in Table 4 for the pseudo-first order model, it is verified that the q_e values obtained by the linearization are very low compared with the experimental values of q_e. In addition, the R^2 determination coefficient is relatively low for most data, which indicates that 2,4-D adsorption in soil is not a first-order reaction.

Fig. 4 shows the adjustments of the pseudo second-order adsorption kinetics obtained for this study.

The higher determination coefficient (R^2) (shown in Table 4) for the pseudo second-order model shows that it provided a better adjustment to the experimental data than the pseudo first-order model. In addition, the q_e (mg/g) calculated using this kinetic model is close to the experimental q_e (mg/g).

Salman & Hameed (2010) studied adsorption kinetics for the removal of 2,4-D from contaminated water using coal and found that the pseudo second-order model fits the experimental data best. This same behavior has been observed in the work of Trivedi *et al.* (2016) in which peanut shells were used in the removal of 2,4-D.

In addition, the pseudo second-order model may be related to the occurrence of chemical adsorption, which can control the reaction rate (Ho & McKay, 1998). According to Ruthven (1984), in the case of chemisorption, it involves the exchange or sharing of electrons between the adsorbate molecules and the surface of the adsorbent, resulting in a chemical reaction. This results essentially in a new chemical bond and therefore much stronger than in the case of the physisorption. The concepts of chemisorption and physisorption are distinct, however the two adsorption mechanisms are not completely independent. The distinction as to whether the species is physically or chemically adsorbed is not very clear, since both processes can often be described in terms of the principles of physical adsorption.

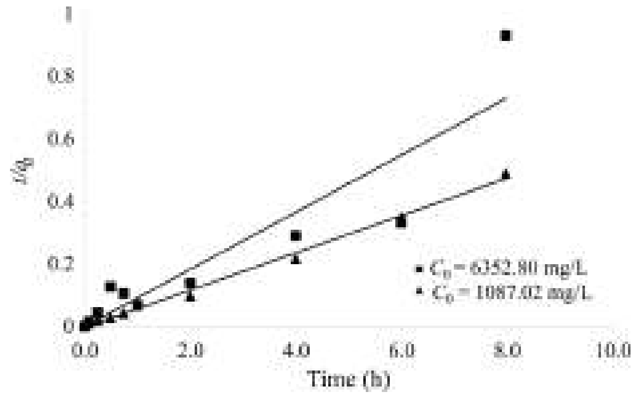

Figure 4 - Results of pseudo second-order kinetic: adsorbate weight, 2.5 g; volume, 50 mL; temperature, 23 °C ± 1 °C.

In general, the differences between physical adsorption and chemical adsorption can be summarized as: Chemical adsorption is highly specific and not all solid surfaces have active sites capable of chemically adsorbing adsorbate. It should be noted that not all molecules present in the fluid can be adsorbed chemically, only those capable of binding to the active site. Physical adsorption, unlike chemical adsorption, is non-specific. From a thermodynamics point of view, the heat involved in the physisorption is generally below 10 kcal/mol, that is, of the order of condensation/vaporization. In the adsorption chemistry, the heat of adsorption is of the order of the heat of reaction, therefore above 20 kcal/mol. It should be added that, since no formation or breakage occurs, the chemical nature of adsorbate is not altered (Nascimento *et al.*, 2014).

In general, it was verified that the kinetic pseudo second-order model is adequate to describe the adsorption process of 2,4-D in the soil in the present study.

3.4. Intraparticle diffusion kinetics

Fig. 5 shows the correlation of q_t *vs.* $t^{(1/2)}$ for the adsorption of 2,4-D in the soil created for the intraparticle diffusion model, including the three steps described in the

Table 4 - Adsorption rate constants of pseudo first-order and pseudo second-order models and q_e values for different initial 2,4-D concentrations: adsorbate weight, 2.5 g; volume, 50 mL; temperature, 23 °C ± 1 °C.

2,4-D concentration (mg/L)	q_e experimental (mg/g)	Pseudo first-order model - Eq. 4			Pseudo second-order model - Eq. 5		
		k_1 (1/h)	q_e (mg/g)	R^2	k_2 (g/mg.h)	q_e (mg/g)	R^2
6352.80	14.59	0.70	6.24	0.22	9.25	10.96	0.85
1087.20	20.69	0.08	6.01	0.07	1.00	16.83	0.99

section on kinetic adsorption (methodology) and separated by the 3 vertical lines highlighted (Fig. 5). In all cases, the quality of the adjustments obtained is defined by the determination coefficient (R^2) for each of the steps.

Table 5 shows the adsorption kinetic constants of the model for the second stage, chosen as the process control stage (highest determination coefficient mean). For the adsorption process using 2,4-D, the intraparticle diffusion model presented a k_D of 12.36 and 4.42 mg/g.h for the concentrations of 6352.80 mg/L and 1087.20 mg/L respectively.

The results show that the higher the concentration used, the higher is the k_D as can be seen in Fig. 5. This result is expected because the higher the concentration used, the greater the motive power for mass transfer and the higher the rate of diffusion of the contaminant in the pores of the adsorbent. This order of velocity can be attributed to the mass and molecular configuration of 2,4-D (Foust *et al.*, 1982).

4. Conclusion

It was possible to verify that the adsorption process of 2,4-D in the aluminoferric red oxisol occurs through different attraction forces, suggesting a diversity of active sites in the soil. Among the models that describe the kinetic adsorption of the pesticide in soil, the Freundlich model provided the best adjustment (R^2 of 0.96). The equilibrium constant and dimensionless exponent, both of the Freundlich model, k_F and n_F respectively, estimated at 34.21 and 3.7, indicate affinity between the adsorbent and the adsorbate, mainly due to the clay and silt content present in the soil and the characteristics of the analyte molecule. This implies a significant reduction in the availability and mobility of the pesticide in soil. In terms of the adsorption kinetics, it has been verified that the pseudo second-order model better represented the contaminant studied. This behavior is related to the molecule of the contaminant, as other research has also related this kinetic model to the adsorption of 2,4-D, even using another substance as an adsorbent. Based on the kinetic tests, it was possible to identify the controlling stage of the process and the high values of the determination coefficient relative to the intraparticle diffusion model. This indicated that the process is strongly controlled by the second step for the concentrations evaluated, as intraparticle diffusion rate is limiting of this process.

Furthermore, the results and conclusions obtained in this study can be used as knowledge and decision making for remediation in contaminated areas, considering that the soil in natural conditions, as in this study, already has a good ability to attenuate contaminants.

Table 5 - Kinetic parameters of intraparticle diffusion model for 2,4-D; adsorbent weight: 2.5 g, volume: 50 mL, temperature: 23 °C ± 1 °C.

2,4-D concentration (mg/L)	k_D (mg/g.h)	R^2
6352.80	12.36	0.87
1087.20	4.42	0.99

References

ABNT (1984). Solo - Análise Granulométrica - NBR 7181. ABNT - Associação Brasileira de Normas Técnicas, Rio de Janeiro, Brasil, 12p. (in Portuguese).

ABNT (2016). Amostras de Solo - Preparação para Ensaios de Compactação e Ensaios de Caracterização - NBR 6457. ABNT - Associação Brasileira de Normas Técnicas, Rio de Janeiro, Brasil, 8 p. (in Portuguese).

Alfonso, L.F.; Germán, G.V.; Carmen, P.C.M. & Hossein, G. (2017). Adsorption of organophosphorus pesticides in tropical soils: The case of karst landscape of northwestern Yucatan. Chemosphere, 166:292-299.

Amarante Junior, O.P.; Santos, T.C.R.; Nunes, G.S. & Ribeiro, M.L. (2003). Breve revisão de métodos de determinação de resíduos do herbicida ácido diclorofenoxiacético (2,4-D). Química Nova, 26(2):223-229. (in Portuguese)

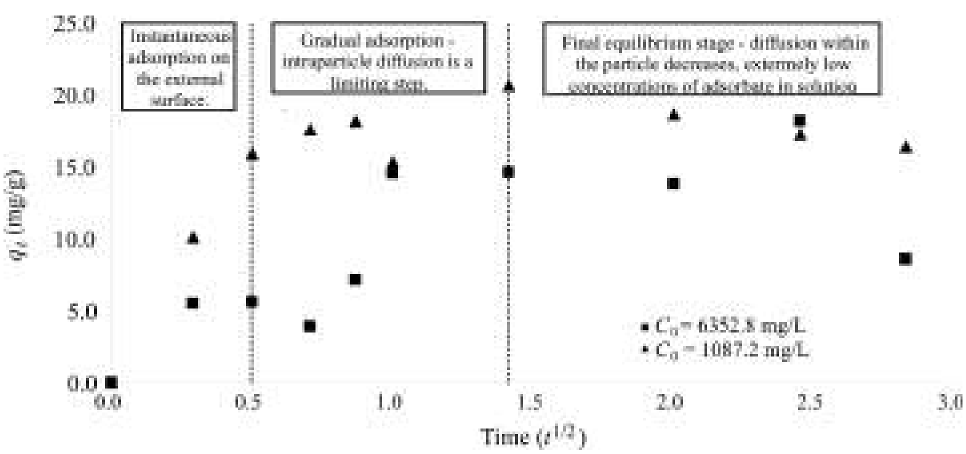

Figure 5 - Adjustment of intraparticle diffusion kinetics to 2,4-D; adsorbent weight, 2.5 g; volume, 50 mL; temperature, 23 °C ± 1 °C.

ASTM (2016). Standard Test Method for 24-h Batch-Type Measurement of Contaminant Sorption by Soils and Sediments - D4646-16. ASTM International, Philadelphia, USA, 5 p.

Bekbölet, M.; Yenigün, O. & Yücel, I. (1999). Sorption studies of 2,4-D on selected soil. Water, Air, and Soil Pollution, 111(1-4):75-88.

Brasil (1973). Levantamento de Reconhecimento dos Solos do Estado do Rio Grande do Sul. Ministério da Agricultura, Recife, 431 p. (in Portuguese).

Brillas, E.; Calpe, J.C. & Cabot, P. (2003). Degradation of the herbicide 2,4-dichlorophenoxyacetic acid by ozonation catalyzed with Fe^{2+} and UVA light. Applied Catalysis B - Environmental, 46(2):381-391.

Chen, J.P.; Wu, S. & Chong, K. (2003). Surface modification of a granular activated carbon by citric acid enhancement of copper adsorption. Carbon, 41(10):1979-1986.

Cotillas, S.; Sáez, C.; Cañizares, P.; Cretescu, I. & Rodrigo, M.A. (2018). Removal of 2,4-D herbicide in soils using a combined process based on washing and adsorption electrochemically assisted. Separation and Purification Technology, 194:19-25.

Crini, G.; Peindy, H.N.; Gimbert, F. & Robert, C. (2007). Removal of C.I. Basic Green 4 (Malachite Green) from aqueous solutions by adsorption using cyclodextrin based adsorbent: Kinetic and equilibrium studies. Separation and Purification Technology, 53(1):97-100.

Delle Site, A. (2000). Factors affecting sorption organic compounds in natural sorbent/water systems and sorption coefficients for selected pollutants: A review. Journal of Physical and Chemical Reference Data, 30(1):187-439.

Embrapa (2009). Manual de análises químicas de solos, plantas e fertilizantes 2nd ed. Silva, F.C. (ed), Embrapa Informação Técnológica, Brasília, 627 p. (in Portuguese).

Foust, S.A.; Wenzel, L.A.; Clump, C.W.; Maus, L. & Andersen, L.B. (1982). Princípios das Operações Unitárias 2nd ed. LTC, Rio de Janeiro, 682 p. (in Portuguese).

Giles, C.H.; MacEwan, T.H.; Nakhwa, S.N. & Smith, D. (1960). Studies in adsorption: Part XI. A system of classification of solution adsorption isotherms and its use in diagnosis of adsorption mechanisms and in measurement of specific surface area of solids. Journal of the Chemical Society, 3973-3993.

Gulnaz, O.; Saygideger, S. & Kusvuran, E.J. (2005). Study of Cu (II) biosorption by dried activated sludge: Effect of physico-chemical environment and kinetics study. Journal of Hazardous Materials, 120(1-3):193-200.

Haque, R. & Sexton, R. (1968). Kinetic and equilibrium study of the adsorption of 2,4- dichlorophenoxyacetic acid on some surfaces. Journal of Colloid and Interface Science, 27(4):818-827.

Ho, Y.S. & McKay, G. (1998). Sorption of dye from aqueous solution by peat. Chemical Engineering Journal, 70(2):115-124.

Ho, Y.S. & McKay, G. (1999). Pseudo-second order model for sorption process. Process Biochemistry, 34(5):451-465.

Khaled, A.; Nemr, A.E.; El-Sikaily, A. & Abdelwahab, O. (2009). Removal of Direct N Blue-106 from artificial textile dye effluent using activated carbon from orange peel: Adsorption isotherm and kinetic studies. Journal of Hazardous Materials, 165(1-3):100-110.

Kodeová, R.; Kocárek, M.; Kode, V.; Drábek, O.; Kozák, J. & Hettmánková, K. (2011). Pesticide adsorption in relation to soil properties and soil type distribution in regional scale. Journal of Hazardous Materials, 186(1):540-550.

Long, F.; Zhu, A.; Shi, H.; Sheng, J.; & Zhao, Z. (2015). Adsorption kinetics of pesticide in soil assessed by optofluidics-based biosensing platform. Chemosphere, 120:615-620.

Mancuso, M.A.C.; Negrisoli, E. & Perim, L. (2011). Efeito residual de herbicidas no solo (“Carryover”). Revista Brasileira de Herbicidas, 10(2):151-164 (in Portuguese).

Martins, C.X.; Salvador, P.M.; Jesus, J.D.; Ferreira, L.F.R.; Américo, J.H.P. & Torres, N.H. (2014). Análise de atrazina em amostras de água e solo por cromatografia gasosa (GC-ECD). Bioenergia em Revista: Diálogos, 3(1):128-138. (in Portuguese)

McKay, G.; Blair, H.S. & Gardner, J.R. (1982). Adsorption of dyes on chitin. I. Equilibrium studies. Journal of applied Polymer Science, 27(8):3043-3057.

Merk, W.; Fritz, W. & Schlünder, E.U. (1981). Competitive adsorption of two dissolved organics onto activated carbon - III: Adsorption kinetics in fixed beds. Chemical Engineering Science, 36(4):759-764.

Nascimento, R.F.; Lima, A.C.A.; Vidal, C.B.; Melo, D.Q. & Raulino, G.S.C. (2014). Adsorção: Aspectos teóricos e aplicações ambientais. Imprensa Universitária, Fortaleza, 256 p. (in Portuguese)

Nethaji, S. & Sivasamy, A. (2017). Graphene oxide coated with porous iron oxide ribbons for 2,4- dichlorophenoxyacetic acid (2,4-D) removal. Ecotoxicology and Environmental Safety, 138:292-297.

Pavlovic, L.; Barriga, C.; Hermosín, M.C.; Cornejo, J. & Ulibarri, M.A. (2005). Adsorption of acidic pesticides 2,4-D, Clopyralid and Picloram on calcined hydrotalcite. Applied Clay Science, 30(2):125-133.

Piaia, B.R.; Zago, M.L.C.; Denardin, E.L.G. & Roehrs, R. (2017). Fitorremediação dos herbicidas 2,4-diclorofenoxiacético e propanil em solo cultivado por erva cidreira (*Melissa officinalis*). Ciência e Natura, 39(1):91-98. (in Portuguese)

Prado, B.; Strozzi, A.G.; Huerta, E.; Duwig, C.; Zamora, O.; Delmas, P.; Casasola, D. & Márquez, J. (2016).

2,4-D mobility in clay soils: Impact of macrofauna abundance on soil porosity. Geoderma, 279:87-96.

Risco, C.; López-Vizcaíno, R.; Sáez, C.; Yustres, A.; Cañizares, P.; Navarro, V. & Rodrigo, M.A. (2016). Remediation of soils polluted with 2,4-D by electrokinetic soil flushing with facing rows of electrodes: A case study in a pilot plant. Chemical Engineering Journal, 285:128-136.

Rodríguez-Rubio, P.; Morillo, E. & Maqueda, C. (2006). Sorption of 2,4-D on natural and organic amended soils in different characteristics. Journal of Environmental Science and Health, Part B, 41(2):145-157.

Roy, A.; Adhikari, B. & Majumder, S.B. (2013). Equilibrium, kinetic, and thermodynamic studies of azo dye adsorption from aqueous solution by chemically modified lignocellulosic jute fiber. Industrial & Engineering Chemical Research, 52(19):6502-6512.

Ruthven, D.M. (1984). Principles of Adsorption and Adsorption Processes. John Wiley & Sons, New York, 433 p.

Salman, J.M. & Hameed, B.H. (2010). Adsorption of 2,4-dichlorophenoxyacetic acid and carbofuran pesticides onto granular activated carbon. Desalination, 256(1-3):129-135.

Sbano, A.; Ferreira, J.V.R.; Peckle, B.A.; Macrae, A. & Direito, I.C.N. (2013). Otimização de método cromatográfico para quantificação do herbicida ácido 2,4-diclorofenoxiacético (2,4-D). Acta Scientiae et Technicae, 1(2):37-46. (in Portuguese)

Silva, A.A. & Silva, J.F. (2007). Tópicos em Manejo de Plantas Daninhas. Editora UFV, Viçosa, 367 p. (in Portuguese)

Souza, F.L.; Saéz, C.; Llanos, J.; Lanza, M.R.V.; Cañizares, P. & Rodrigo, M.A. (2016a). Solar-powered electrokinetic remediation for the treatment of soil polluted with the herbicide 2,4-D. Electrochimica Acta, 190:371-377.

Souza, F.L.; Saéz, C.; Lanza, M.R.V.; Cañizares, P. & Rodrigo, M.A. (2016b). Removal of pesticide 2,4-D by conductive-diamond photoelectrochemical oxidation. Applied Catalysis B: Environmental, 180:733-739.

Spadotto, C.A.; Matallo, M.B. & Gomes, M.A.F. (2003). Sorção do herbicida 2,4-D em solos brasileiros. Pesticidas: Revista de Ecotoxicologia e Meio Ambiente, 13:103-110. (in Portuguese)

Streck, E.V.; Kämpf, N.; Dalmolin, R.S.D.; Klamt, E.; Nascimento, P.C.; Schneider, P.; Giasson, E. & Pinto, L.F.S. (2008). Solos do Rio Grande do Sul, 3ª ed. Emater, Porto Alegre, 222 p. (in Portuguese)

Sun, G. & Xu X. (1997). Sunflower stalks as adsorbents for color removal from textile wastewater. Industrial & Engineering Chemistry Research, 36(3):808-812.

Trivedi, N.S.; Kharkar, R.A. & Mandavgane, S.A. (2016). 2,4-Dichlorophenoxyacetic acid adsorption on adsorbent prepared from groundnut shell: Effect of preparation conditions on equilibrium adsorption capacity. Arabian Journal of Chemistry, 7:22-31.

Vieira, E.M.; Prado, A.G.S.; Landgraf, M.D. & Rezende, M.O.O. (1999). Estudo da adsorção/dessorção do ácido 2,4 diclorofenoxiacético (2,4D) em solo na ausência e presença de matéria orgânica. Química Nova, 22(3):305-308. (in Portuguese)

Xu, M.; Yin, P.; Liu, X.; Dong, X.; Xu, Q. & Qu, R. (2013). Preparation, characterization, adsorption equilibrium, and kinetics for gold-ion adsorption of spent buckwheat hulls modified by organodiphosphonic acid. Industrial & Engineering Chemical Research, 52(24):8114-8124.

Weber, W.J. & Morris, J.C. (1963). Kinetics of adsorption on carbon from solution. Journal of the Sanitary Engineering Division, 89(2):31-60.

WHO (2004). Guidelines for Drinking-water Quality, Vol. 1, 3rd ed. World Health Organization, Geneva, Switzerland, p. 515.

Yue, L.; Ge, C.; Feng, D.; Yu, H.; Deng, H. & Fu, B. (2017). Adsorption-desorption behavior of atrazine on agricultural soils in China. Journal of Environmental Sciences, 57:180-189.

3D Finite Element Analysis of Diaphragm Wall Construction Stages in Sand

R.A. Abdelrahman, A.M. Hassan, M.I. Amer

Abstract. Construction of underground structures may impose a hazardous effect on adjacent buildings due to ground movements caused by the construction of side support system and excavation. Most studies focus on predicting the soil movements due to excavation, however, limited research is performed to predict the effect of the construction process of the side support walls. Therefore, a 3D numerical model is developed to better understand the influence of installing diaphragm walls in sandy soils. A verification model has been used to validate the modeling of diaphragm wall construction sequence and its outputs using field data measurements of a selected case study. The diaphragm wall construction process is simulated using the WIM and WIP methods. This study has proved that WIM method is capable of simulating the construction stages and capturing the changes in soil stresses and displacements. Moreover, the results show that modeling diaphragm wall installation as a plane strain problem leads to the overestimation of the soil displacements. In addition, the effect of related parameters including; panel length, panel width, soil relative density, and moisture condition have been studied. The anticipated soil stresses and displacements during the construction process of diaphragm walls are presented. Finally, the effect of the selected modeling method (WIP or WIM) on the anticipated displacements during the following excavation stage is highlighted.

Keywords: construction stages, diaphragm wall, PLAXIS 3D, sand, WIP, WIM.

1. Introduction

A diaphragm wall is used as a part of side support systems for underground structures such as metro stations, basements, and underpasses. A diaphragm wall is a reinforced concrete structure constructed in-situ panel by panel. The wall can reach depths down to 50 m. The panel length ranges between 2.5 m and 7.0 m. The typical construction sequence of each panel includes three stages: (1) trench excavation under bentonite slurry support, (2), wet concrete injection, and (3) concrete hardening (Clear & Harrison, 1985).

The common practice is to design the side support system without considering the effect of the construction process of the walls. The construction sequence is assumed to have no effect on soil stresses or ground movements. However, previous studies indicate that diaphragm wall construction induces significant changes in stresses and movements of the surrounding soil (Burlon *et al.*, 2013; Poh & Wong, 1998; Symons & Carder, 1993). Several case histories are reported in which the construction of a deep diaphragm wall resulted in the collapse of the constructed panels and settlement values up to 60 mm (Cowland & Thorley, 1984).

Numerical modeling is capable of simulating the diaphragm wall using two methods; WIP (wished in place) and WIM (wished in model). In the WIP method, the diaphragm wall is modeled as a plate element. The sequence of diaphragm wall installation is not considered and no changes in soil stresses or ground movements are assumed (De Moor & Stevenson, 1996). Conversely, in the WIM method, the model is developed to consider the three construction stages of each panel. The first stage involves removing soil elements constituting the ground to be excavated (the trench) and simultaneously applying the hydrostatic bentonite pressure along the sides and bottom of the trench. For the second stage, the hydrostatic wet concrete pressure should replace the hydrostatic bentonite pressure. Ling *et al.* (1994) found, based on field measurements, that the full hydrostatic wet concrete pressure is applied down till a certain depth (the critical depth) after which the wet concrete pressure increases with depth at a rate governed by the unit weight of the bentonite (bi-linear pressure). The critical depth (h_{crit}) is observed to be located approximately at one third of the wall depth. According to Ling *et al.* (1994), the wet concrete behaves as a heavy fluid because the solid particles (aggregates and cement grains) are suspended in the water. As the hydration process takes place, reduction in pore pressure is observed. The hydration mechanism results in the gradual transfer of the load from being a pore pressure into a solid weight. Consequently, the vertical stresses increase and the horizontal stresses acting on the trench sides are reduced. For the third stage, the trench is replaced by an elastic concrete material and the bi-linear

Rowyda A. Abdelrahman, Graduate Student, Department of Public Works, Faculty of Engineering, Cairo University, Giza, Egypt. e-mail: rowyda_adel@hotmail.com.
Asmaa M. Hassan, Ph.D., Assistant Professor, Department of Public Works, Faculty of Engineering, Cairo University, Giza, Egypt. e-mail: asmaa.moddather@cu.edu.eg.
Mohamed I. Amer, Ph.D., Professor, Department of Public Works, Faculty of Engineering, Cairo University, Giza, Egypt. e-mail: m.amer@cu.edu.eg.
Submitted on March 28, 2019; Final Acceptance on August 1, 2019; Discussion open until April 30, 2020.
DOI: 10.28927/SR.423311

pressure is removed. This approach has been adopted in several studies in order to evaluate the effect of installation of diaphragm walls in clayey soils (Ng *et al.*, 1995; Gourvenec & Powrie, 1999; Arai *et al.*, 2008; Li & Lin, 2018).

In this paper, the effect of diaphragm wall installation in sandy soils is evaluated via a 3D numerical model. The paper consists of four parts; the first part validates the diaphragm wall numerical model and its outputs using a case study. The WIP and WIM methods are used to consider the effect of the construction process and the results of both methods are compared to field data measurements. The second part discusses the effect of the construction process on the ground movement and the soil stresses. The third part provides a parametric study to evaluate the effect of related parameters: panel length, panel width, soil relative density, and moisture condition. Finally, the effect of the selected modeling method (WIP or WIM) on the anticipated displacements during the subsequent excavation is highlighted.

2. Case Study and Model Verification

The selected case study is a diaphragm wall constructed to be a part of the basements of a multi-story building in Dokki, Giza, Egypt (El-Sayed & Abdel-Rahman, 2002; Abdel-Rahman & El-Sayed, 2009). The soil stratification at this site is shown in Fig. 1 as well as the results of the SPT tests with depth. The ground water table was monitored at a depth of 2.0 m below the ground surface.

As shown in Fig. 2, the excavation site is 24.6 m times 35.7 m and is surrounded by five existing buildings. Buildings A, B and C are 12 to 14 stories high and are founded on piles with lengths ranging between 14.0 m and 16.0 m and are located at distances of 1.8 m, 3.15 m and 7.15 m away from the excavated site, respectively. Buildings D and E are 5 and 2 story buildings, respectively. Both buildings are founded on shallow foundations at 2 m depth and are located at a distance of 3.2 m from the excavation site.

The excavation depth was 10.8 m below the ground surface, therefore, a side support system was needed. This supporting system was composed of a diaphragm wall supported by two rows of anchors and struts. The diaphragm wall width (w) is 0.6 m, depth (D) is 21 m, and the panels' lengths (L) range between 2.70 m and 6.72 m. The total number of panels is 20.

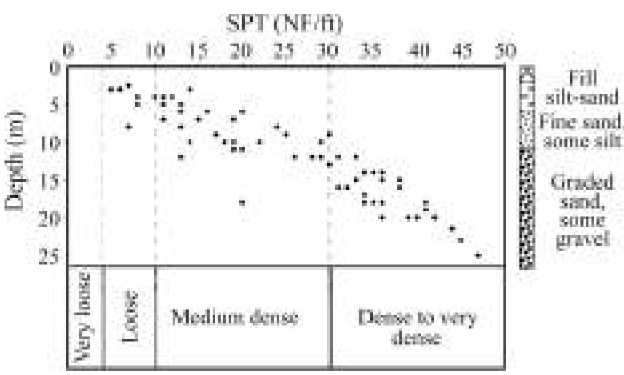

Figure 1 - Soil stratification and SPT data (Abdel-Rahman & El Sayed, 2009).

An optical surveying program was adopted to monitor the settlement of adjacent buildings due to the construction of the side support system and excavation. As shown in Fig. 2, thirty one settlement points (SP-1 to SP-31) were fixed on selected columns at the location of adjacent buildings.

Figure 3 shows the measured total settlements due to construction of the diaphragm wall and excavation down till the designated depth. Despite being founded on piles, considerable settlement values were observed at Buildings A, B, and C. For these buildings, the total settlement ranged between 0.0 mm and 12.5 mm (Fig. 3a). The maximum value occurred at SP-19 (Building B). This point was located at a distance of 3.15 m from the diaphragm wall. None to negligible settlement values were detected at SP-1, SP-2, SP-28, SP-29, and SP-30 which were located at distances of 18 m to 40 m away from the corners of the site. Due to construction of the diaphragm walls, the measured settlements ranged between 0.0 mm and 8.6 mm which implied that at least 44 % of the total settlement values took place before excavation. The diaphragm wall is 21 m deep whilst the piles are 14 m to 16 m deep which may explain why most of the settlement took place during the execution of the diaphragm wall. For Buildings D and E (on shallow foundations), the total settlement ranged between 1.2 mm and 17.8 mm. The maximum value occurred at SP-23 (Building E). This point was located at a distance of 3.2 m from the diaphragm wall. Insignificant settlement value was detected at SP-24, which is located at a distance of about 14 m from the corner of the site. Due to construction of the diaphragm walls, the measured settlements ranged between 0.4 mm and 8.6 mm, which implied that 14 % to 50 % of the total settlement values took place (Fig. 3b).

These measurements confirm the importance of estimating the displacements induced during the construction of the diaphragm walls while studying the effect of installing a side support system and excavation. Therefore, verification models are constructed via the 3D finite element program (PLAXIS©). The soil mass is simulated as a continuum composed of 10-node tetrahedron volume elements. For all soil layers, the Hardening Soil Model (HSM) is applied. Table 1 presents the assigned parameters for each soil layer. For buildings on deep foundation, due to lack of data, a surcharge load of 150 kN/m^2 is simulated at a depth of 16 m below the ground surface. Buildings founded on shallow foundations are simulated as a 40 kN/m^2 surcharge load at 2 m below the ground surface as shown in Fig. 4.

Two models have been studied to determine the effect of the diaphragm wall simulation technique. The dia-

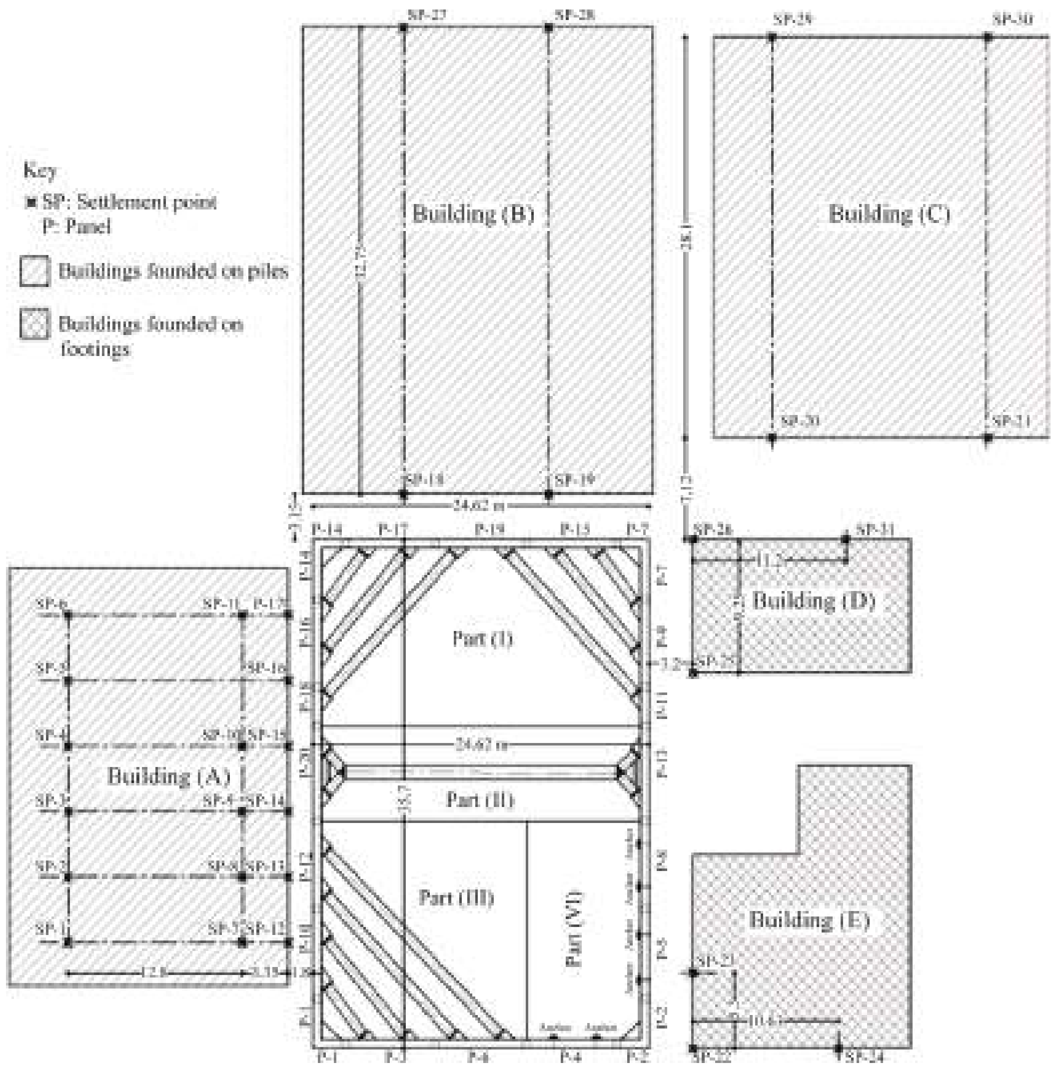

Figure 2 - Excavation site and adjacent buildings (Abdel-Rahman & El Sayed, 2009).

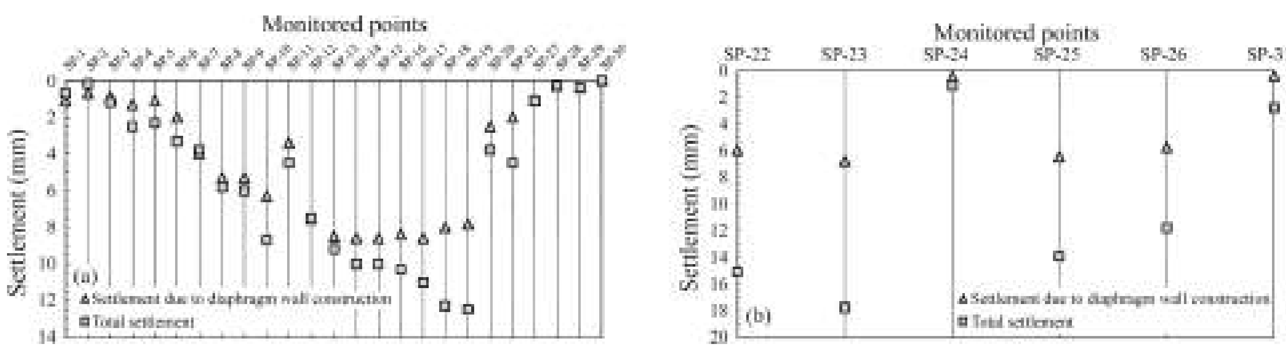

Figure 3 - Field measurements for buildings founded on: (a) deep foundation and (b) shallow foundations.

phragm wall is simulated using either WIP method or WIM method. In the WIP method, the diaphragm wall is simulated as a plate element. The plate element is formed based on Mindlin's plate theory to simulate a thin two-dimensional structure with flexural rigidity and a normal stiffness. Herein, the plate is modeled as an elastic isotropic concrete material and its properties are: unit weight (γ_c) = 24 kN/m^3, Young's modulus (E) = 2.6 x 10^7 kN/m^2 and Poisson's ratio (ν) = 0.20. The model considers the sequence of construction in three stages. At the first stage, the soil initial stresses are generated using the K_o procedure. At

Table 1 - Soil properties for the case study (Hardening Soil Model).

Layer	Fill	Silty sand	Fine sand	Graded sand
Thickness (m)	2	3	6	14
Saturated unit weight, γ (kN/m^3)	17	18	19	20
Secant stiffness in standard drained triaxial test, E^{ref}_{50} (MPa)	6	16	25	25
Tangent stiffness for primary oedometer loading, E^{ref}_{oed} (MPa)	6	16	25	25
Unloading/reloading stiffness, E^{ref}_{ur} (MPa)	18	48	75	75
Power for stress-level dependency of stiffness, m	0.5	0.5	0.5	0.5
Effective cohesion, c' (kPa)	0.01	0.01	0.01	0.01
Effective angle of shearing resistance, ϕ (deg)	29	31	33.5	36
Dilatancy angle, Ψ (deg)	0	1	3.5	6
Poisson's ratio, ν_{ur}	0.2	0.3	0.3	0.3
Earth pressure coefficient at rest, K_o	0.515	0.485	0.448	0.412

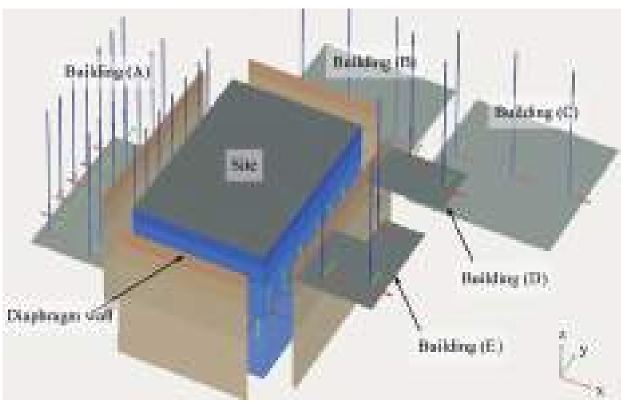

Figure 4 - PLAXIS three dimensional model configuration for case study.

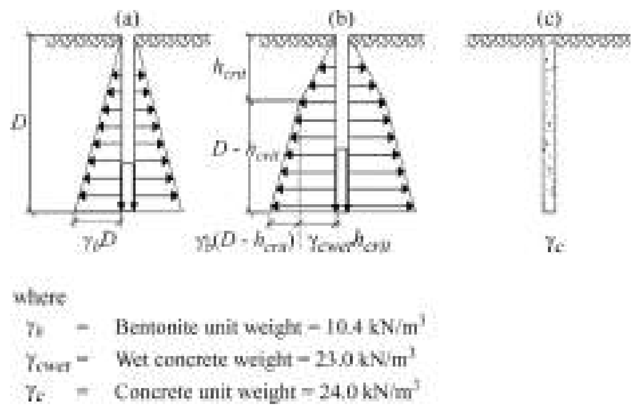

Figure 5 - Construction stages of diaphragm wall.

the second stage, the surcharge loads of adjacent buildings are activated. At the third stage, the diaphragm wall (plate element) is activated.

In the WIM method, the diaphragm wall panels are simulated as volume elements. The model is developed to consider the construction stages of each panel. First, the soil initial stresses are generated using the K_o procedure. Second, the surcharge loads of adjacent buildings are activated. Third, the excavation under slurry support is simulated by deactivating soil elements inside the trench. Simultaneously, the hydrostatic bentonite pressure with a unit weight (γ_b) of 10.4 kN/m^3 is applied along the trench sides and bottom (Fig. 5a). Fourth, wet concrete is poured into the trench replacing the bentonite slurry. Thus, the bentonite hydrostatic pressure is replaced by bi-linear pressure (Fig 5b). A full concrete pressure with a unit weight (γ_{cwet}) of 23 kN/m^3 is applied down to a critical depth (h_{crit}) below which the pressure increases along depth with the bentonite pressure. Fifth, concrete hardens, hence, the bi-linear pressure is removed and the volume elements inside the trench are activated as elastic isotropic concrete volumes with unit weight (γ_c) equal to 24 kN/m^3, $E = 2.6 \times 10^7$ kN/m^2 and Poisson's ratio $\nu = 0.20$ as shown in Fig. 5c. For each panel, the last three stages (third to fifth) are repeated according to the construction schedule executed on site.

Figure 6 depicts that the WIP method underestimates the settlement values at the selected points by 63 % to 85 %. The calculated settlements range between 0.4 mm and 1.6 mm for buildings A, B, and C and between 0.4 mm and 1.2 mm for buildings D and E. On the other hand, the WIM method presents a better prediction. The calculated settlements range between 0.7 mm and 10.6 mm for buildings A, B, and C and between 2.1 mm and 10.1 mm for buildings D and E. Figure 7 presents the horizontal displacement contours using both the WIP and WIM methods. It can be noted that negligible values are acquired using the WIP method, however, higher values are attained using the WIM method. Furthermore, the WIP method shows an almost uniform distribution of displacements all over the site. The WIM method shows a more realistic trend where higher displacement values occur along the diaphragm panels. In

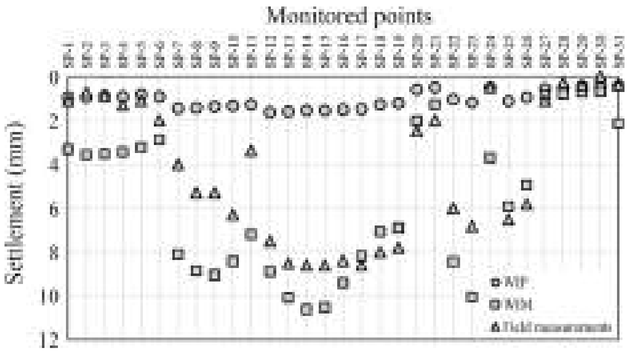

Figure 6 - Field measurements *vs.* calculated settlements using 3D FEM.

addition, concentration of displacements is noticed around the panels especially at the right and bottom sides of the site. By reviewing the panels' lengths and construction schedule, it is found that these higher values occurred where longer successive panels were executed. The model constructed using the WIP method also shows that the construction of diaphragm walls generates insignificant values of straining actions.

Based on the above results, the WIM method is adopted for the parametric study. The current study focuses on investigating the effect of construction of the diaphragm wall on the generated soil stresses and displacements.

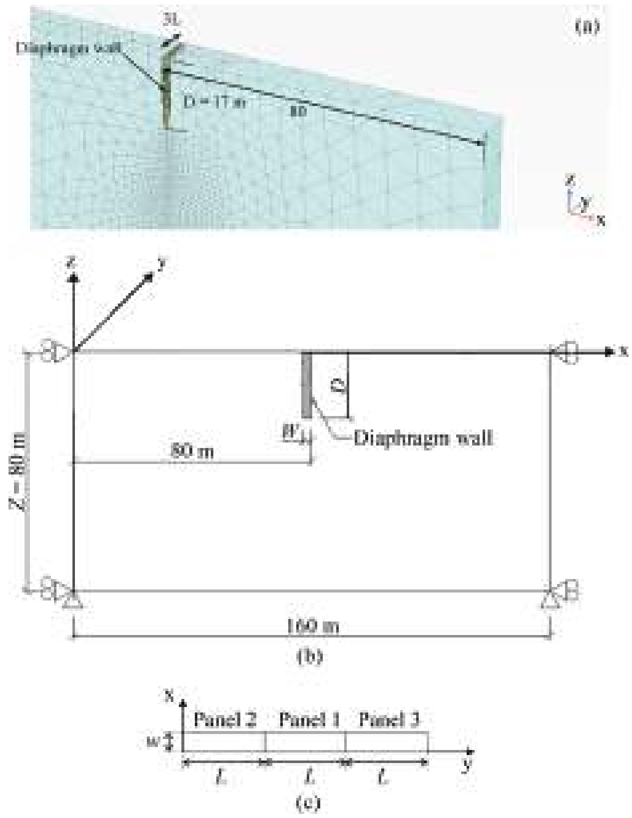

Figure 8 - Proposed model: (a) Meshing (b) Configuration and (c) Panels geometry.

3. Results and Discussion

In order to investigate the effect of diaphragm wall construction on ground movement and soil stresses, a 3D model of a diaphragm wall with a depth (D) of 17 m is simulated (Fig. 8a and b). The diaphragm wall is composed of three panels as presented in Fig. 8c. Panel 1 is a primary panel, panels 2 and 3 are secondary panels. Each panel is simulated in stages according to the construction sequence mentioned in the previous section, with a total number of nine stages. Construction of panel 1 is simulated in stages 1 to 3, followed by panel 2 (stages 4 to 6) and panel 3 (stages 7 to 9).

The effect of parameters related to diaphragm wall geometry including panel length (L = 3 m, 6 m, and infinity) and panel width (w = 0.6 m, 0.9 m, 1.2 m) have been stud-

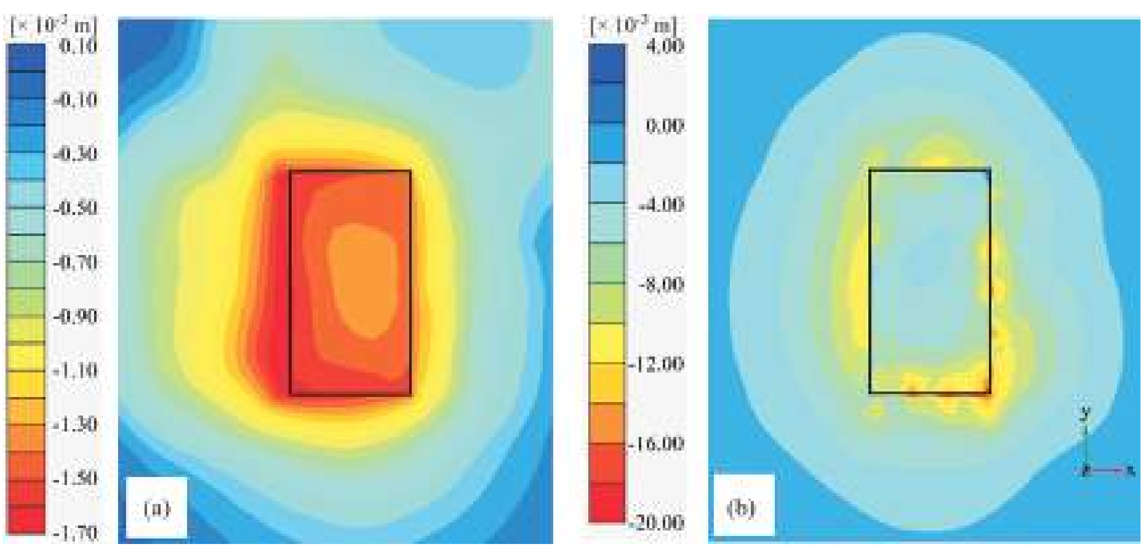

Figure 7 - Horizontal displacement contours: (a) WIP method and (b) WIM method.

ied. In addition, the effect of soil relative density is investigated. The diaphragm wall is constructed in loose, medium dense, and dense sand with properties shown in Table 2. Next, a comparison between constructing the diaphragm wall in dry sand *vs.* saturated sand is conducted.

The model dimensions (80 m times 180 m) are selected such that the model borders have no influence neither on induced settlements, nor on stresses. The bottom of the geometry is fixed and the upper boundaries are fully free to move. For the sides, the displacements normal to the boundary are fixed and the tangential displacements are kept free.

The construction process of the diaphragm wall panels has a major impact on the stress distribution behind the wall. For a diaphragm wall with w = 0.6 m and L = 3.0 m constructed in dry medium dense sand, Fig. 9 depicts the change of horizontal stresses behind the wall along the center of panel 1. In order to understand the trend in which the stresses change, three additional lines are plotted: initial horizontal stress, bentonite pressure, and concrete pressure. For medium dense sand:

$$\text{Initial horizontal stress} = \gamma\, K_o\, Z = 19 \times 0.426\, Z = 8.09\, Z \text{ kN/m}^3\text{/m} \quad (1)$$

$$\text{Bentonite pressure} = \gamma_b\, Z = 10.4\, Z \text{ kN/m}^3\text{/m} \quad (2)$$

$$\text{Concrete pressure} = \gamma_{cwet}\, Z = 23\, Z \text{ kN/m}^3\text{/m} \quad (3)$$

where g is the soil unit weight, K_o is the earth pressure coefficient at rest, Z is the depth below ground surface, γ_b is the bentonite unit weight, and γ_{cwet} is the wet concrete unit weight. The current study is performed in sandy soils, hence, the initial horizontal stress is lower than the subsequent applied pressures (bentonite and concrete). Thus, during the construction of panel 1, the horizontal stresses generally increase (stages 1 to 3, Fig. 9a). This trend is the opposite of the results observed by Ng & Yan (1999). In clayey soils, the initial horizontal stress is larger than the subsequent applied pressures (bentonite and concrete). Therefore, horizontal stresses are reduced during the construction of the panel.

Underneath the wall, the horizontal stress values fall below their initial state (K_o condition) due to the restraint provided by the underlying soil. This trend extends to a distance of about 5 m (0.3D) underneath the wall bottom, which complies with the results of Conti *et al.* (2012).

During the construction of panel 1, the horizontal stresses increase during the stage of trench excavation under bentonite support (stage 1, Fig. 9a).The injection of wet concrete (stage 2, Fig. 9a) leads to a further increase in the horizontal stresses, particularly in the upper third of the retaining wall. The horizontal stresses follow the bi-linear pressure applied during stage 2. However, negligible change is detected during concrete hardening (stage 3, Fig. 9a). The same trend is found when the construction advances from stage 5 to 6 and from stage 8 to 9, as shown in Fig 9b. The construction of panels 2 (stages 4 to 6) and panel 3 (stages 7 to 9) causes a drastic decrease in horizontal stresses behind panel 1 (Fig. 9b). At stage 9, the stresses are less than the initial stresses. This could be further examined using Fig. 10, which shows the total horizontal stress at a distance of 0.1 m behind the panels at a depth of 8.5 m below the ground surface. A horizontal section is plotted with distance measured from the edge of panel 2 normalized by the length of panel (y/L). It is found that the construction of

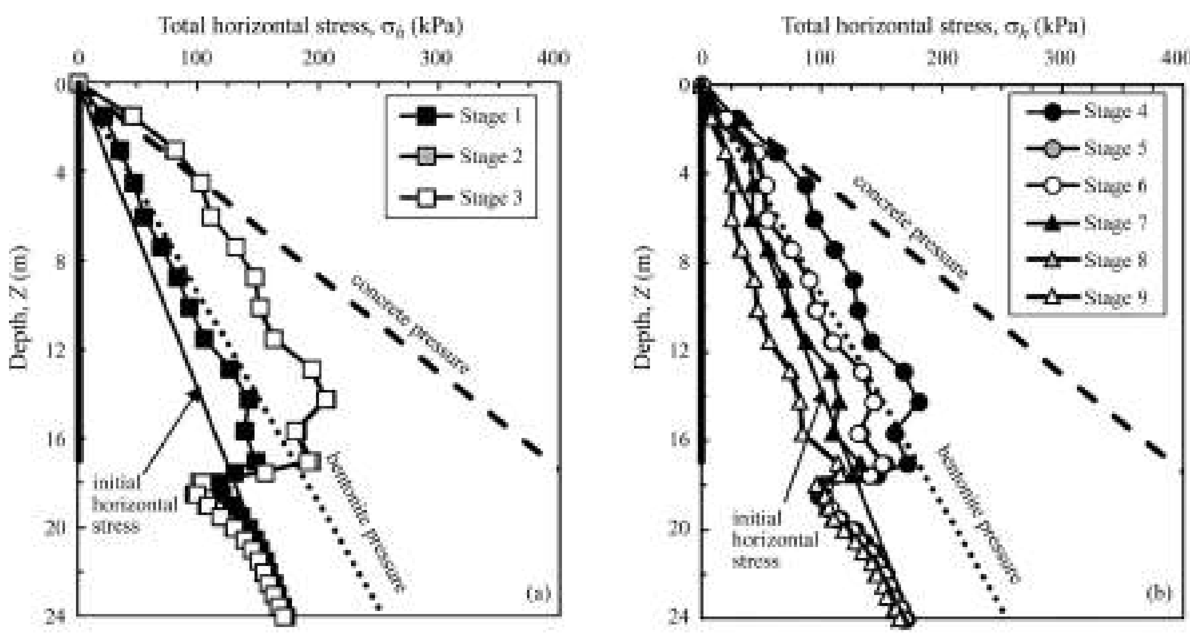

Figure 9 - Horizontal stress distribution with depth across the center of panel 1: (a) construction of panel 1 and (b) construction of panels 2 and 3 (medium dense dry sand, w = 0.6 m, L = 3.0 m, D = 17 m).

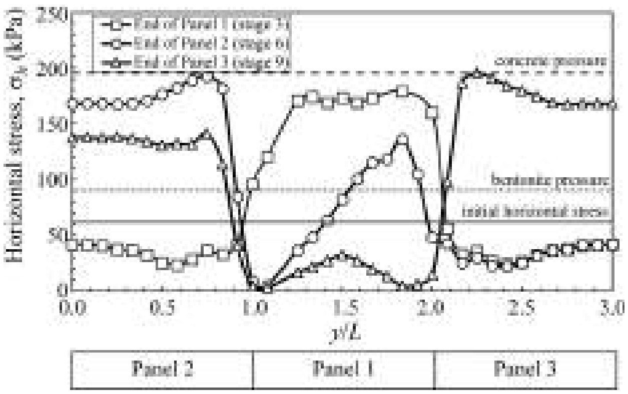

Figure 10 - Horizontal stress distribution at 0.1 m behind the diaphragm wall at 8.5 m depth below ground surface (medium dense dry sand, w = 0.6 m, L = 3.0 m, D = 17 m).

a certain panel causes a maximum increase in the horizontal stresses behind the center of this panel, then, stresses decrease gradually toward the edge of this panel and adjacent panels. This trend is attributed to the lateral stress transfer which is also observed by Conti *et al.* (2012).

Figure 11 inspects the effect of diaphragm wall installation on the soil movement behind the wall along the center of panel 1. During the stages of bentonite and wet concrete injections, the soil horizontal stresses increase, consequently, the soil horizontal displacements increase (Fig. 11a). However, no further horizontal displacements are experienced behind this panel once concrete hardens. The construction of the adjacent panels does not cause any additional displacements to the studied panel. In addition, the maximum horizontal displacement values occur approximately at half the panel depth (0.5D) below the ground surface, which matches the results obtained by Conti *et al.* (2012). Moreover, the effect of diaphragm wall installation almost diminishes at 5 m below the wall toe, *i.e.*, approximately one third of the wall depth (0.3D), which is verified by Ng & Yan (1998).

The soil horizontal displacements are accompanied by settlements near the diaphragm wall. As shown in Fig. 11b, settlement values occur directly behind the wall and become marginal after a distance of 17 m behind the wall which is equivalent to 1D, which matches the results of Powrie & Kantartzi (1996) and Ng & Yan (1998). The settlements increase as the wall installation proceeds. Behind a given panel, about 75 % of the total expected settlement is developed by the end of construction of this panel while the remaining 25 % occurs during the construction of the two adjacent secondary panels.

3.1. Effect of diaphragm wall geometry

Figure 12 presents the effect of the panel length (L) and width (w) on the soil horizontal stresses and displacements. Panels with lengths of 3 m, 6 m and infinity and widths of 0.6 m, 0.9 m, and 1.2 m are selected. A panel length of infinity is attained via plane strain condition, which can be done using a 2D model (Fig. 13). The same procedure adopted for 3D modeling of the construction sequence of the diaphragm wall is used. In engineering practice, 2D modeling is usually adopted because 3D modeling is more complicated and time consuming.

Figure 12a shows that using longer panels leads to higher horizontal stresses behind panel 1, hence, larger val-

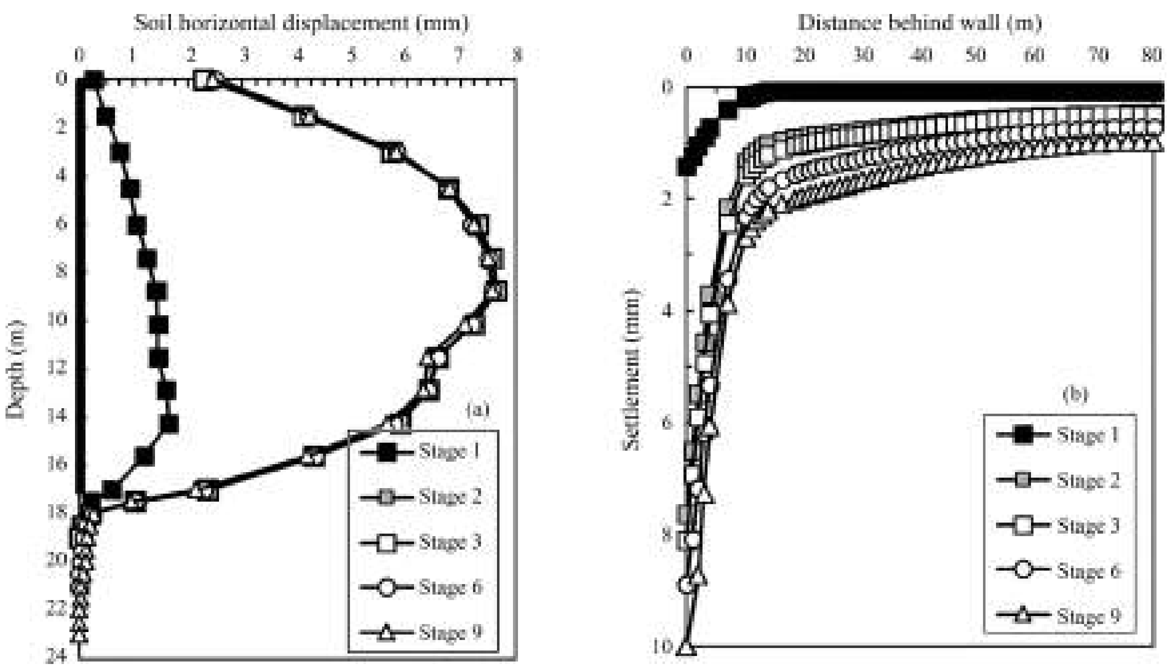

Figure 11 - (a) Soil horizontal displacements along the diaphragm wall and (b) Settlement behind the diaphragm wall (at the center of panel 1 - medium dense dry sand, w = 0.6 m, L = 3.0 m, D = 17 m).

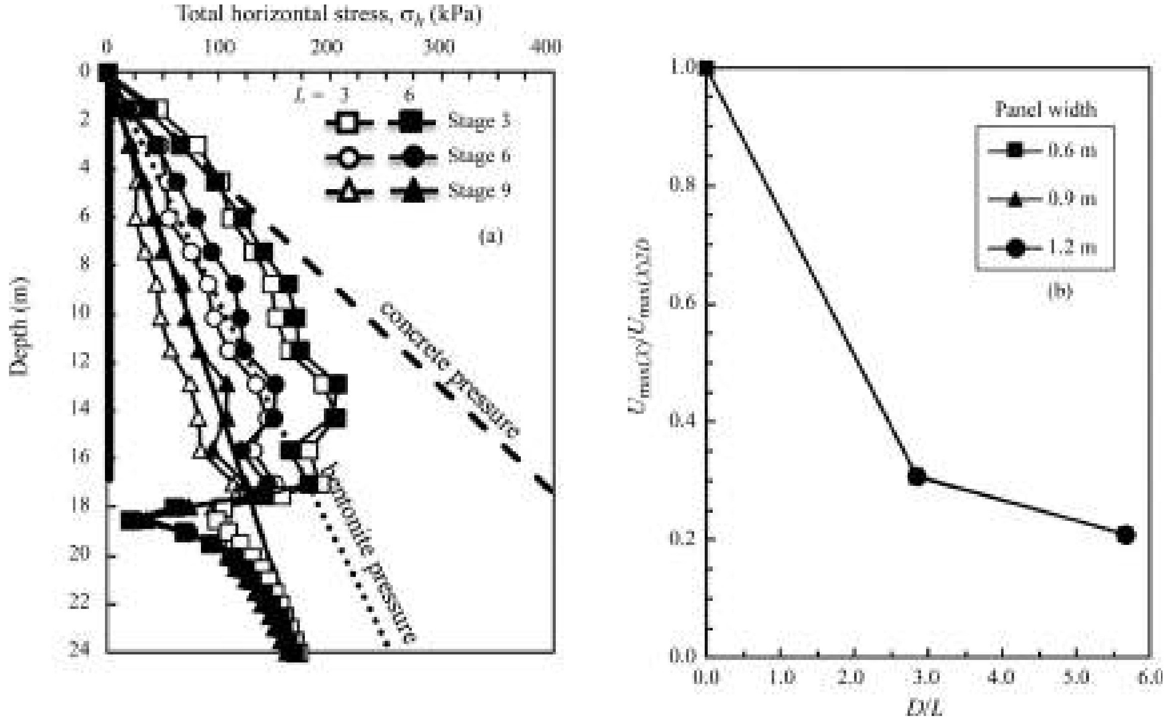

Figure 12 - Effect of panel dimensions on soil: (a) horizontal stresses, (b) horizontal displacements at stage 9 (at the center of panel 1 - medium dense dry sand, D = 17 m).

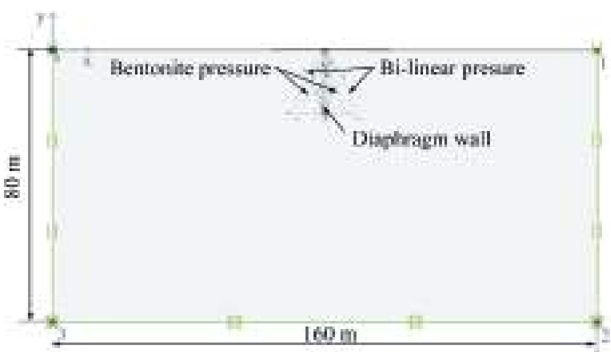

Figure 13 - 2D Model (plane strain condition).

ues of horizontal displacements are expected. In Fig. 12b, the maximum horizontal displacements behind panel 1 are normalized to the maximum values obtained from the plane strain condition ($U_{max(X)}/U_{max(X)2D}$). The results are plotted *vs.* the panel depth to length ratio (D/L). As the panel length increases (D/L reduces), the horizontal displacements increase gradually until reaching a maximum value at D/L = 0 (plane strain condition). The results presented herein show that modeling diaphragm wall installation as a plane strain problem leads to the over-prediction of the soil displacements and stresses during installation by 230 % to 400 %. This approach leads to unrealistic values of ground movement because it does not account for the arching effect (Ng & Yan, 1998). On the other hand, panel width has no effect on soil horizontal displacements during the construction of the diaphragm wall as shown in Fig. 12b.

3.2. Effect of soil relative density and moisture condition

The effect of soil relative density is investigated using sand with three different relative densities presenting loose, medium dense, and dense soil as proposed in Table 2. The angle of shearing resistance (ϕ) is introduced in Fig. 14 as an indication of the soil relative density. As the soil becomes denser, the maximum soil displacements decrease. This is attributed to the fact that the increase in soil relative density is associated with an increase in soil stiffness (E) as shown in Table 2. The rate of decrease in displacement values declines as the relative density increases. At the end of construction of panel 3 (stage 9), the maximum vertical displacement (settlement) decreases from 22 mm for loose sand to 10 mm for medium dense sand (54.5 % reduction), and to 5.5 mm for dense sand (31.3 % reduction).

The diaphragm wall construction sequence is also simulated in saturated sand in order to inspect the effect of moisture on the performance of the wall. First, horizontal stresses are investigated as shown in Fig. 15a. The horizontal stresses decrease during bentonite injection (Stage 1), then increase again during the concrete injection and hardening (stages 2 & 3). This trend contradicts the results obtained from the dry sand case (Fig. 9a). This is attributed to the fact that the initial stresses, in saturated sand, are larger than bentonite pressure and lower than the wet concrete bi-linear pressure. For medium dense sand:

Table 2 - Proposed different granular soil types of different relative density (Hardening Soil Model).

Soil type	Loose	Medium dense	Dense
Saturated unit weight, γ (kN/m^3)	18	19	20
Secant stiffness in standard drained triaxial test, E^{ref}_{50} (MPa)	20	40	60
Tangent stiffness for primary oedometer loading, E^{ref}_{oed} (MPa)	20	40	60
Unloading/reloading stiffness, E^{ref}_{ur} (MPa)	60	120	180
Power for stress-level dependency of stiffness, *m*	0.5	0.5	0.5
Effective cohesion, *c'* (kPa)	0.01	0.01	0.01
Effective angle of shearing resistance, ϕ (deg)	30	35	40
Dilatancy angle, Ψ (deg)	0	5	10
Poisson's ratio, ν_{ur}	0.3	0.3	0.3
Earth pressure coefficient at rest, K_o	0.500	0.426	0.357

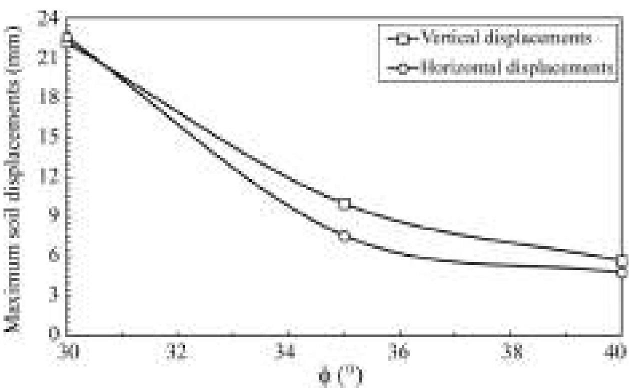

Figure 14 - Effect of soil relative density on maximum soil displacements (at the center of panel 1 - dry Condition, w = 0.6 m, L = 3.0 m, D = 17 m).

$$\text{Initial horizontal stress} = \gamma_{sub} K_o Z + \gamma_w Z = 9 \times 0.426 Z + 10 Z = 13.8 Z \text{ kN/m}^3\text{/m} \quad (4)$$

$$\text{Bentonite pressure} = \gamma_b Z = 10.4 Z \text{ kN/m}^3\text{/m} \quad (5)$$

$$\text{Concrete pressure} = \gamma_{cwet} Z = 23.0 Z \text{ kN/m}^3\text{/m} \quad (6)$$

where γ_{sub} is the soil submerged unit weight, K_o is the earth pressure coefficient at rest, Z is the depth below ground surface, γ_w is the water unit weight, γ_b is the bentonite unit weight, and γ_{cwet} is the wet concrete unit weight. This reduction in stresses during bentonite injection (Stage 1) causes the trench side to move in the reverse direction. Figure 15b shows the horizontal displacements along one side of the trench during stage 1 for dry sand and saturated sand. The positive values of the horizontal displacement indicate that the trench cross section increases (bulging). On the other hand, the negative values of the horizontal displacement indicate that the trench cross section decreases (necking). The maximum necking (saturated sand) or bulging (dry sand) occurs at a depth of 14.25 m (0.84*D*). At stage 2 (Fig. 15c), the horizontal stresses increase again; accordingly, the direction of the horizontal displacement is reversed again and becomes positive for saturated sand. Meanwhile, further increase in the horizontal displacement is noticed at the same stage for dry sand. It is also noted that the depth at which the maximum horizontal displacement occurs is shifted upward. The maximum bulging occurs at depth of 4.5 m (0.26*D*) for saturated sand and at depth of 7.7 m (0.45*D*) for dry sand. Figure 15d shows the maximum horizontal displacement ($U_{\max(X)}$) and settlement ($U_{\max(Z)}$) during construction (stages 1 to 9) for dry and saturated sand. Once the concrete hardens (stage 3), the horizontal displacements become constant and no further change is expected due to the following construction stages. On the other hand, the settlement values continue to increase after stage 3 at a lower rate.

4. Effect of the Modeling Technique on the Displacements During Subsequent Excavation

The effect of the modeling technique is investigated for a diaphragm wall with w = 0.6 m and L = 3.0 m constructed in dry medium dense sand. Two models are developed using WIP and WIM methods. For each model, the soil in front of the diaphragm wall is excavated to a depth of 8 m. Due to excavation, the WIP method overestimates the horizontal displacement of the diaphragm wall by around 50 % (Fig. 16a). The maximum horizontal displacement is about 26 mm using the WIM method and 40 mm using the WIP method. On the other hand, the estimated settlement values behind the wall using the WIP method are higher by 14 %. Nevertheless, the WIP method underestimates the settlement values due to diaphragm wall construction by 87 %; after excavation the effect of using this simplification has less impact on the results (Fig. 16b).

5. Conclusions

In this study, the finite element numerical model succeeded in simulating the complicated construction se-

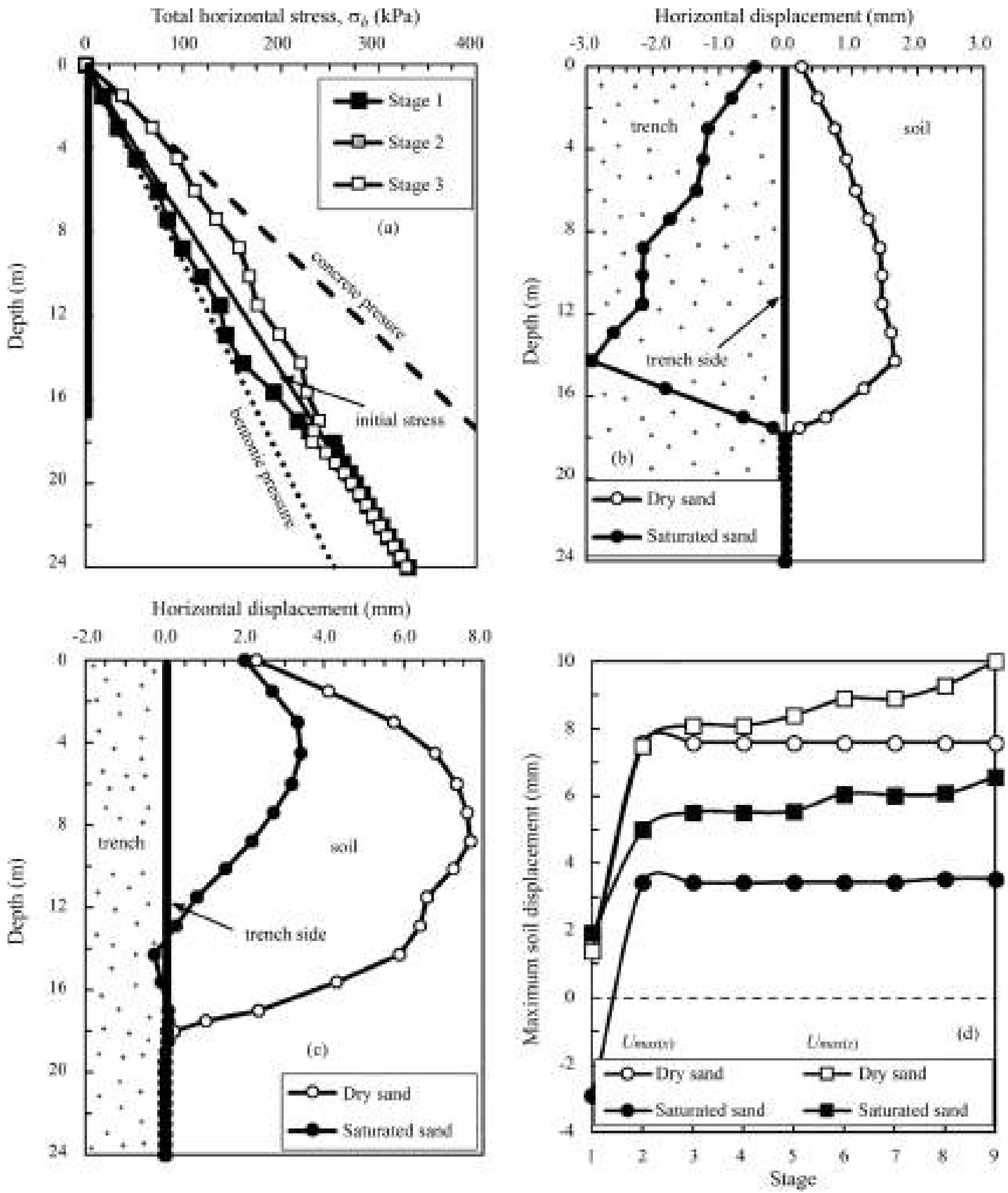

Figure 15 - Effect of moisture condition on: (a) horizontal stresses (b) horizontal displacements at stage 1 (c) horizontal displacements at stage 2 and (d) max displacements for stages 1 to 9 (at the center of panel 1 - medium dense Sand, w = 0.6 m, L = 3.0 m, D = 17 m).

quence of diaphragm walls. The model output has been validated through a comparison with the field measurements of the settlement values recorded during execution of the side support system and excavation of a site in Dokki, Egypt. The diaphragm wall construction process can be simulated using the WIM and WIP methods. The WIP method is the conventional finite element method. The effect of diaphragm wall construction stages is not considered, therefore, no changes in soil stresses or movements are anticipated. On the other hand, this study has proved that the WIM method is capable of simulating the construction stages and capturing the changes in soil stresses and displacements. The construction sequence for each panel is simulated through three stages representing: (1) excavation under slurry support, (2) wet concrete injection, and (3) concrete hardening. The construction sequence is found to have a major impact on the stress distribution behind the wall. In dry sandy soils, an increase in horizontal stresses

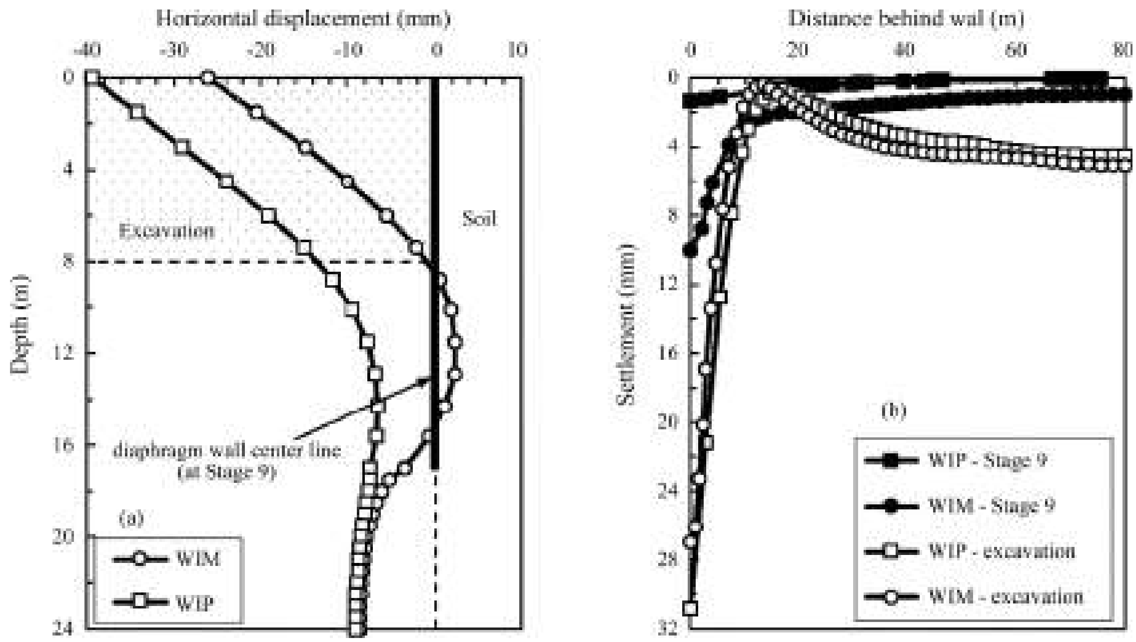

Figure 16 - Effect of modeling technique on: (a) diaphragm wall horizontal displacements after excavation and (b) settlements (along the center of panel 1 - medium dense sand, w = 0.6 m, L = 3.0 m, D = 17 m).

behind the primary panel is expected during the bentonite and wet concrete injection stages. However, a drastic decline in horizontal stresses is noticed during the construction of secondary panels. The installation of the diaphragm wall causes an increase in soil movement. The maximum horizontal displacement values occur approximately at 0.5D below the ground surface. The horizontal displacement along the primary panel take place only during the bentonite and wet concrete injection stages. The construction of secondary panels does not cause any additional horizontal displacement. However, behind the primary panel, about 75 % of the total expected vertical displacements are developed by the end of construction of this panel, while the remaining 25 % occur during the construction of the secondary panels.

In engineering practice, 2D modeling is used as a conventional tool to determine the expected displacements. However, the results presented herein show that modeling diaphragm wall installation as a plane strain problem leads to the overestimation of the displacements. Subsequently, over-designed side support systems are provided. Simulating the actual panel length using a 3D model leads to lower and more realistic values of stresses and displacements. In addition, an increase in soil relative density leads to a pronounced decrease in the induced displacement. Moreover, in saturated sandy soils, initial horizontal stresses are larger than bentonite pressure, therefore, necking of the trench section occurs. Finally, adopting different techniques of modeling the construction sequence of diaphragm wall has a major impact on the estimated displacement during the following excavation stage.

References

Abdel-Rahman, A.H. & El-Sayed, S.M. (2009). Foundation subsidence due to trenching of diaphragm walls and deep braced excavations in alluvium soils. Hamza *et al.* (Eds), Proc. 17th Int. Conf. on Soil Mechanics and Geotechnical Engineering, ISSMGE, Alexandria, Egypt, pp. 1935-1938.

Arai, Y.; Kusakabe, O.; Murata, O. & Konishi, S. (2008). A numerical study on ground displacement and stress during and after the installation of deep circular diaphragm walls and soil excavation. Computers and Geotechnics, 35(5):791-807.

Burlon. S.; Mroueh, H. & Shahrour, I. (2013). Influence of diaphragm wall installation on the numerical analysis of deep excavation. International Journal for Numerical and Analytical Methods in Geomechanics, 37(11):1670-1684.

Clear, A. & Harrison, A. (1985). Concrete pressure on formwork. Construction Industry Research and Information Association, CIRIA Report 108.

Conti, R.; de Sanctis, L. & Viggiani, G.M. (2012). Numerical modeling of installation effects for diaphragm walls in sand. Acta Geotechnica, 7(3):219-237.

Cowland, J.W. & Thorley, C.B.B. (1984). Ground and building settlement associated with adjacent slurry trench excavation. Proc. 3rd Int. Conf. on Ground Movements and Structures, pp. 723-728.

De Moor, E.K. & Stevenson, M.C. (1996). Evaluation of the performance of a multi-propped diaphragm wall during construction. Proc. Int. Symposium on Geotechnical Aspects of Underground Construction in Soft Ground, Balkema, pp. 111-116.

El-Sayed S.M. & Abdel-Rahman, A.H. (2002). Spatial stress-deformation analysis for installation of a diaphragm wall. Faculty of Engineering Scientific Bulletin, Ain Shams University, 37(3):75-90.

Gourvenec, S.M. & Powrie, W. (1999). Three-dimensional finite-element analysis of diaphragm wall installation. Géotechnique, 49(6):801-823.

Li, A.J. & Lin, H.D. (2018). Analyses of ground response induced by diaphragm wall installation. Chen, R.; Zheng, G. & Ou, C. (eds), Proc. 2nd Int. Symposium on Asia Urban Geoengineering. Springer Series in Geomechanics and Geoengineering. Springer, Singapore.

Lings, M.L.; Ng, C.W. & Nash, D.F.T. (1994). The lateral pressure of wet concrete diaphragm wall panels cast under bentonite. Proc. of the Institution of Civil Engineers-Geotechnical Engineering, 107(3):163-172.

Ng, C.W.; Lings, M.L.; Simpson, B. & Nash, D.F.T. (1995). An approximate analysis of the three-dimensional effects of diaphragm wall installation. Géotechnique, 45(3):497-507.

Ng, C.W. & Yan, R.W. (1998). Stress transfer and deformation mechanisms around a diaphragm wall panel. Journal of Geotechnical and Geoenvironmental Engineering, 124(7):638-648.

Ng, C.W. & Yan, R.W. (1999). Three-dimensional modeling of a diaphragm wall construction sequence. Géotechnique, 49(6):825-834.

Poh, T.Y. & Wong, I.H. (1998). Effects of construction of diaphragm wall panels on adjacent ground: field trial. Journal of Geotechnical and Geoenvironmental Engineering, 124(8):749-756.

Powrie, W. & Kantartzi, C. (1996). Ground response during diaphragm wall installation in clay: centrifuge model tests. Géotechnique, 46(4):725-739.

Symons, I.F. & Carder, D.R. (1993). Stress changes in stiff clay caused by the installation of embedded retaining walls in retaining structures. Proc. Conf. organized by the Institution of Civil Engineers, Robinson College, Cambridge.

Bayesian Update of Load Capacity for a Large Steel Piling in a Stratified Soil Profile

J.A. Nietiedt, B.R. Danziger, M.S.S. Almeida

Abstract. This paper applies Bayesian updating of the load capacity of a large steel piling foundation for the high load structure of the Alcântara Wastewater Treatment Plant (WWTP), located near the city of Rio de Janeiro in Brazil. Uncertainty is modeled by *a priori* and *a posteriori* distributions of the piling capacity. The *a posteriori* distribution is determined by updating the *a priori* distribution using a likelihood function, which incorporates records obtained during pile driving. The Bayesian update was applied to a dataset consisting of 645 steel driven piles. Two pile capacity design models and two different likelihood functions were used to verify their influence on the updated capacity estimates. Static and dynamic test results were compared to the updated estimates. The results demonstrate the ability of the Bayesian update technique to significantly improve the reliability of the entire piling.

Keywords: Bayesian theory, reliability, steel piles.

1. Introduction

Pile capacity predictions usually involve numerous uncertainties due to measurement errors in soil properties, limitations of geotechnical investigation, spatial variability across a site, model simplifications, among others. Huang *et al.* (2016) also point out that installation processes may also vary from pile to pile and affect the variability of the ultimate pile capacity. Kay (1976) presented an interesting application of probability theory to develop a consistent set of guidelines for safety factor selection for a range of design methods. He demonstrated that such an approach provides the basis for the optimization of the testing procedure and an improved final design. Kay’s 1976 method makes use of the Bayesian approach, which permits the inclusion of subjectively determined aspects of the design in the formal analysis. A sampling from the “state of nature”, according to Kay (1976), allows for a formal reduction in uncertainty through the application of Bayesian theory.

Estimates of pile and pile group reliability based on load test results have been reported by Baecher & Rackwitz (1982), Zhang *et al.* (2001), Zhang (2004), Zhang *et al.* (2006, 2010, 2014) and Huang *et al.* (2016). Guttormsen (1987) applied the wave equation model for obtaining the likelihood distribution function when performing the Bayesian update for offshore piles. One of the strong points of the application of reliability theory is the possibility of combining various methods, as reported by Lacasse *et al.* (1991) who made use of a pile capacity calculation model and estimation based on some measurement activity to obtain an updated estimate. Vrouwenvelder (1992) emphasized that based on information from testing and monitoring, the engineer may update the estimate of pile capacity. Moreover, as the new estimate is based on more information, the uncertainties are fewer and a corresponding reduction of the safety factor could be justified. Lacasse & Nadim (1994) commented on the importance of adopting rational approaches and well documented projects to account for load capacity uncertainties. Zhang &Tang (2002) applied the Bayesian theory to piling reliability using load test results in the updates. The same approach can have other applications. Baecher & Ladd (1997), for instance, used Bayesian theory in the prediction of clay properties such as undrained strength and overconsolidation ratio. Zhang *et al.* (2004) applied the Bayesian approach to update empirical predictions with regional information or site-specific observations to effectively reduce the uncertainty associated with the correlations. Goh *et al.* (2005) used a Bayesian network algorithm to model the relationship between the undrained shear strength of soil, the effective overburden stress and the undrained side resistance alpha factor for drilled shafts. Li *et al.* (2017) illustrated the application of Bayesian theory to evaluate the spatial variability of soil in slope stability projects.

The objective of this paper is to apply the Bayesian updating technique to update the expected value and variance of the probability distribution of soil resistance to driving for H-section steel piles. For driven piles, the construction processes can be better controlled and the variabilities due to construction are expected to vary in smaller ranges.

Juliano Augusto Nietiedt, M.Sc., Universidade Federal do Rio de Janeiro, COPPE, Rio de Janeiro, RJ, Brazil, e-mail: juliano.auni@gmail.com.
Bernadete Ragoni Danziger, Dr., Full Professor, Departamento de Estruturas e Fundações, Universidade do Estado do Rio de Janeiro, Rio de Janeiro, RJ, Brazil, e-mail: bernadeterd@hotmail.com.
Márcio de Souza Soares de Almeida, Ph.D., Full Professor, Universidade Federal do Rio de Janeiro, COPPE, RJ, Brazil. e-mail: marciossal@gmail.com.
Submitted on May 16, 2019; Final Acceptance on November 6, 2019; Discussion open until April 30, 2020.
DOI: 10.28927/SR.423323

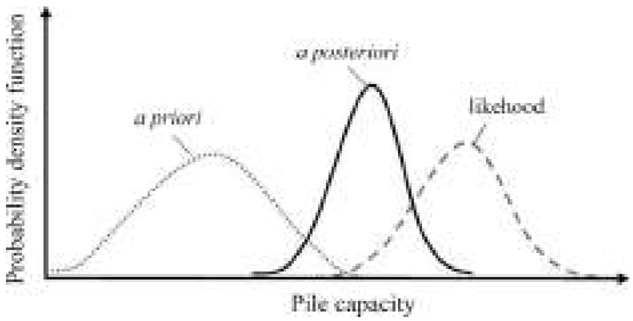

Figure 1 - Relationship between *a priori*, likelihood and *a posteriori* distribution of pile capacity (Lacasse & Goulois, 1989; Lacasse *et al.*, 1991).

2. The Bayesian Updating Approach

The Bayesian updating approach, illustrated in Fig. 1, shows the probability density functions used in the updating procedure. Bayesian updating allows for a reliable estimate of the *a posteriori* pile capacity from *a priori* and likelihood distribution functions. A detailed description of Bayesian concepts is found in applied statistics books (*e.g.*, Ang & Tang, 1984). Equations 1 and 2 allow the estimation of the expected value and the variance of the updated pile capacity (*a posteriori*) based on the expected value and the variance of the *a priori* distribution, as well as the likelihood function.

$$\mu_Q = \frac{\sigma^2_{Q_L} \cdot \mu_{Q_P} + \sigma^2_{Q_P} \cdot \mu_{Q_L}}{\sigma^2_{Q_L} + \sigma^2_{Q_L}} \tag{1}$$

$$\sigma^2_Q = \frac{\sigma^2_{Q_L} \cdot \sigma^2_{Q_P}}{\sigma^2_{Q_L} + \sigma^2_{Q_P}} \tag{2}$$

where μ_Q is the expected value of the updated pile capacity obtained *a posteriori*, μ_{QP} and μ_{QL} are, respectively, the expected value of the pile capacity originally predicted (*a priori*) and that obtained from the measurement activity (likelihood function); σ_Q^2 is the updated variance of the distribution of pile capacity (*a posteriori*) and σ_{QP}^2 and σ_{QL}^2 are, respectively, the variances of the originally estimated distribution, obtained by means of the available field tests (*a priori*) and that obtained from the measurements (the likelihood function).

3. The Test Site

The dataset refers to a Wastewater Treatment Plant (WWTP) in Alcantara, located in the lowlands nearby Rio de Janeiro. The piling dataset is related to the representative area delimited by the solid black line and Alcantara river in Fig. 2. The boreholes identified as SP, SPC and SNB in the figure represent different site investigation campaigns. The triangles and squares represent, respectively, the vane tests and CPTu tests. In the hatched area, nearly 4,000 H shaped W200x71 steel piles have been driven as foundation for the structures of the sewage plant. Each pile driven in the representative area had its performance controlled by three procedures: the complete driving log; the final average penetration for the last 10 hammer blows; and the elastic pile rebound for the same 10 blows. The penetration and elastic rebound at pile head were measured during the end of driving by means of the simple and traditional use of pencil and paper form. In the same representative region, 9 dynamic and 2 static loading tests were also performed.

Figure 3 shows: (i) the pile section; (ii) a typical register for the last 10 blows; and (iii) the plugging condition expected to occur at soil-pile during failure of the steel H piles (toe resistance mobilization as fully plugged and skin friction mobilization throughout the entire pile-soil contact). This plugging condition is commonly used in Brazilian, German (Schenck, 1966; EAB, 2008) and French (French Standard, 1993) foundation practice.

3.1. Soil profile and characterization

The soil profile consists of a very soft superficial clay layer with thickness varying from 8 to 12 m. Below the superficial soft layer, the SPT borings showed a fine-to-coarse dense sand, with thickness varying from 4 to 7 m, followed by a silty-sand/sandy-silt gneissic residual soil stratum. The very soft clay layer has been subjected to 8 CPTu tests, 6 vane tests and 5 sampling logs for laboratory tests, with locations also shown in Fig. 2. The laboratory tests consisted of index tests and oedometer tests. The superficial clay characterization and test results for the WWTP site are similar to those described by Almeida *et al.* (2008). A summary of the main parameters is listed in Table 1.

The mean value and the variance of the standard penetration test "N_{60}" distributions were determined for the representative area.

Spatial variability of the soil profile and geotechnical parameters occurs especially in the more resistant layers, where the CPTu could not penetrate and only the SPT bor-

Table 1 - Soft soil parameters.

Parameter	Range
γ_{sat}(kN/m^3)	13.5-15.5
S_u (kPA)	10-25
S_{ur} (kPA)	3-5
OCR	1.4-2.5
e_0	1.6-3.2
C_c	0.80-1.90
C_s	0.14-0.28
k_v (m/s)	5×10^{-10}-3×10^{-9}
c_v (m^2/s)	1×10^{-8}-2×10^{-7}

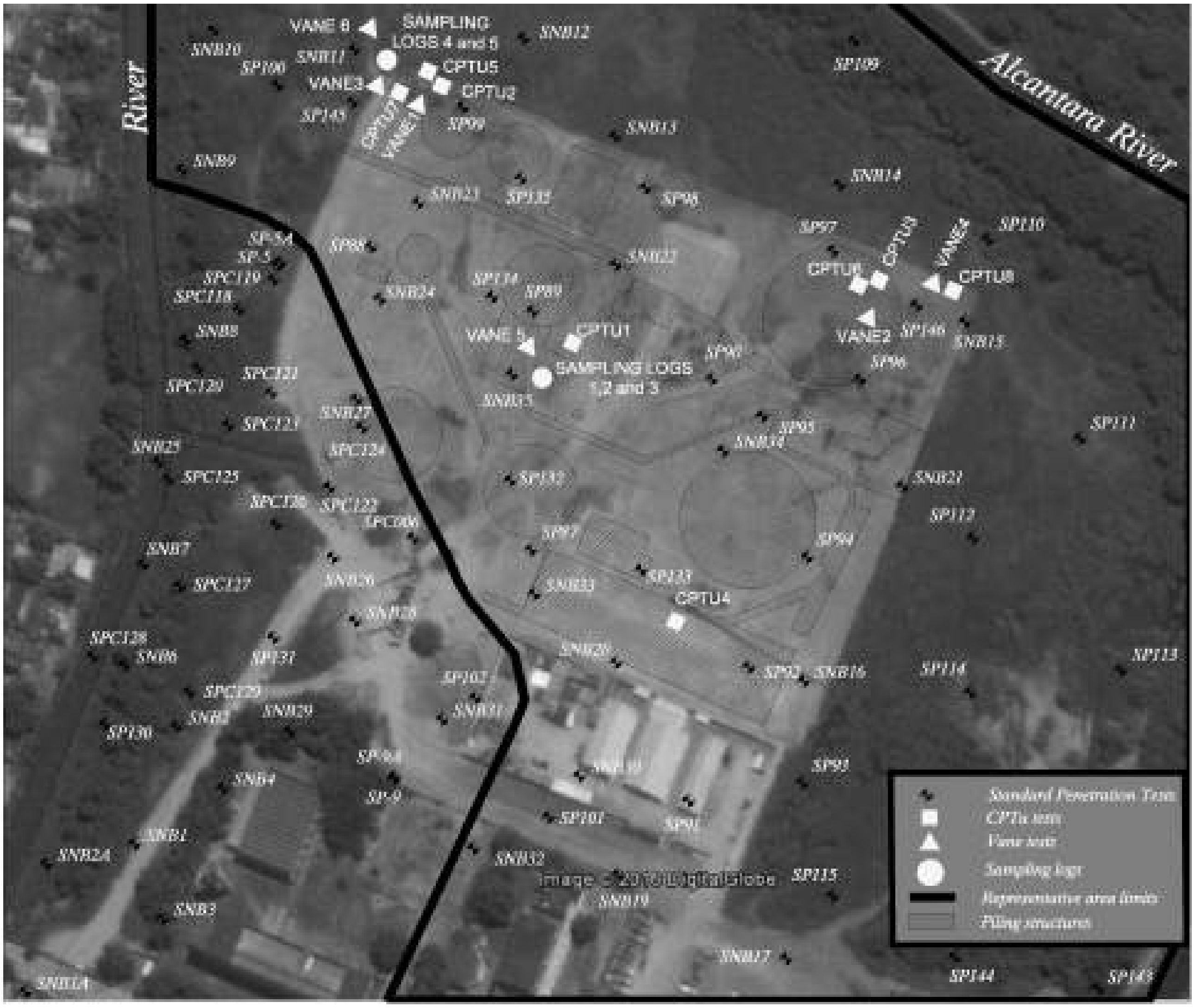

Figure 2 - Wastewater Treatment Plant (WWTP).

ings were available. The layers of dense sand and residual gneissic soil are expected to be responsible for nearly the entire pile capacity.

Figure 4 presents the N_{60} values and the statistical distribution for the 46 borings and investigated depths: the mean, the mean minus the standard deviation and the mean plus the standard deviation, represented in three distinct curves. The typical soil profile for the representative area is also shown in the same figure. The superficial soft soil layer presents a zero N_{60} for nearly the entire depth, and therefore the three statistical curves are superimposed on the depth axis. Some very high outlier values of N_{60}, representing local discontinuities in the final centimeters of penetration with fractional N_{SPT} (*e.g.* 20 blows / 5 cm) were removed from the dataset before the statistical calculation. No boreholes penetrated depths beyond 19 m due to the presence of rock fragments in the residual soil. As the steel H-piles have higher impedance than the SPT sampler and are less affected by small rock fragments within the soil, some piles reached depths of 21.5 m. For these depths the N_{60} values were extrapolated by repeating the last N_{60} penetration resistance available from the boreholes.

In Brazil, selection of appropriate correction factors is required to convert N_{SPT} into N_{60} according to the actual energy delivered during the SPT test. The correction factor used on the interpreted values was that obtained from Cavalcante *et al.* (2003, 2004, 2011) based on actual measurements on the Brazilian dataset, indicated below:

$$N_{60} = 1.37 N_{SPT} \tag{3}$$

4. The *A Priori* Mobilized Pile Resistance

As emphasized in the previous section, the piling site has been divided into representative areas characterized by a selected typical soil profile. The results included in the present paper refer to the representative area and typical soil profile shown in Figs. 2 and 4, respectively.

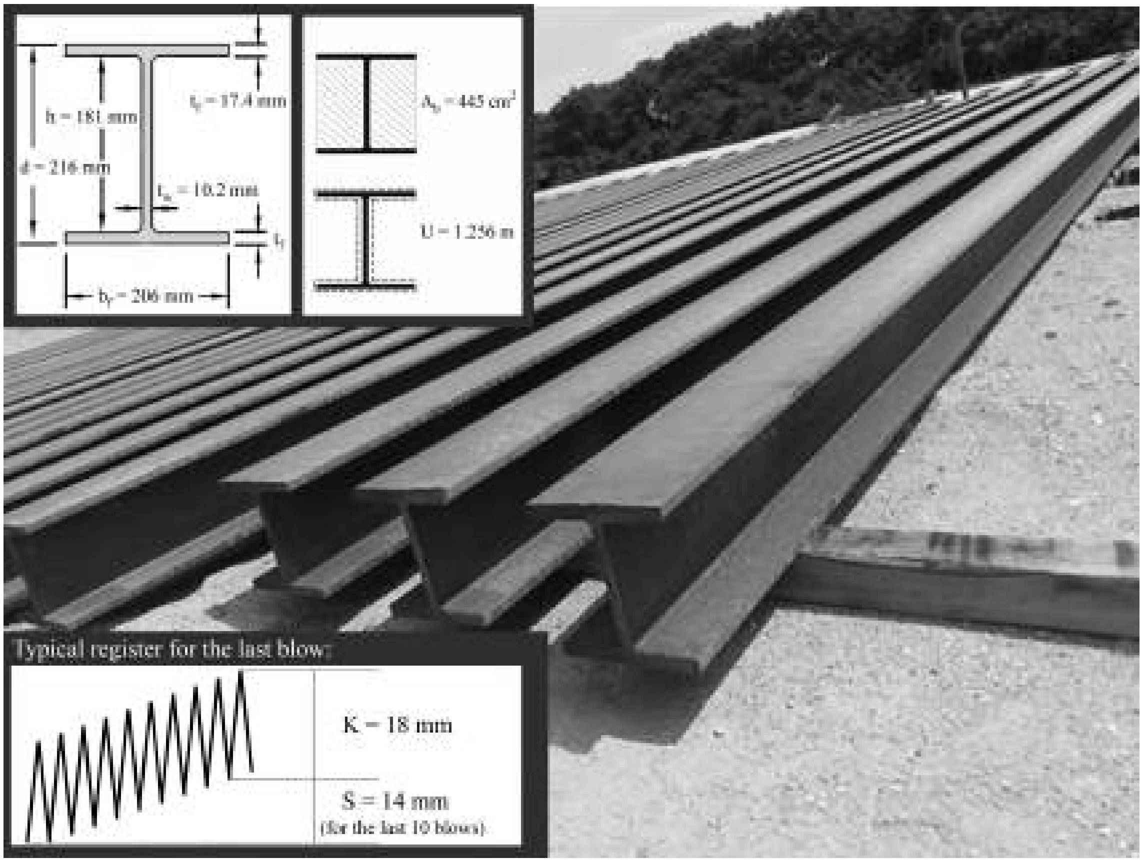

Figure 3 - Pile section and typical register.

For any calculated model, pile capacity is estimated by Eq. 4:

$$Q + W = Q_p + Q_l \tag{4}$$

where Q is the pile capacity, W is the pile weight, Q_p is the tip load capacity and Q_l is the load capacity due to lateral friction. The pile weight is often neglected due to its small influence in the overall pile capacity and Eq. 4 is written as:

$$Q = A_b \cdot q_p + U \sum \tau_l \cdot \Delta_l \tag{5}$$

where A_b is the pile base area, q_p is the unit tip resistance, U is the pile perimeter, τ_l is the unit shaft resistance, Δ_l is the pile length with the same $\tau_{l,rupt}$ value.

A number of methods can be used in the deterministic analysis of pile capacity. In the present analysis the authors have chosen two distinct methods in order to verify the statistical distribution of the pile capacity for different calculation models and their influence on the *a posteriori* updated distribution. These methods are described below.

4.1. Aoki & Velloso method

The first selected calculation model was that of Aoki & Velloso (1975), widely used in Brazil, which estimates the pile capacity from the results of standard penetration tests. This method is based on empirical correlations between q_c (from CPT) and N_{60} (from SPT) established for both sedimentary and residual soil profiles in different regions in Brazil (Aoki & Velloso, 1975, Danziger & Velloso, 1995; Politano *et al.*, 2001). Correction factors are used for different pile types to account for the effects of distinct construction procedures. Comparisons between the estimated pile capacity of this model and that observed from numerous static load tests have shown generally good agreement.

According to Aoki &Velloso (1975), the unit tip resistance and the unit shaft resistance are estimated as:

$$q_p = \frac{q_c}{F_1} = \frac{k \cdot N_{60}}{F_1} \tag{6}$$

$$\tau_l = \frac{f_s}{F_2} = \frac{\alpha \cdot k \cdot N_{60}}{F_2} \tag{7}$$

where F_1, F_2 are correction factors, k and α are dependent on the soil type and q_c and f_s are related to N_{60} by means of the correlations presented above. For steel driven piles, F_1 and F_2 are 1.5 and 3, respectively. Values of k = 220, 1000 and 700 kPa and α = 4, 1.4 and 2.4 % were used for the soft soil layer (silty-clay), sand layer and residual soil layer (sandy-silt).

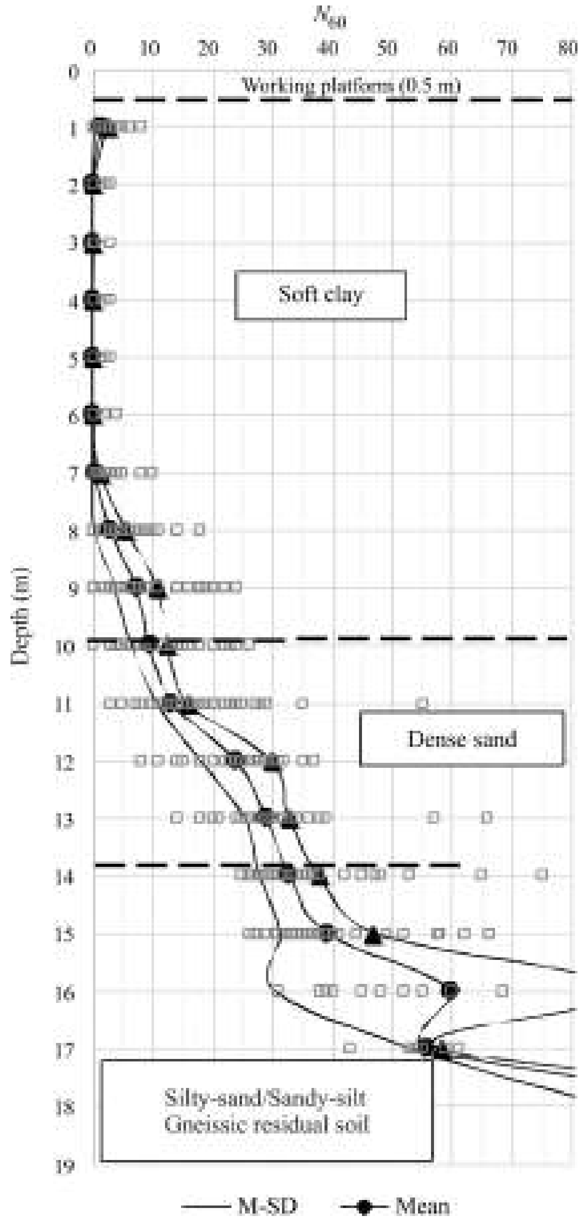

Figure 4 - N_{60} values - Statistical soil boring profile.

4.2. Vesic method

The second method selected for deterministic analysis of pile capacity was the well-known theoretical approach developed by Vesic (1977). Conventional theories consider the tip resistance to be given by the same expression as that used for the load capacity for shallow foundations, excluding the component relative to the ground weight, since this component is very small in this type of foundation, Eq. 8.

$$q_{p,rupt} = C \cdot N_C^* + \sigma_0' \cdot N_\sigma \tag{8}$$

$$\sigma_0' = \frac{(1+2K_0)\sigma_v'}{3} \tag{9}$$

were σ'_v is the vertical effective stress and σ'_0 is the mean effective stress at the foundation base, N_c* and N_σ are the load capacity factors and K_0 is the soil at-rest coefficient and C is the cohesion or undrained shear strength.

The N_σ factor can be determined by any method that takes into account soil deformability prior to failure. The soil deformability in a condition of little volume change (dense strata) was estimated, in the present case, with the elastic soil modulus given by Freitas *et al.* (2012). According to Vesic (1977) the N_σ factor is a function of the friction angle and the reduced stiffness index of the soil.

For pile-soil skin friction, Vesic (1977) proposes Eq. 10, where K_s depends on the initial at-rest condition, construction procedures and pile shape.

$$q_s = K_s \cdot \sigma_v' \tag{10}$$

For application of the Vesic (1977) method, correlations between the soil parameters and N_{60} are necessary. The authors made use of Kulhawy & Maine (1990) guidelines with resulting soil strength parameters summarized in Table 2. An overall working platform consisting of a 0.5 m layer of sandy material was used over the whole region due to the low capacity of the soft soil to support the traffic of the machines.

5. The Soil Resistance to Driving

The soil pile resistance mobilized during pile driving differs from the pile capacity estimated for long term conditions, although the calculations are carried out quite similarly. The resistance mobilized during driving, known in the literature as SRD (soil resistance to driving), is that mobilized during pile penetration from the hammer blows (Toolan & Fox, 1977; Stevens *et al.*, 1982; Semple & Gemeinhardt, 1981).

For both methods adopted for *a priori* estimates, the disturbed undrained resistance of the superficial soft layer was used for the unit adhesion. For both the sandy and high permeability soils, resistance to driving is similar to long-term resistance, even though it is known that aging and dissipation of pore pressure can change soil resistance with time even for coarse soils.

Most theoretical methods for pile capacity consider that the skin friction may not indefinitely increase with overburden pressure, but rather a limiting value may be used. The decrease in unit shaft resistance for very deep piles has been analyzed by Lehane *et al.* (1993), Randolph *et al.* (1994) and Jardine & Chow (1996). Although both se-

Table 2 - Granular soil parameters.

Soil	γ_{sat} (kN/m^3)	φ' (°)	c' (kPa)
Working platform	19	30	5
Dense sand	20	35-40	0
Gneissic residual soil	20	35-45	0

lected methods for *a priori* estimation do not propose any limit, a N_{60} value of 68 blows for 0.30 m penetration was considered as a limit, as no accurate correlation is available for such higher resistances.

5.1. The dataset

For the final driven depth of each pile of the dataset, the bearing load capacities were calculated using the Aoki & Velloso (1975) and Vesic (1977) methods. Three scenarios of the N_{60} profile were formed: mean (M), mean minus standard deviation (M - D) and mean plus standard deviation (M + D), given the closest borehole as the mean value and the variance of N_{60} for the whole site, according to the curves presented in Fig 4. The calculation results for the predicted pile capacity were assembled, composing a large dataset from which the statistical distribution of the *a priori* values was determined.

Figure 5 compares the *a priori* pile capacity for the 645-pile dataset estimated using both selected methods. The piles were driven to depths varying from 13.5 to 21.5 m, with an average embedded length of 16 m and a standard deviation of 1.5 m, resulting in a COV of 0.09. The Vesic (1977) calculation model resulted in values nearly 37 % higher than the Aoki & Velloso (1975) method. Figure 5 shows that for load capacities higher than 2,500 kN for the Vesic method, the M, M-SD and M+SD related values are concentrated over a narrow range. This occurs for the deeper piles embedded into high resistance residual soils, where the N_{60} limit resulted in nearly the same soil resistance independently of the "N_{SPT} profile" used in the calculation. While in the Aoki & Velloso method the unit tip resistance remains constant and total lateral friction resistance increases with pile penetration in the residual soil layer, the Vesic method considers a decrease in unit tip and friction resistance due to the increase in the confining effective stress for a fixed N_{60}. Therefore, a decrease in the calculated soil friction angle occurs, resulting in a decrease in predicted pile capacity. While the values from the Aoki-Velloso method continue to increase with depth at a constant rate, the Vesic method begins to increase at a lower rate when the piles penetrate the residual soil stratum with a fixed N_{60}, causing the inflection and concentration of points in the narrow range observed in Fig. 5. On the other hand, some points at the top center of the graph in the same Fig. 5 presented a different behavior, probably due to an over estimation of the friction angle by the Kulhawy & Mayne (1990) correlation for some undisclosed soil stratum.

The frequency histogram for the *a priori* pile capacity was tentatively analyzed by both normal and lognormal distributions. Better results were found for the normal distribution, as presented in Figs. 6a and 6b. The predicted values from the Aoki & Velloso (1975) method are well represented, whereas those of Vesic (1977) are concentrated between the values of 2,500 and 3,000 kN. The behavior of the normal distribution for the second method is probably affected by the abrupt increase in tip resistance when the piles penetrate the residual soil layer. At depths bellow 16 m, the average contribution of the tip resistance to total pile capacity was nearly 30 % for the Aoki-Veloso method and 60 % for Vesic. This explains the large number of piles with *a priori* capacity ranging from 2,500 to 3,000 kN, calculated using the Vesic model for piles installed through the transition depth where soil profiles move abruptly from the sedimentary to the residual layer.

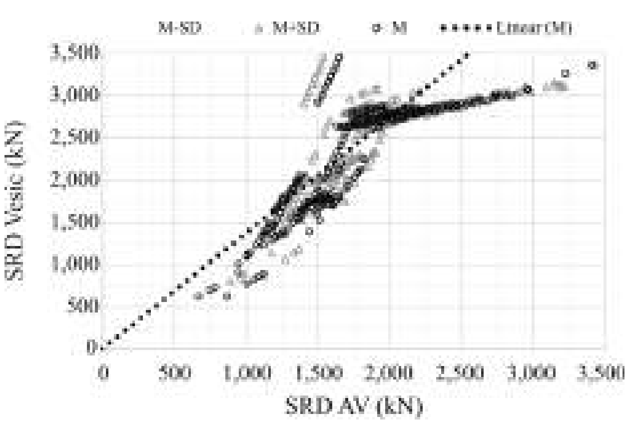

Figure 5 - Expected *a priori* values of SRD (soil resistance to driving) estimated using both calculation models for the 645-pile dataset.

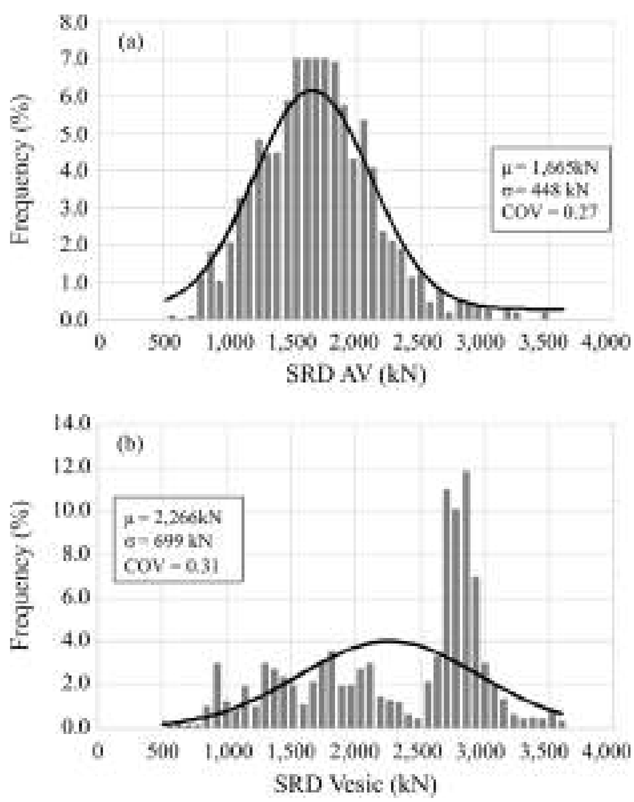

Figure 6 - Histograms for the natural normal distribution curve of SRD (soil resistance to driving): (a) Aoki-Velloso method and (b) Vesic method.

6. Likelihood Function Distribution

The likelihood function is the one that includes on-site results, a sample of the "state of nature", as reported by Kay (1976). The "state of nature" for the present case was obtained from the registers documented during driving for the entire dataset: the average pile set and rebound for the final ten blows. The average pile set was introduced in the Danish formula (Sorensen & Hansen, 1957) and the pile rebound in the Chellis-Aoki formula (Chellis, 1951; Aoki, 1989) for deterministic calculation of the pile capacity at the end of driving.

6.1. The Danish formula

The Danish formula (Sorensen & Hansen, 1957) is still widely used in Brazil for predicting pile capacity of steel piles. The accuracy of the Danish formula has been checked at several sites, as reported by Olson & Flaate (1967). Danziger & Ferreira (2000) used the formula to compare results to more accurate applications of wave equation programs and found good agreement. The formula is described by the following equations:

$$R_u = \frac{\eta \cdot W_H \cdot H}{S + 0.5 S_e} \tag{11}$$

$$S_e = \sqrt{\frac{2\eta \cdot W_H \cdot H \cdot L}{A \cdot E}} \tag{12}$$

where R_u is the ultimate dynamic pile capacity, η is the driving hammer efficiency, W_H is the hammer weight, H is the hammer drop, S is the pile set per hammer blow, S_e is the elastic pile rebound per hammer blow, L is the pile length, A is the pile end area and E is the modulus of elasticity of the pile material (Olson & Flaate, 1967).

All the data necessary for the application is known from the dataset, except the system efficiency. A common value used for the efficiency is 0.7. However, as 9 dynamic loading tests were available in the present case study, the measured efficiency from the dynamic tests was used instead. The average measured efficiency was 75 % with a standard deviation of 21 %. Thus, for each pile in the dataset, the capacity mobilized during pile driving was calculated with the Danish formula using the mean (75 %), mean minus the standard deviation (54 %) and mean plus the standard deviation (96 %) of hammer efficiency and those values were included in the dataset forming the first likelihood function.

6.2. Chellis-Aoki rebound formula

The second formula used is based on pile rebound at final penetration. The use of pile rebound was initially proposed by Chellis (1951) and later modified by Aoki (1989). The formula uses the direct relationship between the pile capacity mobilized during driving and the elastic shortening of the pile. The elastic shortening of the pile can be obtained by reducing the part attributable to the soil from the total measured rebound K. The Chellis-Aoki rebound formula is calculated as follows:

$$R_u = \frac{C_2 \cdot A \cdot E}{\alpha \cdot L} \tag{13}$$

$$C_2 = K - C_3 \tag{14}$$

where R_u is the pile mobilized capacity, C_2 is the elastic shortening of the pile shaft, C_3 is the soil rebound for which Aoki (1989) suggests a value of 2 or 3 mm or a value close to the pile set, A is the pile section area, E is the modulus of elasticity of the pile material, L is the pile length and α depends on the pile transfer between toe and friction resistance. If only the pile tip resists the load, the α value is 1, whereas if the tip resistance is zero, α is 0.5. For typical cases, in which part of the pile capacity is due to the tip and part comes from friction resistance, Aoki (1989) suggests α = 0.7 as an approximate value. As the pile capacity had already been predicted, the authors made use of the range of α estimated from the *a priori* pile capacity calculations. The first 8-12 m of the soil profile is formed by soft clay, so almost 90 % of the bearing capacity is mobilized in the last few meters. Therefore, α does not vary significantly (μ = 0.9, COV = 0.025) and no bias is expected due to correlation between *a priori* and likelihood functions.

Figure 7a presents the histograms associated with the likelihood function obtained from the Danish formula and

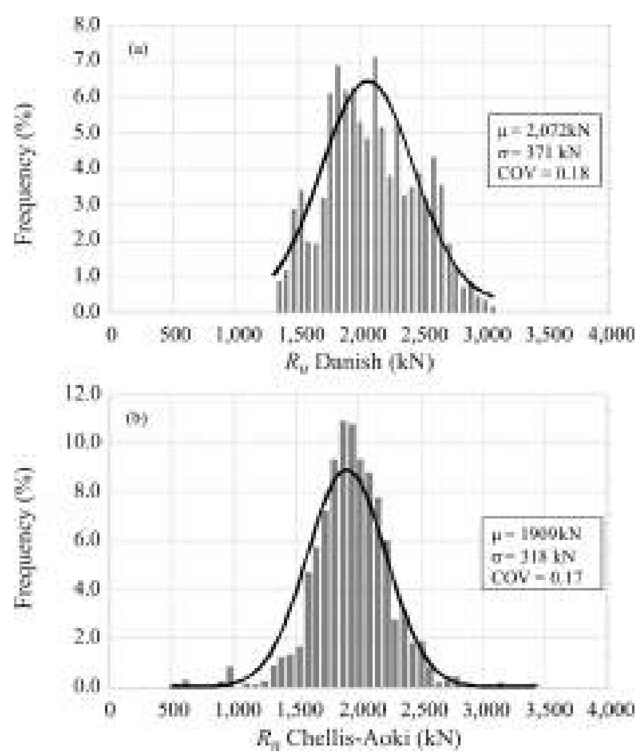

Figure 7 - Histograms for the likelihood function distributions of pile capacity R_u: (a) Danish and (b) Chellis-Aoki.

Fig. 7b for that related to Chellis-Aoki formula. Figure 7 also illustrates that the expected value of mobilized pile capacity from the statistical distribution of both selected likelihood functions was very close, as well as the COV. In fact, both results came from the same dataset, from different registers but from the same site, thus consisting of the same “state of nature”.

Figure 8 compares the pile capacity estimated with the two selected likelihood functions. In spite of the scatter, which is reasonable due to uncertainty in the hammer efficiency, elastic rebound of the soil and actual drop height, most of the results concentrate close to the 45° line between ±30 %.

7. The *A Posteriori* Distribution

Equations 1 and 2 were used to update the SRD value for each pile estimated *a priori* by using both likelihood functions, resulting in the *a posteriori* SRD estimates. For each pile, the mean values in Eqs. 1 and 2 were obtained as the specific *a priori* prediction and estimates from the dynamic formulas. The variance values were derived from the statistical distribution of the whole dataset, containing all analyzed piles and the uncertainties involved. Every pile has its own updated estimates and the set of all pile forms the *a posteriori* distribution.

Figures 9a and 9b present the histograms associated with the *a posteriori* distribution obtained from the Aoki-Velloso method updated with the Danish and Chellis-Aoki formulas respectively, and Figs. 10a and 10b represent *a posteriori* distribution histograms obtained from the Vesic method updated with the Danish and Chellis-Aoki formulas respectively. The *a posteriori* pile capacity always has a value between that obtained *a priori* and the one corresponding to the likelihood function, moving closer to the distribution of lower variance. The coefficient of variation of the *a posteriori* distribution is always lower than that of the other distributions since the *a posteriori* distribution includes information from both *a priori* and likelihood function, reducing the uncertainty of the estimate.

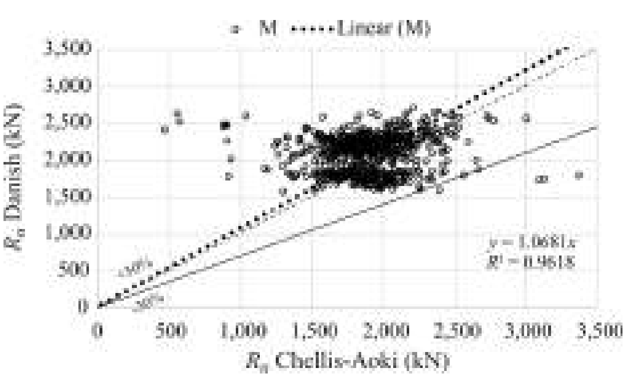

Figure 8 - Expected values of the likelihood function of pile capacity R_u for the two dynamic formulas.

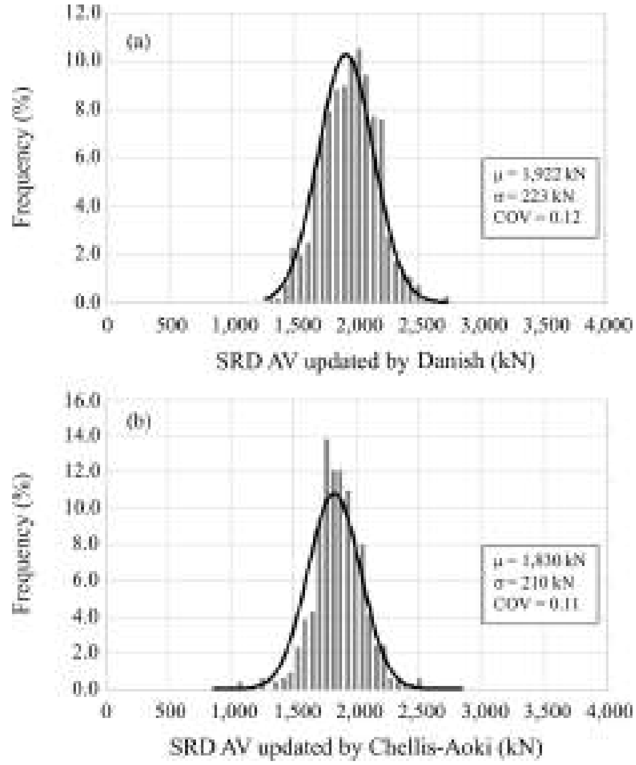

Figure 9 - Histograms for the *a posteriori* distributions for the Aoki-Velloso Method of SRD: (a) updated with Danish formula and (b) updated with Chellis-Aoki formula.

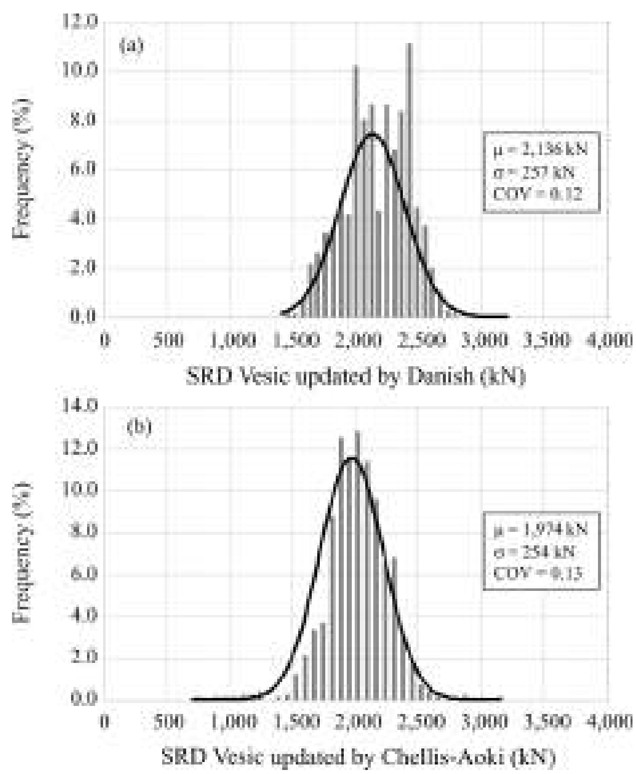

Figure 10 - Histograms for the *a posteriori* distributions for the Vesic Method of SRD: (a) updated with Danish formula and (b) updated with Chellis-Aoki formula.

Figure 11 summarizes the updating procedure for both pile capacity methods (Aoki & Velloso and Vesic). Figure 11a shows the expected values *a posteriori* updated using the Danish formula as the likelihood function, whereas in Fig. 11b the Chellis-Aoki formula was applied. Unlike the *a priori* estimates, where the Vesic method resulted in capacities 37 % higher than those from Aoki-Velloso, for the *a posteriori* estimates this difference is very low, 7.9 %, when updated with Chellis-Aoki, and 10 % when updated with the Danish formula. After the updates, the uncertainties evidenced in the *a priori* comparisons were not observed. The update greatly reduced the uncertainty between the different calculation methods, reducing the uncertainty to a significantly lower level.

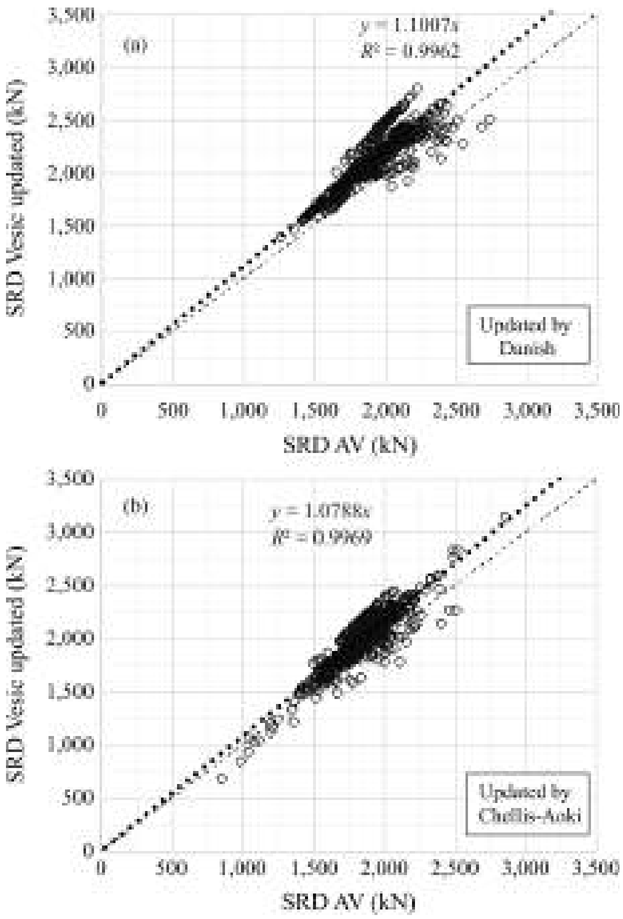

Figure 11 - *A posteriori* expected value of SRD (soil resistance to driving) using both calculation models (Aoki-Velloso, and Vesic), updated with (a) Danish formula and (b) Chellis-Aoki formula.

8. Load Test Results

The pile load test results are summarized in Tables 3 and 4. Table 3 includes the results from nine dynamic tests and Table 4 the results of two slow maintained static load tests. Pile 148 suffered structural damage during the dynamic test and its results were not included in the following analysis. The conventional pile capacity from the static load tests was obtained through extrapolation according to Van der Veen (1953), a common method used in Brazil when physical failure is not reached during the load test. The load settlement curve of pile E-106 presented a nearly linear behavior up to the maximum testing load. That is the reason why the authors did not use the extrapolated capacity for this pile, consistent with Van der Veen (1953).

The *a priori* and *a posteriori* estimates of pile capacity are now compared to the load tests (8 dynamic and 1 static), as presented in Table 5 and Fig. 12. The mobilized pile resistance in the dynamic test was interpreted with CAPWAP, as presented by Rausche *et al.* (1972). In Fig. 12a the *a priori* pile capacity estimated using the Aoki-Velloso method is represented in the vertical axis, with the statistical distribution indicated by its statistical range and the expected value by the middle point. Figures 12b and 12c compare the *a posteriori* expected values updated with the Chellis-Aoki and Danish dynamic formulas,

Table 3 - Dynamic test results.

Pile	Embedded length (m)	Final set (mm/10 blows)	Transferred energy (kJ)	Tip resistance (%)	CAPWAP capacity (kN)
113	17.4	5	38.2	21.0	2,850
114	16.4	10	46.3	27.4	2,790
115	16.4	5	43.0	26.7	2,770
116	16.1	5	38.7	28.8	2,950
148*	17.4	20	23.1	7.4	1,450
156	17.9	10	22.6	15.4	2,530
240	18.8	1	29.8	16.9	2,400
260	17.6	1	28.8	14.0	2,320
265	17.7	9	25.6	8.8	2,310

Note: * Pile was damaged during the tests.

Table 4 - Static tests results.

Pile	Embedded length (m)	Maximum testing load (kN)	Maximum testing displacement (mm)	Permanent displacement (mm)	Van der Veen extrapolated capacity (kN)
172	16.9	1,400	14.87	1.25	2,160
106	15.7	1,000	8.09	1.91	*

Note: * No Van der Veen extrapolated capacity was considered for pile 106.

respectively. Similar results are found when the estimated *a priori* values are calculated using the Vesic method. Figures 12b and 12c illustrate the decrease in uncertainty, clearly observed by the relative reduction of the statistical range for each tested pile. The comparison of Fig. 12a with Figs. 12b and 12c demonstrates that the update with both the Danish and the Chellis-Aoki formulas were quite efficient in estimating the expected pile capacity within a narrow range and approximating the expected value to the results of the pile load tests. With the exception of pile E-106, all the other tests presented in Figs. 12b and 12c indicated measured pile capacities higher than the updated. Since the tests were performed with an interval of at least 190 days after the end of driving, the higher pile capacity can be attributed both to a higher hammer energy during the tests, compared to the final driving, and also to an increase in soil resistance over time due to pore pressure dissipation. The extent of the pile capacity increase, due to both higher energy (which can cause a higher mobilized resistance) and an increase in soil resistance over time was nearly 30 % and 19 % for the Aoki & Velloso and Vesic methods, respectively.

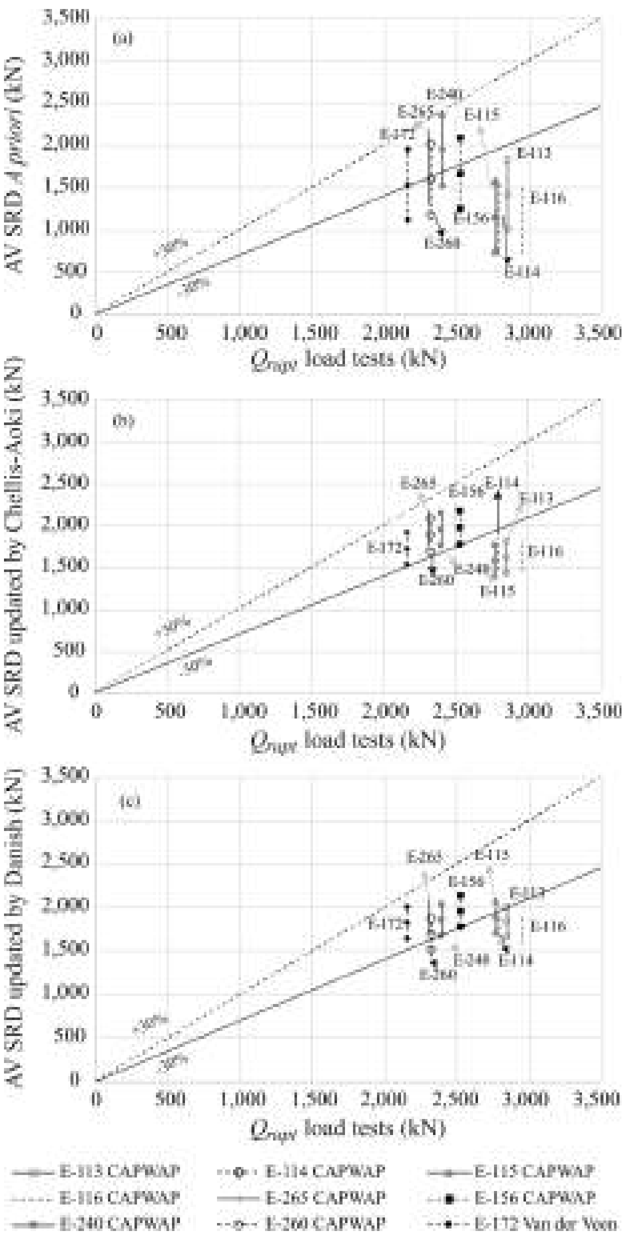

Figure 12 - Comparisons between estimates of SRD (soil resistance to driving) using Aoki-Velloso method and load pile tests: (a) *a priori* estimate (b) *a posteriori* estimate updated with Chellis-Aoki formula and (c) *a posteriori* estimate updated with Danish formula.

Table 5 - Statistical distributions of the database.

Method	Q_{rupt} expected value (kN)	Standard deviation (kN)	COV
Calculations[1]			
AV	1,665	448	0.27
Vesic	2,262	701	0.31
Dynamic Formulas[1]			
Chellis-Aoki	1,909	318	0.17
Danish	2,072	371	0.18
Updated by Chellis-Aoki[1]			
AV	1,830	210	0.11
Vesic	1,974	254	0.13
Updated by Danish[1]			
AV	1,922	223	0.12
Vesic	2,136	257	0.12
Dynamic Load Tests[2]			
CAPWAP	2,615	239	0.09

Note: [1]645 piles; [2]8 piles.

The decrease in uncertainty due to Bayesian updating can be interpreted in terms of the coefficient of variation (COV). Table 5 shows the variability ranges for each method including the expected value (mean), variance and COV with respect to all 645 piles and 8 dynamic load tests. There is a very significant decrease in the variability of the expected capacities due to updating. The *a priori* pile capacity estimated using the Aoki & Velloso and Vesic methods presented COV of 0.27 and 0.31, respectively. The likelihood functions (dynamic formulas) presented lower uncertainties as they made use of the sample from the "state of nature". Such "state of nature" uncertainty produced COV of 0.18 and 0.17 for the Danish and Chelli-Aoki formulas, respectively. After Bayesian updating, COV fell to 0.12 and 0.11 for the Aoki & Velloso method updated with Danish and Chellis-Aoki likelihood functions, respectively. For the Vesic method, COV fell to 0.12 and 0.13 using the Danish and Chellis-Aoki likelihood functions, respectively. The COV of the dynamic load tests, 0.09, was very close to that for the *a posteriori* estimates. Therefore, the Bayesian update was quite effective in improving the reliability of the estimated pile capacity, reducing the uncertainty to a range very close to that obtained with dynamic tests.

Figure 13 summarizes the Bayesian procedure applied in this paper using the Aoki & Velloso method. Similar results were obtained for the Vesic method. Figure 13a shows the three statistical normal curves for the *a priori* (Aoki & Velloso method), likelihood (Danish formula) and *a posteriori* (Aoki & Velloso updated by Danish) distributions. Figure 13b presents the Aoki & Velloso *a priori* distribution using the Chellis-Aoki formula for the likelihood and *a posteriori* distributions. The flattened shape of the *a priori* distribution is attributed to its high variance due to uncertainties involving the limitation of the calculation methods, spatial variability and limitations of the SPT tests. Both likelihood functions are narrower due to the lower variance and consequently lower uncertainty. The *a posteriori* distributions are even narrower reflecting lower variance, and therefore even lower uncertainty. As expected, the mean *a posteriori* pile resistance is between the mean values for the *a priori* and likelihood distributions, being

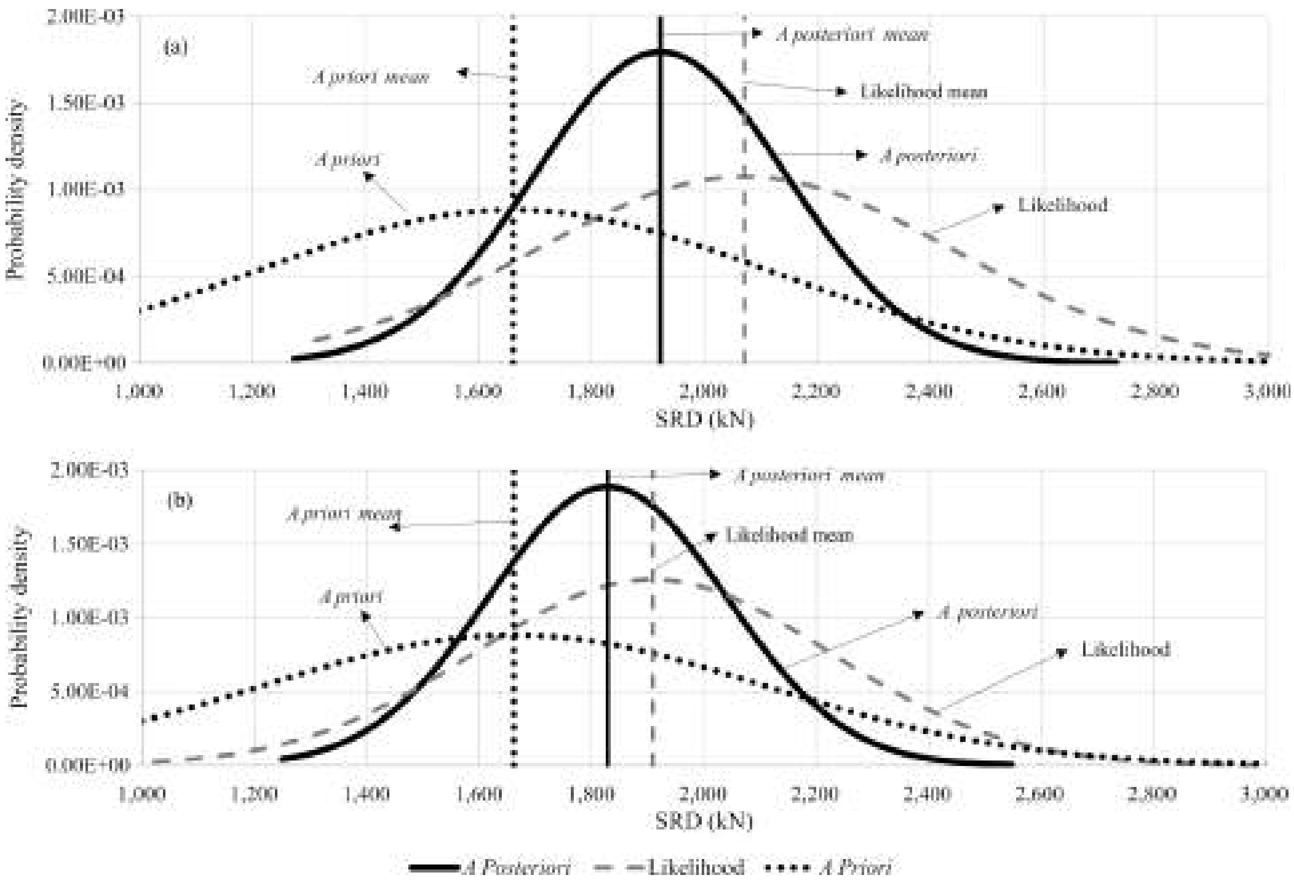

Figure 13 - Comparison between *a priori*, likelihood and *a posteriori* normal distributions of SRD (soil resistance to driving) for the Aoki-Velloso method: (a) with respect to Danish likelihood distribution and (b) with respect to Chellis-Aoki likelihood distribution.

closer to the likelihood mean value due to its lower variance. Figure 13 is a real representation of Fig. 1 and shows the proper functioning of the procedure applied in this paper.

9. Conclusions

This paper presents the application of the Bayesian updating procedure to a comprehensive steel piling dataset in a sedimentary soil profile in Rio de Janeiro, Brazil.

Two methods for estimating the *a priori* pile capacity were used, as well as two likelihood functions, for updating the soil resistance mobilized by the piling at the end of driving. The updating procedure was able to practically eliminate significant model uncertainties of the *a priori* predictions.

Although different, the Chellis-Aoki and Danish likelihood functions revealed very close statistical distribution and were both efficient in reproducing a sampling from the "state of nature." The functions also demonstrated their efficiency in obtaining an improved *a posteriori* estimate of pile capacity including a much lower uncertainty range.

The pile capacity *a posteriori* always had a value between that obtained *a priori* and the one corresponding to the likelihood function, thus closer to the distribution of lower variance. The coefficient of variation of the *a posteriori* distribution was always lower than that of the other distributions, since the *a posteriori* distribution includes information from both (*a priori* and "likelihood function"), reducing the uncertainty of the estimate.

The updated estimates were then compared to the results of dynamic and static load tests. The comparisons indicated measured pile capacity nearly 30 % and 19 % higher than the updated for the Aoki-Velloso and Vesic methods, respectively. The higher values measured may be attributed to set up effects and a higher energy adopted in the tests compared to final driving.

The Bayesian updating technique can be applied to a single pile, a group of piles, as in the present paper, as well as to a combination of estimated pile capacity and static or dynamic load tests. The practical application to different pile types, sites and various soil formations can produce relevant statistical information concerning the accuracy of different geotechnical calculation methods. Focus on continuous application can contribute significantly to a more rational design and better quality control systems, with resulting improvement to piling safety.

References

Almeida, M.S.; Futai, M.M.; Lacerda, W.A. & Marques, M.E.S. (2008). Laboratory behavior of Rio de Janeiro soft clay. Soils and Rocks, 31(1):77-84.

Ang, A.H.S. & Tang, W.H. (1984). Probability Concepts in Engineering Planning and Design. John Wiley & Sons, Hoboken, vol.1 and 2, 574 p.

Aoki, N. & Velloso, D.A. (1975). An approximate method to estimate the bearing capacity of piles. Proc. 5th Pan-American Conf. on Soil Mech. and Found. Engn, Buenos Aires, v. 1, pp. 367-376.

Aoki, N. (1989). A new dynamic load test concept. Proc. 12th Int. Conf. on Soil Mech. and Found. Engn., ISSMFE, Rio de Janeiro, v. 14, pp. 1-4.

Baecher, G.B. & Ladd, C.C. (1997). Formal observational approach to staged loading. J. Transportation Research Board, 1582 (1) 49-52.

Baecher, G.B. & Rackwitz, R. (1982). Factors of safety and pile load tests. Int. J. Numerical Anal. Meth. Geomech., 6(4):409-424.

Cavalcante, E.H.; Danziger, B.R. & Danziger, F.A.B. (2011). Measurement of drop height and impact velocity in the Brazilian SPT system. Soils and Rocks, 34(3):207-218.

Cavalcante, E.H.; Danziger, F.A.B. & Danziger, B.R. (2004). Estimating the SPT penetration resistance from rod penetration based on instrumentation. Proc. 2nd Conf. Geotechnical and Geophysical Site Characterization, Millpress, The Netherlands, v. 1, pp. 293-298.

Cavalcante, E.H.; Danziger, F.A.B.; Danziger, B.R. & Bezerra, R.L. (2003). Recent experience on SPT instrumentation in Brazil. Proc. 12th Pan-American Conf. on Soil Mech. and Geotech. Engn, Cambridge, Mass, v. 1, pp. 423-428.

Chellis, R.D. (1951). Pile Foundations. McGraw-Hill, New York, 681 p.

Danziger, B.R. & Ferreira, J.S. (2000). Back-analyses of steel pile driving records for quality assurance. Proc. 6th Applic. of Stress-Wave Theory to Piles, Rotterdam, v. 1, pp. 657-663, Balkema.

Danziger, B.R. & Velloso, D.A. (1995). Correlations between the CPT and the SPT for some Brazilian soils. Proc. Int. Symposium on Cone Penetration Testing, CPT '95, v.2, Swedish Geotechnical Society, Linkoping, Sweden, pp. 155-160.

EAB German Geotechnics Association (DGGT). (2008). Recommendations on Excavations. 2nd revised edition, Ernst & Sohn, Berlin, 284 p.

Freitas, A.C.; Pacheco, M.P. & Danziger, B.R. (2012). Estimating Young moduli in sands from the normalized N_{60} blow count Soils & Rocks, 35(1):89-98.

French Standard (1993). Règles Techniques de Conception et de Calcul des Fondations des Ouvrages de Génie Civil. Ministère de L'Equipement, du Logement et des Transports, CCTG, 62(V), Paris.

Goh, A.T.; Kulhawy, F.H. & Chua, C.G. (2005). Bayesian neural network analysis of undrained side resistance of drilled shafts. J. Geotechn. Geoenviron. Engn., 131(1):84-93.

Guttormsen, T.R. (1987). Uncertainty in offshore geotechnical engineering: Application of Bayesian theory to pile driving predictions. Research Report Société Nationale Elf Aquitaine, Oslo.

Huang, J.; Kelly, R.; Li, D.; Zhou, C. & Sloan, S. (2016). Updating reliability of single piles and pile groups by load tests. Computers and Geotechnics, 73(1):221-230.

Jardine, R.J. & Chow, F.C. (1996). New design methods for offshore piles. Marine Technology Directorate, London, v. 96-10, 48 p.

Kay, J.N. (1976). Safety Factor Evaluation for Single Piles in Sand. J. of Geotechn. Engn. Div., 102(10):1093-1108.

Kulhawy, F.H. & Mayne, P.W. (1990). Manual on Estimating Soil Properties for Foundation Design. No. EPRI-EL-6800. Electric Power Research Inst. Cornell Univ., Ithaca.

Lacasse, S. & Nadim, F. (1994). Reliability issues and future challenges in geotechnical engineering for offshore structures. NGI Publication, 191:1-30.

Lacasse, S. & Goulois, A. (1989). Reliability analysis of axial pile capacity. Proc. 12th Int. Conf. on Soil Mech. and Found. Engn., ISSMFE, Rio de Janeiro, pp. 845-848.

Lacasse, S.; Tan, A.H.; Keaveny, J.M.; Goulois, A. & Boisard, P. (1991). Expert assistant for updating axial pile capacity from pile driving observations. Proc. Int. Symp. Field Measurements in Geomech. Sorum, Balkema, v. 3, pp. 423-431.

Lehane, B.M.; Jardine, R.J.; Bond, A.J. & Frank, R. (1993). Mechanisms of shaft friction in sand from instrumented pile tests. J. of Geotechn. Geoenviron. Engn., 119(1):19-35.

Li, X.Y.; Zhang, L.M.; Gao, L. & Zhu, H. (2017). Simplified slope reliability analysis considering spatial soil variability. Engineering Geology, 216(12):90-97.

Olson, R.E. & Flaate, K.S. (1967). Pile-driving formulas for friction piles in sand. J. Soil Mech. Found. Division, 93(6):279-296.

Politano, C.F.; Danziger, F.A.B. & Danziger, B.R. (2001). CPT-SPT Correlations for residual soils. Soils and Rocks, 24(1):55-71.

Randolph, M.F.; Dolwin, R. & Beck, R. (1994). Design of driven piles in sand. Géotechnique, 44(3):427-448.

Rausche, F.; Moses, F. & Goble, G.G. (1972). Soil resistance predictions from pile dynamics. J. Soil Mech. Found. Division, 98(9):917-937.

Schenck, W. (1966). Pfahlgrundungen, Grundbau-Taschenbuch, band.1, 2, Auflage, pp. 577-657.

Semple, R.M. & Gemeinhardt, J.P. (1981). Stress history approach to analysis of soil resistance to pile driving. Proc. 13th OTC., Houston, v. 1, pp. 165-172.

Sorensen, T. & Hansen, J.B. (1957). Pile driving formulae: An investigation based on dimensional considerations and statistical analysis. Proc. 4th Int. Conf. Soil Mech. Found. Engn., London, v. 2, pp. 61-65.

Stevens, R.S.; Wiltsie, E.A. & Turton, T.H. (1982). Evaluating pile drivability for hard clay, very dense sand, and rock. Proc. 14th OTC, v. 1, pp. 465-481.

Toolan, F.E. & Fox, D.A. (1977). Geotechnical planning of piled foundations for offshore platforms. Proc. ICE, 62(1):221-230.

Van Der Veen, C. (1953). The bearing capacity of a pile. Proc. 3rd Int. Conf. on Soil Mech. and Found. Engn., ICSMFE, Zurich, v. 2, pp. 84-90.

Vesic, A.S. (1977). Design of Pile Foundations. NCHRP Synthesis of Highway Practice, Washington, D.C, 42(1).

Vrouwenvelder, A. (1992). Effects of inspection on the reliability of foundation piles. Proc. 4th Int. Conf. Applic. of Stress-Wave Theory to Piles, v. 1, pp. 657-663, Balkema, Rotterdam.

Zhang, I.; Tang, W. & Ng, C. (2001). Reliability of axially loaded driven pile groups. J. Geotech. Geoenviron. Engn., 127(12):1051-1060.

Zhang, J.; Li, J.P. & Huang, H.W. (2014). Calibrating cross-site variability for reliability-based design of pile foundations. Comp. Geotech., 62:154-163.

Zhang, L.M. & Tang, W.H. (2002). Use of load tests for reducing pile length. Proc. Int. Deep Found. Congress, ASCE, Orlando, v. 2, pp. 993-1005.

Zhang, L.M. (2004). Reliability verification using proof pile load tests. J. Geotech. Geoenviron. Engn., 130(11):1203-1213.

Zhang, L.M.; Li, D. & Tang, W.H. (2006). Level of construction control and safety of driven pile groups. Soils Found., 46(4):415-425.

Zhang, L.M.; Zhang, J. & Tang, W.H. (2010). Expected design factor of safety from a pile load test program. Geotechnical Special Publication, (199):1972-1981.

Zhang, L.; Tang, W.H.; Zhang, L. & Zheng, J. (2004). Reducing uncertainty of prediction from empirical correlations. J. Geotech. Geoenviron. Engn., 130(5):526-534.

Shear Creep Properties of Weak Interlayer in Slope Based on Stationary Parameter Fractional Derivative Burgers Model

W.B. Ma, Z.G. Zhao, P. Li, Q. Liu, C.Q. Yang, J. Li, W.B. Luo

Abstract. Based on special engineering geological conditions of a cut-slope area at Heitanping hilly-pass along Yongzhou - Jishou highway, shear creep properties of weak interlayer in this slope (about 30 m deep) have been studied by shear creep test to obtain shear creep curves. Shear creep constitutive model can be obtained by stationary parameter fractional derivative Burgers model, and long-term shear strength of the weak interlayer can be determined after the analysis of the shear creep curves. The research results show that the shear creep curves under different shear stresses have the same change tendency, which can be divided into three stages: instantaneous elastic stage, primary creep stage, and stationary creep stage, where both the instantaneous elastic deformation and primary creep time are increasing with the shear stress. On the basis of the shear creep constitutive equation, stress-strain isochrones of the soil have been constructed to identify the relationship between shear modulus *G* and time *t*. After the combination of deformation of the short-term shear strength and the *G-t* relationship, long-term shear strengths in different lengths of time have been obtained, which results in difference from the short-term shear strength. So the long-term shear strength should draw much attention to provide important theoretical references for the slope safety assessment.

Keywords: creep soil, direct shear creep test, fractional derivative Burgers model, long-term shear strength, non-attenuation, weak interlayer.

1. Introduction

With the rapid development of Chinese economy, highway network is becoming increasingly important (Li *et al.*, 2016; Roy & Sarkar, 2016). Because of the complex terrain in China, the highway usually goes through the mountains, and the landslide is the most common and dangerous geological hazard in the highway construction (Ilori *et al.*, 2010; China Geological Environmental Monitoring Institute 2014; Tiwari *et al.*, 2015). Once the landslide happens, the investment and time of the construction will be increased, and finally, it causes buildings collapse and casualties (Hasegawa *et al.*, 2009; Rackwitz *et al.*, 2013). Difficulties of slope treatments are varied in different geological conditions, and the treatment of slope with weak interlayer will be the most difficult part. The slope will slide along the weak interlayer, and the most important factor of the landslide is the mechanical properties of the weak interlayer. So the mechanical properties of the weak interlayer must be studied in detail. Since shear failure of the weak structural plane in slope is the major factor in slope instability of massive engineering projects, and the soil under long-term stress has a creep feature, shear creep properties of the weak interlayer must be studied in detail.

At present, a series of studies have been carried out on the shear creep properties of the weak interlayer in slope. Wang *et al.* (2007) analyzed the creep properties of the weak interlayer in Jurassic red clastic rocks in Wanzhou based on creep tests and Singh-Mitchell model. Based on the study of shear creep properties of soils in different regions, Jeong *et al.* (2009) determined the relationship between the power-law index and shear strain rate. Xu *et al.* (2010) built the power function model of the shear stiffness-shear stress by the in-situ shear test study of the weak interlayer in slope. Yang & Cheng (2011) studied the shear creep properties of shale by the direct shear creep test with the combination of a non-linear visco-elastic shear creep model. Le *et al.* (2012) studied the mechanism of soil creep deformation and recommended an enhanced explanation for the creep compression mechanisms of clays. Ma *et al.* (2014) carried out a detailed study on the shear creep properties of the simulative deep-sea sediment, and the shear creep constitutive equation was obtained by fitting the test data with Burgers model. The constitutive equations of soil

Wen-Bo Ma, Associate Professor, College of Civil Engineering and Mechanics, Xiangtan University, Xiangtan, China, and Department of Civil and Environmental Engineering, Michigan Technological University, Houghton, MI, USA. e-mail: mawenbo@xtu.edu.cn; wenboma@mtu.edu.
Zeng-Gang Zhao, M.Sc. Student, College of Civil Engineering and Mechanics, Xiangtan University, Xiangtan, China. e-mail: zzg15581689221@163.com.
Peng Li, Senior Engineer, Powerchina Zhongnan Engineering Corporation Limited, Changsha, China. e-mail: 491003275@qq.com.
Qi Liu, Ph.D. Student, College of Civil Engineering and Mechanics, Xiangtan University, Xiangtan, China. e-mail: liu_qi4013@163.com.
Cai-Qian Yang, Full Professor, College of Civil Engineering and Mechanics, Xiangtan University, Xiangtan, China, and College of Civil Engineering, Southeast University, Nanjing, Jiangsu, China. e-mail: ycqjxx@hotmail.com.
Jie Li, Associate Professor, College of Civil Engineering and Mechanics, Xiangtan University, Xiangtan, China. e-mail: melijie@sina.com.
Wen-Bo Luo, Ph.D., Full Professor, College of Civil Engineering and Mechanics, Xiangtan University, Xiangtan, China, and Hunan Key Laboratory of Geomechanics and Engineering Safety, Xiangtan University, Xiangtan, China. e-mail: luowenbo@xtu.edu.cn.
Submitted on November 30, 2017; Final Acceptance on November 6, 2019; Discussion open until April 30, 2020.
DOI: 10.28927/SR.423337

were generally studied by conventional methods or models. However, there were fewer assessments of the practical project combining the fractional derivative constitutive model and the long-term shear strength.

The fractional derivative constitutive model has recently become a hotspot in geotechnical constitutive model research. Based on the results of creep test, performed on the marble in the Jinping II hydropower station in China, Chen *et al.* (2014) proposed a time-dependent damage constitutive model by fractional calculus theory and damage variables to describe these time-dependent damage characteristics. Based on the experimental study of the surrounding rock of the deep and long tunnels at Jinping II hydropower station, He *et al.* (2016) found that the non-stationary parameter fractional derivative constitutive model can reflect the whole creep process very well. Lai *et al.* (2016) summarized the investigation progresses and applications of the fractional derivative model in geotechnical engineering and indicated that the fractional derivative model is one of the most effective and accurate approaches to describe the rheology phenomenon.

Due to the design service life of slopes in highway engineering being usually more than 50 years, the stability analysis of the slope should be based on the long-term shear strength of soil. Cheng *et al.* (2009) obtained the long-term shear strength of the weak interlayer collected from two typical redbed soft rock slopes. Zhou *et al.* (2012) analyzed the major mode of the soil erosion in karst areas by combining the long-term shear strength of brown clay, which had been obtained by the long-term creep properties study of the brown clay. Yang *et al.* (2013) studied the shear creep properties of attenuation creep soil by the direct shear creep test, and proposed the long-term shear strength of the attenuation creep soil to assess the long-term stability of the northern slope of an open-pit mine in Fushun City, Liaoning Province, China. Zhu & Yu (2014) studied attenuation creep soil by creep test, and the long-term shear strength of the attenuation creep soil was deduced by the creep curves and isochronous curve method. Most researches focused on attenuation creep soil, while there are many non-attenuation creep soils in the practical project (*e.g.*, this weak interlayer), which need the assessments of the long-term stability too.

Based on special engineering geological conditions of a cut-slope area at Heitanping hilly-pass along Yongzhou-Jishou highway, it was found that there was an obvious weak interlayer in this slope (depth about 27.8-31.2 m, Fig. 1), and the landslide occurred easily along the weak interlayer. The creep curves of the weak interlayer under constant compressive stress (determined by the soil overburden pressure) and different shear stresses were obtained by using the direct-shear creep apparatus to study the shear creep properties of the weak interlayer. Then, shear creep constitutive equation and long-term shear strength can be obtained, which provides the theoretical basis for the safe treatment of the slope in this area.

2. Soil Samples Preparation and Test Arrangement

2.1. Soil samples preparation

The soil samples were taken from the weak interlayer of a cut-slope area at Heitanping hilly-pass along Yongzhou - Jishou highway (depth about 27.8-31.2 m, Fig. 1). The borehole, 36.5 m deep, was above the water line. All the soil samples were listed in Table 1. The rock mass is better at a depth of 11.5-17.6 m, and the Rock Quality Designation (RQD) is more than 80 %; the rock stratum in the depth of 17.6-27.8 m was broken, and the RQD was almost zero; the rock stratum in the depth of 27.8-31.2 m was poor with strongly weathered sandy mudstone soil, which was supposed as sliding zone in the middle layer (Fig. 1); the rock stratum in the depth of 31.2-32 m was better than the one in the depth of 27.8-31.2 m, with strongly-weathered rock. So it could be considered that the rock stratum in the depth of 27.8-31.2 m was the weak interlayer, with about

Table 1 - Soil samples (hole depth 36.5 m, no water level).

Depth of soil layer (m)		Description of lithology
Silty-clay slate	0.0-7.8	The main component is silty clay, which contains fully weathered slate.
	7.8-11.5	It is mainly composed of strongly weathered soil, which is supposed as sliding zone in shallow layer.
Strongly weathered slate	11.5-17.6	The core exhibits short column rocks, and the RQD is locally greater than 80 %.
	17.6-27.8	The rock mass is broken, and the RQD is almost zero.
Strongly weathered sandy mudstone soil (the weak interlayer)	27.8-31.2	This layer is mainly composed of strongly weathered sandy-mudstone soil, which is supposed as sliding zone in the middle layer, and the test samples for this study were taken from this layer.
Medium weathered slate	31.2-32.0	The stratum is mainly broken rock and has palimpsest texture and slaty structure.
	32.0-36.5	It is mainly composed of medium weathered slate with palimpsest texture, and slaty structure, where the size of broken rocks is 2-7 cm.

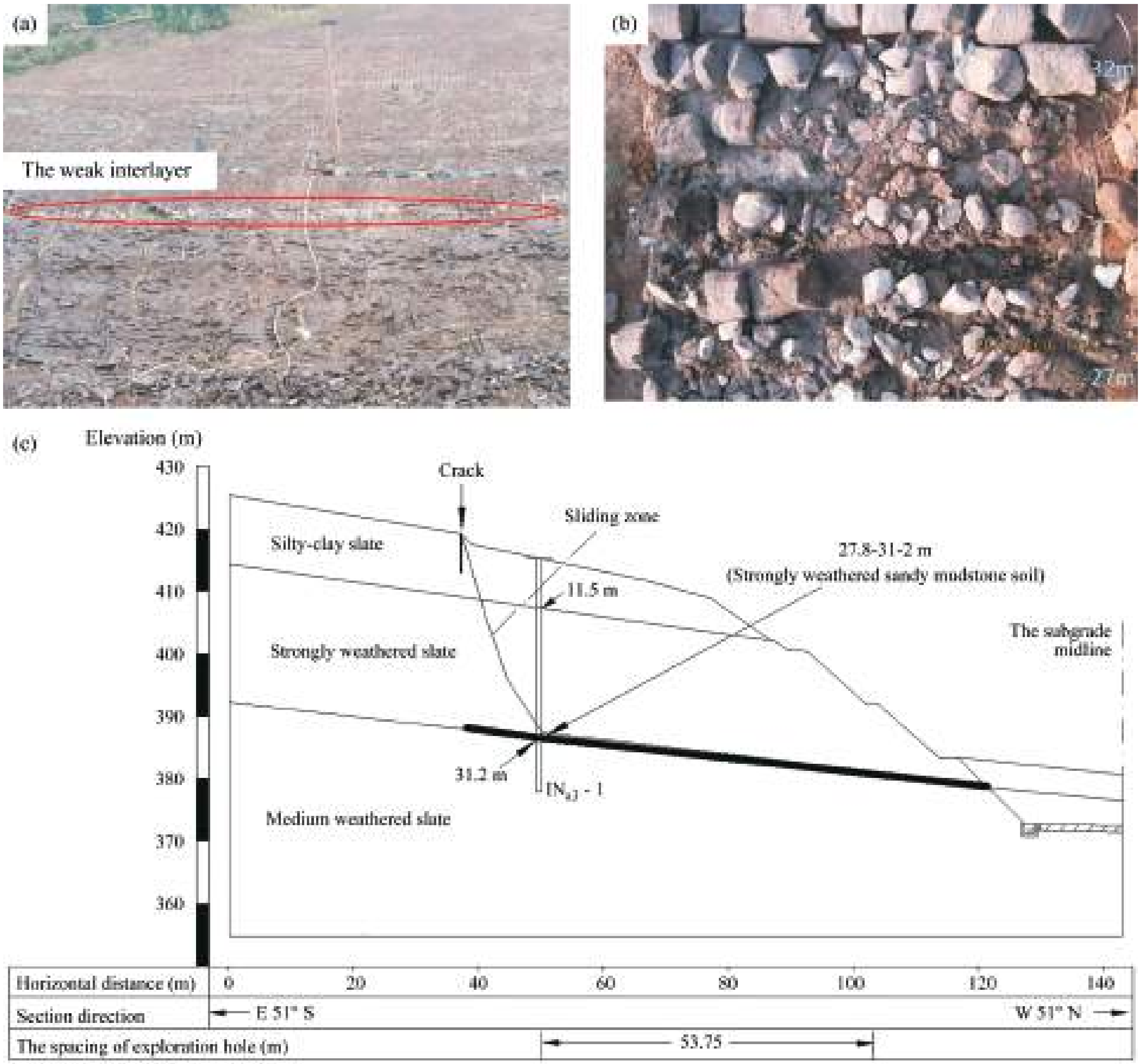

Figure 1 - The slope of Heitanping hilly-pass and the borehole soil samples. (a) The slope of Heitanping hilly-pass. (b) Borehole soil samples (depth of 27.8-31.2 m). (c) The section of the slope.

11.45 % water content homogeneous soil. The samples of the weak interlayer could be prepared by 20 mm-high ring knife, and a total of 5 ring samples were taken, 4 of which were used to determine the shear strength parameters c, φ, one for the shear creep test, keeping in humidistat to prevent dryness.

2.2. Test arrangement

Based on Table 1, the overburden pressure σ of the weak interlayer was calculated as 785 kPa, which can be exerted to the soil samples as vertical pressure by weights. The cohesion c = 5 kPa and internal friction angle φ = 10.30° of the soil samples can be obtained by conventional slow direct shear test (The Construction Department of the People's Republic of China 1999). And the short-term shear strength τ_f of the soil samples under the overburden pressure σ (785 kPa) was 148 kPa.

As shown in Fig. 2, the direct shear creep apparatus was refitted by conventional direct shear apparatus. The undisturbed soil samples were consolidated under the vertical pressure p (i.e., the overburden pressure σ) until the vertical dial indicator had stable data. The horizontal shear stress ($\tau_i = \tau_f/n$) was applied with step loads (load levels n = 4) as τ_1 (40 kPa), τ_2 (80 kPa), τ_3 (120 kPa), τ_4 (143 kPa, where the soil sample was damaged at this load level). Each level of the load was sustained 12 d, and finally, the soil sample was

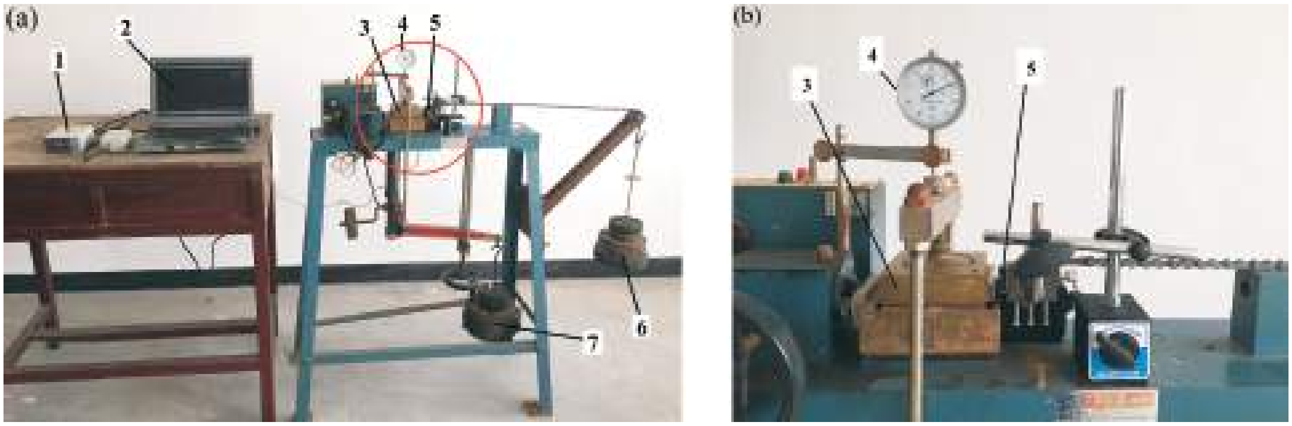

Figure 2 - Direct shear creep apparatus. (a) Direct shear creep apparatus. (b) Partial enlarged detail.

destructed under the shear stress τ_4 (Fig. 3). The moisturizing treatment should be done around the shear box during the test to prevent soil water from evaporating.

3. Analysis of Test Results

Fig. 3 shows the direct shear creep curves of the weak interlayer under constant compressive stress (the overburden pressure) and step shear stresses, which can be converted into the shear creep curves under separate loading by Tan Tjongkie theory (Zhu & Yu, 2014; Wang *et al.*, 2015; Zhu & Yu, 2015) (Fig. 4). It can be seen that all of the shear creep curves can be divided into three stages: instantaneous elastic stage, primary creep stage, and stationary creep stage.

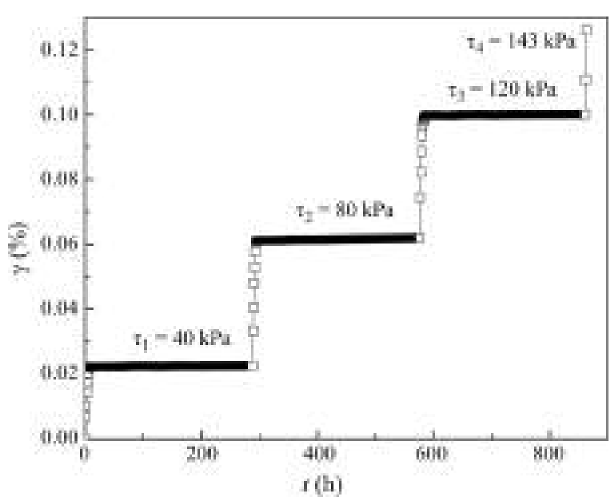

Figure 3 - Shear creep curves under step loading.

Under the constant shear stress, the shear instantaneous elastic stage occurs. The instantaneous elastic displacement increases with the increase of shear stress macroscopically, where the relative displacements of internal soil particles increase with the increase of shear stress microscopically.

The primary creep stage is relatively short (about 10 h), and enters into the stationary creep stage soon. As time increases, the weakness of soil will irregularly deform to fail (called softening effect), which results in relative displacements and rearranges tight connecting of the clay particles (called hardening effect). The hardening effect process increases with time until it reaches the dynamic equilibrium with the softening effect. Since the soil has high plasticity, which needs a relatively short time to reach the maximum hardening effect, besides, it shows that the primary creep stage of soil is very short, and transfers into the stationary creep stage soon.

In the stationary creep stage, the shear creep curves of the soil sample show constant creep rates, and the creep deformation rates (0.847293-0.894393 $\times$ 10^{-6}/s) are lower than the average value of 0.885793 $\times$ 10^{-6}/s. It is shown that the rate of the hardening effect is smaller than the rate of the softening effect when the soil samples are subjected to the shear stress, which makes the soil creep keep constant.

4. Creep Model and Creep Parameter

4.1. Creep model

The stress of the spring is proportional to the strain, the stress of the dashpot is proportional to the strain rate, which constitute the mechanical model of elastomer and Newtonian fluid, respectively. If they are combined, visco-

Table 2 - Stable creep rate (unit: /s $\times$ 10^{-2}).

Load level	$d\gamma/dt$ (τ_1 = 40 kPa)	$d\gamma/dt$ (τ_2 = 80 kPa)	$d\gamma/dt$ (τ_3 = 120 kPa)	Average
Creep rate	2.353592	2.484425	2.436647	2.460536

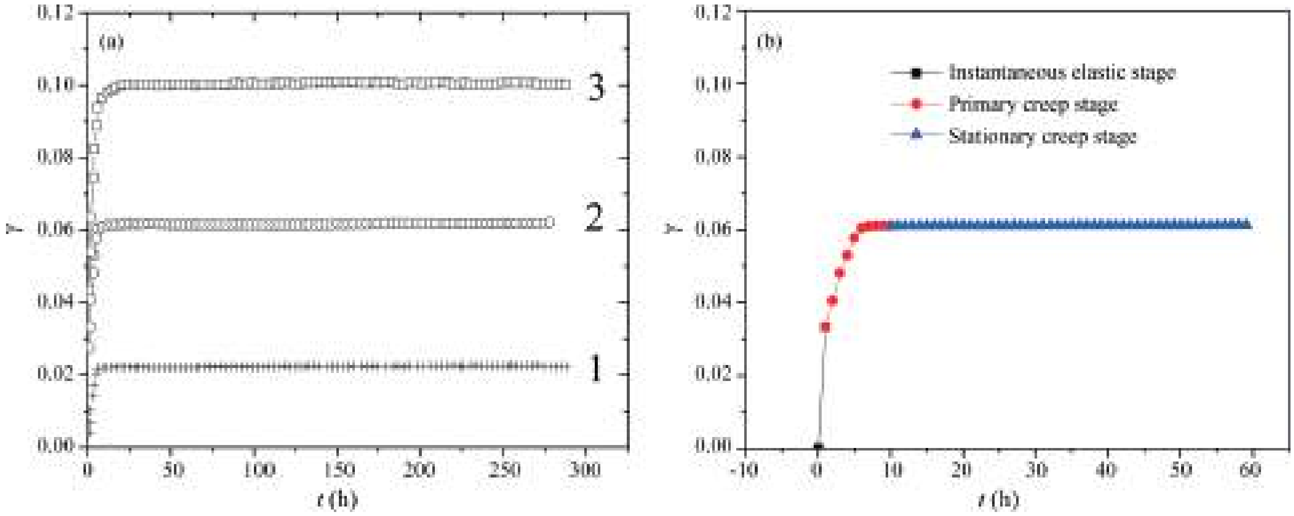

Figure 4 - Shear creep curves under separate loading. (a) Shear creep curves under separate loading (τ (kPa): 1-40; 2-80; 3-120). (b) Partial enlarged detail of No. 2 creep curve.

elastic characteristics of some complex fluids can be described, such as Maxwell model (Fig. 5 (a)) can be obtained by connecting spring and dashpot in series, and Kelvin model (Fig. 5 (b)) can be obtained by connecting spring and dashpot in parallel (Kang *et al.*, 2015).

The creep constitutive equation of the Maxwell model is as follows:

$$\varepsilon(t) = \frac{\sigma_0}{\beta} \cdot t + \frac{\sigma_0}{E} \tag{1}$$

where σ_0 is constant stress. E is an elastic constant and β is a viscosity coefficient.

The creep curve of Maxwell model is a straight line. After the constant stress σ_0 is applied, the instantaneous elastic strain $\frac{\sigma_0}{E}$ is produced, and then the deformation occurs at a constant rate $\frac{\sigma_0}{\beta}$, that is to say, under a certain stress, the material can gradually produce infinite deformation, which is the characteristic of fluid (Lewandowski & Chorazyczewski, 2010). Therefore, Maxwell model is not suitable for the model that needs to be established in this paper.

The creep equation of Kelvin model is as follows:

$$\varepsilon(t) = \frac{\sigma_0}{E}\left(1 - e^{-\frac{Et}{\beta}}\right) \tag{2}$$

the strain increases with time. When $t \to \infty$, $\varepsilon \to \frac{\sigma_0}{E}$, such as an elastic solid (Lewandowski & Chorazyczewski, 2010), because it has no instantaneous elasticity, it cannot be used to describe the creep constitution of the soil sample studied in this paper.

The K-H model is composed of an elastomer and a Kelvin model in series (Fig. 6). Its creep equation is as follows:

$$\varepsilon(t) = \frac{\sigma_0}{E_1} + \frac{\sigma_0}{E_2}\left(1 - e^{-\frac{E_2 t}{\beta}}\right) \tag{3}$$

The K-H model describes solids with instantaneous elasticity and delayed elasticity (Xiong *et al.*, 2015). K-H

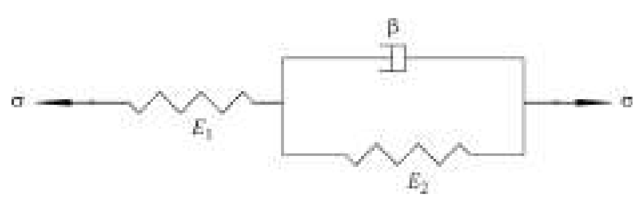

Figure 6 - K-H rheological model.

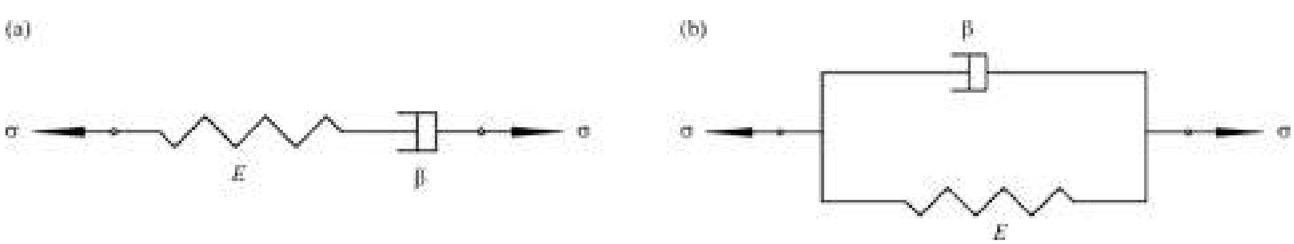

Figure 5 - (a) Maxwell model and (b) Kelvin model.

creep model was used to fit the creep curve of this paper by means of OriginPro software. The fitting curve is shown in Fig. 7 (a). The fitting accuracy R^2 of the separate loading is 0.9678, 0.9825 and 0.9891, respectively.

The Burgers model is made up of Kelvin model and Maxwell model in series (Fig. 8), which also reflects the softening and hardening characteristics of rheological materials. From this viewpoint, it is reasonable to characterize the creep characteristics of soil samples in this paper than other models (Xiong *et al.*, 2015). The creep equation of Burgers model is as follows:

$$\varepsilon(t)=\sigma_0\left[\frac{1}{E_1}+\frac{t}{\beta_1}+\frac{1}{E_2}\left(1-e^{-\frac{E_2 t}{\beta_2}}\right)\right] \tag{4}$$

The Burgers creep model was used to fit the experimental curve with the help of OriginPro software. The fitting curve is shown in Fig. 7 (b). The fitting accuracy R^2 of the hierarchical loading is 0.9704, 0.9875 and 0.9883, respectively.

In recent years, some scholars have used fractional derivative creep model to describe the creep characteristics of rock and soil, which have a good fitting effect on nonlinear creep curve (Zhou *et al.*, 2012). The constitutive equations with fractional derivative have been proved to be a valuable tool to handle viscoelastic properties (Khan *et al.*, 2009; Lai *et al.*, 2016; Heymans & Bauwens, 1994).

In order to describe the creep curve more accurately, the non-stationary parameter fractional derivative Burgers model and stationary parameter fractional derivative Burgers model (fractional order α = 1/8, 2/8, 3/8, 4/8, 5/8, 6/8, 7/8) were selected respectively to fit the creep curves of the weak interlayer for parameter identification (Podlubny, 1999).

Replacing the traditional Newton dashpot with Abel dashpot was the essence of the fractional derivative constitutive model (Darabi *et al.*, 2011). And the definition of Abel kernel $I_\alpha\,(t)$ was expressed as

$$I_\alpha=\begin{cases}\dfrac{1}{\Gamma(1-\gamma)t^{\alpha}}, & t>0\\ 0, & t\le 0,\ \ 0\le\alpha\le 1\end{cases} \tag{5}$$

where $\Gamma(z)$ is the Gamma function.

The fractional derivative can reflect the memory effect of viscoelasticity because it is actually the Volterra integral of Abel kernel function (Koeller, 1984; Darabi *et al.*, 2011). Thus, the fractional derivative constitutive model can describe the time effect of the viscoelastic material very well. And the constitutive relationship of the Abel dashpot is expressed as

$$\sigma(t)=\eta^{\alpha}D^{\alpha}[\varepsilon(t)]=\eta^{\alpha}I_{\alpha}\,d\varepsilon \tag{6}$$

where η^a is the viscosity parameter of the Abel dashpot. It is an ideal solid when $\alpha = 0$, and it is an ideal fluid when $\alpha = 1$. D^α is the Riemann-Liouville fractional derivative operator, which is expressed as

$$D^{\alpha}[f(t)]=\frac{1}{\Gamma(1-\alpha)}\frac{d}{dt}\int_0^t\frac{f(t-\xi)}{\xi^{\alpha}}d\xi,\quad (1\le\alpha\le 1) \tag{7}$$

Fractal phenomena are prevalent in many subjects. A number of studies (Orczykowska *et al.*, 2015; Cajic *et al.*,

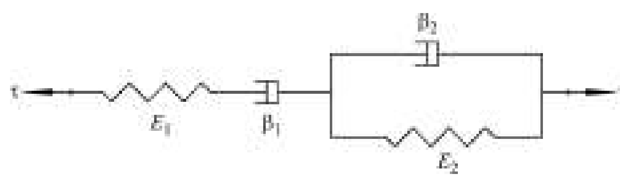

Figure 8 - Burgers rheological model.

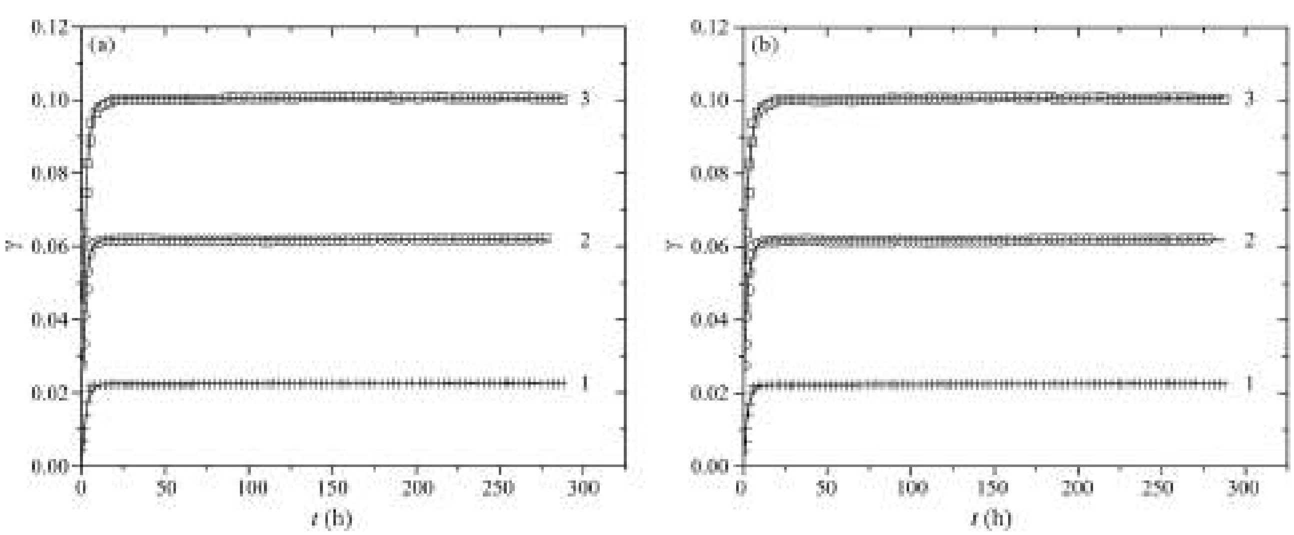

Figure 7 - Creep curve fitting results of K-H model and Burgers model (τ (kPa): 1-40; 2-80; 3-120; the solid-line curves are the fitting curves). (a) K-H model fitting curve (b) Burgers model fitting curve.

2017; Podlubny, 1999) have shown that the self-similarity spring-dashpot fractance can be used to describe fractional element (*i.e.*, Abel dashpot). The fractal network system composed of springs and dashpots, combined with fractal theory, determine the order of fractional order in creep constitutive equation. By means of Heaviside operator, the constitutive relationship of the spring-dashpot fractance (Fig. 5) can be deduced as follows (Podlubny, 1999).

The constitutive relation of the spring-dashpot fractance (Fig. 9) is expressed as

$$\tau = GT\gamma \tag{8}$$

where T is the operator to be solved. The Eq. (8) can be used to describe both spring in a special case of $T = 1$, and the Newtonian dashpot in a special case of $T = (\eta/G)D$ (where η is the viscosity coefficient of the dashpot, $D = \frac{d}{dt}$ is the first time derivative). Due to the series rule, the total stress is the same as that of the series components, while the total strain is the sum of the strain of all components. The total strain of the fractance shown in Fig. 9 can be expressed as

$$\gamma = \gamma_1 + \frac{\tau_1}{G} = \gamma_2 + D^{-1}\frac{\tau_2}{\eta} \tag{9}$$

Combining Eq. (8), the Eq. (9) can be further rewritten into

$$\gamma = (1+T)\gamma_1 = \left(1 + D^{-1}\frac{GT}{\eta}\right)\gamma_2 \tag{10}$$

Due to the parallel rule, the total strain is the same as that of the parallel components, while the total stress is the sum of the stress of all components. The total stress of the fractance can be expressed as

$$\tau = GT\gamma = \tau_1 + \tau_2 = GT(\gamma_1 + \gamma_2) \tag{11}$$

Combing Eq. (10) and Eq. (11), we get

$$T\left(\frac{1}{1+T} + \frac{1}{1+\dfrac{TGD^{-1}}{\eta}}\right)\gamma = T\gamma \tag{12}$$

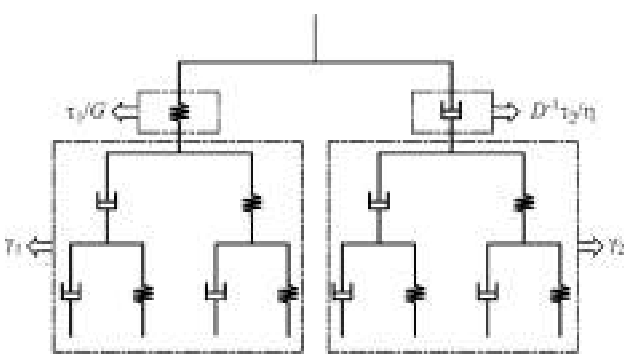

Figure 9 - Spring-dashpot fractance.

This indicates that the operator T needs to satisfy:

$$\frac{1}{1+T} + \frac{1}{1+\dfrac{TGD^{-1}}{\eta}} = 1 \tag{13}$$

According to the Heaviside calculus, the operator D can be used as a parameter. The constitutive operator of the spring-dashpot fractance T can be expressed as

$$T = \lambda^{1/2} D^{1/2} \tag{14}$$

where $\lambda = \eta/G$, and $D^{1/2} = \frac{d^{1/2}}{dt^{1/2}}$ is 1/2 derivative of time. Then, the constitutive relation of the spring-dashpot fractance shown in Fig. 5 can be expressed as

$$\tau = G(\lambda)^{1/2}\frac{d^{1/2}\gamma}{dt^{1/2}} \tag{15}$$

Equation (15) is the special case of the fractional derivative constitutive model as $\alpha = 1/2$.

By defining the fractance shown in Fig. 9 as a new element, and then replacing the dashpot of the fractance shown in Fig. 9 with the new element, a double fractance can be obtained. By the use of the computing method above, the constitutive operator of the double fractance can be expressed as

$$T = \lambda^{1/4} D^{1/4} \tag{16}$$

By defining the fractance shown in Fig. 9 as a new element, and then replacing the spring of the fractance shown in Fig. 9 with the new element, the other double fractance can be obtained. By the use of the computing method above, the constitutive operator of the new double fractance can be expressed as

$$T = \lambda^{3/4} D^{3/4} \tag{17}$$

In general, the following equation can be proved (Podlubny, 1999): by replacing the spring and the dashpot of the fractance shown in Fig. 9 by the operators $T_1 = \lambda^a p^a$ and $T_2 = \lambda^b p^b$, the multiple fractance can be obtained. And the constitutive operator of the multiple fractance can be expressed as

$$T = \lambda^{\frac{a+b}{2}} p^{\frac{a+b}{2}} \tag{18}$$

By replacing the dashpot in the Maxwell body of the Burgers model with the spring-dashpot fractance, the fractional derivative Burgers model (Ma *et al.*, 2014; Chen *et al.*, 2014; Zhao *et al.*, 2016; Xue *et al.*, 2016) can be obtained. As show in Fig. 10. The rheological constitutive equation can be expressed as

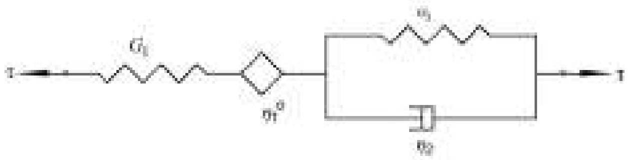

Figure 10 - Fractional derivative Burgers rheological model.

$$\tau+\frac{\eta_2}{G_2}D\tau+\left(\frac{\eta_1^\alpha}{G_1}+\frac{\eta_1^\alpha}{G_2}\right)D^\alpha\tau+\frac{\eta_1^\alpha\eta_2}{G_1G_2}D^{1+\alpha}\tau \\ =\eta_1^\alpha D^\alpha\gamma+\frac{\eta_1^\alpha\eta_2}{G_2}D^{1+\alpha}\gamma \tag{19}$$

By Laplace transform, the creep constitutive equation is expressed as

$$\gamma(t)=\tau\left[\frac{1}{G_1}+\frac{1}{\eta_1^\alpha}\frac{t^\alpha}{\Gamma(1+\alpha)}+\frac{1}{G_2}(1-e^{-t(G_2/\eta_2)})\right] \tag{20}$$

Five creep parameters need to be identified by fitting in the non-stationary parameter fractional derivative Burgers model: G_1, G_2, η_1^α, η_2 and α. Four creep parameters needed to be identified by fitting in the stationary parameter fractional derivative Burgers model: G_1, G_2, η_1^α, and η_2 (fractional order α = 1/8, 2/8, 3/8, 4/8, 5/8, 6/8, 7/8).

4.2. Creep parameter identification

Fig. 11 and Table 3 show the fitting results, and the correlation coefficient R^2, which was obtained by fitting the shear creep curves (Fig. 4) with Eq. 20. Accordingly, the three models could well describe the creep properties of the weak interlayer with high fitting precision ($R \geq 0.9077$); while the correlation coefficient of the non-stationary parameter fractional derivative Burgers model was lower, the stationary parameter fractional derivative Burgers model had a high correlation coefficient. And the correlation coefficient was the highest when the fractional order α = 1/8. So the fractional derivative Burgers model could describe the creep properties of the weak interlayer better when the fractional order α = 1/8.

Table 4 showed the creep parameters of the soil under different shear stresses, which were obtained by fitting tested shear creep curves with the stationary parameter

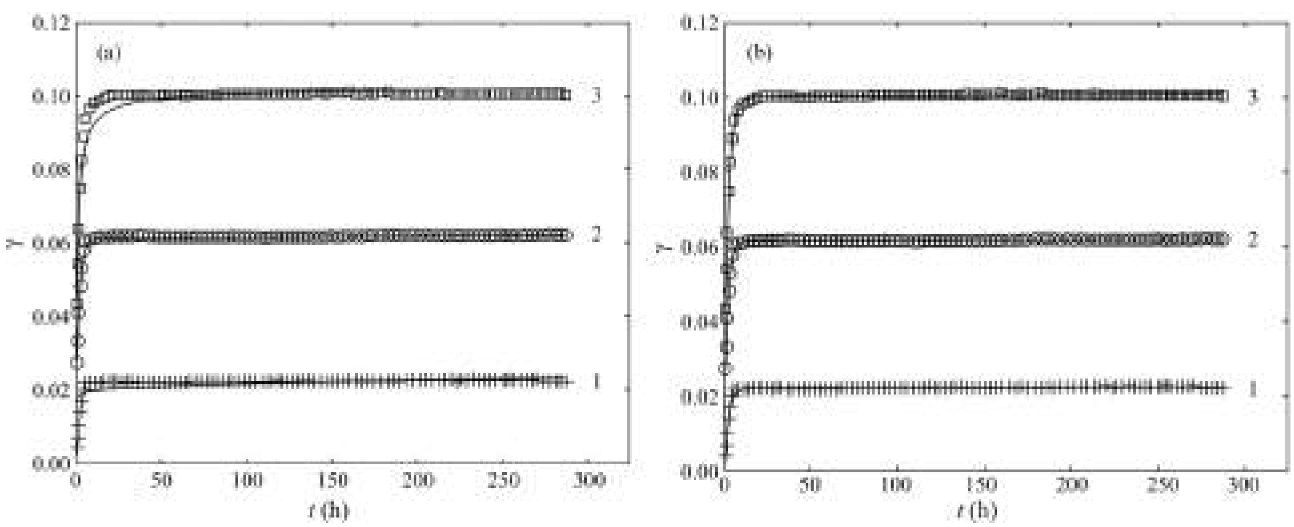

Figure 11 - Fitting shear creep curves of soil by different creep models (τ (kPa): 1-40; 2-80; 3-120; the solid-line curves are the fitting curves). (a) Non-stationary parameter fractional derivative Burgers model. (b) Stationary parameter fractional derivative Burgers model (α = 1/8).

Table 3 - Correlation coefficient R^2 of the creep models.

Shear stress τ (kPa)	Correlation coefficient R^2 of the fractional derivative Burgers model							
	Non-stationary α	α = 1/8	α = 2/8	α = 3/8	α = 4/8	α = 5/8	α = 6/8	α = 7/8
40	0.9077	0.9871	0.9864	0.9865	0.9865	0.9867	0.9865	0.9866
80	0.9436	0.9894	0.9891	0.9892	0.9893	0.9893	0.9894	0.9894
120	0.9672	0.9961	0.9956	0.9955	0.9955	0.9954	0.9954	0.9954
Average	0.9395	0.9909	0.9904	0.9904	0.9904	0.9905	0.9904	0.9905

Table 4 - Creep parameters (stationary parameter fractional derivative Burgers model, α = 1/8).

Shear stress τ(kPa)	G_1(kPa)	G_2(kPa)	η_1^α(kPa.h)	η_2(kPa.h)
40	2.3384×10^3	1.9555×10^3	4.5832×10^3	6.4165×10^3
80	3.1576×10^3	2.1387×10^3	4.8812×10^3	6.4173×10^3
120	2.8803×10^3	1.9545×10^3	4.7351×10^3	6.8617×10^3
Average	2.7921×10^3	2.0162×10^3	4.7332×10^3	6.5652×10^3

fractional derivative Burgers model (α = 1/8). Obviously, these four creep parameters (G_1, G_2, η_1^α, η_2) fluctuated slightly with the increase of shear stress, which finally tended to a constant value (*i.e.*, material constant), indicating that their average values can be used for the shear creep parameters of the weak interlayer in the slope.

5. Analyses of Long-term Shear Strength

The short-term shear strength can be obtained by a conventional shear strength test, where the soil samples were damaged in a very short time. And the short-term shear strength can be used in the short-term stability analysis of slopes. But the resistance of rock and soil under long-term load is different from that under short-term load. The strength of rock and soil decreases with the increase of load time. Therefore, the study of the long-term shear strength of soil is very important to slope stability analysis.

In order to obtain the long-term shear strength of the soil, it is needed to analyze the creep properties of the soil. For attenuation creep soil, the shear strain keeps a constant with the increase of time (Fig. 12) if the shear stress τ is less than the attenuation shear strength τ_∞ (Yang *et al.*, 2013) (*i.e.*, $\tau < \tau_\infty$), while the shear strain develops continuously with the increase of time until destruction if the shear stress τ is more than the attenuation shear strength τ_∞ (*i.e.*, $\tau > \tau_\infty$), indicating that the long-term shear strength, *i.e.*, the attenuation shear strength τ_∞, can be obtained on the basis of the isochronous curve method (Guo *et al.*, 2005; Xie *et al.*, 2014; Zhu & Yu, 2014; Gao *et al.*, 2015; Simsiriwong *et al.*, 2015).

For non-attenuation creep soil, the shear strain develops continuously with the increase of time until creep destruction, *i.e.*, there is no attenuation shear strength τ_∞ (Feng *et al.*, 2018; Ter-Martirosyan and Ter-Martirosyan, 2013). The long-term shear strength of such soil cannot be obtained by the isochronous curve method, but there are so many engineering projects that need to evaluate the long-term stability of such soil. In this paper, long-term shear strengths of such soil under different periods (such as 10 years, 20 years, 50 years, 100 years, etc.) can be deduced on the basis of the shear creep constitutive equation and the short-term shear strain corresponding to the short-term shear strength of the soil, which are deduced as follows.

Based on the shear creep constitutive equation above, the isochronous curves of shear stress-shear strain of the soil (Fig. 13) can be deduced for the curve between the shear elastic modulus G and time t (Fig. 14), which is fitted by the equation as follows.

$$G = \frac{1}{a + bt^{(c-1)}} \tag{16}$$

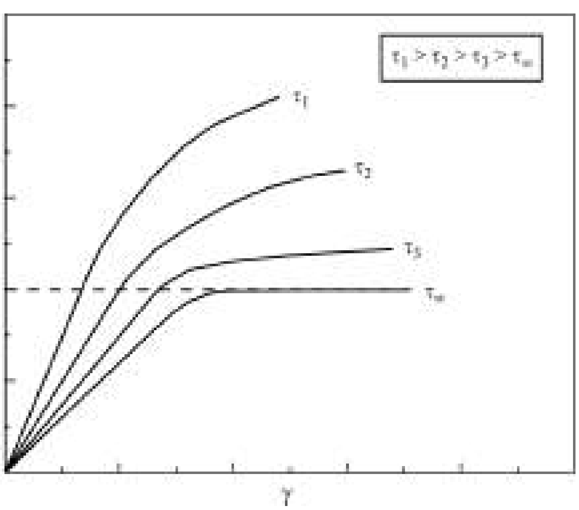

Figure 12 - Isochronous curves of stress-strain (attenuation creep soil).

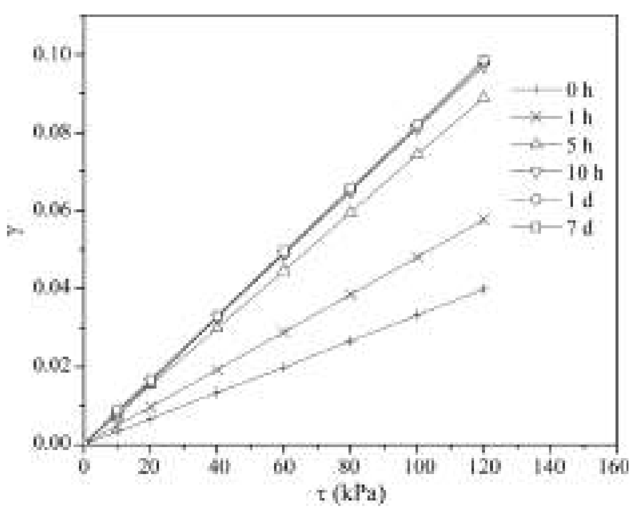

Figure 13 - The isochronous curves of shear stress-shear strain.

Table 5 - The comparison of the long-term shear strength and the short-term shear strength.

Time t (year)	Short-term	10	20	30	40	50	60	70	80	90	100
G (MPa)	3.007	0.352	0.217	0.160	0.127	0.106	0.092	0.081	0.072	0.066	0.060
τ_c (kPa)	143.00	41.55	25.58	18.80	14.99	12.53	10.80	9.51	8.51	7.72	7.06
τ_c/τ_f (%)	100.0	29.1	17.9	13.1	10.5	8.8	7.6	6.7	6.0	5.4	5.0

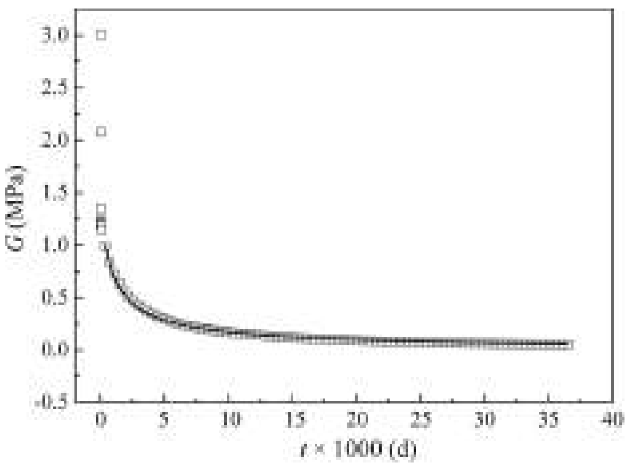

Figure 14 - The curve of the shear elastic modulus G-time t.

And the fitted G-t equation is showed as follows.

$$G = \frac{1}{0.72354 + 0.00157 \times t^{0.87826}} \tag{17}$$

The equation has a high fitting precision for the high correlation coefficient R^2 (R^2 = 0.95564).

The shear strain γ_{f0} = 0.047553 according to the short-term shear strength under the transient loading can be calculated on the basis of the shear elastic modulus G_0 = 3.0072 × 10^3 kPa and the short-term shear strength τ_f = 148 kPa under the overburden pressure σ = 785 kPa, which is considered as the limit of the soil damage. Thus, the long-term shear strength τ_{c10} = 41.55 kPa of the soil at 10 years can be calculated by using the critical shear strain γ_f = 0.117772 (the shear strain corresponding to the short-term shear strength) and the shear elastic modulus G = 0.35277 × 10^3 kPa when t = 3650 d. It shows that τ_{c10} is 29.1 % of the short-term shear strength in Table 5 as well as the other long-term shear strengths.

6. Conclusions

The shear creep properties of the weak interlayer in the slope (at Heitanping hilly-pass along Yongzhou-Jishou highway) were studied by direct shear creep apparatus, which was the modified direct shear apparatus. The shear creep constitutive equation of the soil was obtained by comparing two different creep models for the long-term shear strengths. In this study, the following conclusions can be drawn:

1) The shear creep properties of the weak interlayer are obtained by the modified direct shear creep apparatus. All shear creep curves can be divided into three stages: instantaneous elastic stage, primary creep stage, and stationary creep stage. The primary creep stage is relatively short and increases with the increase of shear stress.
2) The shear creep constitutive equation of the soil has been obtained by the stationary parameter fractional derivative Burgers model (fractional order α = 1/8) which has the best-fitted results of the shear creep curves of the soil compared with non-stationary parameter fractional derivative Burgers model.
3) The relationship between shear elastic modulus G- time t has been obtained by the isochronous shear stress-shear strain curves on the basis of the shear creep constitutive equation above. It is found that the long-term shear strengths, which are deduced by the G-t equation and the shear strain according to the short-term shear strength, decrease with the increase of time. Therefore, it is necessary to assess the weak interlayer by use of the long-term shear strength at different time.

Acknowledgments

The research was supported by the National Key R&D Program of China (2017YFC0504505), the National Natural Science Foundation of China (Grant Nos. 11502226 and 51434002), the Innovative Venture Technology Investment Project of Hunan Province (2018GK5028), the Key R&D Program of Hunan Province (2018WK2111), the Key Research and Development Plan of Hunan Province (No. 2017WK2032) and the Hunan Provincial Innovation Foundation for Postgraduate (No. CX2017B342). The project was supported by Open Fund of Key Laboratory of Road Structure and Material of Ministry of Transport (Changsha University of Science & Technology). Authors also acknowledge the technical support from the Hunan Key Laboratory of Geomechanics and Engineering Safety.

References

Cajic, M.; Karlicic, D. & Lazarevic, M. (2017). Damped vibration of a nonlocal nanobeam resting on viscoelastic foundation: fractional derivative model with two retardation times and fractional parameters. Meccanica, 52(1-2):363-382.

Chen, B.R.; Zhao, X.J.; Feng, X.T.; Zhao, H.B. & Wang, S.Y. (2014). Time-dependent damage constitutive model for the marble in the Jinping II hydropower station in China. Bulletin of engineering geology and the environment, 73(2):499-515.

Cheng, Q.; Zhou, D.P. & Feng, Z.J. (2009). Research on shear creep property of typical weak intercalation in redbed soft rock. Chinese Journal of Rock Mechanics and Engineering, 28(S1):3176-3180 (in Chinese).

China Geological Environmental Monitoring Institute. (2014). Chinese geological disasters Bulletin 2013. China geological environment information site. http://www.cigem.gov.cn. Accessed 10 June 2014.

Darabi M.K.; Abu Al-Rub R.K.; Masad E.A; Huang C.W. & Little D.N. (2011). A thermo-visco-elastic-visco-plastic-viscodamage constitutive model for asphaltic materials. International Journal of Solids and Structures, 48(1):191-207.

Feng H.; Lai Y.M.; Liu E.L.; Luo H.W. & Liu X.Y. (2018) A creep constitutive model for frozen soils with different contents of coarse grains. Cold Regions Science and Technology. 145:119-126.

Gao, D.D.; Wang, P.B.; Li, M. & Luo, W.B. (2015). Modelling of nonlinear viscoelastic creep behaviour of hot-mix asphalt. Construction & Building Materials, 95:329-336.

Guo, Y.C.; Xin, C.L.; Song, M.S. & He, Y.D. (2005). Study on short-and long-term creep behavior of plastics geogrid. Polymer testing, 24(6):793-798.

Hasegawa, S.; Dahal, R.K.; Nishimura, T.; Nonomura, A. & Yamanaka, M. (2009). DEM-based analysis of earthquake-induced shallow landslide susceptibility. Geotechnical and Geological Engineering, 27(3):419-430.

He, Z.L.; Zhu, Z.D.; Zhu, M.L. & Li, Z.J. (2016). An unsteady creep constitutive model based on fractional order derivatives. Rock Mechanics & Rock Engineering, 37(3):737-744 (in Chinese).

Heymans, N. & Bauwens, J.-C. (1994). Fractal rheological models and fractional differential equations for viscoelastic behavior. Rheologica Acta, 33(3):210-219.

I. Podlubny (1999). Fractional Differential Equations. New York. Academic Press, p. 271-273.

Ilori, A.O.; Essien, N.U. & Edet, A.E. (2010). Geotechnical, Geological, and Hydrologic Characterization of a 52 km Electrical Power Transmission Line Alignment Route in Southeastern Nigeria. Geotechnical and Geological Engineering, 28(6):907-923.

Jeong, S.W.; Leroueil, S. & Locat, J. (2009). Applicability of power law for describing the rheology of soils of different origins and characteristics. Canadian Geotechnical Journal, 46(9):1011-1023.

Kang J.H.; Zhou F.B.; Liu C. & Liu Y.K. (2015). A fractional non-linear creep model for coal considering damage effect and experimental validation. International Journal of Non-Linear Mechanics, 76:20-28.

Khan, M.S.; Hyder, Ali & Qi, H.T. (2009). On accelerated flows of a viscoelastic fluid with the fractional Burgers' model. Nonlinear Analysis: Real World Applications, 10(4):2286-2296.

Koeller R.C. (1984). Applications of fractional calculus to the theory of viscoelasticity. Journal of Applied Mechanics, 51(2):299-307.

Lai, J.X.; Mao, S.; Qiu, J.L.; Fan, H.B.; Zhang, Q.; Hu, Z.N. & Chen, J.X. (2016). Investigation progresses and applications of fractional derivative model in geotechnical engineering. Mathematical Problems in Engineering, 2016(3):1-15.

Le, T.M.; Fatahi, B. & Khabbaz, H. (2012). Viscous behaviour of soft clay and inducing factors. Geotechnical and Geological Engineering, 30(5):1069-1083.

Li, B.; Wu, L.; Chen, J.; Peng, Y.X.; Chen, C.H. & Zhou, C.X. (2016). The influences of destruction effects of earthquake faults on the dynamic stability of highway slopes. Geotechnical and Geological Engineering, 34(5):1513-1523.

Ma, W.B.; Rao, Q.H.; Li, P.; Guo, S.C. & Feng, K. (2014). Shear creep parameters of simulative soil for deep-sea sediment. Journal of Central South University, 21(12):4682-4689.

Orczykowska, M.; Dziubinski, M. & Owczarz, P. (2015). Structural analysis of gluten-free doughs by fractional rheological model. Korea-Australia Rheology Journal, 27(1):33-40.

R. Lewandowski & B. Chorazyczewski (2010). Identification of the parameters of the Kelvin-Voigt and the Maxwell fractional models, used to modeling of viscoelastic dampers. Computers and Structures, 88(1-2):1-17.

Rackwitz, F.; Savidis, S.A. & Rickriem, J. (2013). Web-based data and monitoring platform for complex geotechnical engineering projects. Geotechnical and Geological Engineering, 31(3):927-939.

Roy, N. & Sarkar, R. (2016). A review of seismic damage of mountain tunnels and probable failure mechanisms. Geotechnical & Geological Engineering, 35(1):1-28.

Simsiriwong, J.; Sullivan Jr., R.W.; T.E.L. & Hilton, H.H. (2015). A statistical approach to characterize the viscoelastic creep compliances of a vinyl ester polymer. Polymer Testing, 48:183-198.

Ter-Martirosyan, Z.G. & Ter-Martirosyan, A.Z. (2013). Rheological properties of soil subject to shear. Soil Mechanics & Foundation Engineering, 49(6):219-226.

The Construction Department of the People's Republic of China. (1999). GB/T50123-1999, Standard for soil test method. Beijing: China Planning Press, 110-112 (in Chinese).

Tiwari, R.C.; Bhandary, N.P. & Yatabe, R. (2015). 3D SEM approach to evaluate the stability of large-scale landslides in Nepal Himalaya. Geotechnical and Geological Engineering, 33(4):773-793.

Wang, M.Y.; Zhang, N.; Li, J.; Ma, L.J. & Fan, P.X. (2015). Computational method of large deformation and its application in deep mining tunnel. Tunnelling & Underground Space Technology, 50:47-53.

Wang, Z.J.; Yin, K.L. & Jian, W.X. (2007). Experimental research on creep of incompetent beds in Jurassic red clastic rocks in Wanzhou. Rock and Soil Mechanics, 28(S1):40-44 (in Chinese).

Xie, Y.J.; Fu, Q.; Long, G.C.; Zheng, K.R. & Song, H. (2014). Creep properties of cement and asphalt mortar. Electric Power Automation Equipment, 70:9-16.

Xiong, L.X.; Li, T.B.; Yang, L.D. & Yuan, X.W. (2014). A study on stationary and nonstationary viscoelastic models of greenschist. Arabian Journal of Geosciences, 8(5):2477-2486

Xu, B.T.; Yan, C.H.; Liu, J.X. & Chen, H.Y. (2010). Study of shear deformation constitutive model of weak intercalated layers in slope. Rock and Soil Mechanics, 31(S2):65-69 (in Chinese).

Xue, Y.; Mishra, B. & Gao, D. (2016). Numerical and laboratory analysis of relaxation tests for determining time-dependent properties of rock. Geotechnical & Geological Engineering, 35(2):615-629.

Yang, S.Q. & Cheng, L. (2011). Non-stationary and nonlinear visco-elastic shear creep model for shale. International Journal of Rock Mechanics and Mining Sciences, 48(6):1011-1020.

Yang, T.H.; Xu, T.; Liu, H.Y.; Zhang, C.M.; Wang, S.Y.; Rui, Y.Q. & Shen, L. (2013). Rheological characteristics of weak rock mass and effects on the long-term stability of slopes. Rock Mechanics & Rock Engineering, 47(6):2253-2263.

Zhao, Y.L.; Wang, Y.X.; Wang, W.J.; Wan, W. & Tang, J.Z. (2016). Testing study on crack propagation due to rheological fracture in quasi-brittle material under compression-shear or double torsional loading. Geotechnical & Geological Engineering, 34(5):1655-1667.

Zhou, H.W.; Wang C.P.; Duan, Z.Q.; Zhang, M. & Liu, J.F. (2012). Time-based fractional derivative approach to creep constitutive model of salt rock£®Scientia Sinica Physica, Mechanica & Astronomica, 42(3):310-318.

Zhou, J.; Tang, Y.Q.; Yang, P.; Zhang, X.H.; Zhou, N.Q. & Wang, J.X. (2012). Inference of creep mechanism in underground soil loss of karst conduits I. Conceptual model. Natural hazards, 62(3):1191-1215.

Zhu, Y.B. & Yu, H.M. (2014). An improved Mesri creep model for unsaturated weak intercalated soils. Journal of Central South University, 21(12):4677-4681.

Zhu, Y.B. & Yu, H.M. (2015). Unsaturated creep behaviors of weak intercalated soils in soft rock of Badong formation. Journal of Mountain Science, 12(6):1460-1470.

Technical Note

Soils and Rocks
v. 42, n. 3

Prediction of Load-Settlement Curves by the DMT in an Unsaturated Tropical Soil Site

N.M. Silva, B.P. Rocha, H.L. Giacheti

Abstract. Several methods for prediction of the load-settlement curves of shallow foundations have been proposed based on *in-situ* testing data. However, the good accuracy of such prediction depends on the definition of appropriate soil stiffness. Seasonal variability and its influence on the soil behavior need to be considered for unsaturated tropical soils. In this context, this study uses a procedure to determine the complete load-settlement curves of shallow foundations by the flat dilatometer test (DMT) in an unsaturated tropical soil site, considering seasonal variability. The DMT and the plate load tests carried out at the experimental research site of the University of São Paulo (São Carlos, Brazil) are presented and discussed. It was found that the DMT is an adequate test for predicting soil stiffness, and the presented procedure allows a good estimate of the complete load-settlement curves. It was also observed that seasonal variability should be considered in the prediction of such curves for the studied site.

Keywords: flat dilatometer test (DMT), *in-situ* tests, load-settlement curve, seasonal variability, tropical soils.

1. Introduction

Several methods are available to predict the load-settlement curve based on *in-situ* test data (Schmertmann, 1986; Mayne *et al.*, 2000; Briaud, 2007). However, in most cases, these methods consider that the deformability modulus is constant (Lehane & Fahey, 2004). Moreover, the accuracy of these curves' prediction depends on the adequate definition of soil stiffness for the deformation level imposed by the foundation element (Mayne, 2001, Shin & Das, 2011).

The plate load test has been commonly used to represent the behavior of shallow foundations (Consoli *et al.*, 1998; Menegotto, 2004, Tang *et al.*, 2018). The utilization of plate load test results allows minimization of the effects of the "scale" factor, soil sample disturbance, and selected technique on the input information for a foundation design (Reznik, 1993).

The flat dilatometer (DMT) has been shown to be an accurate test technique for site characterization (Marchetti *et al.*, 2001; Marchetti & Monaco, 2018), compacted fill analyses (Queiroz *et al.*, 2012; Amoroso *et al.*, 2015), laterally loaded pile analyses (Robertson *et al.*, 1987; Marchetti *et al.*, 1991), as well as to predict foundation settlements (Schmertmann, 1986; Monaco *et al.*, 2006; Anderson *et al.*, 2007; Monaco *et al.*, 2014). Very few studies evaluating the applicability of such test for predicting the complete load-settlement curves of shallow foundations in unsaturated tropical soils have been found in the literature.

Soils formed in tropical weather regions are influenced by drying and wetting cycles, which lead to the formation of thick profiles of unsaturated soils. It is important to consider seasonal variability in these soil sites caused by soil suction, which is related to the water content through a soil-water retention curve (SWRC). Therefore, the behavior of unsaturated soils cannot be considered without taking into account soil suction (ψ) and the site variability (Giacheti *et al.*, 2019).

This study presents the results of flat dilatometer and plate load tests for prediction of the load-settlement curves of shallow foundations in an unsaturated tropical sandy soil. The DMT and plate load tests were carried out in different months of the year to better understand the influence of seasonal variability on the load-settlement curve prediction in the studied site.

2. Flat Dilatometer Test (DMT)

2.1. Principles of test procedure and interpretation

Marchetti (1980) and Marchetti *et al.* (2001) describe the flat dilatometer, which has a steel blade 14 mm thick, 94 mm wide and an expandable circular steel membrane (60 mm diameter) mounted on one face. The blade is connected, by an electro-pneumatic tube, running through the insertion rods, to a control unit on the surface. The authors also describe the test procedure which starts by inserting the dilatometer into the ground. By use of a control unit with a pressure regulator, a gauge and an audio signal, the operator determines the p_0-pressure required to just begin to

Nathália Marques da Silva, M.Sc., Departamento de Geotecnia, Universidade de São Paulo, São Carlos, SP, Brazil. e-mail: nathmdasilva.eng@usp.com.
Breno Padovezi Rocha, Ph.D., Departamento de Geotecnia, Universidade de São Paulo, São Carlos, SP, Brazil and Departamento de Engenharia Civil e Ambiental, Universidade Estadual Paulista, Bauru, SP, Brazil. e-mail: brenop@sc.usp.br.
Heraldo Luiz Giacheti, Ph.D., Professor, Departamento de Engenharia Civil e Ambiental, Universidade Estadual Paulista, Bauru, SP, Brazil and Departamento de Geotecnia, Universidade de São Paulo, São Carlos, SP, Brazil. e-mail: h.giacheti@unesp.br.
Submitted on March 15, 2019; Final Acceptance on August 1, 2019; Discussion open until April 30, 2020.
DOI: 10.28927/SR.423351

move the membrane and the p_1-pressure required to move it 1.1 mm into the ground. The blade is then advanced into the ground by one depth increment, typically 200 mm, using common field equipment.

The DMT interpretation starts by first determining three intermediate parameters (Marchetti, 1980; Marchetti *et al.*, 2001): the material index (I_D), the horizontal stress index (K_D) and the dilatometer modulus (E_D), which are defined as:

$$\text{Material index, } I_D = \frac{p_1 - p_0}{p_0 - u_0} \tag{1}$$

$$\text{Horizontal stress index, } K_D = \frac{p_0 - u_0}{\sigma'_v} \tag{2}$$

$$\text{Dilatometer modulus, } E_D = 34.7(p_1 - p_0) \tag{3}$$

where u_0 is the pre-insertion in situ equilibrium pore pressure and σ'_v is the pre-insertion in situ vertical effective stress.

A detailed description of the DMT equipment and test procedure can be found in Marchetti (1980), Marchetti *et al.* (2001) and Marchetti & Monaco (2018).

2.2. Prediction of shallow foundation settlements by the DMT

Predicting the settlements of shallow foundations is often considered the main application of the DMT (Schmertmann, 1986; Monaco *et al.*, 2006; Failmezger *et al.*, 2015). The accumulated experience suggests that the constrained modulus (M_{DMT}), which is determined according to Marchetti (1980), can be assumed as an adequate operative or the working strain modulus for most practical purposes. This modulus is defined by Eq. 4:

$$M_{DMT} = R_M \cdot E_D \tag{4}$$

where M_{DMT} = constrained modulus from DMT, R_M = correction factor, a function of I_D and K_D.

Lehane & Fahey (2004) investigated the influence of the disturbance caused by the DMT blade installation on the constrained modulus prediction in sands. The authors proposed an equation for estimating the constrained modulus for working condition (M_{DV}). According to Lehane and Fahey (2004), M_{DV} is more relevant to settlement prediction than $E_{D,}$ and can be considered an operational modulus applied by the dilatometer at a 1.8 % settlement ratio (δ/B_{eq}), according to Eq. 5:

$$M_{DV} = 1.3 f_{aniso} \frac{E_D}{\sqrt{K_D}} \quad \text{at} \quad \frac{\delta}{B_{eq}} = 1.8\,\% \tag{5}$$

where δ = settlement, B_{eq} = the square root of the base width of the foundation element, f_{aniso} = inherent anisotropy factor.

Décourt (1999) proposed an approach to extrapolate the plate load test data by analyzing the results of 145 load tests on shallow foundations and on rigid steel plates carried out all over the world in very different soils.

Dos Santos *et al.* (2019) integrated Décourt's (1999) approach for the representation of the normalized load-settlement curve and Lehane & Fahey's (2004) considerations about M_{DV}, to predict a complete load-settlement curve. This approach was tested and compared with plate load tests carried out in a tropical sandy soil from an experimental research site in Bauru-SP, Brazil. Good agreement between the load-settlement curve predicted by the DMT and those determined by the plate load tests was found.

Figure 1 shows the representation of a typical curve, defined according to the approach used (Dos Santos *et al.*, 2019), where q = applied stress; q_{app} = applied stress at working condition; q_{uc} = load at conventional soil failure; δ = settlement; B_{eq} = square root of the base width of the foundation element.

The normalized load-settlement curve is represented together with the data point where the conventional rupture occurs. It is also possible to observe the representation of the DMT working load condition (δ/B_{eq} = 1.8 %) in this curve. Since the DMT membrane is 60 mm (B) in diameter and expands 1.1 mm (δ), a settlement ratio (δ/B) equal to 1.8 % is mobilized during the test.

3. Study Site

The DMT and plate load tests were carried out at the experimental research site of the University of São Paulo, in São Carlos-SP (Brazil). In this site, the subsoil is a clayey fine sand with two well-defined layers: Cenozoic Sediments with lateritic behavior (up to around 6.0 m depth) overlaying the residual soil derived from Sandstone with non-lateritic behavior. The groundwater level varies sea-

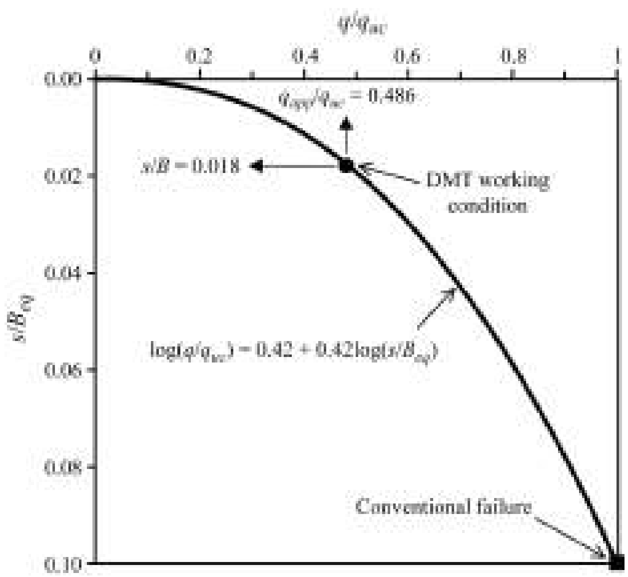

Figure 1 - Representation of the load-settlement curve based on the DMT (Dos Santos *et al.*, 2019).

sonally between 9 and 12 m below the ground surface. Both horizons can be classified as clayey sand (SC) according to USCS.

The tropical climate provides wet and hot seasons (October to April) that are followed by dry winters. This type of tropical weather can lead to variations in the *in-situ* soil suction since it features high annual temperatures with wet summers and dry winters. The seasonal variation's influence on soil suction can lead to significant changes in the *in-situ* test data, as discussed by Giacheti *et al.* (2019) based on CPT data. Figure 2 shows the soil profile together with dry unit weight (γ_d), void ratio (e) and Atterberg limits (w_L and w_P) of the studied site up to 12 m depth.

The soil-water retention curves (SWRCs) at 2.0, 5.0 and 8.0 m depths were determined by Machado & Vilar (1998) to examine the influence of soil suction on the soil strength and stiffness parameters (Fig. 3). The purpose of the laboratory investigation was to assess the influence of suction on the soil behavior. Figure 4 shows the data of the unsaturated oedometer tests carried out on undisturbed soil samples collected at 2.0, 5.0 and 8.0 m depths for different soil suction values. It shows that the pre-consolidation stress (σ'_p) values increase as the soil suction increases.

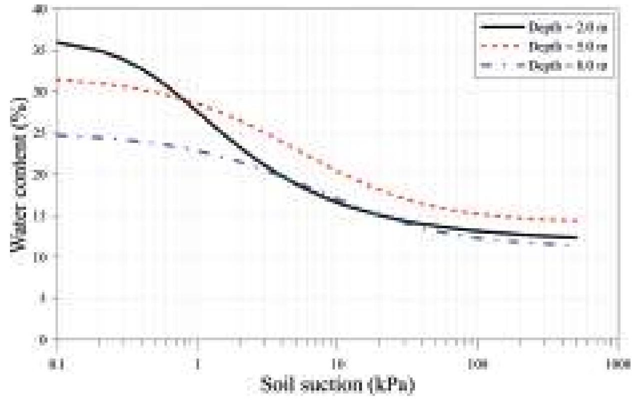

Figure 3 - Soil-water retention curves for the soil collected at 2.0 m, 5.0 m and 8.0 m depths (adapted from Machado & Vilar, 1998).

4. In-Situ Tests

4.1. DMT and plate load tests

The plate load tests were carried out on a rigid steel plate (25 mm thick and with 0.80 m diameter) at 1.5, 4.0, 6.0 and 8.0 m depths by Costa (1999) and Macacari (2001). The tests were carried out in natural and inundated conditions, allowing the evaluation of the influence of suction on the load-settlement curve. A total of 18 plate load tests were considered. A summary of the plate load tests used in this study is presented in Table 1. It should be mentioned that an average curve was considered for the inundated condition at 1.5 and 6.0 m depths. These tests were selected by considering the soil suction and water content profile by means of the SWRCs during the DMTs.

The DMTs were performed in March and October, 2016 and April and October, 2017 by Rocha (2018). Three DMT tests and one soil sampling were performed in each of these periods. Soil sampling was carried out up to 7.75 m

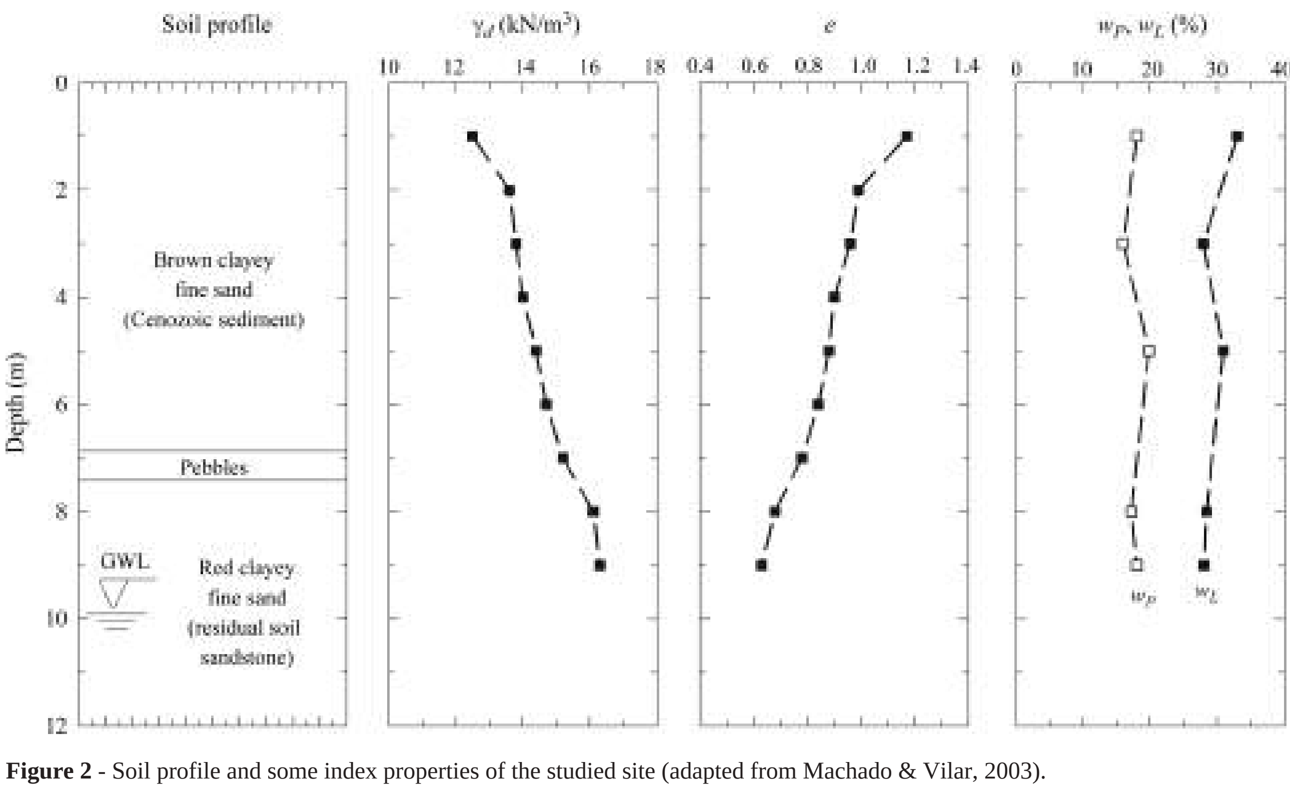

Figure 2 - Soil profile and some index properties of the studied site (adapted from Machado & Vilar, 2003).

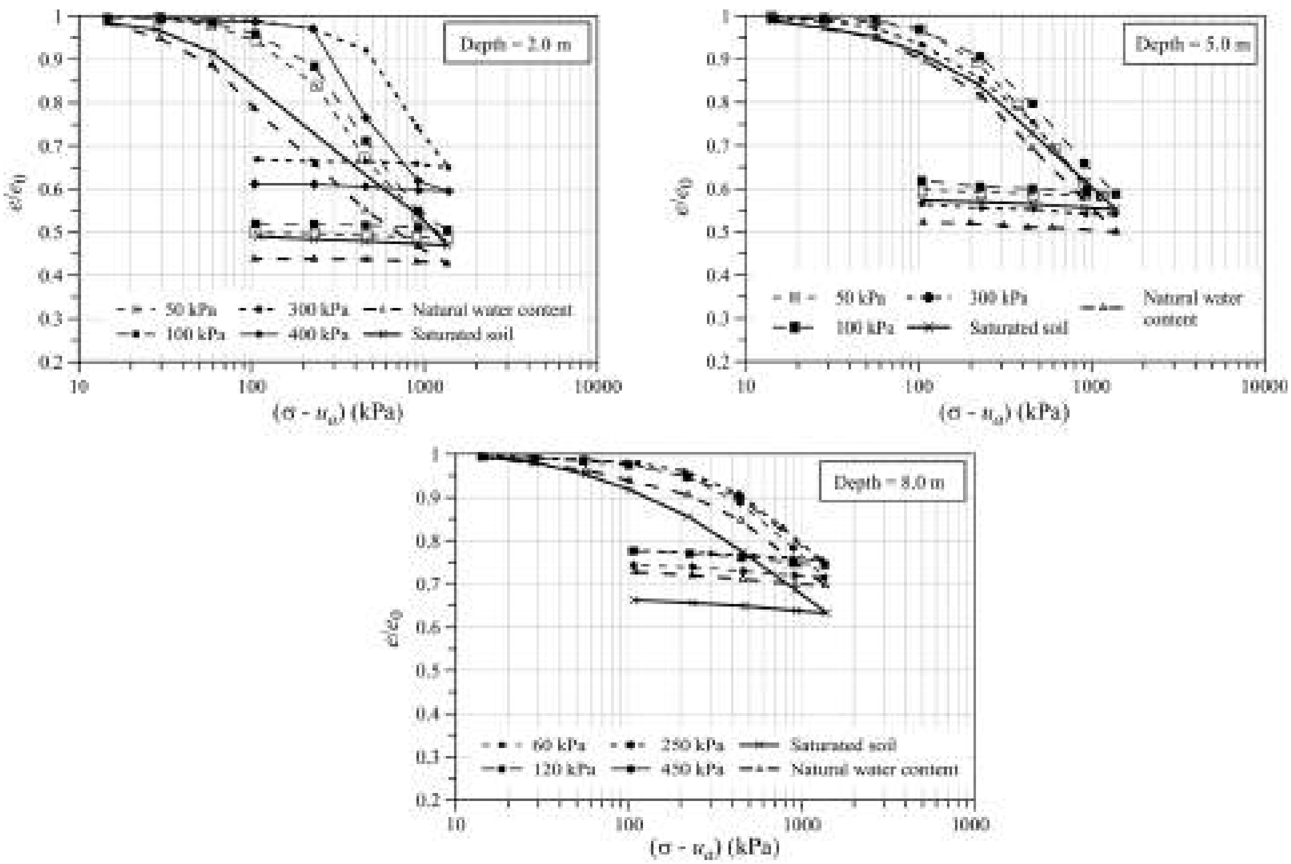

Figure 4 - Data of the oedometer tests performed on undisturbed soil samples collected at 2.0, 5.0 and 8.0 depths for soil suction values (Machado, 1998).

depth by using a helical auger to collect samples at 0.75 m intervals, to determine the water content profile and its variation in each test. The DMTs, soil sampling (undisturbed and disturbed samples), and plate load test locations are presented in Fig. 5. The average I_D, K_D and E_D profiles determined in each campaign are presented in Fig. 6.

4.2. Seasonal variability

The seasonal variability of the DMT data was assessed while considering the variation in the soil suction and water content values by means of the SWRCs. Figure 7 shows the soil suction and the water content profiles deter-

Table 1 - A summary of the plate load tests previously carried out in the study site.

Depth (m)	Designation	Loading procedure	Soil condition	Soil suction (kPa)	Author
1.5	Average curve (Q1, Q2, QS1, QS2, SS1, SS2, SS3, S-40)	Slow/Quick	Inundated	-	Costa (1999)
1.5	S1	Slow	Natural	10	Costa (1999)
1.5	S2	Slow	Natural	31	Costa (1999)
4.0	N4C1	Quick	Natural	18	Macacari (2001)
4.0	N4C2	Quick	Inundated	-	Macacari (2001)
6.0	N6C1	Quick	Natural	16	Macacari (2001)
6.0	Average curve (N6C2, S6C3, S6C4)	Quick	Inundated	-	Macacari (2001)
8.0	N8C1	Quick	Natural	4	Macacari (2001)
8.0	N8C2	Quick	Natural	6	Macacari (2001)

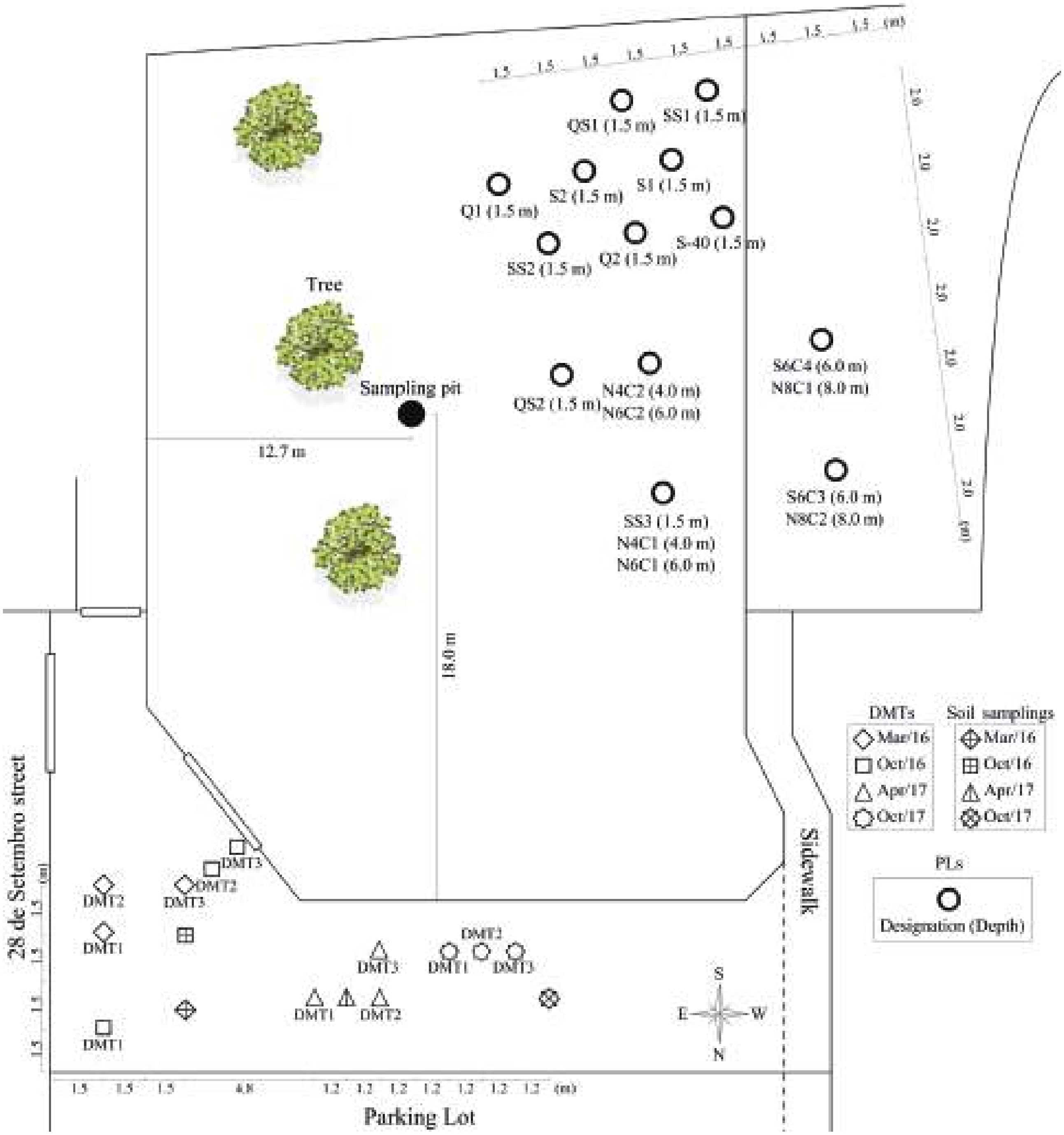

Figure 5 - Schematic representation of DMT, soil sampling and plate load tests positions at the study site.

mined during the execution of the DMT and the plate load tests.

The water content values determined in the plate load tests are similar to the water content profiles determined with the tests carried out in March and October, 2016 and April, 2017. The results of these plate load tests were those that best characterized the soil water content conditions (Fig. 7a), and they were considered in this study.

Figure 7b shows that the water content determined in the tests (ranging from 15 to 20 %) tends to be in a region of the SWRCs where a little change in water content causes a considerable change in soil suction. The tests which resulted in higher water content profiles (Mar/16 and Apr/17) showed soil suction values always lower than 10 kPa. There were significant changes in soil suction, ranging from 13 to 130 kPa up to 5.0 m depth in the dry seasons (Oct/16 and

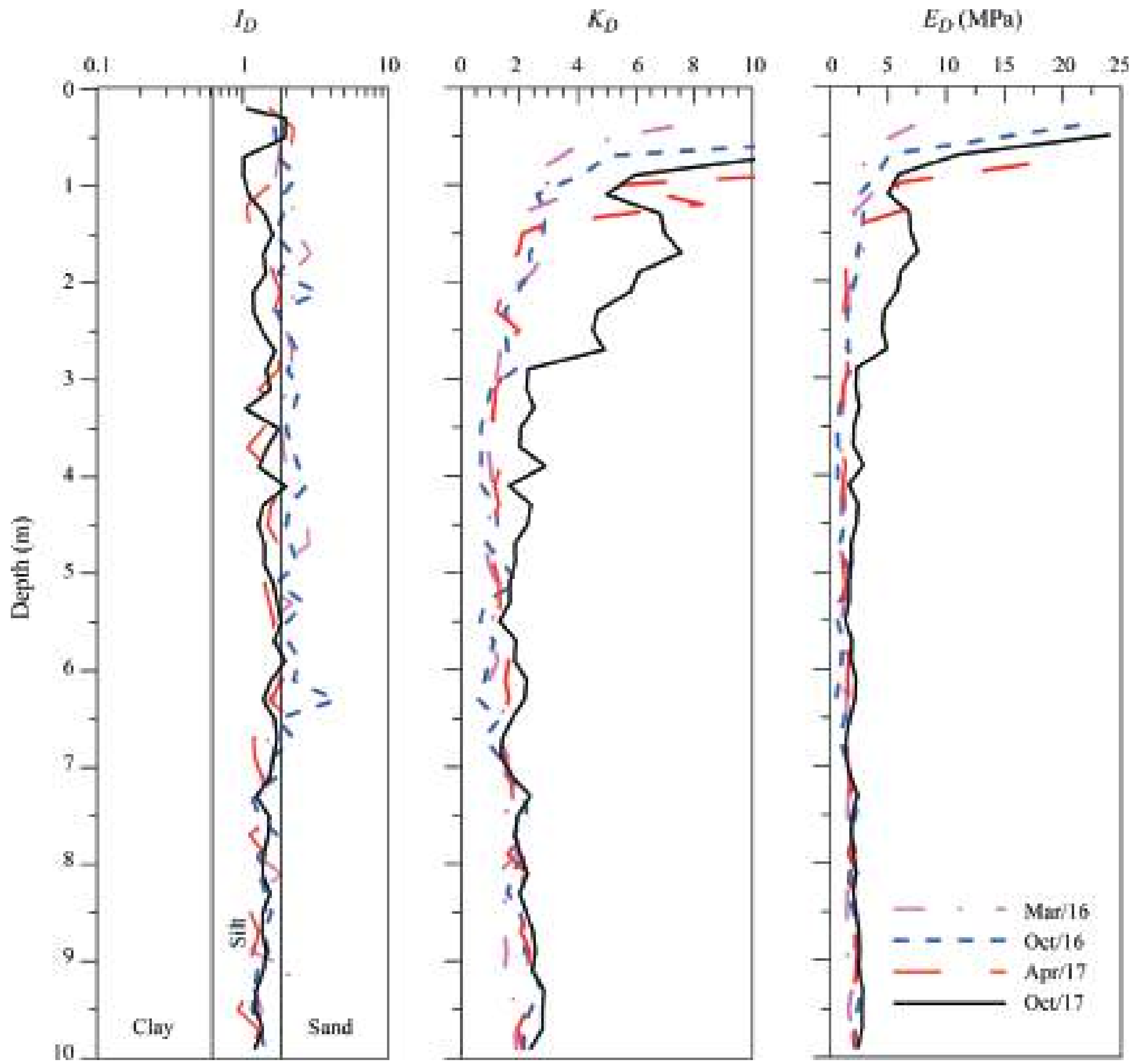

Figure 6 - I_D, K_D and E_D profiles at the study site (adapted from Rocha, 2018).

Oct/17). It is important to investigate the changes in soil suction, mainly for the design of foundations because the bearing capacity of shallow foundations is directly influenced by soil suction (Costa, 1999 and Reznik, 1994).

4.3. Constrained modulus by the DMT

Seasonal variability influences the average *MDMT* and *MDV* profiles determined in each *in situ* test campaign, as shown in Fig. 8. M_{DV} is not really affected by seasonal variability, while M_{DMT} is, mainly up to 5.0 m depth in the tests conducted in Oct/17. This occurs because both parameters (E_D and K_D) are influenced by soil suction in the studied soil, as shown by Rocha (2018). The ratio between E_D and K_D is used to calculate M_{DV} (Eq. 5), and it hides the influence of suction on the prediction of the load-settlement curve. Another relevant aspect of M_{DV} is the possibility of considering the soil anisotropy by using the inherent anisotropy factor (f_{aniso}). As the investigated soil suffered intense pedogenetic and morphogenetic processes during its formation (tropical soil), which led to a homogeneous and isotropic soil (Vaz, 1996), corrections due to the soil anisotropy are not relevant.

5. Load-Settlement Curves

The DMT and plate load test data obtained in different periods of the year were used to predict the complete load-settlement curves as described by Dos Santos *et al.* (2019).

The DMTs carried out in Mar/16 and Apr/17 were considered representative of the wet season, and the tests carried out in Oct/16 were considered representative of the dry season based on the water content profile and soil water retention curves (Fig. 7). Considering the unsaturated condition makes it possible to assess the seasonal variability influence on the prediction of the load-settlement curves by the DMT. The DMTs carried out in Oct/17 were not considered to predict the complete load-settlement curves because the *in-situ* soil suction values measured by tensiometers (4

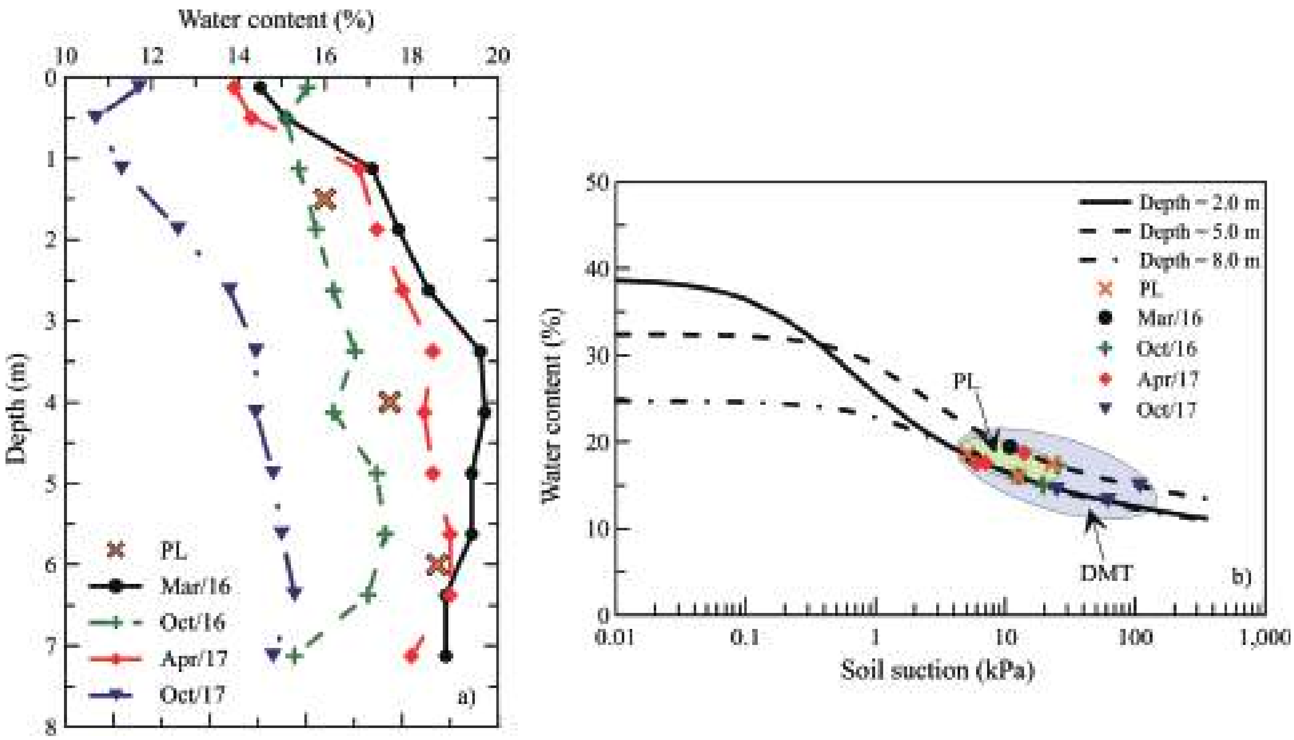

Figure 7 - a) Water content profiles determined during the execution of the DMT and the plate load tests (PL); b) Soil suction for each DMT and plate load tests (PL) by means of the SWRCs.

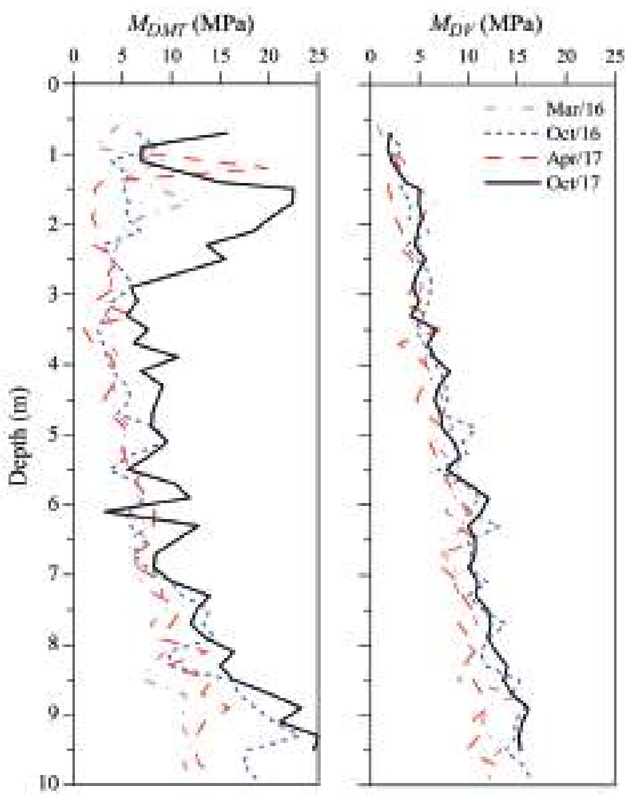

Figure 8 - Average M_{DMT} and M_{DV} profiles determined by DMT tests.

to 31 kPa) or estimated by the water content profile and the SWRCs (5 to 23 kPa) during the plate load tests did not reach values as high as those estimated by the water content profile and the SWRCs during the DMT campaign (25 to 130 kPa), as can be seen in Fig. 7.

The prediction of the load-settlement curves for the wet and dry conditions was made by using the average M_{DMT} values within the zone of influence of the foundation element, considered equal to $2B$ (B = 0.80 m). The curves were also predicted by considering the average M_{DMT} values plus and minus one standard deviation, to represent the site variability.

The load-settlement predictions for the wet condition were compared with the inundated plate load tests and the plate load tests with soil suction (ψ) lower than 10 kPa (Fig. 9). The load-settlement predictions for the dry condition were compared with the plate load tests carried out with soil suction (ψ) values between 15, 18 and 31 kPa (Fig. 10). For both conditions, the load-settlement curve prediction was carried out for different embedment depths (1.5, 4.0, 6.0 and 8.0 m depths).

The load-settlement curves determined with the DMT are in good agreement with the plate load test results (Fig. 9 and Fig. 10), mainly for the dry condition. All the load-settlement curves were in the region delimited by the average M_{DMT} values plus and minus one standard deviation (σ),

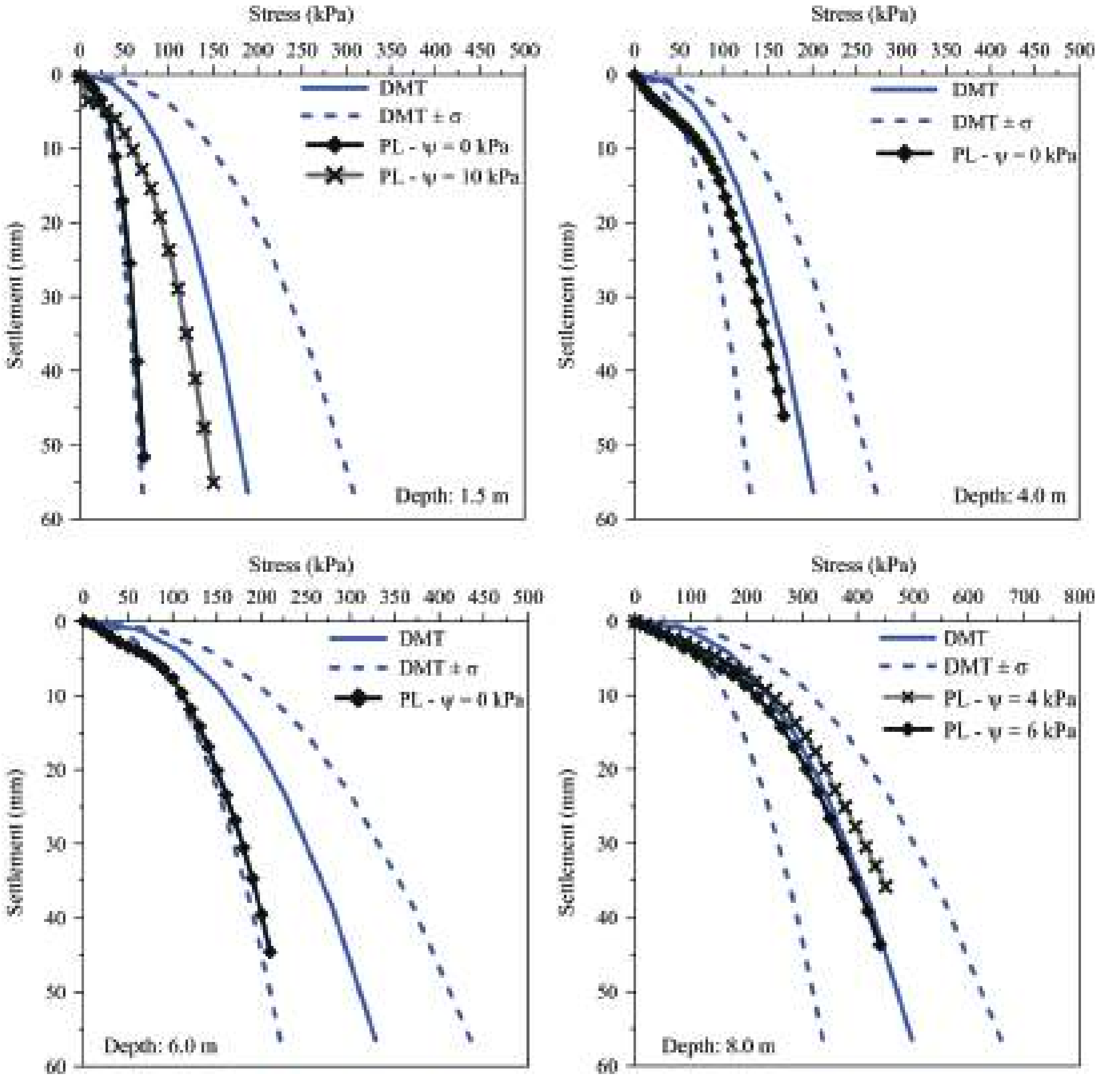

Figure 9 - Load-settlement curves predicted by the DMT and determined by the plate load tests for the wet season condition (Costa, 1999; Macacari, 2001; Rocha, 2018).

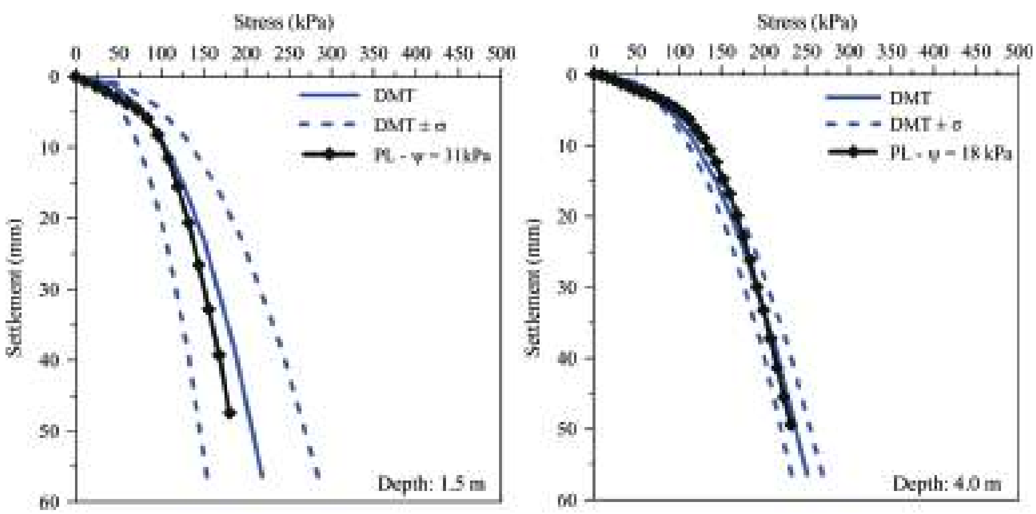

Figure 10 - Load-settlement curves predicted by the DMT and determined by the plate load tests for the dry season condition (Costa, 1999; Macacari, 2001; Rocha, 2018).

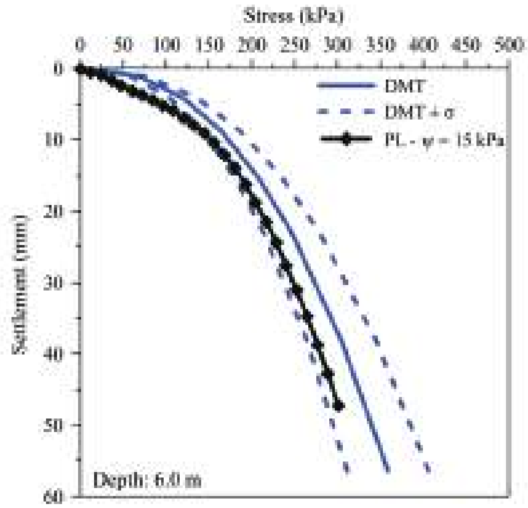

Figure 10 (cont.) - Load-settlement curves predicted by the DMT and determined by the plate load tests for the dry season condition (Costa, 1999; Macacari, 2001; Rocha, 2018).

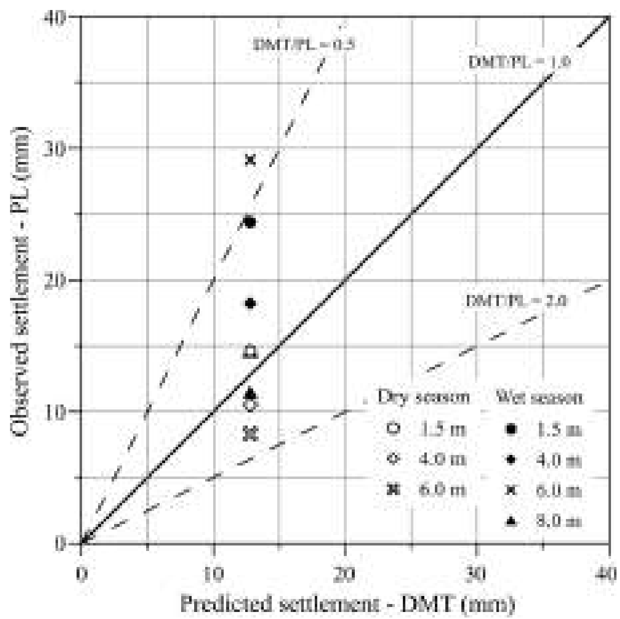

Figure 11 - Settlements predicted by the DMT *vs.* those measured by the plate load tests for the wet and dry seasons.

which is expected considering the (seasonal and spatial) variability of the investigated site.

Figure 11 shows the differences between the settlements predicted by the DMT for the working condition (δ/B_{eq} = 1.8 %, *i.e.* for 12.78 mm) and those measured by the plate load tests for both the wet and dry conditions. Good agreement was observed, since most of the data points are within the satisfactory range indicated by Monaco *et al.* (2006).

6. Conclusions

The prediction of the complete load-settlement curves for shallow foundations using the DMT and the influence of seasonal variability on this prediction was discussed.

The DMT is an adequate test for predicting soil stiffness, and the presented procedure allows providing a good estimate of the complete load-settlement curves for the study site.

The DMT also works well for predicting settlements in the working conditions, as presented and discussed by Marchetti *et al.* (2001), with the advantage of not requiring the collection of undisturbed samples and performance of laboratory tests.

In addition, the M_{DMT} profiles were influenced by soil suction (ψ) up to around 5.0 m depth in the study site. For this reason, seasonal variability should be considered in the prediction of load-settlement curves in unsaturated tropical soils, as the one herein.

Acknowledgments

The authors gratefully acknowledge the financial support from the São Paulo Research Foundation (FAPESP) for this research (Grant No.2015/17260-0). They also thank the M.Sc. scholarship from the National Council for Scientific and Technological Development (CNPq) for the first author and the Ph.D. scholarship from the Coordination of Improvement of Higher Education Personnel (CAPES) for the second author.

References

Amoroso, S.; Rollins, K.M.; Monaco, P. & Thorp, A. (2015). Use of SDMT testing for measuring soil densification by ground improvement in Christchurch, New Zealand. Proc. 3rd International Conference on the Flat Dilatometer, Roma, DMT 15, v. 1. p. 177-184.

Anderson, J.B.; Townsend, F.C. & Rahelison, L. (2007). Load testing and settlement prediction of shallow foundation. Journal of Geotechnical and Geoenvironmental Engineering, 133(12):1494-1502. DOI: 10.1061/(ASCE)1090-0241(2007)133:12(1494).

Briaud, J.L. (2007). Spread footings in sand: Load settlement curve approach. Journal of Geotechnical and Geoenvironmental Engineering, 133(8):905-920. DOI:10.1061/(ASCE)1090-0241(2007)133:8(905).

Consoli, N.C.; Schnaid, F. & Milititsky, J. (1998). Interpretation of plate load tests on residual soil site. Journal of Geotechnical and Geoenvironmental Engineering, 124(9):857-867. DOI: 10.1061/(ASCE)1090-0241(1998)124:9(857).

Costa, Y.K.J. (1999). Study of the Behavior of an Unsaturated Soil through Plate Load Tests. M.Sc. Thesis, Department of Geotechnical Engineering, University of São Paulo, São Carlos, 138 p. (in Portuguese).

Décourt, L. (1999). Behavior of foundations under working load conditions. Proc. 11th Pan-American Conference on Soil Mechanics and Geotechnical Engineering, 4: pp. 453-488. London: International Society for Soil Mechanics and Geotechnical Engineering.

Dos Santos, R.A.; Rocha, B.P. & Giacheti, H.L. (2019). DMT for load-settlement curve prediction in a tropical sandy soil compared to plate load tests. Geotechnical Testing Journal, 43 (in press). DOI:/10.1520/GTJ20180079.

Failmezger, R.; Till, P.; Frizzell, J. & Kight, S. (2015). Redesign of shallow foundations using dilatometer tests - More case studies after DMT'06 Conference. Proc. 3rd International Conference on the Flat Dilatometer, Rome, DMT 15, v. 1. p. 83-91.

Giacheti, H.L.; Bezerra, R.C.; Rocha, B.P. & Rodrigues, R.A. (2019). Seasonal influence in CPT: An unsaturated soil site example. Journal of Rock Mechanics and Geotechnical Engineering, 11(2):361-368. DOI: 10.1016/J.JRMGE.2018.10.005.

Lehane, B.M. & Fahey, M. (2004). Using SCPT and DMT data for settlement prediction in sand. Proc. 2nd International Conference on Site Characterization ISC'2, Rotterdam, the Netherlands: Millpress Science, pp. 1673-1680.

Macacari, M.F. (2001). Variation of the Bearing Capacity with Suction and Depth in Plate Load Tests in Collapsible Soil. M.Sc. Thesis, Department of Geotechnical Engineering, University of São Paulo, São Carlos, 96 p. (in Portuguese).

Machado, S.L. (1998). Application of Elasto-Plasticity Concepts to Unsaturated Soils. Ph.D. Dissertation, Department of Geotechnical Engineering, University of São Paulo, São Carlos, 361 p. (in Portuguese).

Machado, S.L. & Vilar, O.M. (1998). Shear strength of unsaturated soil: Lab tests and predicting equations. Solos e Rochas, 21(2):65-78. (in Portuguese).

Machado, S.L. & Vilar, O.M. (2003). Geotechnical Characteristics of an Unsaturated Soil Deposit at São Carlos, Brazil. Characterization and Engineering Properties of Natural Soils. Tan *et al.* (eds.), Swets & Zeitlinger, Lisse, pp. 1305-1321.

Marchetti, S. (1980). *In situ* tests by flat dilatometer. Journal of Geotechnical Engineering Division, 106(3):299-331.

Marchetti, S. & Monaco, P. (2018). Recent improvements in the use, interpretation, and applications of DMT and SDMT in practice. Geotechnical Testing Journal, 41(5):837-850. DOI: 10.1520/GTJ20170386.

Marchetti, S.; Monaco, P.; Totani, G. & Calabrese, M. (2001). The Flat Dilatometer Test (DMT) in soil investigations: A Report by the ISSMGE Committee TC16. Proc. 2nd International Flat Dilatometer Conference. Reston, VA: American Society of Civil Engineers, pp. 7-48.

Marchetti, S.; Totani, G.; Calabrese, M. & Monaco, P. (1991). P-y curves from DMT data for piles driven in clay. Proc. 4th Int. Conf. on Piling and Deep Foundations, DFI, Stresa, v. 1, p. 263-272.

Mayne, P.W. (2001). Stress-Strain-Strength-Flow Parameters from Enhanced In-situ Tests. Proc. International Conference on In-Situ Measurement of Soil Properties & Case Histories. Parahyangan Catholic University, Bandung, pp. 27-41.

Mayne, P.W.; Brown, D.; Vinson, J.; Schneider, J.A. & Finke, K.A. (2000). Site characterization of Piedmont residual soils at the NGES, Opelika, Alabama. Proc. National Geotechnical Experimentation Sites, GSP 93, edited by Benoît, J. & Lutenegger, A.J.. ASCE, Reston, pp. 160-185. DOI:10.1061/9780784404843.ch07.

Menegotto, M.L. (2004). Stress-settlement curve predicton of plate load tests on unsaturated soil. Department of

Geotechnical Engineering, University of São Paulo, São Carlos, 219 p. (in Portuguese).

Monaco, P.; Amoroso, S.; Marchetti, S.; Marchetti, D.; Totani, G.; Cola, S. & Simonini, P. (2014). Overconsolidation and stiffness of Venice Lagoon sands and silts from SDMT and CPTU. J. Geotech. Geoenviron. Eng., 140(1):215-227. DOI: 10.1061/(ASCE)GT.1943-5606.0000965.

Monaco, P.; Totani, G. & Calabrese, M. (2006). DMT-Predicted *vs.* observed settlements: A review of the available experience. Proc. Conf. On the Flat Dilatometer, Washington D.C., pp. 244-252.

Queiroz, A.C.G.; Camapum de Carvalho, J. & Guimarães, R.C. (2012). Using DMT to determine overconsolidation ratio (OCR) in compacted fills. Soils & Rocks, 35(2):161-167.

Reznik, Y.M. (1994). A method for interpretation of plate load test results. Geotechnical Testing Journal, 17(1):72-79.

Reznik, Y.M. (1993). Plate load tests of collapsible soils. Journal of Geotechnical Engineering, ASCE, 119(3):608-615.

Robertson, P.K.; Davies, M.P. & Campanella, R.G. (1987). Design of laterally loaded driven piles using the flat dilatometer. Geotechnical Testing Journal, 12(1):30-38.

Rocha, B.P. (2018). Geotechnical Characterization of Unsaturated Tropical Soils by In Situ Tests. Ph.D. Thesis. Dissertation, Department of Geotechnical Engineering, University of São Paulo, São Carlos, 240 p. (in Portuguese).

Schmertmann, J.H. (1986). Dilatometer to compute foundation settlement. Proc. In Situ `86, GSP No. 6, Reston, VA: American Society of Civil Engineers, pp. 303-321.

Shin, E.C. & Das, B.M. (2011). Developments in elastic settlement estimation procedures for shallow foundations on granular soil. KSCE Journal of Civil Engineering, 15(1):77-89. DOI:10.1007/s12205-011-1028-9.

Tang, Y.; Vo, T.; Taiebat, H.A. & Russell, A.R. (2018). Influences of Suction on Plate Load Tests on Unsaturated Silty Sands. Journal of Geotechnical and Geoenvironmental Engineering, 144(8):04018043. https://doi.org/10.1061/(ASCE)GT.1943-5606.0001897

Vaz, L.F. (1996). Genetic classification of soils and rock weathering layers in Tropical regions. Solos e Rochas, 19(2):117-136 (in Portuguese).

SOILS and ROCKS
An International Journal of Geotechnical and Geoenvironmental Engineering

Publication of
ABMS - Brazilian Association for Soil Mechanics and Geotechnical Engineering
SPG - Portuguese Geotechnical Society
Volume 42, N. 3, September-December 2019

Author index

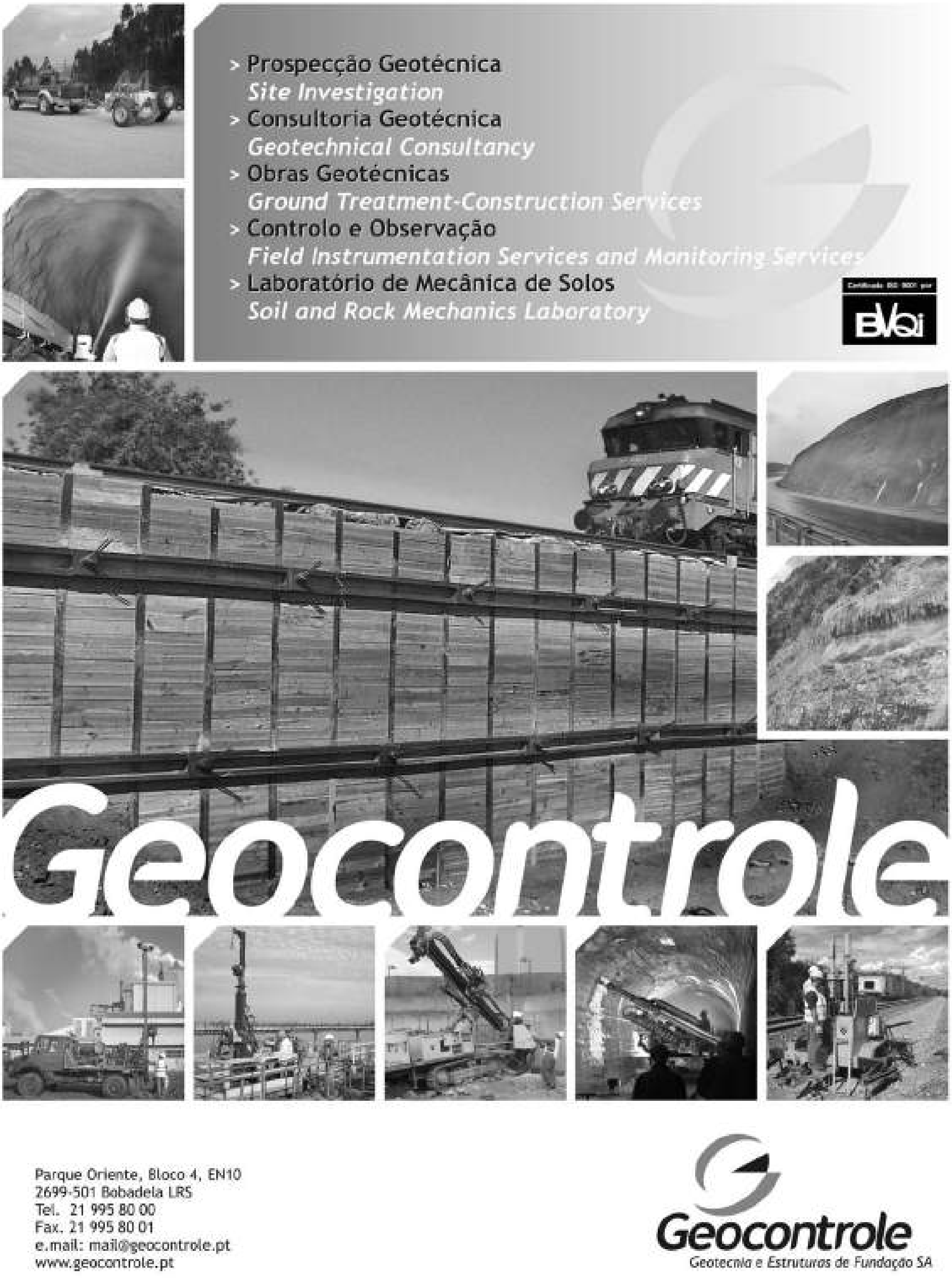

> Prospecção Geotécnica
Site Investigation
> Consultoria Geotécnica
Geotechnical Consultancy
> Obras Geotécnicas
Ground Treatment-Construction Services
> Controlo e Observação
Field Instrumentation Services and Monitoring Services
> Laboratório de Mecânica de Solos
Soil and Rock Mechanics Laboratory
BVQi
Geocontrole
Parque Oriente, Bloco 4, EN10
2699-501 Bobadela LRS
Tel. 21 995 80 00
Fax. 21 995 80 01
e.mail: mail@geocontrole.pt
www.geocontrole.pt
Geocontrole
Geotecnia e Estruturas de Fundação SA


Geotechnic and Rehabilitation

Instructions for Submission of Manuscripts

Category of the Papers

Soils and Rocks is the international scientific journal edited by the Brazilian Association for Soil Mechanics and Geotechnical Engineering (ABMS) and the Portuguese Geotechnical Society (SPG). The aim of the journal is to publish (in English) original research and technical works on all geotechnical branches.

According to its content the accepted paper is classified in one of the following categories: Article paper, Technical Note, Case Study or Discussion. An article paper is an extensive and conclusive dissertation about a geotechnical topic. A paper is considered as a technical note if it gives a short description of ongoing studies, comprising partial results and/or particular aspects of the investigation. A case study is a report of unusual problems found during the design, construction or the performance of geotechnical projects. A case study is also considered as the report of an unusual solution given to an ordinary problem. The discussions about published papers, case studies and technical notes are made in the Discussions Section.

When submitting a manuscript for review, the authors should indicate the category of the manuscript, and is also understood that they:

a) assume full responsibility for the contents and accuracy of the information in the paper;

b) assure that the paper has not been previously published, and is not being submitted to any other periodical for publication.

Manuscript Instructions

Manuscripts must be written in English. The text is to be typed in a word processor (preferably MS Word), **single column**, using ISO A4 page size, left, right, top, and bottom margins of 25 mm, Times New Roman 12 font, and line spacing of 1.5. All lines and pages should be numbered. The text should be written in the third person.

The first page of the manuscript must include the title of the paper followed by the names of the authors with the abbreviation of the most relevant academic title. The affiliation, address and e-mail must appear below each author´s name. An abstract of 200 words follows after the author´s names. A list with up to six keywords at the end of the abstract is required.

Although variations on the sequence and title of each section are possible, it is suggested that the text contains the following sections: Introduction, Material and Methods, Results, Discussions, Conclusions, Acknowledgements, References and List of Symbols. A brief description of each section is given next.

Introduction: This section should indicate the state of the art of the problem under evaluation, a description of the problem and the methods undertaken. The objective of the work should be clearly presented at the end of the section.

Materials and Methods: This section should include all information needed to the reproduction of the presented work by other researchers.

Results: In this section the data of the investigation should be presented in a clear and concise way. Figures and tables should not repeat the same information.

Discussion: The analyses of the results should be described in this section.

Conclusions: The content of this section should be based on the data and on the discussions presented.

Acknowledgenments: If necessary, concise acknowledgements should be presented in this section.

References: References to other published sources must be made in the text by the last name(s) of the author(s), followed by the year of publication, similarly to one of the two possibilities below:

…while Silva & Pereira (1987) observed that resistance depended on soil density… or *It was observed that resistance depended on soil density (Silva & Pereira, 1987).*

In the case of three or more authors, the reduced format must be used, *e.g.*: Silva *et al.* (1982) or (Silva *et al.*, 1982). Two or more citations belonging to the same author(s) and published in the same year are to be distinguished with small letters, *e.g.*: (Silva, 1975a, b, c.). Standards must be cited in the text by the initials of the entity and the year of publication, *e.g.*: ABNT (1996), ASTM (2003).

Full references shall be listed alphabetically at the end of the text by the first author´s last name. Several references belonging to the same author shall be cited chronologically. Some examples are listed next:

Papers: Bishop, A.W. & Blight, G.E. (1963). Some aspects of effective stress in saturated and unsaturated soils. Geotechnique, 13(2):177-197.

Books: Lambe, T.W. & Whitman, R.V. (1979). Soil Mechanics, SI Version. John Wiley & Sons, New York, 553 p.

Book with editors: Sharma, H.D.; Dukes, M.T. & Olsen, D.M. (1990). Field measurements of dynamic moduli and Poisson's ratios of refuse and underlying soils at a landfill site. Landva, A. & Knowles, G.D. (eds), Geotechnics of Waste Fills - Theory and Practice, American Society for Testing and Materials - STP 1070, Philadelphia, pp. 57-70.

Proceedings (printed matter or CD-ROM): Jamiolkowski, M.; Ladd, C.C.; Germaine, J.T. & Lancellotta, R. (1985). New developments in field and laboratory testing of soils. Proc. 11th Int. Conf. on Soil Mech. and Found. Engn., ISSMFE, San Francisco, v. 1, pp. 57-153. (specify if CD ROM).

Thesis and dissertations: Lee, K.L. (1965). Triaxial Compressive Strength of Saturated Sands Under Seismic Loading Conditions. PhD Dissertation, Department of Civil Engineering, University of California, Berkeley, 521 p.

Standards: ASTM (2003). Standard Test Method for Particle Size Analysis of Soils - D 422-63. ASTM International, West Conshohocken, Pennsylvania, USA, 8 p.

Internet references: Soils and Rocks available at http://www.abms.com.br and downloaded on August 6th 2003.

On line first publications must also bring the digital object identifier (DOI) at the end.

Figures shall be either computer generated or drawn with India ink on tracing paper. Computer generated figures must be accompanied by the corresponding digital file (.tif, .jpg, .pcx, etc.). All figures (graphs, line drawings, photographs, etc.) shall be numbered consecutively and have a caption consisting of the figure number and a brief title or description of the figure. This number should be used when referring to the figure in text. Photographs should be black and white, sharp, high contrasted and printed on glossy paper.

Tables shall be numbered consecutively in Arabic and have a caption consisting of the table number and a brief title. This number should be used when referring to the table in the text. Units should be indicated in the first line of the table, below the title of each column. Acronyms should be avoided. When applicable, the units should come right below the corresponding column heading. Additional comments can be placed as footnotes.

Equations shall appear isolated in a single line of the text. Numbers identifying equations must be flushed with the right margin. International System (SI) units must be used. The definitions of the symbols used in the equations must appear in the List of Symbols. It is recommended that the symbols used are in accordance with Lexicon in 8 Languages, ISSMFE (1981) and the ISRM List of Symbols.

The text of the submitted manuscript (including figures, tables and references) intended to be published as an article paper or a case history should not contain more than 30 pages, formatted according to the instructions mentioned above. Technical notes and discussions should have no more than 15 and 8 pages, respectively. Longer manuscripts may be exceptionally accepted if the authors provide proper explanation for the need of the required extra space in a cover letter.

Discussion

Discussions must be written in English. The first page of a discussion should contain:

The title of the paper under discussion;

Name of the author(s) of the discussion, followed by their position, affiliation, address and e-mail. The author(s) of the discussion should refer to himself (herself/themselves) as the reader(s) and to the author(s) of the paper as the author(s).

Figures, tables and equations should be numbered following the same sequence of the original paper. All instructions previously mentioned for the preparation of article papers, case studies and technical notes also apply to the preparation of discussions.

Editorial Review

Each paper will be evaluated by reviewers selected by the editors according to the subject of the paper. The authors will be informed about the results of the review process. If the paper is accepted, the authors will be required to submit a version of the revised manuscript with the suggested modifications. If the manuscript is rejected for publication, the authors will be informed about the reasons for rejection. In any situation comprising modification of the original text, classification of the manuscript in a category different from that proposed by the authors, or rejection, the authors can reply presenting their reasons for disagreeing with the reviewer comments.

Submission

The author(s) must upload a digital file of the manuscript to the Soils and Rocks website.

Follow Up

The online management system will provide a password to the corresponding author, which will enable him/her to follow the reviewing process of the submitted manuscript at the Soils and Rocks website.

Volume 42, N. 3, September-December 2019

Table of Contents